


**(F)UV Spectral Analysis of
15 Hot, Hydrogen-Rich
Central Stars of PNe**



Dissertation
der Mathematisch-Naturwissenschaftlichen Fakultät
der Eberhard Karls Universität Tübingen
zur Erlangung des Grades eines
Doktors der Naturwissenschaften
(Dr. rer. nat.)

vorgelegt von
Marc Ziegler
aus Bad Mergentheim

Tübingen
2012

The cover picture shows the “Dumbbell Nebula”, a planetary nebula named as M 27 in the famous catalogue by french astronomer Charles Messier (1730 – 1817). The image is kindly provided by D. Goldman¹.

Tag der mündlichen Prüfung:	18.07.2013
Dekan:	Prof. Dr. W. Rosenstiel
1. Berichterstatter:	Prof. Dr. K. Werner
2. Berichterstatter:	Prof. Dott. A. Santangelo

¹<http://astrodonimaging.com>

Contents

1	Stellar evolution	1
1.1	Pre-Main Sequence	1
1.2	From the Main Sequence to the AGB	3
1.3	AGB phase: thermal pulses, nucleosynthesis, and stellar winds	4
1.4	Post-AGB evolution	6
1.5	Spectral classification scheme for CSPNe	8
1.6	Thesis motivation	9
2	Stellar spectra	11
2.1	Stellar spectra	11
2.2	Stellar atmospheres and radiative transfer	13
2.2.1	Physical assumptions	13
2.2.2	Radiative transfer equation	15
2.3	Numerical modeling of stellar spectra with <i>TMAP</i>	15
2.3.1	Preparatory steps	15
2.3.1.1	Atomic data	16
2.3.1.2	IrOnIc	17
2.3.1.3	Frequency grid	19
2.3.2	Numerical solution of the radiative transfer equation	19
2.3.3	Synthetic spectra	19
2.3.4	<i>OWENS</i>	19
3	Observations	21
3.1	<i>FUSE</i>	21
3.2	<i>HST</i>	22
3.3	<i>IUE</i>	22
3.4	Optical observations	22

4	The Sample Objects	25
4.1	DAO-type ionizing stars	26
4.1.1	Abell 7	26
4.1.2	Abell 31	27
4.1.3	Abell 35	28
4.1.4	Abell 39	29
4.1.5	NGC 3587	29
4.1.6	NGC 6720	30
4.1.7	NGC 6853	31
4.1.8	NGC 7293	32
4.1.9	PuWe 1	33
4.1.10	Sh 2-174	34
4.2	O(H)-type ionizing stars	35
4.2.1	Abell 36	35
4.2.2	Lo 1	36
4.2.3	LSS 1362	36
4.2.4	NGC 1360	37
4.2.5	NGC 4361	39
5	Analysis method	43
5.1	General aspects	43
5.2	Interstellar absorption and reddening	43
5.3	Effective temperature and surface gravity	46
5.4	Abundances	47
5.4.1	Hydrogen and helium	49
5.4.2	Carbon, nitrogen, and oxygen	49
5.4.3	From fluorine to argon	50
5.4.4	Iron-group elements	51
5.5	Mass, luminosity, and distance	51
5.6	Radial velocity	55
6	Results and discussion	57
6.1	General results	57
6.1.1	Mean mass	57
6.1.2	Luminosities	60
6.1.3	Distances	60
6.1.4	Chemical abundances	60
6.2	Individual results	65
6.2.1	Individual results for DAO-type stars	67
6.2.1.1	A 7	67

6.2.1.2	A 31	68
6.2.1.3	A 35	69
6.2.1.4	A 39	72
6.2.1.5	NGC 3587	73
6.2.1.6	NGC 6720	73
6.2.1.7	NGC 6853	75
6.2.1.8	NGC 7293	77
6.2.1.9	PuWe 1	78
6.2.1.10	Sh 2–174	78
6.2.2	Summary for the DAO-type WDs	80
6.2.3	Individual results for O(H)-type stars	82
6.2.3.1	A 36	82
6.2.3.2	Lo 1	84
6.2.3.3	LSS 1362	84
6.2.3.4	NGC 1360	85
6.2.3.5	NGC 4361	87
6.2.4	Summary for the O(H)-type WDs	88
7	Conclusions	93
A	Atomic-data statistics	102
B	Observational details	105
C	Solar abundances	107
D	Determination of n_{HI} and $E_{\text{B}-\text{V}}$	108
D.1	A 7	109
D.2	A 31	110
D.3	A 35	111
D.4	A 39	112
D.5	NGC 3587	113
D.6	NGC 6720	114
D.7	NGC 6853	115
D.8	NGC 7293	116
D.9	PuWe 1	117
D.10	Sh 2 – 174	118
D.11	A 36	119
D.12	Lo 1	120
D.13	LSS 1362	121
D.14	NGC 1360	122

D.15 NGC 4361	123
E Line fits for individual elements and abundances	124
E.1 A 7	125
E.2 A 31	129
E.3 A 35	133
E.4 A 39	141
E.5 NGC 3587	145
E.6 NGC 6720	149
E.7 NGC 6853	153
E.8 NGC 7293	161
E.9 PuWe 1	169
E.10 Sh 2 – 174	173
E.11 A 36	181
E.12 Lo 1	185
E.13 LSS 1362	189
E.14 NGC 1360	197
E.15 NGC 4361	205
F List of Acronyms	209
G Acknowledgements	211

List of Figures

1.1	Hertzsprung-Russell diagram	2
1.2	AGB star interior	5
1.3	Time evolution of the interior of an AGB star between two TP	6
1.4	Nuclei chart	7
2.1	Spectrum of the Sun	12
2.2	Radiative transfer through a plane-parallel atmosphere	16
2.3	Temperature and density stratification, and ionization fractions of all elements (example)	18
3.1	<i>IUE</i> , <i>FUSE</i> , and <i>HST</i>	22
3.2	Optical path of the <i>FUSE</i> instrument	23
4.1	Images of A 7 and A 31	27
4.2	Images of A 35 and A 39	28
4.3	Images of NGC 3587 and NGC 6720	30
4.4	Images of NGC 6853 and NGC 7293	31
4.5	Images of PuWe 1 and Sh 2–174	33
4.6	Images of A 36 and Lo 1	35
4.7	Images of LSS 1362 and NGC 1360	37
4.8	Image of NGC 4361	39
5.1	Calculated model grid	44
5.2	Example for determination of E_{B-V}	45
5.3	Example for determination of n_{HI}	46
5.4	Example for a combined photospheric model SED + ISM model template	47
5.5	Examples for determination of T_{eff} and $\log g$	48
5.6	Flow diagram of abundance determination	49
5.7	Optical H and He lines in LSS 1362	50
5.8	$\log T_{\text{eff}} - \log g$ diagram for mass determination	53
5.9	Determination of stellar magnitudes from SED fits	54
6.1	$\log T_{\text{eff}} - \log g$ diagram (all objects)	58
6.2	$T_{\text{eff}} - \log g$ diagram for post-EHB stars (A 35, Sh 2–174)	59
6.3	Mass distribution of analyzed stars	60

6.4	Comparison of derived distances with literature values	61
6.5	Photospheric abundances of A 7	67
6.6	Photospheric abundances of A 31	69
6.7	Photospheric abundances of A 35	70
6.8	Cr, Mn, Co, Ni lines in A 35	71
6.9	Photospheric abundances of A 39	72
6.10	Photospheric abundances of NGC 3587	74
6.11	Photospheric abundances of NGC 6720	75
6.12	Photospheric abundances of NGC 6853	76
6.13	Photospheric abundances of NGC 7293	77
6.14	Photospheric abundances of PuWe 1	79
6.15	Photospheric abundances of Sh 2–174	80
6.16	Cr, Mn, Co, Ni lines in Sh 2–174	81
6.17	Photospheric abundances of A 36	82
6.18	Photospheric abundances of Lo 1	83
6.19	Photospheric abundances of LSS 1362	85
6.20	Photospheric abundances of NGC 1360	86
6.21	Photospheric abundances of NGC 4361	88
6.22	Chemistry of sample stars depending on T_{eff}	90
6.23	Chemistry of sample stars depending on $\log(T_{\text{eff}}^4/g)$	91
D.1	n_{HI} and $E_{\text{B-V}}$: A 7	109
D.2	n_{HI} and $E_{\text{B-V}}$: A 31	110
D.3	n_{HI} and $E_{\text{B-V}}$: A 35	111
D.4	n_{HI} and $E_{\text{B-V}}$: A 39	112
D.5	n_{HI} and $E_{\text{B-V}}$: NGC 3587	113
D.6	n_{HI} and $E_{\text{B-V}}$: NGC 6720	114
D.7	n_{HI} and $E_{\text{B-V}}$: NGC 6853	115
D.8	n_{HI} and $E_{\text{B-V}}$: NGC 7293	116
D.9	n_{HI} and $E_{\text{B-V}}$: PuWe 1	117
D.10	n_{HI} and $E_{\text{B-V}}$: Sh 2 – 174	118
D.11	n_{HI} and $E_{\text{B-V}}$: A 36	119
D.12	n_{HI} and $E_{\text{B-V}}$: Lo 1	120
D.13	n_{HI} and $E_{\text{B-V}}$: LSS 1362	121
D.14	n_{HI} and $E_{\text{B-V}}$: NGC 1360	122
D.15	n_{HI} and $E_{\text{B-V}}$: NGC 4361	123
E.1	A 7: C, N, and O lines (<i>FUSE</i>)	125
E.2	A 7: F, Si, P, S, and Ar lines (<i>FUSE</i>)	126
E.3	A 7: Fe lines (<i>FUSE</i>)	127
E.4	A 31: C, N, and O lines (<i>FUSE</i>)	129
E.5	A 31: F, Si, P, S, and Ar lines (<i>FUSE</i>)	130

E.6	A 31: Fe lines (<i>FUSE</i>)	131
E.7	A 35: C, N, and O lines (<i>FUSE</i>)	133
E.8	A 35: He, C, N, and O lines (<i>STIS</i>)	134
E.9	A 35: F, Si, P, S, and Ar lines (<i>FUSE</i>)	135
E.10	A 35: Ne, Mg, Al, Si, and Ar lines (<i>STIS</i>)	136
E.11	A 35: Fe lines (<i>FUSE</i>)	137
E.12	A 35: Fe lines (<i>STIS</i>)	138
E.13	A 39: C, N, and O lines (<i>FUSE</i>)	141
E.14	A 39: F, Si, P, S, and Ar lines (<i>FUSE</i>)	142
E.15	A 39: Fe lines (<i>FUSE</i>)	143
E.16	NGC 3587: C, N, and O lines (<i>FUSE</i>)	145
E.17	NGC 3587: F, Si, P, S, and Ar lines (<i>FUSE</i>)	146
E.18	NGC 3587: Fe lines (<i>FUSE</i>)	147
E.19	NGC 6720: C, N, and O lines (<i>FUSE</i>)	149
E.20	NGC 6720: F, Si, P, S, and Ar lines (<i>FUSE</i>)	150
E.21	NGC 6720: Fe lines (<i>FUSE</i>)	151
E.22	NGC 6853: C, N, and O lines (<i>FUSE</i>)	153
E.23	NGC 6853: He, C, N, and O lines (<i>STIS</i>)	154
E.24	NGC 6853: F, Si, P, S, and Ar lines (<i>FUSE</i>)	155
E.25	NGC 6853: Ne, Mg, Al, Si, and Ar lines (<i>STIS</i>)	156
E.26	NGC 6853: Fe lines (<i>FUSE</i>)	157
E.27	NGC 6853: Fe lines (<i>STIS</i>)	158
E.28	NGC 6853: H and He lines (optical)	159
E.29	NGC 7293: C, N, and O lines (<i>FUSE</i>)	161
E.30	NGC 7293: He, C, N, and O lines (<i>STIS</i>)	162
E.31	NGC 7293: F, Si, P, S, and Ar lines (<i>FUSE</i>)	163
E.32	NGC 7293: Ne, Mg, Al, Si, and Ar lines (<i>STIS</i>)	164
E.33	NGC 7293: Fe lines (<i>FUSE</i>)	165
E.34	NGC 7293: Fe lines (<i>STIS</i>)	166
E.35	NGC 7293: H and He lines (optical)	167
E.36	PuWe 1: C, N, and O lines (<i>FUSE</i>)	169
E.37	PuWe 1: F, Si, P, S, and Ar lines (<i>FUSE</i>)	170
E.38	PuWe 1: Fe lines (<i>FUSE</i>)	171
E.39	Sh 2 – 174: C, N, and O lines (<i>FUSE</i>)	173
E.40	Sh 2 – 174: He, C, N, and O lines (<i>STIS</i>)	174
E.41	Sh 2 – 174: F, Si, P, S, and Ar lines (<i>FUSE</i>)	175
E.42	Sh 2 – 174: Ne, Mg, Al, Si, and Ar lines (<i>STIS</i>)	176
E.43	Sh 2 – 174: Fe lines (<i>FUSE</i>)	177
E.44	Sh 2 – 174: Fe lines (<i>STIS</i>)	178
E.45	A 36: He, C, N, and O lines (<i>STIS</i>)	181

E.46	A 36: Ne, Mg, Al, Si, and Ar lines (<i>STIS</i>)	182
E.47	A 36: Fe lines (<i>STIS</i>)	183
E.48	Lo 1: C, N, and O lines (<i>FUSE</i>)	185
E.49	Lo 1: F, Si, P, S, and Ar lines (<i>FUSE</i>)	186
E.50	Lo 1: Fe lines (<i>FUSE</i>)	187
E.51	LSS 1362: C, N, and O lines (<i>FUSE</i>)	189
E.52	LSS 1362: He, C, N, and O lines (<i>STIS</i>)	190
E.53	LSS 1362: F, Si, P, S, and Ar lines (<i>FUSE</i>)	191
E.54	LSS 1362: Ne, Mg, Al, Si, and Ar lines (<i>STIS</i>)	192
E.55	LSS 1362: Fe lines (<i>FUSE</i>)	193
E.56	LSS 1362: Fe lines (<i>STIS</i>)	194
E.57	LSS 1362: H and He lines (optical)	195
E.58	NGC 1360: C, N, and O lines (<i>FUSE</i>)	197
E.59	NGC 1360: He, C, N, and O lines (<i>STIS</i>)	198
E.60	NGC 1360: F, Si, P, S, and Ar lines (<i>FUSE</i>)	199
E.61	NGC 1360: Ne, Mg, Al, Si, and Ar lines (<i>STIS</i>)	200
E.62	NGC 1360: Fe lines (<i>FUSE</i>)	201
E.63	NGC 1360: Fe lines (<i>STIS</i>)	202
E.64	NGC 1360: H and He lines (optical)	203
E.65	NGC 4361: He, C, N, and O lines (<i>STIS</i>)	205
E.66	NGC 4361: Ne, Mg, Al, Si, and Ar lines (<i>STIS</i>)	206
E.67	NGC 4361: Fe lines (<i>STIS</i>)	207

List of Tables

4.1	Names of the ionizing stars for the analyzed gaseous nebulae.	26
4.2	Summary of the main literature values for the sample stars .	41
5.1	Analyzed C, N, and O lines	51
5.2	Analyzed F, Ne, Na, Mg, Al, Si, P, S, and Ar lines	52
5.3	Flux values for the B, V, R, J, H, and K band	55
5.4	Lines used for the determination of v_{rad}	56
6.1	General results	64
6.2	Comparison of CS abundances with PN abundances	89
A.1	Model-atom statistics: H–Ar	103
A.2	Model-atom statistics: Ca–Ni	104
B.1	Observation log: O(H)-type ionizing stars of gaseous nebulae	105
B.2	Observation log: DAO-type ionizing stars of gaseous nebulae	106
C.1	Solar abundances	107
E.1	Abundances of A 7	128
E.2	Abundances of A 31	132
E.3	Abundances of A 35	139
E.4	Abundances of A 39	144
E.5	Abundances of NGC 3587	148
E.6	Abundances of NGC 6720	152
E.7	Abundances of NGC 6853	160
E.8	Abundances of NGC 7293	168
E.9	Abundances of PuWe 1	172
E.10	Abundances of Sh 2 – 174	179
E.11	Abundances of A 36	184
E.12	Abundances of Lo 1	188
E.13	Abundances of LSS 1362	196
E.14	Abundances of NGC 1360	204
E.15	Abundances of NGC 4361	208

Summary

The aim of this thesis was the precise determination of basic stellar parameters and metal abundances for a sample of 15 ionizing stars of gaseous nebulae. Strategic lines of metals for the expected parameter range are located in the ultraviolet (UV) and far-ultraviolet (FUV) range. Thus high-resolution, high-S/N UV and FUV observations obtained with the *Hubble Space Telescope (HST)* and the *Far Ultraviolet Spectroscopic Explorer (FUSE)* were used for the analysis. For the calculation of the necessary spectral energy distributions the *Tübingen NLTE Model-Atmosphere Package (TMAP)* was used. The model atmospheres included most elements from H–Ni in order to account for line-blanketing effects. For each object a small grid of model atmospheres was calculated. As the interstellar medium (ISM) imprints its influence in the *Space Telescope Imaging Spectrograph (STIS)* and especially the *FUSE* range, the program *OWENS* was employed to calculate the interstellar absorption features. Both, the photospheric model spectral energy distribution (SED) as well as the ISM models were combined to enable the identification of most of the observed absorption lines.

The analyzed sample covers a range of $70 \text{ kK} < T_{\text{eff}} < 136 \text{ kK}$, and surface gravities from $\log(g/\text{cm/sec}^2) \approx 5.4 - 7.4$, thus representing different stages of stellar evolution. For a large number of elements, abundances were determined for the first time in these objects. Lines of C, N, O, F, Ne, Si, P, S, and Ar allowed to determine the corresponding abundances. For none of the objects lines of Ca, Sc, Ti, and V could be found. Only a few objects were rich in Cr, Mn, Fe, Co, and Ni lines. Most of the analyzed stars exhibited only lines of Fe (ionization stages $\nu - \text{VIII}$) from the iron-group elements. No signs for gravitational settling (the gravitational force exceeds the radiation pressure and elements begin to sink from the atmosphere into deeper layers) were found. This is expected as the values of the surface gravities of the sample are still too small to start gravitational settling. For the elements C, N, O, Si, P, and S we find increasing abundances with increasing $\log(T_{\text{eff}}^4/g)$, while the abundances for Ar and Fe decrease. The latter is unexpected as the higher the T_{eff}^4/g ratio, the more the radiative force dominates the gravitational force and, thus, the elements should be kept in the atmosphere.

The determined abundances were compared with previous literature values, with abundances predicted from diffusion calculations, with abundances from Asymptotic Giant Branch (AGB) nucleosynthesis calculations, and, if available, with abundances found for the corresponding nebulae. The agreement was of mixed quality.

The derived T_{eff} and $\log g$ values confirmed some literature values while others had to be revised (e.g. for LSS 1362 and NGC 1360). However, most of them

agree with the previous literature values within the error limits. No difference in T_{eff} can be found for DAO and O(H)-type stars, but O(H)-type stars have a lower $\log g$ (5.4 – 6.0) compared to the DAOs (6.5 – 7.4). The exception is the O(H)-type central star of the planetary nebula (CSPN) of Lo 1 with $\log g = 7.0$.

A comparison of the positions of each object with stellar evolutionary tracks for post-AGB stars in the $\log T_{\text{eff}} - \log g$ diagram lead to the respective stellar masses. The derived mean mass of the analyzed sample ($\bar{M} = 0.536 \pm 0.023 M_{\odot}$) agrees within the error limits with the expected mean mass for these objects. In the literature $\bar{M} = 0.638 \pm 0.145 M_{\odot}$ can be found for DA-type white dwarfs, the immediate successors of DAO-type white dwarfs. For two objects (A 35, Sh 2–174) extremely low masses were found. For A 35 the derived mass ($M_{A35} = 0.523 \pm 0.05 M_{\odot}$) lies at the lower end of possible masses predicted for post-AGB stars. The very low mass of Sh 2–174 ($M_{\text{Sh}2-174} = 0.395 \pm 0.05 M_{\odot}$) points at Sh 2–174 being a post-extended horizontal branch (EHB) star and not a CSPN. If a stellar mass is too low, it is impossible for the star to reach the thermally pulsing AGB phase and, thus, to develop a planetary nebula (PN). Post-EHB stars evolve directly from the Horizontal Branch (HB) to the white dwarf (WD) cooling sequence. The low masses for A 35 and Sh 2–174 support literature works that classify the two corresponding nebulae as ionized H II regions and not as PNe.

Zusammenfassung

Das Ziel der vorliegenden Arbeit war die Bestimmung grundlegender Sternparameter sowie die Metallhäufigkeiten von 15 ausgewählten, Gasnebel ionisierenden Sternen. Im erwarteten Parameterbereich befinden sich wichtige Metalllinien im ultravioletten (UV) und fernen-ultravioletten (FUV) Spektralbereich. Daher wurden hochaufgelöste, und mit einem hohen Signal-zu-Rausch-Verhältnis ausgestattete Beobachtungen, die mit dem *Hubble-Weltraum-Teleskop (HST)* und dem *Far Ultraviolet Spectroscopic Explorer (FUSE)* gewonnen wurden, analysiert. Die Berechnung der dafür notwendigen Modellspektren wurde mit dem *Tübingen NLTE Model-Atmosphere Package (TMAP)* durchgeführt. Um Lineblanketing Effekte zu berücksichtigen beinhalteten die Modellatmosphären nahezu alle Elemente von H–Ni. Für jedes der untersuchten Objekte wurden kleine Modellgitter gerechnet. Da das interstellare Medium (ISM) den Bereich des *Space Telescope Imaging Spectrograph (STIS)* und im speziellen den *FUSE* Bereich stark beeinflusst und die photosphärischen Linien überlagert, wurde mit dem Programm *OWENS* zusätzlich die interstellare Absorption modelliert. Die Kombination des photosphärischen und des interstellaren Spektrums ermöglichte es, die meisten der in den Beobachtungen vorhandenen Absorptionslinien zu identifizieren.

Der Temperaturbereich der untersuchten Objekte liegt zwischen $70 \text{ kK} < T_{\text{eff}} < 136 \text{ kK}$, die Oberflächenschwerebeschleunigungen zwischen $\log(g/\text{cm/sec}^2) \approx 5.4 - 7.4$. Damit wird ein weiter Bereich der Sternentwicklung erfasst. Die Häufigkeiten einer Vielzahl von Elementen wurden zum ersten Mal für diese Objekte ermittelt. Linien von C, N, O, F, Ne, Si, P, S und Ar ermöglichten es, die entsprechenden Häufigkeiten zu bestimmen. Für keines der Objekte konnten Linien von Ca, Sc, Ti und V gefunden werden. Nur wenige Objekte waren reich an Cr, Mn, Fe, Co und Ni Linien. Die meisten der analysierten Sterne zeigten von den Eisengruppenelementen nur Fe Linien (Ionisationsstufen v–viii). Es wurden keine Anzeichen für *gravitational settling* gefunden, bei welchem die Gravitation den Strahlungsdruck übersteigt, woraufhin die Elemente aus der Atmosphäre in tiefere Schichten absinken. Dieses Ergebnis war zu erwarten, da die Oberflächenschwerebeschleunigungen des Samples noch nicht für das Einsetzen des *gravitational settling* ausreichen. Für die Elemente C, N, O, Si, P und S fand sich ein Anstieg der Häufigkeiten mit steigendem $\log(T_{\text{eff}}^4/g)$, wohingegen die Häufigkeiten von Ar und Fe sinken. Letzteres ist unerwartet, da bei einem größeren Verhältnis von T_{eff}^4/g die radiative Kraft die Gravitationskraft überwiegt, und durch den damit verbundenen Strahlungsauftrieb die Elemente in der Atmosphäre gehalten werden sollten.

Die gefundenen Häufigkeiten wurden mit Literaturwerten, mit Häufigkeiten

aus Diffusionsrechnungen und AGB Nukleosynthesemodellen, als auch, sofern vorhanden, mit den Häufigkeiten des entsprechenden Nebels verglichen. Die Übereinstimmung der entsprechenden Werte waren von uneinheitlicher Qualität.

Die in der Arbeit ermittelten Werte für T_{eff} und $\log g$ können einige Literaturwerte bestätigen, andere wurden korrigiert (z.B. für LSS 1362 und NGC 1360). Im Rahmen der Fehlergrenzen stimmen die meisten der ermittelten Werte jedoch mit den Literaturwerten überein. Es kann kein Unterschied zwischen T_{eff} für Sterne der Spektralklassen DAO und O(H) festgestellt werden, jedoch besitzen die Sterne des Typs O(H) ein deutlich niedrigeres $\log g$ (5.4 – 6.0) verglichen mit den DAO Objekten (6.5 – 7.4). Eine Ausnahme hiervon bildet der O(H)-Zentralstern von Lo 1 mit $\log g = 7.0$.

Ein Vergleich der Sternpositionen im $\log T_{\text{eff}} - \log g$ Diagramm mit Sternentwicklungsrechnungen lieferte die zugehörigen Sternmassen. Die mittlere Masse des analysierten Samples ($\bar{M} = 0.536 \pm 0.023 M_{\odot}$) ist kleiner als für diese Objekte erwartet. In der Literatur finden sich z.B. mittlere Massen für DA Weiße Zwerge (die unmittelbaren Nachfolger von DAO Weißen Zwergen) von $\bar{M} = 0.638 \pm 0.145 M_{\odot}$. Die mittlere Masse unseres Samples stimmt unter Berücksichtigung der Fehlergrenzen mit dem Wert für DA Weiße Zwerge überein. Zwei der untersuchten Objekte (A 35, Sh 2–174) erwiesen sich als extrem massearm. Für A 35 liegt die ermittelte Masse ($M_{A35} = 0.523 \pm 0.05 M_{\odot}$) am unteren Massenlimit für mögliche post-AGB Sterne. Die sehr geringe Masse von Sh 2–174 ($M_{\text{Sh}2-174} = 0.395 \pm 0.05 M_{\odot}$) deutet darauf hin, dass es sich bei dem Objekt eher um ein *post-EHB* Stern, und nicht um einen ZSPN handelt. Falls die Masse eines Sternes zu gering ist durchläuft dieser nicht die AGB Phase und ist daher nicht in der Lage einen PN auszubilden. Diese geringen Massen für A 35 und Sh 2–174 stützen die Klassifizierung der beiden zugehörigen Nebel in der jüngeren Literatur als ionisierte H II Regionen und nicht als PN.

CHAPTER 1

Stellar evolution

For a long time, stars were considered to be firm undergoing no changes in time. With the rise of modern spectroscopy and increasing computing power, we know that stars follow a complex evolution from their birth to their final stages. The evolutionary details depend on various factors such as the initial stellar mass M_i , the chemical composition, stellar winds, binarity etc.

This thesis deals with the ionizing stars of gaseous nebulae, especially CSPNe, an evolutionary phase in the late stages of stellar evolution for stars with intermediate mass ($M_i \approx 0.8 - 8 M_\odot^1$). To get a better understanding of the origin and fate of CSPNe stellar evolution for intermediate mass stars will be briefly discussed below. This work will hereby restrain to single-star evolution. The following standard single-star evolutionary scenario is getting more and more complex as binary interaction is taken into account. A nice review of binary star evolution can be found in Batten (1995).

Stellar evolution is often depicted in the Hertzsprung-Russell diagram (HRD)². Commonly, the two parameters stellar luminosity L and the effective temperature T_{eff} , in their combination characteristic for each stellar evolutionary phase, are plotted against each other. A HRD is shown in Fig. 1.1. The main evolutionary stages for intermediate-mass stars are labeled. These stages will be briefly discussed below.

1.1 Pre-Main Sequence

Stars are born in extended gas and dust clouds, like e.g. the Orion Nebula, due to a collapse and subsequent fragmentation. In the case of spherically symmetric, homogeneous clouds of an ideal gas a collapse will only start if the clouds exceed

¹ $M_\odot = 1.989 \cdot 10^{30} \text{ kg}$

²named after Ejnar Hertzsprung (1873 – 1967) and Henry Norris Russell (1877 – 1957)

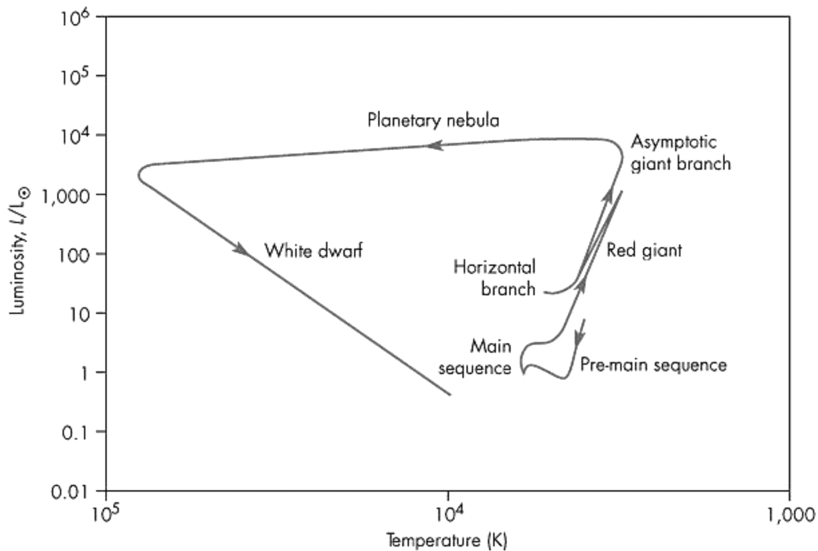


Figure 1.1: HRD (A. Zijlstra, priv. comm.) showing schematically the evolution for single stars with initial masses between ≈ 0.8 and $8 M_{\odot}$.

the critical *Jeans mass* given by

$$M_J = 1.2 \cdot 10^5 M_{\odot} \left(\frac{T}{100 \text{ K}} \right)^{3/2} \left(\frac{\rho}{10^{-24} \text{ g cm}^{-3}} \right)^{-1/2} \mu^{-3/2}, \quad (1.1)$$

For typical values of the density ($\rho = 10^{-24} \text{ g cm}^{-3}$), the temperature ($T = 100 \text{ K}$), and the mean molecular weight ($\mu = 1$), one can derive a lower mass limit of roughly $10^5 M_{\odot}$. This is only a rough estimate, as effects such as magnetic fields, rotation, turbulence etc. are neglected. Such a collapsing cloud fragments and forms *protostars*. Due to the rising pressure and temperature in the interior of the protostar H-core burning sets in and the protostar becomes a star. Objects with masses $\lesssim 0.08 M_{\odot}$ are not able to ignite the H-core burning and are called *brown dwarfs*.

1.2 From the Main Sequence to the AGB

At the very beginning of the lifetime of a star, i.e. with the ignition of the H-core burning, the star can be found on the Main Sequence (MS) in the HRD. MS stars are in *hydrostatic equilibrium*, i.e. the gravitational force is compensated by the forces acting outwards (radiation pressure, gas pressure, centrifugal force). This can be written as

$$\frac{\partial P}{\partial m} = -\frac{Gm}{4\pi r^4}, \quad (1.2)$$

where P is the total pressure acting outwards, r the distance from the center, G the gravitational constant, and the column mass m is used as depth variable. The timescale for which a star resides on the MS depends on its mass M , and hence its luminosity L . Both quantities are correlated by the *mass-luminosity relation*

$$\frac{M}{L} \propto \frac{g}{T_{\text{eff}}^4}. \quad (1.3)$$

A star resides on the MS until $\approx 10\%$ of the H content in the core is converted into He. One can approximately estimate the time-scale for the MS phase using

$$\tau \approx 10^{10} \left(\frac{M}{M_{\odot}} \right)^{-2.5} \text{ yrs.} \quad (1.4)$$

The Sun will therefore reside $\approx 10^{10}$ yrs on the MS. In general, stars with lower masses will evolve slower compared to higher mass stars.

Hydrogen fusion can either take place in the pp-chain, or for higher core temperatures ($\gtrsim 1.8 \cdot 10^7$ K for solar chemical composition) via the CNO-cycle. With the exhaustion of H in the core, the nuclear core burning ceases there and continues in a H-burning shell around the core. Due to the reduced radiative pressure, the core contracts, increasing the pressure and the temperature, leading to an expansion of the stellar envelope. The evolution from the MS to the following Red Giant Branch (RGB) phase is fast and leads to an observational gap in the HRD (*Hertzsprung gap*). The stellar atmosphere expands and the star moves to higher luminosities along the RGB. RGB stars are convectively unstable. A nearly vertical limit called *Hayashi line* (HL) defined as the locus in the Hertzsprung-Russell diagram of fully convective stars of given parameters (Kippenhahn & Weigert 1990) is the borderline that separates hydrostatically stable and unstable stars in the HRD. The depth of the convection zone on the RGB depends on the stellar mass. For higher masses, the convection penetrates layers already affected by the nuclear burning processes. Thus, elements synthesized in the former H-core burning are brought up to the surface. This mixing process is called *first*

dredge-up. For the following evolution the stellar mass plays a crucial role. Stars with masses $M_i \gtrsim 1.8 M_\odot$ (Herwig 2005) have a non-degenerate, convective core. In contrast, stars with $M_i \lesssim 1.8 M_\odot$ have a radiative and degenerate core. This has two main consequences. For the higher-mass stars the core material shows a rather uniform distribution due to convective mixing processes.

Secondly, He-core burning is either ignited in a flash for stars with $M \approx 0.8 - 1.8 M_\odot$ due to the degenerate matter in the core, or quiescently in the case of more massive stars due to a non-degenerate He core. After the ignition of He-core burning the star is located on the HB in the HRD where He is burned quiescently. The He-core burning phase lasts $\approx 10\%$ of the H-core burning time. The He-core burning produces C and O via the triple α reaction $\alpha + \alpha \rightarrow {}^8\text{Be}$ and subsequently ${}^8\text{Be}(\alpha, \gamma){}^{12}\text{C}$. Oxygen is synthesized via ${}^{12}\text{C}(\alpha, \gamma){}^{16}\text{O}$. A C/O core forms for all AGB stars with masses $\lesssim 8 M_\odot$. More massive AGB stars also ignite C burning and end up as ONeMg WD or core-collapse supernovae.

When the He in the core is used up He-burning begins in a shell atop of the C/O core. It is separated from the H-burning shell by a He-rich intershell region. The star is now moving along the AGB in the HRD, again moving towards higher luminosities. The interior of an AGB star is shown in Fig. 1.2. A H-rich convective shell separates the H-burning shell from the stellar atmosphere. The convection after the ceasing of He-core burning is called *second dredge-up*, and is increasing the atmospheric abundance of ${}^4\text{He}$ and ${}^{14}\text{N}$.

1.3 AGB phase: thermal pulses, nucleosynthesis, and stellar winds

The double-shell burning on the AGB is unstable and leads to thermal pulses (TP) with a typical time interval of a few 10^5 yrs depending on the stellar mass (Herwig 2005). Causal for the onset of TPs is the instability of the He-burning shell. After the He-core burning has ceased, due to a lack of fuel in the He-rich intershell region, the core contracts and heats up the He-burning shell. This increases the fusion rate which leads to an expansion of the stellar envelope and, therefore, a cooling of the outer H-burning shell until the H burning almost stops. Thus, no He is produced to feed the He burning which leads to an ebbing of the He burning. The star contracts until the temperature in the H-burning shell is again sufficiently high for H-burning. Helium is collected in the intershell region and He burning is reactivated when enough material has been accumulated. The cycle begins again. TPs generate pulse-driven convection zones (PDCZ) (Fig. 1.3), transporting H-rich material in deeper layers, where either C releases neutrons via ${}^{13}\text{C}(\alpha, n){}^{16}\text{O}$, or Ne via ${}^{22}\text{Ne}(\alpha, n){}^{25}\text{Mg}$. The neutron flux density is rather small ($10^5 - 10^{11} \text{ cm}^{-2} \text{ sec}^{-1}$). The neutrons can be captured by heavy atoms

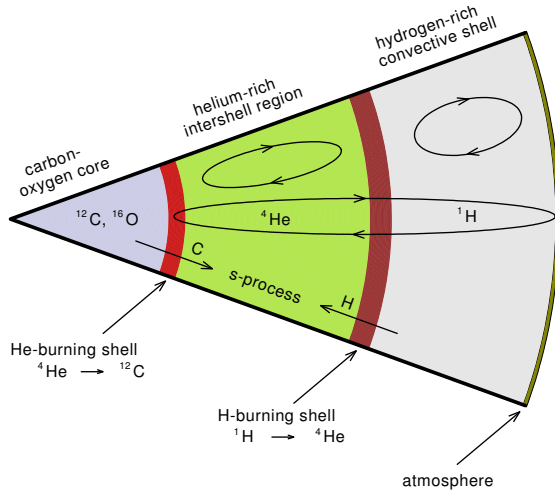


Figure 1.2: Cut through an AGB star indicating convective regions (Rauch 2006).

$(Z, A) + n \rightarrow (Z, A + 1) + \gamma$ like ^{56}Fe and create nuclei up to ^{208}Pb . That process is called *s-process* (“s” for slow). If an unstable nucleus is created in such a *s-process*, it has enough time to undergo a β -decay before a second *n*-capture takes place. The produced elements synthesized in the *s-process* therefore follow the stable path in the nuclear chart (Fig. 1.4). The elements are dredged up to the surface by the PDCZ, before they are released to the ISM by the occurring AGB wind. AGB stars are one of the main sources for heavy elements in the Universe besides supernovae. In supernovae however, a much larger neutron flux is present. Thus, possibly unstable nuclei do not have the time to undergo a β -decay before capturing more neutrons. This case is called *r-process* (“r” for rapid). The *r-process* synthesizes nuclei up to radioactive isotopes like ^{235}U and ^{238}U .

The nucleosynthesis on the AGB depends on a number of reactions. A decrease in $^{14}\text{N}(p, \gamma)$ or an increase in the triple- α rate leads to stronger He-flashes, and therefore to a more efficient third dredge-up penetrating deeper layers. This further enriches the envelope with ^{12}C and other elements (Herwig 2006).

AGB stars have luminosities of $L \approx 10^4 L_{\odot}$ and radii up to $10^3 R_{\odot}$. The gravity on the surface is small and the thermal particle velocity is close to the escape velocity. Additional radiative pressure leads to stellar winds with typical velocities of around 10 km sec^{-1} . Stars with initial masses of $M_i \approx 8 M_{\odot}$ shed about 90 % of their mass with mass-loss rates of up to $10^{-4} M_{\odot} \text{ yr}^{-1}$ and end up with

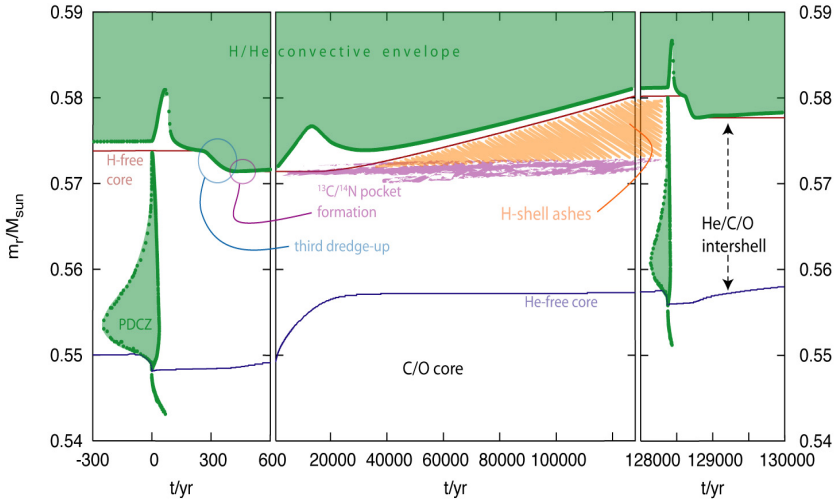
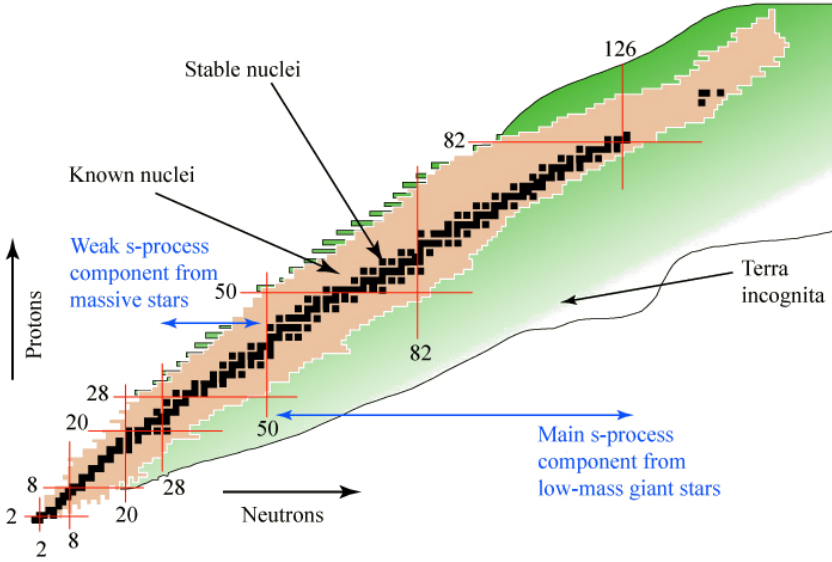


Figure 1.3: Time evolution of the interior of an AGB star between TP 14 and 15 for a star with $M = 2 M_{\odot}$ and a metallicity of $Z = 0.01$ (Herwig 2005). The time interval consists of 12 000 time steps as indicated by the dotted green line.

the characteristic WD mass of $M_{\text{WD}} \approx 0.6 M_{\odot}$. For AGB stars with $T_{\text{eff}} < 4 \text{ kK}$ dust formation can take place. Massive dust shells may hide stars at the tip of the AGB evolution such that only the infrared radiation of the dust shell is visible. The dust is driven away by radiation pressure taking along gas. The mass loss prevents some of the most massive AGB stars to undergo supernovae explosions, and it enriches the ISM with nuclear processed material and is therefore important for the galactic chemical evolution.

1.4 Post-AGB evolution

The star leaves the AGB when the mass of the envelope has decreased to $\approx 10^{-2} M_{\odot}$, due to the mass loss on the AGB. In the subsequent post-AGB phase the mass-loss rate drops significantly by several orders of magnitude compared to the AGB mass-loss rate. During some $10^3 - 10^5$ yrs, the star moves towards higher T_{eff} at constant luminosities in the HRD. The increasing UV flux begins to ionize the previously expelled material and a PN is formed.

Figure 1.4: Nuclei chart³.

Post-AGB tracks strongly depend on the previous stellar evolution. The initial mass, the mass-loss rate (on the AGB as well as during the post-AGB evolution), but also the numerical treatment of the third dredge-up (that determines the atmospheric chemistry) have an influence on post-AGB tracks. Blöcker (1995b) showed that stars with the same core mass can end up on different evolutionary tracks. A star with a higher initial mass and a stronger mass-loss rate will evolve on a higher temperature track as a star with an initially lower mass and a lower mass-loss rate. Higher-mass progenitor stars having a more efficient third dredge-up will also follow a hotter evolutionary track as lower-mass progenitors with less efficient third dredge-up.

After the cessation of all nuclear burning the star enters the WD cooling track. The only source of energy remaining is provided by gravitational energy released due to the contraction of the star. The UV flux of the CSPN decreases as the central star (CS) becomes cooler. The luminosity of a $\approx 0.2 M_{\odot}$ PN with a typical expansion velocity of $v_{\text{exp}} \approx 20 \text{ km sec}^{-1}$, will decrease within about 30 000 yrs as the density declines and the relaxation time therefore increases.

³http://cococubed.asu.edu/pix_pages/agb.shtml

Due to the decreasing radiative pressure heavy elements are removed from the stellar atmosphere. This is called gravitational settling. In CSPNe He is nearly fully ionized and, thus, not affected by radiative pressure. Subsolar He abundances have been believed to indicate ongoing gravitational settling. However, the work of Unglaub & Bues (1998, 2000) showed, that a weak stellar wind of the order of $\dot{M} \geq 10^{-12} M_{\odot} \text{ yr}^{-1}$ is needed to explain the He abundance of DAO-type WDs. Thus, gravitational settling will start when gravitation exceeds the radiation pressure and the mass loss. With the onset of gravitational settling heavier elements are removed from the stellar atmospheres of evolved WDs.

The upper mass limit for WDs is called *Chandrasekhar mass*⁴ and can be calculated using the formula

$$M_{\text{Ch}} = \left(\frac{2}{\mu_e} \right) \cdot 1.459 M_{\odot}, \quad (1.5)$$

(Padmanabhan 2001) with the mean molecular weight per free electron μ_e . For WDs exceeding the Chandrasekhar mass limit, the degenerate electron gas can not provide enough pressure to stabilize the star. These WDs collapse and become neutron stars.

1.5 Spectral classification scheme for CSPNe

For the post-AGB phase two independent evolutionary scenarios exist. H-rich post-AGB stars evolve as described above. About 75 % of all post-AGB stars belong to this group. The rest, e.g. the PG 1159-type stars, is H-deficient. The reason is a late thermal pulse (LTP) that causes the H-depletion. These stars return to the AGB once again and are thus called “born-again AGB stars” (Schönberner 1979; Iben et al. 1983).

This thesis focusses on H-rich CS. They can be further subdivided. DA-type stars exhibit only H Balmer lines in the optical wavelength range. DAO-type stars are characterized by He II lines in the optical in addition to the H Balmer lines (Wesemael et al. 1985). A vast majority of the analyzed sample belongs to the DAO group. Five of the analyzed stars (A 36, Lo 1, LSS 1362, NGC 1360, NGC 4361) belong to the class of O(H) stars (e.g. Pottasch 1996) characterized by spectra comparable to young and massive O-type stars with an additional He II $\lambda 4686\text{\AA}$ absorption line (Méndez 1991).

Some stars are not massive enough to undergo the stellar evolution as described above. Post-EHB stars did not have enough mass in their He-burning core on the

⁴named after Subrahmanyan Chandrasekhar (1910 – 1995)

HB to reach the AGB phase (Greggio & Renzini 1990). Therefore they did not develop a PN, but evolved directly to the WD cooling sequence. Bergeron et al. (1994) stated that most DAO-type WDs are post-EHB stars. The results of Gianninas et al. (2010), however, show, that this evolutionary connection is not needed to explain the observed parameters for DAO-type WDs.

1.6 Thesis motivation

About 75% of all stars will undergo the previously discussed standard evolutionary scenario for H-rich post-AGB stars. During the last two decades, the main effort was laid on understanding the evolution of H-deficient stars. H-rich post-AGB stars were investigated only sparsely. This is somehow astonishing as the main contribution of matter to the ISM is made on the AGB during a relatively long phase, and not in the post-AGB phase. H-rich post-AGB stars display the same chemical abundance pattern like the precursor AGB stars at their moment of descent from the AGB, and thus help to understand the enrichment of the ISM with metals. Metals play an important role for several reasons: (a) metal-line blanketing is important to calculate reliable model atmospheres and, thus, precise abundance determinations are highly desirable, (b) they enable to determine T_{eff} accurately using ionization equilibria, and (c) they set constraints on AGB nucleosynthesis calculations, and, thus, directly affect our understanding of stellar evolution. T_{eff} and g are also necessary to derive the stellar mass, which is deduced by comparing a star's position in the $\log T_{\text{eff}} - \log g$ diagram with theoretical evolutionary tracks. As CSPNe are the immediate precursor stars of WDs, their masses cluster around the mean mass for WDs, e.g. $\overline{M}_{\text{DA}} = 0.638 \pm 0.145 M_{\odot}$ from Gianninas et al. (2011) for DA-type WDs.

For CSPNe only a few systematic analyses of heavy element abundances are available in the literature. Bauer & Husfeld (1995) calculated non-local thermodynamical equilibrium (NLTE) model atmospheres for seven sd(O)-type stars⁵ and four CSPNe (PHL 932, NGC 1535, NGC 2392, NGC 7293) and derived abundances for H, He, C, N, O, Mg, Al, and Si for most of the sample. They analyzed optical spectra obtained at the 3.6 m European Southern Observatory (ESO) telescope at La Silla, Chile. Bauer & Husfeld describe the derived metal abundances for the sd(O) stars as not homogeneous. The high-gravity objects in their sample, however, show similar metal abundances.

A more extended analysis was presented recently in a series of papers by Good et al. (2004, 2005) investigating optical and *FUSE* observations, respectively, for a sample of 16 DAO-type WDs. Their NLTE model atmospheres included

⁵subdwarf stars of spectral type O

H, He, C, N, O, Si, Fe, and Ni. They compared the chemistry derived with T_{eff} , $\log g$, and the He abundance obtained from the optical with abundances derived with parameters obtained from the *FUSE* range. The abundances derived from *FUSE* data were 1 – 10 times higher than derived from optical data due to the difference of the temperature structure of the atmospheres calculated with parameters derived from the *FUSE* and from the optical wavelength ranges. All analyzed objects showed C abundances $n_{\text{C}}/n_{\text{H}} < 10^{-4}$. Good et al. were not able to fit O lines reliably. Silicon abundances did not exceed $n_{\text{Si}}/n_{\text{H}} \approx 10^{-4}$, and Fe abundances were all below $n_{\text{Fe}}/n_{\text{H}} \approx 4.7 \cdot 10^{-4}$. Nickel abundances were only poorly constrained.

Recently Gianninas et al. (2010) derived T_{eff} , $\log g$, and $n_{\text{He}}/n_{\text{H}}$ for a sample of 29 DAO and 18 DA-type WDs, analyzing optical spectra. They calculated NLTE model atmospheres including H, He, and in addition C, N, and O (at solar abundances), to avoid the Balmer-line problem. Their sample covers a wide range for T_{eff} ($\approx 44 - 95$ kK) and $n_{\text{He}}/n_{\text{H}}$ ($2.8 \cdot 10^{-4} - 1.4 \cdot 10^{-1}$), while the derived $\log g$ is in a narrow range between $\approx 7.0 - 8.0$. They found higher masses (mean mass $\bar{M} = 0.65 M_{\odot}$ with a dispersion of $\sim 0.16 M_{\odot}$) for the DAO stars than previous analyses, comparing their results with post-AGB tracks from Wood (1995). They conclude that a connection between DAO-type WDs and the EHB is no longer necessary.

The sample stars analyzed in this thesis cover a wide range of T_{eff} and $\log g$ values, and therefore mark different evolutionary stages around the “knee” of the post-AGB evolution, marking the transition from post-AGB stars to WDs.

CHAPTER 2

Stellar spectra

The main work of this thesis is the modeling of stellar spectra. It is therefore important to understand their origin. This chapter begins with a short historic introduction (Sect. 2.1) and then discusses the radiative transfer through a stellar atmosphere (Sect. 2.2). The programs used to calculate the model atmospheres and the SEDs are introduced in Sect. 2.3.

2.1 *Stellar spectra*

Astronomy is one of the oldest scientific fields. Besides some satellite missions to planets and a number of asteroid and meteorite fragments, neutrinos, the Cosmic rays, gravitational waves, our knowledge of astronomical objects is largely based on the analysis of the light emitted by these. The analysis of the radiation intensity as a function of the wavelength is called *spectral analysis*. It enabled astronomers to determine basic physical and chemical properties of stars, galaxies, and other astronomical objects that can not be studied in a laboratory. In the case of stars the main parameters are the effective temperature T_{eff} , the surface gravity g , the chemical abundance pattern of the stellar atmosphere, and stellar wind. These parameters are derived from a comparison of observed with model spectra.

Short historical overview

In 1802, William Hyde Wollaston (1766 – 1828), an English doctor, physicist, and chemist, discovered seven dark lines in the solar spectrum. In the years 1814 – 1815, these lines were also discovered by their later eponym Joseph von Fraunhofer (1787 – 1826). A spectrum of the Sun displaying the spectral lines is shown in Fig. 2.1.

It was not until 1859 that Robert Bunsen (1811 – 1899) and Gustav Kirchhoff (1824–1887) were able to expound the origin of the lines found by Wollaston and

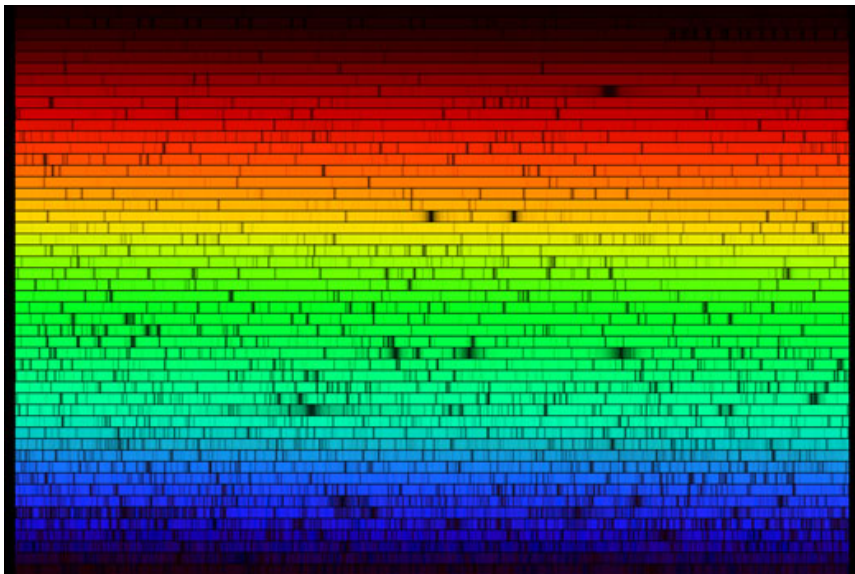


Figure 2.1: Spectrum of the Sun¹ showing many spectral lines.

Fraunhofer. Bunsen and Kirchhoff explained the observed lines with electronic transitions in atoms. The development of the spectral analysis was the birth of modern astronomy.

When photography became part of the astronomical tools in the 19th century it was possible to gain spectra from fainter objects. In the beginning the collected stellar spectra were classified according to their visual appearance. This led to the famous *Harvard spectral sequence* using the letters from A to Q (without J) to sort the spectra accumulated. Later it was recognized that classifying stars according to their effective temperatures makes more sense. Therefore some classes of the Harvard sequence were dropped. This resulted in the today well known sequence O, B, A, F, G, K, M. Later on the classes L and T were added. The sequence can be further subdivided by roman numbers 0 – 9. Our Sun is classified as G2 V star.

¹http://www.noao.edu/image_gallery/html/im0600.html, N. A. Sharp, NOAO/NSO/Kitt Peak FTS/AURA/NSF

2.2 Stellar atmospheres and radiative transfer

A stellar atmosphere is defined as the layer of a star in which the photons are absorbed, emitted, or scattered before reaching the observer. A compact stellar atmosphere, as it is the case for post-AGB and post-EHB stars analyzed in this thesis, can be characterized by three main parameters. The effective temperature T_{eff} , the surface gravity g , and the chemical composition. Other parameters such as magnetic fields, stellar winds, or rotation will be left aside in the following discussion as they are not considered in the analyses presented in this work.

Stars are not in thermodynamic equilibrium (TE) as they emit radiation into space. Local thermodynamic equilibrium (LTE), i.e. thermodynamical equilibrium for small volume elements, is only applicable if the mean free path of the photons is short. This holds for high pressure and low temperature objects. Thus, this assumption can not be made for ionizing stars of gaseous nebulae. Therefore, local thermodynamic equilibrium (LTE) models can only serve as start models for further NLTE model calculations.

The energy flow can be radiative, convective, or by heat conduction. For the analyzed stars we can restrict ourselves to radiative transfer because the density of the atmosphere is too small for heat conduction and also convection does not play any role for the atmosphere of hot, post-AGB and post-EHB stars.

2.2.1 Physical assumptions

In the framework of *TMAP*, several assumptions are made to simplify the equations of the radiation transfer through the stellar atmosphere. The photons travelling through the stellar atmosphere, interacts with the latter. These interactions can either be absorption, emission, or scattering processes.

The assumptions made in the framework of *TMAP* are:

1. **plane-parallel atmosphere:** The focus of stars that are analyzed with *TMAP* lies on evolved post-AGB stars. In this stage of stellar evolution, the atmosphere is very thin compared to the stellar radius. Therefore the assumption of a *plane-parallel atmosphere* is justified. This is surely not valid for AGB or RGB stars with their extended atmospheres, but for all objects analyzed in this work.
2. **hydrostatic equilibrium:** The second assumption is the *hydrostatic equilibrium*. The sum of radiative, turbulence, and gaseous pressure compensates the gravitational force on each mass element in the atmosphere. This is expressed by

$$\frac{dP}{dm} = g, \quad (2.1)$$

with P being the sum of the pressures acting outwards. In other words: the stellar atmosphere is at rest and neither accretion nor wind effects play a significant role.

3. **radiative equilibrium:** The third assumption is the *radiative equilibrium*. A volume element absorbs the same energy per unit time as it emits. In its integral form the radiative equilibrium can be written as

$$\int_0^{\infty} \kappa_{\nu} (S_{\nu} - J_{\nu}) d\nu = 0, \quad (2.2)$$

where $J_{\nu} = \frac{1}{4\pi} \oint I_{\nu} d\Omega$ is the solid angle averaged specific intensity, $S_{\nu} = \eta_{\nu}/\kappa_{\nu}$ the source function, η_{ν} the emission coefficient and κ_{ν} the opacity.

4. **statistical equilibrium:** In the case of NLTE model atmospheres the rate equations have to be taken into account. For each atomic level i of each ionization stage of each element, the condition of *statistical equilibrium*

$$n_i \sum_{i \neq j} P_{ij} - \sum_{j \neq i} n_j P_{ji} = 0, \quad (2.3)$$

holds, where the rate coefficients $P_{ij} = R_{ij} + C_{ij}$ are the sums of the radiative and collisional transition rates and n_i and n_j denote atomic occupation numbers. The rate coefficients can be divided into:

- bound-bound transitions: either radiatively (RBB) or collisionally (CBB). Spectral lines are caused by RBB transitions.
- bound-free transitions: either radiative (RBF) or collisional (CBF) induced ionization and recombination processes.
- free-free transitions: Bremsstrahlung

Equation 2.3 therefore describes the invariance of the atomic occupation numbers with time.

5. **charge conservation:** With the total number of chemical species N_{ATOM} , the charge $q(l)$ of ion l , the assumptions of *charge conservation* can be written as

$$\sum_{k=1}^{N_{ATOM}} \sum_{l=1}^{N_{ION}(k)} q(l) \left[\sum_{i=1}^{NL(l)} n_{kli} + \sum_{i=1}^{LTE(l)} n_{kli}^* \right] = n_e, \quad (2.4)$$

with $N_{ION}(k)$ the number of ionization stages of species k , and the number of LTE and NLTE levels per ion as $LTE(l)$ and $NL(l)$, respectively.

6. **particle conservation:** The *particle conservation* can be expressed as

$$N = n_e + \left[\sum_{i=1}^{NL(l)} n_i + \sum_{i=1}^{LTE(l)} n_i^* + n_p \right] \sum_{k=1}^{NATOM} y_k, \quad (2.5)$$

with the total particle density N , and $NATOM$, $NL(l)$, and $LTE(l)$ as introduced above.

2.2.2 Radiative transfer equation

The radiative transfer equation can be written as

$$\mu \frac{dI_\nu(z)}{dz} = \eta_\nu - \kappa_\nu I_\nu(\mu), \quad (2.6)$$

with $\mu = \cos \vartheta$ and ϑ being the angle between the direction of propagation of the radiation beam and the surface normal (Fig. 2.2). Introducing the optical depth

$$\tau_\nu(z) = - \int_0^z \kappa_\nu(z') dz', \quad (2.7)$$

the radiation transfer equation can be written as

$$\pm \mu \frac{\partial I_\nu(\pm\mu)}{\partial \tau_\nu} = S_\nu - I_\nu(\pm\mu), \quad (2.8)$$

where the algebraic sign defines either an inward or an outward directed beam. The radiative transfer equation 2.8, the rate equations, and the equations for statistical and thermodynamical equilibrium built a coupled equation system. The intensities I_ν depend on the temperature and the occupation numbers at all depth points. In the case of NLTE model atmospheres the occupation numbers themselves depend on I_ν . Such a system of equation can only be solved in an iterative process described in Sect. 2.3.2.

2.3 Numerical modeling of stellar spectra with TMAP

For the determination of T_{eff} , $\log g$, and the chemical composition of a star, synthetic model atmospheres and SEDs were calculated. *TMAP* provided all necessary tools to calculate stellar model atmospheres and SEDs.

2.3.1 Preparatory steps

Before a model atmosphere calculation can be started, preparatory steps concerning the atomic data and the frequency grid have to be made.

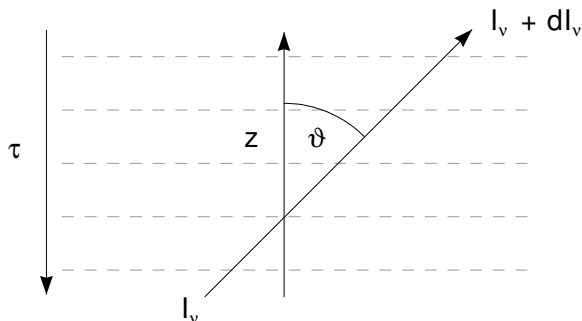


Figure 2.2: Radiative transfer through a plane-parallel atmosphere.

2.3.1.1 Atomic data

For the calculation of the model atmospheres and SEDs atomic data containing all relevant physical quantities (e.g. the considered ionization stages, the disposition of NLTE and LTE levels, etc.) is required. These were obtained from the *Tübingen Model-Atom Database (TMAD)*². For the elements H, He, C, N, O, F, Ne, Na, Mg, Al, Si, P, S, and Ar “classical” model atoms are constructed as described by Rauch (1997). Due to the large amount of atomic levels and line transitions, iron-group elements (Ca–Ni) had to be processed with the *Iron Opacity and Interface* (Rauch & Deetjen 2003, *IrOnIc*, Sect. 2.3.1.2). The final model atom file is then processed and checked by the *TMAP* auxiliary program *ATOMS2*.

As the parameter range of the sample concerning T_{eff} and $\log g$ is rather large, the atomic data had to be adapted individually for each object to avoid numerical problems and instabilities due to too-low occupation numbers for individual ionization stages. Therefore a model atom file including all ionization stages was created and subsequently adapted for each parameter set. The final statistics for the model atoms before this adjustment for each individual star is shown in Tab. A.1 and Tab. A.2.

Despite the adjustment of the atomic data some models were hardly to converge. Especially the lowest ionization stages of the iron-group elements caused difficulties. In such cases the f -values for the whole ionization stage was reduced using an option in the program *PRO2* or the whole ionization stage was excluded from the calculation of the atmospheric structure and later on added in a line-formation (i.e. the temperature correction is switched off and large model atoms

²<http://astro.uni-tuebingen.de/~TMAD/TMAD.html>

are used) calculation. As an example Fig. 2.3 shows the temperature and density stratification, as well as the ionization fractions of all ions for the final model of A 35.

2.3.1.2 *IronIc*

Iron-group elements (Ca–Ni) have some 10^5 energy levels and hundreds of millions corresponding line transitions in the Kurucz (1991, 2009) data. Taking these lines into account individually is a task impossible with today's computing power. *IronIc* applies a statistical approach using “super lines” and “super levels”. The levels of each ion are typically split into seven bands (Haas 1997), each being treated as a NLTE “super level” L , with an averaged energy E_L , and a statistical weight G_L according to

$$E_L = \frac{\sum_{l \in L} E_l g_l^*}{\sum_{l \in L} g_l^*}, \quad (2.9)$$

$$G_L = e^{E_L/kT^*} \cdot \sum_{l \in L} g_l^*, \quad (2.10)$$

with $g_l^* = a_s g_l e^{E_l/kT^*}$. E_l is the energy and g_l the statistical weight of an atomic level l . T^* is the temperature for which the regarded ionization stage is most populated, and a_s is the abundance relative to Fe for individual iron-group element s . In this thesis $a_s = 1$.

Kurucz's³ line lists, as well as the Opacity Project (Seaton et al. 1994) and the IRON Project (Hummer et al. 1993), provided the necessary input data for the calculation of the radiative cross-sections. The Kurucz data itself is subdivided into LIN (laboratory measured and theoretical lines) and POS (only laboratory measured) lists. The latter therefore possesses reliable, “good” wavelength positions and are thus used to identify “good” lines and to determine the chemical abundances. For the calculation of the model atmospheres LIN data is used. This ensures that all opacities are considered in the calculation of the temperature stratification of the stellar atmospheres.

For elements heavier than Ni no atomic data is available for the expected parameter regime and therefore these elements could not be included in this analysis.

³<http://kurucz.harvard.edu/>

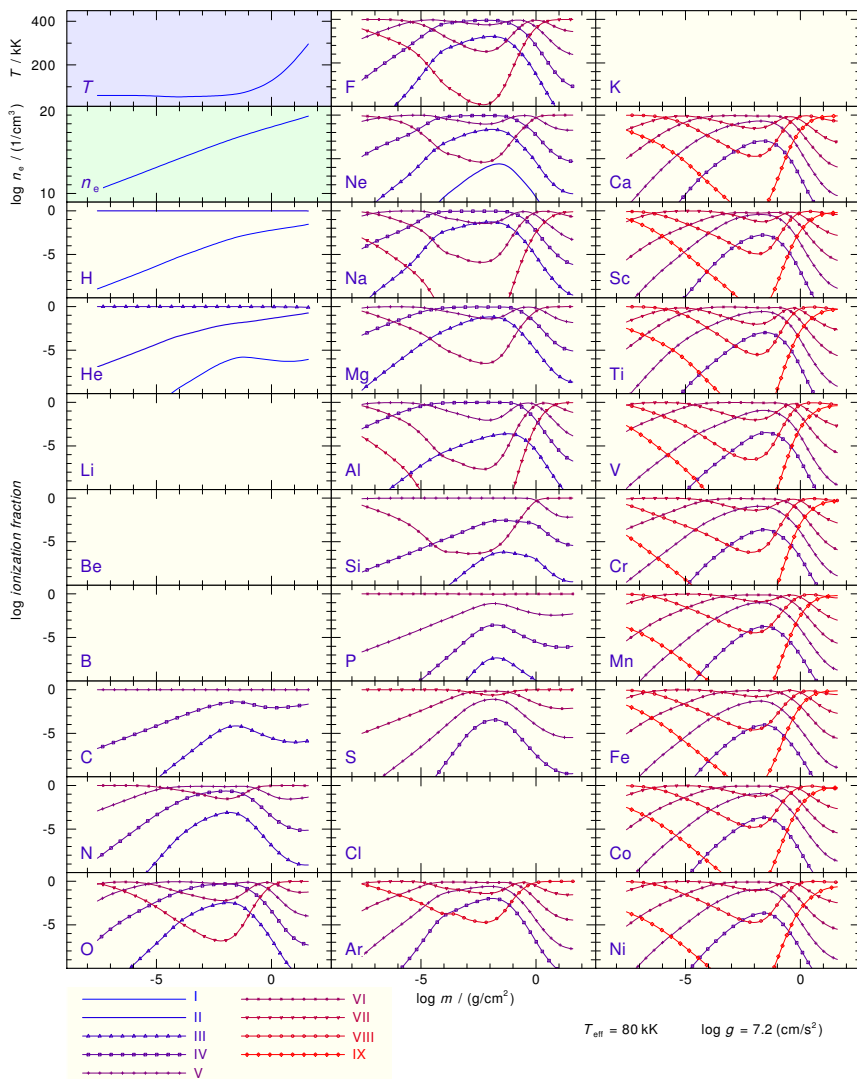


Figure 2.3: Temperature and density stratification, and ionization fractions of all elements considered in the final model of A 35.

2.3.1.3 Frequency grid

After the creation of the model atoms file, the frequency grid is created using the auxiliary program *SETF2*. This is needed in order to discretize frequency integrals. For the considered line transitions *SETF2* creates a frequency grid considering T_{eff} in order to account for the appropriate Doppler line broadening. Individual options in the atomic data file allow to adjust the points red- and bluewards of each spectral line-core.

2.3.2 Numerical solution of the radiative transfer equation

The radiative transfer equation (Eq. 2.8) is solved within the program *PRO2*. Building on the works of Cannon (1973) and Scharmer (1981) on the *operator splitting* methods, *PRO2* uses the *Accelerated Lambda Iteration* (ALI, Werner & Husfeld 1985). Due to the strong coupling of the equations for the radiative transport, the radiative equilibrium, the hydrostatic equilibrium, and the particle conservation, a simultaneous solution of the system of equations is required. *Approximate Lambda Operators* (ALOs) are one possible method to decouple the radiative transfer equations from the rest of the system.

The solution of the radiative transfer equation is obtained in a two step iteration cycle. The outer cycle is called *Scharmer iteration* and gives a formal solution by iterating the radiation field. The ansatz for the radiation field J_ν is given by

$$J_\nu = \Lambda^* S_\nu^n + (\Lambda - \Lambda^*) S_\nu^{n-1}. \quad (2.11)$$

The approximate lambda operator Λ^* operates on the current source function S_ν^n at the frequency ν and for the iteration step n . The correction term, $(\Lambda - \Lambda^*) S_\nu^{n-1}$, in which the exact lambda operator Λ is acting on the source function of the previous iteration step S_ν^{n-1} has to be added to ensure the convergence to the exact solution $J = \Lambda S$. The second, inner cycle, calculates the rate equations using the Newton-Raphson method.

2.3.3 Synthetic spectra

For the comparison with the observations model SEDs are calculated with the program *LINE1_PROF* considering the latest line-broadening theories (especially Stark broadening) and the multiplett-splitting. The necessary atomic data is also retrieved from *TMAD* and processed as described above.

2.3.4 OWENS

Before the light of a star reaches the telescopes and the detectors it has to pass the ISM. The ISM leaves its imprints on the observations and poses a problem

for the identification and analysis of the photospheric lines. Especially the *FUSE* range shows a large number of interstellar molecular H_2 absorption lines that, amongst others, impede the analysis of the photosphere. Therefore modeling the influence of the ISM is inevitable in order to identify all photospheric lines.

OWENS, developed by M. Lemoine and the French *FUSE* Team, enables the user to model interstellar absorption lines depending on the parameters of the ISM cloud, such as the chemical composition, the radial and turbulent velocity, and the cloud temperature. The fit is iteratively improved by using a χ^2 minimization (Lemoine et al. 2002; Hébrard & Moos 2003). It is also possible to adjust the parameters manually. The observations read-in have to be divided into smaller wavelength intervals, for each of which either a Gaussian or a double Gaussian, with arbitrarily order, can be chosen as fit polynomial, to account for the resolution of the observation.

In order to identify all photospheric features, the photospheric model SEDs and the ISM model absorption templates are combined, improving the fit to the observations significantly (cf. Taresch et al. 1997). This method is the standard method for our analysis and enabled to improve both, the photospheric model SEDs and the ISM absorption templates. However, the main concern of this work lies on the analysis of the photospheric spectra. Quantitative results for the ISM will therefore not be given in this thesis.

CHAPTER 3

Observations

CSPNe and post-EHB stars are hot ($T_{\text{eff}} \gtrsim 30 \text{ kK}$) objects. Thus all elements are highly ionized (ionization stages for iron-group elements $v - \text{viii}$). The strategic lines of the iron-group elements are located in the UV and FUV wavelength range inaccessible from ground-based observatories. For this analysis *FUSE* and *HST/STIS* observations were used. These were retrieved from the Multimission Archive at Space Telescope Science Institute (MAST)¹ archive.

All observations were smoothed with a low-pass filter (Savitzky & Golay 1964). Details for all analyzed observations of the O(H)-type CSPNe and the DAO-type stars are displayed in Tab.B.1 and Tab.B.2, respectively. For four objects optical observations from various sources were available. Optical observations allow to precisely determine the H/He-abundance ratio that can not be analyzed in the UV and FUV range due to strong interstellar features blending the photospheric lines. The H and He lines also enable to cross-check T_{eff} and $\log g$.

3.1 FUSE

FUSE (Fig. 3.1) was active from June 24, 1999 until its failure in 2007. *FUSE* was built with four co-aligned mirrors each 39 cm-by-35 cm. Two mirrors were coated with SiC and two with LiF (Fig. 3.2). The different coating optimized the reflection at shorter, respectively longer wavelength ranges. *FUSE* covered the range from 910 – 1180 Å with a resolving power $R = \lambda/\Delta\lambda = 20\,000 - 25\,000$. More details on the mission can be found in the *FUSE* instrument and data handbook (Oegerle et al. 2000). For objects with multiple exposures, for

¹<http://archive.stsci.edu/> Some of the data presented in this paper were obtained from the Mikulski Archive for Space Telescopes (MAST). STScI is operated by the Association of Universities for Research in Astronomy, Inc., under NASA contract NAS5-26555. Support for MAST for non-HST data is provided by the NASA Office of Space Science via grant NNX09AF08G and by other grants and contracts.

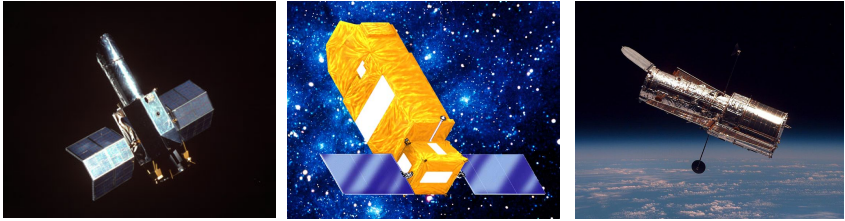


Figure 3.1: *IUE*², *FUSE*³, and *HST*⁴ (from left to right).

each segment the exposures were co-added in order to increase the S/N-ratio.

3.2 HST

HST (Fig. 3.1) was launched on April 20, 1990. The primary mirror has a diameter of 2.4 m. *STIS* onboard *HST* provides high-S/N observations from 1140 – 1730 Å with $R = \lambda/\Delta\lambda = 45\,800$. All analyzed observations were performed with the E140M grating and the FUV-MAMA (Multi-Anode Microchannel Array) detector.

3.3 IUE

IUE (Fig. 3.1) was a satellite that was launched on January 26, 1978 and deactivated on September 30, 1996. The telescope contained a mirror with 45 cm in diameter. The satellite contained four Echelle spectrographs, the short wavelength prime (SWP), the short wavelength redundant (SWR), the long wavelength prime (LWP) and the long wavelength redundant (LWR), covering the wavelength ranges from 1150 – 1970 Å and 1750 – 3300 Å, respectively. *IUE* had a resolution of 0.1 – 0.3 Å (high resolution) and 6 – 7 Å (low resolution).

3.4 Optical observations

For a small number of objects (LSS 1362, NGC 1360, NGC 6853, NGC 7293) additional optical observations were available and were used to derive the H/He-

²<http://sci.esa.int/science-e/www/object/index.cfm?fobjectid=28875>

³http://fuse.pha.jhu.edu/Graphics/instrument/osc_satellite.gif

⁴http://en.wikipedia.org/wiki/File:Hubble_01.jpg

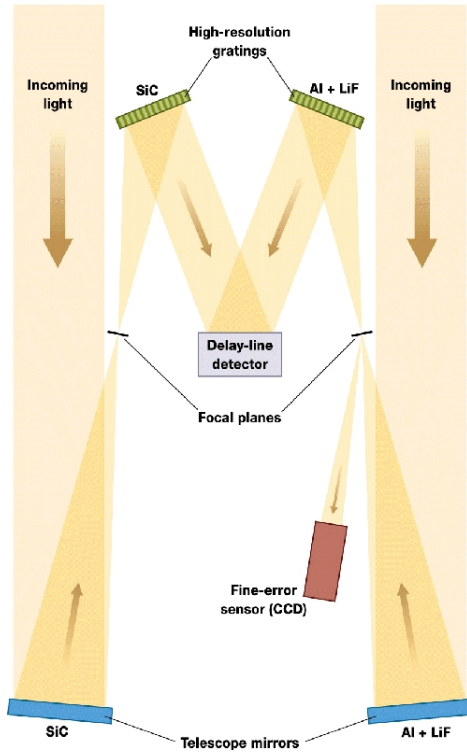


Figure 3.2: Optical path of the *FUSE* instrument⁶.

abundance ratio and to cross-check T_{eff} and $\log g$.

The optical longslit spectrum of NGC 1360 was obtained in September 1994 using the TWIN spectrograph at the 3.5 m telescope at Calar Alto observatory (DSAZ⁵). It covers the range from 3721 – 6849 Å with a dispersion of 72 Å mm⁻¹ (resolution ~ 3 Å).

TWIN was also used to gain optical longslit spectra for the CSPNe NGC 6853 and NGC 7293. Both observations cover the range from 3965 – 6792 Å with a dispersion of 36 Å mm⁻¹ (resolution ~ 1.5 Å). The spectrum of NGC 6853 is contaminated to a small extent by emission lines, which could not be removed

⁵<http://www.caha.es/>

⁶http://fuse.pha.jhu.edu/Graphics/instrument/optical_path.gif

during the data reduction, due to spatial inhomogeneities of the PN.

The optical spectrum for LSS 1362 was obtained using the 3.6 m ESO telescope and the Cassegrain Echelle Spectrograph (CASPEC, D'Odorico et al. 1983). It covers the wavelength range between 3900 and 4800 Å with a mean resolution of ≈ 0.15 Å.

For most objects only *FUSE* and low-resolution *IUE* observations were available. The latter were applied for the determination of the interstellar reddening only. The *STIS* observation for A 35 had to be scaled by a factor of 1.995 in order to match the *IUE* flux level. The offset is possibly due to bad centering of the exciting star during the observation (Herald & Bianchi 2002).

The Sample Objects

In this chapter the sample stars will be introduced by outlining some previous literature results. The summary concentrates on the characteristics of the ionizing stars rather than that of the nebulae. As our sample objects are divided into the spectral classes DAO and O(H) we will separate the objects according to this scheme beginning with the DAO-type stars (Sect. 4.1) that represent the majority (10 out of 15) of our sample stars. The introduction of the O(H)-type objects follows in Sect. 4.2. Table 4.2 summarizes the most recent literature values for T_{eff} , $\log g$, and the abundances of He, C, N, O, Si, Fe, and Ni.

The images of the nebulae shown in this chapter are taken from various sources. The images of A 7, NGC 3587, NGC 7293, and A 36 are taken from the Planetary Nebula Image Catalogue (PNIC)¹ database. The references within the PNIC database can be found in the footnotes. The images of A 31, A 39, NGC 6853, PuWe 1, and Sh 2–174 are used with kind permission of D. Goldman². If not noted otherwise the latter images are composites of two narrow-band images ([O III] – magenta; H α – blue-green), and an additional R:G:B image for proper colors of the stars. For all other images the references can be found in the corresponding footnotes. For all images N is up and E is left.

The objects are most prominently known according to their nebulae names. Table 4.1 gives the names of the ionizing stars for each nebula as found in the literature or via <http://www.astronomy.villanova.edu/WDCatalog/index.html>. For simplicity the thesis will refer to the stars by their nebulae names.

¹<http://www.astro.washington.edu/users/balick/PNIC/>

²<http://astrodonimaging.com>

Table 4.1: Names of the ionizing stars for the analyzed gaseous nebulae.

PN	CS	PN	CS	PN	CS
A 7	WD 0500 – 156	Lo 1	–	NGC 6720	WD 1851 + 329
A 31	WD 0851 + 090	LSS 1362	–	NGC 6853	WD 1957 + 225
A 35	WD 1250 – 226	NGC 1360	CPD – 26 389	NGC 7293	WD 2226 – 210
A 36	–	NGC 3587	WD 1111 + 552	PuWe 1	WD 0615 + 556
A 39	WD 1625 + 280	NGC 4361	–	Sh 2–174	WD 2342 + 806

4.1 DAO-type ionizing stars

4.1.1 Abell 7

Abell 7 (A66 7, PN G215.5–30.8, Fig. 4.1) was discovered by Abell (1966) in Palomar Observatory Sky Survey (POSS) plates. The PN is located in a distance of $d = 676^{+267}_{-150}$ pc (Harris et al. 2007, trigonometric parallaxes). Méndez et al. (1981) calculated H+He NLTE model atmospheres in order to derive stellar parameters from optical observations obtained at the Cerro Tololo Inter–American Observatory (CTIO, Chile). They derived $T_{\text{eff}} = 75 \pm 10$ kK, $\log g = 7.0 \pm 0.5$, and a He abundance of $n_{\text{He}}/(n_{\text{He}} + n_{\text{H}}) = 1 \pm 0.5\%$ for the CS. They concluded that the low He abundance is a signal for gravitational settling. A reddening of $E_{B-V} = 0.1$ was measured by Harris et al. (1997). Recent analyses led to slightly higher values for T_{eff} and $\log g$. Napiwotzki (1999) analyzed optical observations taken with TWIN and found $T_{\text{eff}} = 99 \pm 18$ kK and $\log g = 7.03 \pm 0.43$. Good et al. (2004) derived $T_{\text{eff}} = 99.2 \pm 2.3$ kK and $\log g = 7.68 \pm 0.06$ from FUV observations taken with *FUSE*. Both works confirmed the low He abundance found by Méndez et al. ($n_{\text{He}}/n_{\text{H}} = 3.24 \cdot 10^{-2}$, Napiwotzki; $n_{\text{He}}/n_{\text{H}} = 2.00 \cdot 10^{-2}$, Good et al.). Gianninas et al. (2010) analyzed the H Balmer lines and derived $T_{\text{eff}} = 82.7 \pm 3.8$ kK, $\log g = 7.47 \pm 0.13$, and $n_{\text{He}}/n_{\text{H}} = 4.37 \cdot 10^{-2}$.

Good et al. (2005) analyzed *FUSE* and optical observations to determine metal abundances. From the *FUSE* range they found a chemical abundance pattern of $n_{\text{C}}/n_{\text{H}} = 4.17^{+3.84}_{-1.09} \cdot 10^{-5}$, $n_{\text{N}}/n_{\text{H}} = 6.43^{+23.3}_{-5.96} \cdot 10^{-6}$, $n_{\text{Si}}/n_{\text{H}} = 2.27^{+1.04}_{-1.08} \cdot 10^{-5}$, and the two iron-group elements $n_{\text{Fe}}/n_{\text{H}} = 8.22^{+7.25}_{-3.82} \cdot 10^{-5}$ and $n_{\text{Ni}}/n_{\text{H}} = 0^{+8.94}_{-0} \cdot 10^{-6}$. They were not able to determine an O abundance. Good et al. also derived the same abundances from optical observations, and found they were smaller. The CS of A 7 is likely member of a binary system with an additional faint, red companion (Ciardullo et al. 1999).

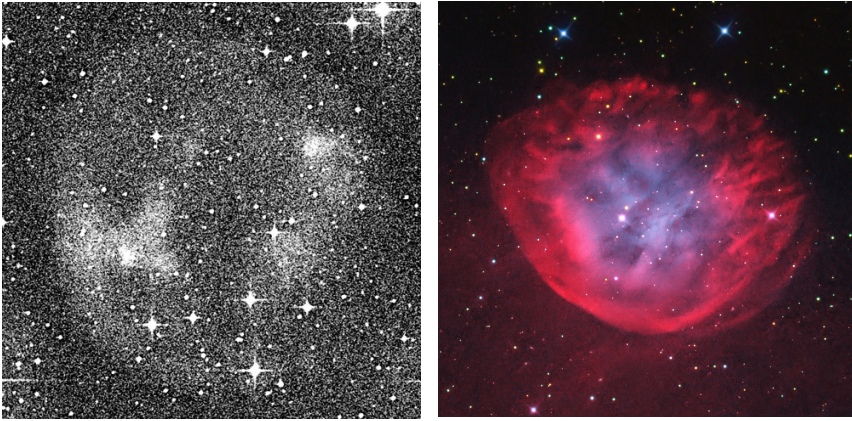


Figure 4.1: Images of the PNe A 7³ (left, FOV⁴: 5' × 5') and A 31 (FOV: 11' × 11'). Grey in the image of A 7 is coded as log(POSS – II/UKSTU red).

4.1.2 *Abell 31*

Abell 31 (A66 31, PNG219.1+31.2, Fig. 4.1) was first mentioned in Abell (1966). A trigonometric distance determination by Benedict et al. (2009) using the *HST* led to $d = 621^{+91}_{-70}$ pc confirming a previous result by Harris et al. (2007, $d = 568^{+131}_{-90}$ pc, trigonometric parallax). Benedict et al. also derived a surface gravity and found $\log g = 6.99 \pm 0.14$ from $g = GM/R^2$ and $\log g = 6.6 \pm 0.3$. They derived R from the Stefan-Boltzmann relation as well as from the Eddington flux. The necessary mass is obtained from a comparison of absolute magnitudes with post-AGB models.

An early analysis by Pottasch et al. (1978) used the Zanstra method (Sect. 5.3) to derive the temperature for the CS and found $T_Z = 77$ kK. Kaler & Feibelman (1985) analyzed UV data achieved with the *IUE* and derived $T_Z = 114 \pm 9$ kK.

³The Second Palomar Observatory Sky Survey (POSS-II) was made by the California Institute of Technology with funds from the National Science Foundation, the National Aeronautics and Space Administration, the National Geographic Society, the Sloan Foundation, the Samuel Oschin Foundation, and the Eastman Kodak Corporation. The Oschin Schmidt Telescope is operated by the California Institute of Technology and Palomar Observatory.

The Digitized Sky Survey was produced at the Space Telescope Science Institute under U.S. Government grant NAG W-2166. The images of these surveys are based on photographic data obtained using the Oschin Schmidt Telescope on Palomar Mountain and the UK Schmidt Telescope. The plates were processed into the present compressed digital form with the permission of these institutions. http://archive.stsci.edu/cgi-bin/dss_form

⁴field of view

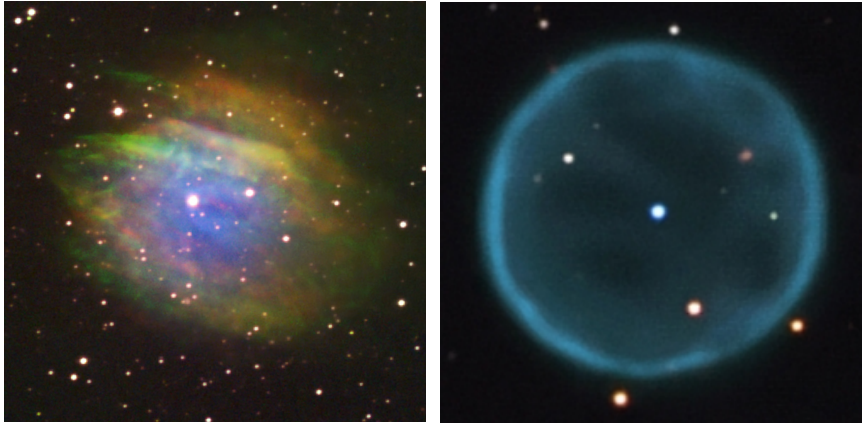


Figure 4.2: Images of the nebula A 35 (left, FOV: $20'' \times 20''$) and the PN A 39 (FOV: $4' \times 4'$). The narrow-band image of A 35 was taken by Dean Salman⁵. The picture is a composite of $H\alpha$, [O III], and [S II].

Harris et al. (1997) determined a reddening of $E_{B-V} = 0.07$. A recent study by Good et al. (2004) determined $T_{\text{eff}} = 74.7 \pm 6 \text{ kK}$ and $\log g = 6.95 \pm 0.15$ from the Balmer line spectrum and $T_{\text{eff}} = 93.9 \pm 3.2 \text{ kK}$ and $\log g = 7.43 \pm 0.15$ from the Lyman lines. Metal abundances were determined by Good et al. (2005). They give $n_{\text{C}}/n_{\text{H}} = 4.09^{+5.50}_{-1.52} \cdot 10^{-5}$, $n_{\text{N}}/n_{\text{H}} = 5.45^{+50.2}_{-0} \cdot 10^{-7}$, $n_{\text{O}}/n_{\text{H}} = 3.04^{+0.649}_{-0.902} \cdot 10^{-5}$, and $n_{\text{Si}}/n_{\text{H}} = 9.42^{+4.33}_{-2.42} \cdot 10^{-6}$. With an abundance of $n_{\text{Fe}}/n_{\text{H}} = 3.16^{+2.20}_{-1.52} \cdot 10^{-4}$, iron is roughly ten times solar while Ni ($n_{\text{Ni}}/n_{\text{H}} = 7.36^{+234}_{-0} \cdot 10^{-7}$) is clearly sub-solar. Ciardullo et al. (1999) report a possible physical companion.

4.1.3 Abell 35

Abell 35 (A66 35, PN G303.6+40.0, Sh 2–313, Fig. 4.2) was discovered in 1966 (Abell 1966) and was classified as a PN. Borkowski et al. (1990) explained the asymmetric structure of the nebula as an interaction between the PN and the surrounding ISM. The observed bow shock being located at the equilibrium sphere of the ram pressure of the accelerated PN gas and the stellar wind ram pressure. Frew & Parker (2010) claim A 35 to be a “bowshock nebula in a photoionized Strömgen sphere in the ambient ISM”. This scenario does not include a PN. Weidmann & Gamen (2011), however, classify A 35 as a binary PN (? + G8 IV) with a bc-CSPN (corresponding to binarity for the cool CSPN).

⁵<http://www.ccdimages.com/>

The exciting star of A66 35, BD 22 3467, is a resolved binary system (Jacoby 1981; de Marco 2009) composed of a DAO-type WD and a G8-type companion. The latter dominates the spectrum longward of 2800 Å. The WD is located in a distance of $d = 163^{+96}_{-58}$ pc (Perryman et al. 1997; Gatti et al. 1998, HIPPARCOS). Herald & Bianchi (2002) determined the stellar parameters of both components and found $T_{\text{eff}} = 80 \pm 3$ kK, $\log g = 7.7$ for the DAO-type WD, and $T_{\text{eff}} = 5$ kK, $\log g = 3.5$ for the cool companion. For the latter result they used models calculated by Kurucz. They also investigated the chemical composition of the exciting star and determined abundances for He ($n_{\text{He}}/n_{\text{H}} = (2.5 - 4.3) \cdot 10^{-2}$), C ($n_{\text{C}}/n_{\text{H}} = (1.4 - 2.7) \cdot 10^{-6}$), N ($n_{\text{N}}/n_{\text{H}} < 6.8 \cdot 10^{-8}$), O ($n_{\text{O}}/n_{\text{H}} = (2.5 - 4.9) \cdot 10^{-6}$), Si ($n_{\text{Si}}/n_{\text{H}} < 3.2 \cdot 10^{-7}$), and Fe ($n_{\text{Fe}}/n_{\text{H}} = 3.2 \cdot 10^{-6} - 1.6 \cdot 10^{-5}$).

4.1.4 Abell 39

Abell 39 (A66 39, PN G047.0+42.4, Fig. 4.2) is a possible yet not confirmed binary system discovered by Abell (1966). The system is located in a distance of $d = 530$ pc (Phillips 2005, determined using the visual magnitude of the CS and the extinction). The CSPN is showing a 2'' off-set of the center of the PN. This is usually explained with the interaction between the ISM and the nebula. In the case of A 39 Jacoby et al. explain the offset with a former nonsymmetric mass-loss episode.

One of the first analysis of A 39 using UV spectra obtained with *IUE* derived $T_{\text{Z}} = 86 \pm 2$ kK from He II (Kaler & Feibelman 1985). No evidence for a stellar wind was detected in *IUE* observations (Patriarchi & Perinotto 1991). Good et al. (2004) derived effective temperature and surface gravity from Balmer and Lyman lines and found $T_{\text{eff}} = 72.5 \pm 6.1$ kK and $T_{\text{eff}} = 87.9 \pm 4.7$ kK, respectively $\log g = 6.76 \pm 0.16$ and $\log g = 7.06 \pm 0.15$. With the values for T_{eff} and $\log g$ from the Balmer lines they derived $n_{\text{He}}/n_{\text{H}} = 0.1$, from the Lyman lines $n_{\text{He}}/n_{\text{H}} = 0.04$. In a subsequent paper Good et al. (2005) analyzed metal abundances of C, N, Si, Fe, and Ni using *FUSE* data and found $n_{\text{C}}/n_{\text{H}} = 1.66^{+21.4}_{-0.952} \cdot 10^{-6}$, $n_{\text{N}}/n_{\text{H}} = 4.08^{+\infty}_{-3.87} \cdot 10^{-5}$, $n_{\text{Si}}/n_{\text{H}} = 3.00^{+5.11}_{-1.27} \cdot 10^{-6}$, $n_{\text{Fe}}/n_{\text{H}} = 3.74^{+15.3}_{-0} \cdot 10^{-6}$ and $n_{\text{Ni}}/n_{\text{H}} = 9.93^{+88.7}_{-0} \cdot 10^{-6}$. They also derived the column density of interstellar neutral hydrogen ($n_{\text{HI}} = 0.79 \cdot 10^{20}$ cm⁻²) and the reddening ($E_{\text{B-V}} = 0.13$).

4.1.5 NGC 3587

NGC 3587 ("Owl Nebula", M97, PN G148.4+57.0, Fig. 4.3) was discovered by Pierre Méchain in 1781. It is located in a distance of $d = 425$ pc (Phillips 2005, cf. distance determination of A 39). Pottasch et al. (1978) used UV data taken with the Astronomical Netherlands Satellite (ANS) to determine blackbody temperatures for a sample of CSPNe. For NGC 3587 they derived $T_{\text{eff}} = 75$ kK

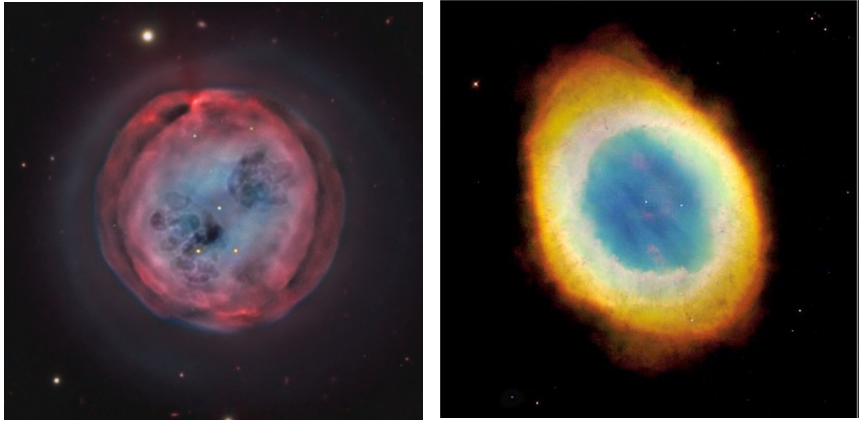


Figure 4.3: Images of the PNe NGC 3587⁷ (left, FOV: $6' \times 6'$; images with the filters Strömgren b and y, $H\alpha$ and β as well as [O III] were taken by the Star Shadows Remote Observatory SSRO) and NGC 6720⁸ (FOV: $2' \times 2'$, North is approximately 30° CW from up, east is to the left, R:G:B – [N II] : [O III] : He II).

while Kaler (1983) give a Zanstra temperature of $T_Z = 112 \pm 5$ kK from H I and $T_Z = 107 \pm 3$ kK from He II. These values were confirmed from analyses of optical observations obtained with the Keck telescope ($T_{\text{eff}} = 110$ kK, $\log g = 6.7$, McCarthy et al. 1997), as well as from a fit to optical H lines in TWIN spectra obtained at the Calar Alto Observatory ($T_{\text{eff}} = 93.0 \pm 5.6$ kK, $\log g = 6.94 \pm 0.31$, Napiwotzki 1999).

NGC 3587 is emitting soft X-ray radiation (Leahy et al. 1996). Chu et al. (1998) analyzed ROSAT HRI⁶ data and were able to show, that the source of the X-ray radiation is the CS.

4.1.6 NGC 6720

A first report about NGC 6720 (“Ring Nebula”, M 57, PN G063.1+13.9, Fig. 4.3) was published by Charles Messier in 1850. M 57 was extensively studied with more than 676 entries in the SIMBAD database. The trigonometric distance is $d = 700_{-200}^{+450}$ pc (Harris et al. 2007). Harris et al. (1997) determined $E_{B-V} = 0.08$. O’Dell et al. (2007) calculated a nebular age of $t = 7000$ yr. The large size ($30''$ semiminor axis), and the low surface brightness indicate NGC 6720 being

⁶High Resolution Imager

⁷www.starshadows.com/gallery/display.cfm?imgID=304

⁸<http://heritage.stsci.edu/1999/01/>



Figure 4.4: Images of the PNe NGC 6853 (left, FOV: $12' \times 12'$, R:G:B – [N II] : H α : [O III]) and NGC 7293⁹ (FOV: $25' \times 25'$, composite of H α and [O III] images).

a evolved PN. The same authors find a stellar mass of $M = 0.61 - 0.62 M_{\odot}$, using evolutionary tracks from Blöcker (1995b). Literature values for T_{eff} strongly depend on the applied method, and, in the case of NGC 6720, spread a wide range from $T_{\text{eff}} = 162 \text{ kK}$ (Kaler & Jacoby 1989), $T_{\text{Z}} = 109.6 \text{ kK}$, $T_{\text{Z}} = 120.6 \text{ kK}$ (both from Phillips 2003, from H I and He II, respectively), $T_{\text{eff}} = 101.2 \pm 4.6 \text{ kK}$ (Napiwotzki 1999), down to $T_{\text{eff}} = 80 \text{ kK}$ from McCarthy et al. (1997). Napiwotzki (1999) also derived $\log g = 6.88$ and $n_{\text{He}}/n_{\text{H}} = 0.072$.

4.1.7 NGC 6853

NGC 6853 (“Dumbbell Nebula”, M 27, PNG060.8–03.6, Fig. 4.4) is one of the first PNe that was ever discovered (Charles Messier 1764), and it has been investigated many times ever since. It is located at a distance of $d = 405_{-25}^{+28} \text{ pc}$ (Benedict et al. 2009, trigonometric parallax). Analyzing the proper motion of NGC 6853, a binary nature of the object was discussed by Cudworth (1973, 1977). He gives a minimum separation of the two components of about 2 500 AU. A recent astrometrical analysis by Benedict et al. (2003) using *HST* gave no hints for a binary nature, confirming a previous result by Ciardullo et al. (1999).

Kreysing et al. (1992) reported a point-source X-ray emission from NGC 6853 in ROSAT data. Feibelman (1994) investigated *IUE* spectra and claimed the detection of P Cygni profiles in the N V and C IV resonance doublets. Benedict

⁹<http://hubblesite.org/newscenter/newsdesk/archive/releases/2004/32/image/d>

et al. (2009) used the relation $g = MG/R^2$ to calculate the surface gravity for NGC 6853. They derived $\log g = 6.89 \pm 0.08$. The literature values for T_{eff} and $\log g$ derived from model spectra of the DAO-type CS range from $T_{\text{eff}} = 108.6$ kK, $\log g = 6.72$ (Napiwotzki 1999) to $T_{\text{eff}} = 125$ kK, $\log g = 6.5$ (Traulsen et al. 2005) and $T_{\text{eff}} = 144$ kK, $\log g = 7.7$ (Bohlin et al. 1982). The latter give $E_{B-V} = 0.06$, which is slightly smaller than the value of Harris et al. (1997, $E_{B-V} = 0.09$). Traulsen et al. also determined the abundances for He ($n_{\text{He}}/n_{\text{H}} = 0.1$), C ($n_{\text{C}}/n_{\text{H}} = 8 \cdot 10^{-4}$), N ($n_{\text{N}}/n_{\text{H}} = 2 \cdot 10^{-5}$), O ($n_{\text{O}}/n_{\text{H}} = 4 \cdot 10^{-4}$) and Si ($n_{\text{Si}}/n_{\text{H}} = 4 \cdot 10^{-6}$). With the parameters of Traulsen et al., Werner et al. (2005) derived a roughly solar F abundance from F VI λ 1139.50Å. Recently, $T_{\text{eff}} = 86.7 \pm 5.4$ kK, $\log g = 7.36 \pm 0.18$, and $n_{\text{He}}/n_{\text{H}} = 5.13 \cdot 10^{-2}$ were determined from H Balmer lines (Gianninas et al. 2010).

4.1.8 NGC 7293

NGC 7293 (“Helix Nebula”, PN G036.1–57.1, Fig. 4.4) was discovered in the 17th century by K. L. Harding. A trigonometric distance of $d = 216_{-12}^{+14}$ pc was determined by Benedict et al. (2009). Bohlin et al. (1982) analyzed *IUE* observations and determined $T_{\text{eff}} = 123$ kK and $\log g = 8.0$ by using the Zanstra method and H+He composed model atmospheres. They derived $E_{B-V} = 0.01$, while Harris et al. (1997) found $E_{B-V} = 0.03$. By fitting H δ with H+He model atmospheres, Napiwotzki (1999) found $T_{\text{eff}} = 103.6 \pm 5.5$ kK and $\log g = 7.0 \pm 0.22$. A surface gravity $\log g = 7.34 \pm 0.06$ was calculated by Benedict et al. (2009) using the formula $g = MG/R^2$. The value for the effective temperature from Napiwotzki (1999) was refuted by Traulsen et al. (2005), arguing that neither N IV nor O IV lines were visible in the observed spectra of NGC 7293, thus implying a higher T_{eff} . In addition, the small emission core of He II 1640.42 Å visible in *STIS* spectra, requires $T_{\text{eff}} > 120$ kK. For their final fit Traulsen et al. applied $T_{\text{eff}} = 120 \pm 6$ kK and $\log g = 6.3 \pm 0.2$. A chemical composition of $n_{\text{He}}/n_{\text{H}} = 0.03$, $n_{\text{C}}/n_{\text{H}} = 3 \cdot 10^{-4}$, $n_{\text{N}}/n_{\text{H}} = 5 \cdot 10^{-5}$, $n_{\text{O}}/n_{\text{H}} = 3.5 \cdot 10^{-4}$ and $n_{\text{Si}}/n_{\text{H}} = 4 \cdot 10^{-6}$ was derived. Werner et al. (2005) analyzed the *FUSE* observation of NGC 7293 using T_{eff} and $\log g$ from Traulsen et al. and determined a F abundance of approximately solar. Werner et al. (2007) found a strong Ar underabundance of a factor of ≈ 50 .

$T_{\text{eff}} = 94.6 \pm 3.4$ kK and $\log g = 7.62 \pm 0.12$ were determined by Gianninas et al. (2010) from optical H Balmer lines. They also derived $n_{\text{He}}/n_{\text{H}} = 1.26 \cdot 10^{-2}$.

Guerrero et al. (2001) reported a point source X-ray emission at the CS position. They state that a fit of the measured X-ray spectrum is impossible using only one component. As a possible explanation for the hard X-ray emission, they suppose a companion dMe star, the soft component originates from the CS itself



Figure 4.5: Images of the PN PuWe 1 (left, FOV: $21' \times 21'$) and the nebula Sh 2-174 (FOV: $35' \times 35'$).

(Guerrero et al. 2000). Werner et al. (2007) found the Ar abundance to be ≈ 50 times underabundant compared to solar using the parameter values of Napiwotzki (1999, $T_{\text{eff}} = 106 \text{ kK}$, $\log g = 7.0$) with only little difference if the parameters by Traulsen et al. (2005) were applied.

4.1.9 PuWe 1

The PN PuWe 1 (PN G158.9+17.8, Fig. 4.5) was discovered in 1980 (Purgathofer & Weinberger 1980) in POSS observations. They considered a PN to be an object showing broad [O III] emission lines, with no features of another object-class. The classification as a PN was rejected by Acker et al. (1987) as they found no emission lines in their observations. At a distance of $d = 365^{+47}_{-37} \text{ pc}$ (Harris et al. 2007, trigonometric parallax) it is one of the closest nebulae, and, having an angular diameter of $20' \times 20'$ (Purgathofer & Weinberger 1980), PuWe 1 is also one of the largest nebulae known. The size and its low excitation hints at an old nebula. A nebular expansion velocity v_{exp} of 27, 20, and 27 km sec^{-1} was determined by Giesecking et al. (1986) from [O III], $\text{H}\alpha$, and [N III] respectively. The interstellar extinction is $E_{\text{B-V}} = 0.23$ (Kaler et al. 1990). A more recent analysis of Harris et al. (1997) found $E_{\text{B-V}} = 0.14$. According to Ciardullo et al. (1999) the possible companion already reported by Purgathofer & Weinberger (1980) is not a physical companion.

A first determination of the CS parameters using the Zanstra method led to $T_{\text{Z}} = 107 \text{ kK}$ for He II and $T_{\text{Z}} = 71 \text{ kK}$ for H I (Kaler 1983). McCarthy et al. (1997)

derived $T_{\text{eff}} = 110 \text{ kK}$ and $\log g = 7.0$ from optical spectra. From a comparison of H+He+C+N+O NLTE models with H Balmer lines Gianninas et al. (2010) derived $T_{\text{eff}} = 93.2 \pm 3.1 \text{ kK}$, $\log g = 7.57 \pm 0.12$, and $n_{\text{He}}/n_{\text{H}} = 2.24 \cdot 10^{-2}$.

4.1.10 Sh 2–174

Sh 2–174 (PN G120.3+18.3, Fig. 4.5) was first classified as an H II region by Sharpless (1959). A nebular distance of $d = 560 \text{ pc}$ was determined by Phillips (2005). Frew & Parker (2010) classify the PN Sh 2–174 as a Strömgren zone in the ISM, e.g. a low-mass H II region being ionized by a hot WD. The recent work by Weidmann & Gamen (2011) lists Sh 2–174 as a PN with a DAO-type CS.

Napiwotzki & Schönberner (1993) analyzed GD 561 (WD 2324+806), a DAO-type (Bergeron et al. 1992) star, off-center from the geometrical center of the nebula. From their analysis they derived a distance of GD 561 in agreement with the distance of the nebula (Fich & Blitz 1984, $d = 220 \pm 520 \text{ pc}$, kinematic distance). As the derived nebular radius ($r = 0.3 \text{ pc}$) is of the order of the expected value for old PNe, they concluded, that GD 561 is the CS of Sh 2–174. The off-center position is most likely caused by the interaction between the PN and the ISM. It took approximately 10 000 years for GD 561 to reach its current position (Kerber et al. 2004), and therefore Sh 2–174 would represent an evolved stage of PN evolution.

Napiwotzki (1999, 2003) used simple H+He composed NLTE model atmospheres, in order to fit the optical hydrogen Balmer lines. As model atmospheres without the elements C, N, and O suffer from the so called Balmer-line problem (higher T_{eff} are required for a proper fit of the higher order Balmer lines), only the highest available Balmer lines were taken into account to derive the photospheric parameters. The analysis yielded $T_{\text{eff}} = 69 \pm 3 \text{ kK}$, $\log g = 6.70 \pm 0.18$, and $n_{\text{He}}/n_{\text{H}} = 2.8 \cdot 10^{-3}$. By comparison of these parameters in a $\log T_{\text{eff}} - \log g$ diagram with evolutionary tracks a very low mass of $M = 0.43 \pm 0.03 M_{\odot}$ was determined. This extremely low mass does not fit in the canonical post-AGB evolution, but rather points at a post-RGB scenario, where the H-rich envelope is stripped away by the interaction with a companion star during the RGB phase, leaving behind a low-mass star, unable to ignite He-burning. A recent work on the Balmer-line problem on a sample of DA and DAO white dwarfs by Gianninas et al. (2010), determined photospheric parameters of GD 561, based on optical and *FUSE* observations. Calculating H+He+C+N+O NLTE model atmospheres they derived $T_{\text{eff}} = 74 \text{ kK}$, $\log g = 7.16$, and $n_{\text{He}}/n_{\text{H}} = 2.2 \cdot 10^{-3}$.

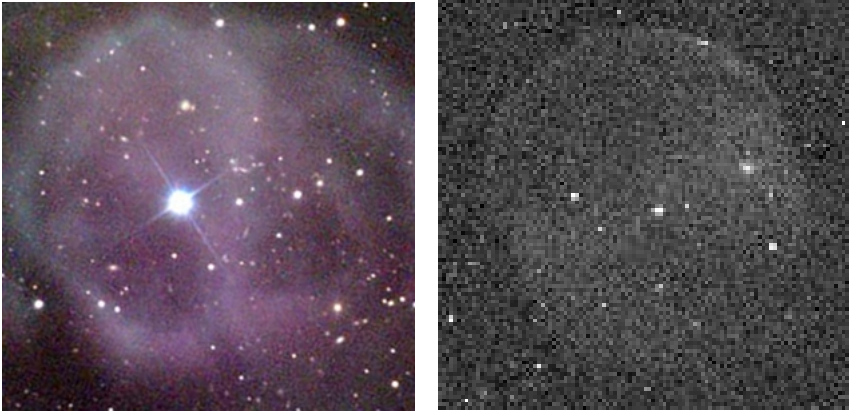


Figure 4.6: Images of the PNe A 36¹⁰ (left, FOV: 3'.8 × 3'.8) and Lo 111 (FOV: 3'.8 × 3'.8).

4.2 *O(H)*-type ionizing stars

4.2.1 *Abell 36*

Discovered by Abell (1955), Abell 36 (A66 36, PNG 318.4+41.4, Fig. 4.6) is the brightest of the Abell objects with a magnitude of $m_V = 11.57$. It is located at a distance of $d = 770$ pc (Phillips 2005). A possible variability of the CS was already reported by Abell (1966). The CS is classified as a subdwarf O star (e.g. Lasker & Hesser 1971). A first NLTE spectral analysis by Méndez et al. (1981) found $T_{\text{eff}} = 65 \pm 10$ kK, $\log g = 5.2 \pm 0.5$, and a He content of $n_{\text{He}}/(n_{\text{He}} + n_{\text{H}}) = 0.13 \pm 0.04$. Kaler & Feibelman (1985) derived $T_Z = 73 \pm 1$ kK. Traulsen et al. (2005) analyzed *HST* and *FUSE* observations and determined $T_{\text{eff}} = 113 \pm 6$ kK, $\log g = 5.6 \pm 0.2$, and the abundances $n_{\text{He}}/n_{\text{H}} = 0.2$, $n_{\text{C}}/n_{\text{H}} = 2.0 \cdot 10^{-4}$, $n_{\text{N}}/n_{\text{H}} = 1.0 \cdot 10^{-4}$, $n_{\text{O}}/n_{\text{H}} = 5.0 \cdot 10^{-4}$, and $n_{\text{Si}}/n_{\text{H}} = 5.0 \cdot 10^{-6}$.

The presence of Fe VII lines in UV observations obtained with *IUE* were reported by Feibelman & Bruhweiler (1990). Assuming $T_{\text{eff}} = 95$ kK and $\log g = 5.5$, Deetjen (1999) derived a subsolar Fe abundance of -1.3 dex from *IUE* data. Werner et al. (2003) analyzed *HST/STIS* spectra and confirmed the presence of Fe VII lines, but found no signs for Fe VI lines. Apparao & Tarafdar (1989) found X-ray emission in European X-Ray Observatory Satellite (EXOSAT) observations. Jordan et al. (2005) report a probable detection of a weak magnetic field

¹⁰<http://www.noao.edu/outreach/aop/observers/abell36.html>, Mike O'Connor, Tristan Dilapo and Gary Kielich/Adam Block/NOAO/AURA/NSF

¹¹http://www.blacksdies.org/images/non_ngc_pn/Add2003/lo1.jpg

for A 36 discovered from spectro-polarimetry at the Very Large Telescope (VLT). This result has been refuted by Leone et al. (2011), who found no signs for an effective magnetic field.

4.2.2 *Lo 1*

Longmore 1 (Lo 1, PN G255.3–59.6, Fig. 4.6) was discovered and classified as a PN by Longmore (1977). Lo 1, located at a distance of 800 pc (Ishida & Weinberger 1987), does possess a high-gravity O(H) CS (Méndez et al. 1985). Based on a NLTE model atmosphere analysis of optical observations Méndez et al. (1985) derived $T_{\text{eff}} = 65 \pm 10$ kK and $\log g = 5.7 \pm 0.3$. No evidence for a stellar wind was found in UV and optical observations, (Méndez et al. 1985; Patriarchi & Perinotto 1991). Herald & Bianchi (2004) analyzed *FUSE* and *IUE* observations and found significantly higher values for the effective temperature and the surface gravity ($T_{\text{eff}} = 120 \pm 10$ kK, $\log g = 6.7_{-0.7}^{+0.3}$). Their main argument for the higher T_{eff} was the strong O VI doublet in the *FUSE* range that could only be reproduced properly with $T_{\text{eff}} = 120$ kK and an O abundance of five times solar. All other elements in their models had solar abundances.

4.2.3 *LSS 1362*

For LSS 1362 (PN G273.6+06.1, Fig. 4.7) only a handful of analyses are available. The first report about LSS 1362 can be found in Drilling (1983) who discovered twelve subluminescent O stars. A spectroscopical distance of $d = 1.1$ pc was determined by Heber et al. (1988b). Schönberner & Drilling (1984) analyzed *IUE* observations of LSS 1362 and determined $T_{\text{eff}} = 110$ kK from fitting the slope of the UV continuum. They also reported Fe V – VII lines in the observation. Heber & Drilling (1984) employed NLTE model atmosphere calculations and found $T_{\text{eff}} = 100 \pm 20$ kK and $\log g = 5.2 \pm 0.3$, as well as $n_{\text{H}}/n_{\text{He}} = 0.1 \pm 0.03$. Heber et al. (1988a) investigated optical spectra of a small sample of nine sd(O) stars. The observations were taken with the Cassegrain Echelle Spectrograph (CASPEC) at the 3.6 m ESO telescope. They describe LSS 1362 as the most extreme case of their sample, because of all metallic lines being in emission. Amongst the nine objects in their study it is also the only one revealing a faint PN in ESO sky survey plates. Heber et al. (1988a) proposed that the lack of nebular surroundings around the other sample stars possibly originates in the born again scenario (Iben et al. 1983; Schönberner 1979). Heber et al. (1988a) analyzed the optical H and He lines and derived $T_{\text{eff}} = 100$ kK, $\log g = 5.3$ and a He abundance of 0.1 in number fractions. They also classified LSS 1362 as having a non-carbon line spectrum.

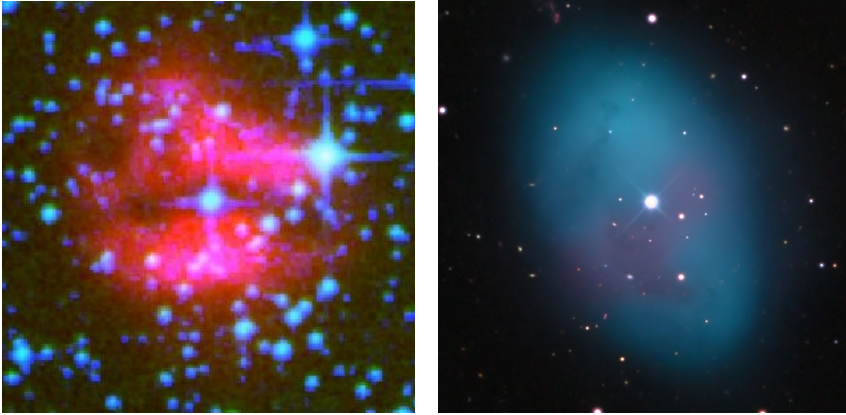


Figure 4.7: Images of the PNe LSS 1362¹² and NGC 1360¹³ (FOV: $8'.8 \times 8'.8$).

Tweedy (1993) reported about Fe VII lines in *IUE* spectra of LSS 1362. Traulsen et al. (2005) derived $T_{\text{eff}} = 114 \pm 6$ kK, $\log g = 5.7 \pm 0.2$ and a chemical abundance pattern of $n_{\text{He}}/n_{\text{H}} = 0.1$, $n_{\text{C}}/n_{\text{H}} = 2 \cdot 10^{-4}$, $n_{\text{N}}/n_{\text{H}} = 1 \cdot 10^{-4}$, $n_{\text{O}}/n_{\text{H}} = 2 \cdot 10^{-4}$ and $n_{\text{Si}}/n_{\text{H}} < 4 \cdot 10^{-4}$. Werner et al. (2005) found an upper limit of roughly solar for the F abundance from F VI λ 1139.50Å. No abundance determination for the iron-group elements can be found in the literature although attempts were made (cf. Hoffmann et al. 2004).

Herald & Bianchi (2011) investigated FUV, UV, and optical spectra of H-rich CSPNe. They derived $T_{\text{eff}} = 119.4$ kK $\log g = 5.7 \pm 0.3$ and a mass-loss rate of $\log \dot{M} = -8.7 M_{\odot} \text{ yr}^{-1}$. Recently a kilogauss magnetic field was discovered by Jordan et al. (2005). Leone et al. (2011) analyzed VLT observations and do not find an effective magnetic field. They conclude that either the field is much weaker than reported by Jordan et al. or that it has a more complex form “leading to cancellations”.

4.2.4 NGC 1360

NGC 1360 (PN G220.3–53.9, Fig. 4.7) was discovered by Haro & Luyten (1962). Its CS is CPD-26° 389 (Perryman et al. 1997, $m_{\text{v}} = 11.34$, HIPPARCOS). Based on HIPPARCOS data Acker et al. (1998) derived a distance of 350_{-180}^{+1000} pc.

Since its discovery many investigations with partially contrary results have

¹²http://crescent.astro.illinois.edu/projects/spitzer-pne/LSS_1362_img.php

¹³<http://www.martinpughastrophotography.id.au/images/NGC1360.jpg>

been published. Méndez & Niemelä (1977) reported that the CS of NGC 1360 is a single-lined spectroscopic binary with a period of about eight days. Radial velocity measurements by Wehmeyer & Kohoutek (1979) could not confirm this result. Instead, a nearly constant radial velocity of $v_{\text{rad}} = 52.3 \pm 4.3 \text{ km sec}^{-1}$ was observed. Both analyses are based on optical observations. Guinan et al. (1984) and Zuckerman & Aller (1986) again favored the binary nature analyzing UV data taken with *IUE*. Latest investigations lead to $v_{\text{rad}} = 41.8 \pm 4 \text{ km sec}^{-1}$ (Durand et al. 1998) with no radial velocity variations.

Guinan et al. (1984) found indications for outflowing plasma in ultraviolet *IUE* measurements. Heap (1986), also using *IUE* observations, denied this result and found no hints for a stellar wind in NGC 1360. The available observations from *FUSE* and *HST/STIS* do not show any signs for a stellar wind.

A wide spread of values for T_{eff} and $\log g$ of NGC 1360 can be found in the literature. The range spans from $T_{\text{eff}} = 60_{-5}^{+10} \text{ kK}$ and $\log g = 5.23 \pm 0.23$ (Méndez et al. 1981), to $T_{\text{eff}} = 140 \text{ kK}$ and $\log g = 6.00$ (Hoare et al. 1996). Traulsen et al. (2005) used line blanketed model atmospheres including H, He, C, N, and O, to analyze *FUSE* and *HST/STIS* observations and derived $T_{\text{eff}} = 97 \text{ kK}$, $\log g = 5.3$ using the O IV – VI ionization equilibrium. The latter paper also gives derived abundances for He ($n_{\text{He}}/n_{\text{H}} = 0.25$), C ($n_{\text{C}}/n_{\text{H}} = 2 \cdot 10^{-4}$), N ($n_{\text{N}}/n_{\text{H}} = 5 \cdot 10^{-5}$), O ($n_{\text{O}}/n_{\text{H}} = 2 \cdot 10^{-4}$) and Si ($n_{\text{Si}}/n_{\text{H}} = 4 \cdot 10^{-5}$). Using the parameters of Traulsen et al. a F abundance of roughly solar was found by Werner et al. (2005). Werner et al. (2004) identified Ne VII $\lambda 973.3 \text{ \AA}$ in the *FUSE* observation of NGC 1360. They calculated NLTE model atmospheres including He, C, O, and Ne using the parameters given by Hoare et al. (1996), and determined a roughly solar Ne abundance. A further analysis by Werner et al. (2007) based on the parameters by Traulsen et al. (2005) found a slightly supersolar Ar abundance.

The first extreme ultraviolet (EUV) analysis of NGC 1360 was done by Hoare et al. (1996). An overall good fit to the *Extreme Ultraviolet Explorer (EUVE)* observation was obtained with a H, He, C, N, and O composed model atmosphere at $T_{\text{eff}} = 110 \text{ kK}$ and $\log g = 6.0$. Hoare et al. concluded that the remaining distinctions between their model fit and the observations were due to missing opacities (and therefore line blanketing) caused by further light metals.

Feibelman & Bruhweiler (1990) and Tweedy (1993) reported the presence of Fe VI and Fe VII absorption lines in the photospheric spectrum of NGC 1360 taken with *IUE*. As these were weaker than expected, the assumption arose that either T_{eff} was higher than previously thought or that Fe was subsolar (Werner et al. 2003).

Recently, kilogauss magnetic fields were detected for the first time directly in NGC 1360 and three other CSPNe (Jordan et al. 2005) using spectropolarimetry with the FORS1 instrument at the VLT. According to Jordan et al., this result



Figure 4.8: Image of the PN NGC 4361¹⁴ (FOV: $2'.3 \times 2'.3$).

supports the idea that asymmetrical PNe could be the result of such magnetic fields. Leone et al. (2011) do not find an effective magnetic field. They suggest that either the field is weaker than found by Jordan et al. (2005) or that the field is much more complex, leading to cancellations of the field.

Herald & Bianchi (2011) determined $T_{\text{eff}} = 104.5 \text{ kK}$, $\log g = 5.7^{+0.3}_{-0.2}$, and a mass-loss rate of $\lesssim 1 \cdot 10^{-10} M_{\odot} \text{ yr}^{-1}$. Already in 1985 de Korte et al. have shown from EXOSAT data, that NGC 1360 is radiating X-rays, associated with the CSPN.

4.2.5 NGC 4361

The first report about NGC 4361 (PN G294.1+43.6, Fig. 4.8) can be found in Curtis (1918). The same author also gives the diameter of $\approx 80''$ for the halo PN. Bensby & Lundström (2001) find an angular diameter of $63''$. They derive a mean distance of 1.44 kpc from Meatheringham et al. (1988), Méndez et al. (1992), Zhang (1993), Pottasch (1996), and Maciel & Cazetta (1997).

The literature values for the effective temperature for the CS differ significantly. From equivalent widths of optical absorption lines Aller (1968) found $T_{\text{eff}} = 40 \text{ kK}$. Zanstra temperatures of $T_Z = 42 \pm 2 \text{ kK}$ and $T_Z = 98 \pm 2 \text{ kK}$ (from H I respectively He II) were derived from Kaler (1983). Kudritzki et al. (1984) analyzed optical spectra using H+He NLTE model atmospheres. They found $T_{\text{eff}} = 80 \pm 10 \text{ kK}$ and $\log g = 5.5 \pm 0.3$. de Freitas Pacheco et al. (1986) derived

¹⁴www.noao.edu/outreach/aop/observers/n4361.html, Elliot Gellman and Duke Creighton/Adam Block/NOAO/AURA/NSF

three different temperatures for the CS. A colour temperature of $T_{\text{col}} = 102$ kK, a Zanstra temperature from H I of $T_Z = 39.5$ kK, and a Zanstra temperature from He II of $T_Z = 86.5$ kK. The same work also gives $E_{\text{B-V}} = 0.15$. Traulsen et al. (2005) analyzed *FUSE* and *HST/STIS* observations and derived $T_{\text{eff}} = 126 \pm 6$ kK, $\log g = 6.0 \pm 0.2$, and the abundances $n_{\text{He}}/n_{\text{H}} = 0.1$, $n_{\text{C}}/n_{\text{H}} = 8.0 \cdot 10^{-3}$, $n_{\text{N}}/n_{\text{H}} = 6.0 \cdot 10^{-5}$, $n_{\text{O}}/n_{\text{H}} = 5.0 \cdot 10^{-4}$, and $n_{\text{Si}}/n_{\text{H}} = 2.0 \cdot 10^{-6}$. They also find $M = 0.59 M_{\odot}$.

Point-source X-ray emission was detected by Apparao & Tarafdar (1989) using the Einstein Observatory.

Table 4.2: Summary of the main literature values for the DAO-type (upper part) and O(H)-type stars. The values for T_{eff} and $\log g$ are rounded and taken from UV and FUV analyses if available.

object	T_{eff} [kK]	$\log g$ [cm sec $^{-2}$]	$n_{\text{He}}/n_{\text{H}}$	$n_{\text{C}}/n_{\text{H}}$	$n_{\text{N}}/n_{\text{H}}$	$n_{\text{O}}/n_{\text{He}}$	$n_{\text{Si}}/n_{\text{H}}$	$n_{\text{Fe}}/n_{\text{H}}$	$n_{\text{Ni}}/n_{\text{H}}$
A 7	83 ± 4	7.5 ± 0.1	4.37·10 $^{-2}$	4.17 $^{+3.84}_{-1.09}$ ·10 $^{-5}$	6.43 $^{+23.3}_{-5.96}$ ·10 $^{-6}$	—	2.27 $^{+1.04}_{-1.08}$ ·10 $^{-5}$	8.22 $^{+7.25}_{-3.82}$ ·10 $^{-5}$	0 $^{+8.95}_{-0}$ ·10 $^{-6}$
A 31	94 ± 3	7.5 ± 0.2	—	4.09 $^{+5.50}_{-1.52}$ ·10 $^{-5}$	5.45 $^{+50.2}_{-0}$ ·10 $^{-7}$	3.04 $^{+0.649}_{-0.902}$ ·10 $^{-5}$	9.42 $^{+4.33}_{-2.43}$ ·10 $^{-6}$	3.16 $^{+2.20}_{-1.52}$ ·10 $^{-4}$	7.36 $^{+2.34}_{-0}$ ·10 $^{-7}$
A 35	80 ± 3	7.7 $^{+0.13}_{-0.18}$	2.5 – 4.3·10 $^{-2}$	1.4 – 2.7·10 $^{-6}$	< 6.8·10 $^{-8}$	2.5 – 4.9·10 $^{-6}$	< 3.2·10 $^{-7}$	0.3 – 1.6·10 $^{-5}$	—
A 39	88 ± 5	7.1 ± 0.2	4.00·10 $^{-2}$	1.66 $^{+21.4}_{-0.952}$ ·10 $^{-6}$	4.08 $^{+68}_{-3.87}$ ·10 $^{-5}$	—	3.00 $^{+5.11}_{-1.27}$ ·10 $^{-6}$	3.74 $^{+15.3}_{-0}$ ·10 $^{-6}$	9.93 $^{+88.7}_{-0}$ ·10 $^{-6}$
NGC 3587	94 ± 6	6.9 ± 0.3	8.5 ± 2.2·10 $^{-2}$	—	—	—	—	—	—
NGC 6720	101 ± 5	6.9 ± 0.3	7.2 ± 1.4·10 $^{-2}$	—	—	—	—	—	—
NGC 6853	126 ± 6	6.5 ± 0.2	1.0·10 $^{-1}$	8.0·10 $^{-4}$	2.0·10 $^{-5}$	4.0·10 $^{-4}$	4.0·10 $^{-6}$	—	—
NGC 7293	120 ± 6	6.3 ± 0.2	3.0·10 $^{-2}$	3.0·10 $^{-4}$	5.0·10 $^{-5}$	3.5·10 $^{-4}$	4.0·10 $^{-6}$	—	—
PuWe 1	94 ± 6	7.1 ± 0.2	2.0 ± 0.7·10 $^{-2}$	—	—	—	—	—	—
Sh 2–174	74	7.2	2.2·10 $^{-3}$	—	—	—	—	—	—
A 36	95	5.5	—	—	—	—	—	—	—
Lo 1	120 ± 10	6.7 $^{+0.3}_{-0.7}$	—	—	—	2.45·10 $^{-3}$	—	—	—
LSS 1362	119	5.7 ± 0.3	1.0·10 $^{-1}$	2.0·10 $^{-4}$	1.0·10 $^{-4}$	2.0·10 $^{-4}$	< 4.0·10 $^{-4}$	—	—
NGC 1360	97 ± 5	5.3 ± 0.2	2.5·10 $^{-1}$	2.0·10 $^{-4}$	5.0·10 $^{-5}$	2.0·10 $^{-4}$	4.0·10 $^{-5}$	—	—
NGC 4361	126 ± 6	6.0 ± 0.2	1.0·10 $^{-1}$	8.0·10 $^{-3}$	6.0·10 $^{-5}$	5.0·10 $^{-4}$	2.0·10 $^{-6}$	—	—

CHAPTER 5

Analysis method

This chapter gives an overview of the methods applied in this analysis to derive the various stellar parameters. We will follow the standard procedure for all objects. First, the incorporation of the influence of the ISM is discussed (Sect. 5.2). Then the determination of T_{eff} and $\log g$ (Sect. 5.3) followed by the analysis of the chemical abundances (Sect. 5.4) is depicted. The final step is the identification of the stellar evolutionary status of the star and hence the determination of its mass, luminosity, and distance, using $\log T_{\text{eff}} - \log g$ diagrams in conjunction with suitable evolutionary tracks (Sect. 5.5) either for hot, H-rich post-AGB stars or post-EHB stars, respectively.

5.1 General aspects

The calculated model grids for each object are initially centered around the latest literature values for T_{eff} (± 10 kK), $\log g$ (± 0.3), and the chemical composition. For some objects the grids had to be extended to a wider range in $\log g$ (± 0.6). The abundances for elements that were not determined in previous analyses were assumed to be solar and later on adjusted. For elements without corresponding lines in the observation or with lines strongly blended by ISM absorption features upper limits were determined. The final model grid is shown in Fig. 5.1.

5.2 Interstellar absorption and reddening

In a first preparatory step, the influence of interstellar dust and matter on the detected stellar flux had to be taken into account.

Photons of high energy are scattered out leading to a *reddening*, $E_{\text{B-V}}$, of the original spectrum. For the determination of $E_{\text{B-V}}$, *FUSE* and low-resolution *IUE* observations were applied. If available, additional photometric magnitudes in the B, V, R, J, H, and K band were used. The stellar fluxes in these bands are

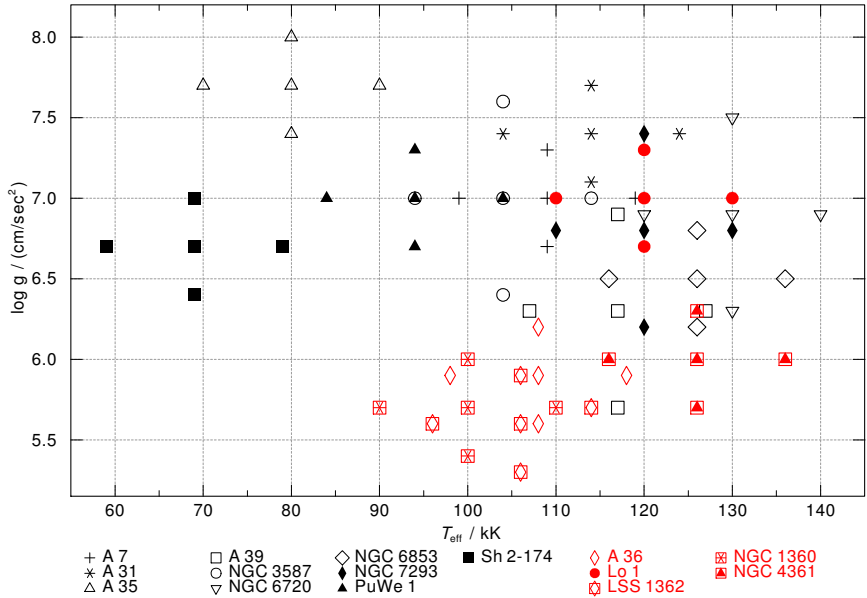


Figure 5.1: Calculated model grid.

less affected by the interstellar medium. Therefore the model SEDs are normalized using the photometric magnitudes. The reddening law of Fitzpatrick (1999) with the standard value $R_V = 3.1$ is applied. Fig. 5.2 shows an example for A 7. The best fit is achieved for $E_{B-V} = 0.08 \pm 0.04$. Within the error limits this is in agreement with $E_{B-V} = 0.1$ from Harris et al. (1997). The value well reproduces the 2200 Å bump that is believed to originate in interstellar polycyclic aromatic hydrocarbons (PAHs, Allamandola et al. 1985).

The *interstellar neutral hydrogen*, H I, induces the second major influence of the ISM on photospheric spectra. For the determination of its column density, n_{HI} , models with a different amount of n_{HI} were compared with Ly α at 1216 Å (whenever *STIS* spectra were available) or with Ly β in the *FUSE* range. Fig. 5.3 shows a section of the *FUSE* range of A 7 around Ly β , compared to synthetic model SEDs with different values for n_{HI} . The best fit is achieved for $n_{\text{HI}} = (4.0 \pm 1.5) \cdot 10^{20} \text{ cm}^{-2}$. However, it has to be mentioned that we make the assumption of a single H I cloud between the star and the observer although it is possible that multiple clouds are in the line of sight.

A huge problem for the analysis of the photospheric spectrum is the influence of interstellar line absorption blending photospheric features. Especially

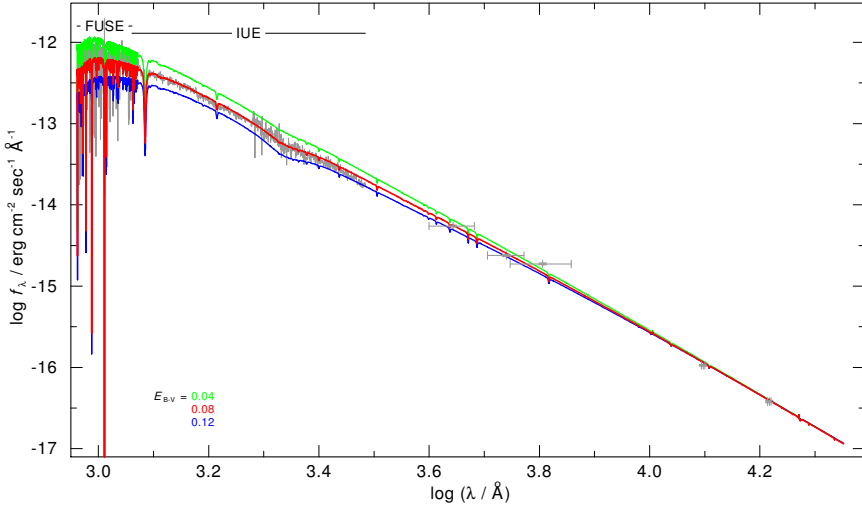


Figure 5.2: Determination of E_{B-V} for A7 using observations (grey) from *FUSE* (911 – 1152 Å), *IUE* (1152 – 3000 Å), and photometric data. For clarity, the *FUSE* observation was smoothed with a Gaussian of 0.1 Å FWHM. The model SEDs were smoothed with a Gaussian of 0.1 Å FWHM in the *FUSE* range and with 7 Å FWHM in the *IUE* range. The continuum flux was normalized to match the H-band flux level at 16 500 Å.

the *FUSE* range is interspersed with numerous interstellar H_2 and H I lines besides lines of other species. This situation enforced the simultaneous modeling of photospheric and ISM line absorption. For this purpose the program *OWENS* was used (Sect. 2.3.4). The ISM model spectra in this work include lines of H I , H_2 ($J = 0 - 9$), $\text{HD I} - \text{II}$, $\text{C II} - \text{IV}$, $\text{N I} - \text{III}$, N V , O I , O VI , Mg II , Al II , $\text{Si II} - \text{IV}$, P II , $\text{S II} - \text{III}$, S VI , $\text{Ar I} - \text{II}$, Mn II , Fe II , and Ni II .

Figure 5.4 shows a section of the *FUSE* observation of NGC 6720. In the upper panel a pure photospheric model SED is compared to the observation. All stellar lines are blended by interstellar absorption features. The situation improves significantly as a combined photospheric + ISM model SED is used (bottom panel). The combined SEDs enabled to identify nearly all observed features in the observations.

Unfortunately, most ISM lines are much stronger than the photospheric ones and thus even a strong change of the stellar abundances does not change the combined fit significantly. In contrast to that, strong stellar lines, e.g. the N V or the C IV resonance doublets in the *STIS* range, change the shape of the combined model SEDs to a considerable degree and, thus, allow to roughly derive the

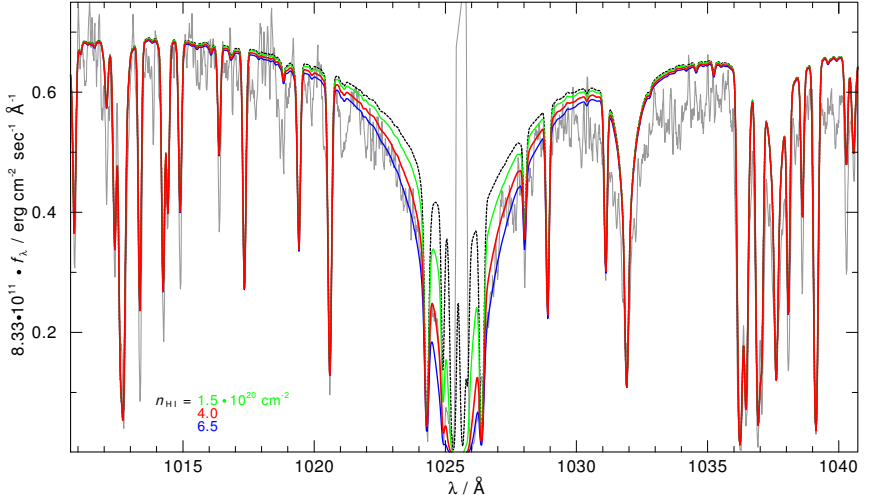


Figure 5.3: Section of the *FUSE* spectrum of A7 around Ly β compared with synthetic model SEDs with different values of $n_{\text{H I}}$. The dashed line is without interstellar H I.

corresponding stellar abundances.

5.3 Effective temperature and surface gravity

The precise determination of T_{eff} and $\log g$ was one of the goals of this work. To derive T_{eff} precisely, metal lines of subsequent ionization stages are necessary. These allow to analyze the *ionization equilibrium* of an element:

An increasing T_{eff} will lead to a decreasing population of the lower ionization stages and an increasing population of higher ionization stages. A lowering of T_{eff} has the contrary effect. In the relevant parameter regime of our sample stars numerous metal lines are expected in the UV and FUV range.

The O IV – vI ionization equilibrium is commonly used to derive T_{eff} . The more ionization equilibria are analyzed the more reliable is the resulting T_{eff} . Iron-group elements are more sensitive for changes in T_{eff} and allow in principal to get smaller error bars on T_{eff} . For the analyzed parameter regime a large number of iron-group lines from the ionization stages v – vIII is expected. Figure 5.5 shows a comparison of O IV – vI lines in the *STIS* observation of NGC 7293 with model SEDs for three different T_{eff} . The sections also contain Fe vI and vII lines becoming stronger with decreasing T_{eff} as Fe vIII lines (not shown in the sections)

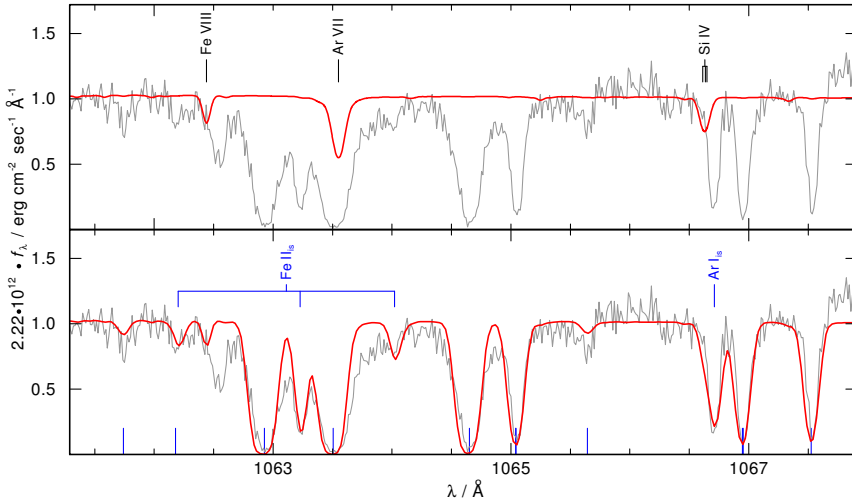


Figure 5.4: Section of the *FUSE* observation (grey) of NGC 6720 compared to a pure photospheric model SED (top panel) and a combined photospheric + ISM model SED. Blue marks at the bottom indicate interstellar H_2 lines.

becomes weaker.

For the determination of $\log g$, line wings especially of the elements He, C, and O are used. Whenever optical spectra were available $\log g$ was derived from the H and He line wings as well. Figure 5.5 displays the determination of $\log g$ for NGC 6853 and NGC 7293 using He II λ 1640.42Å.

Before reliable photospheric models were available the Zanstra method was used to derive a temperature for the CS (Zanstra 1927). Under the assumption that the PN is optically thick in the Lyman continuum the intensity ratio of lines from H I or He II can be used to derive T_Z for the CS.

5.4 Abundances

The model atmosphere calculations started using either literature values for the abundances or, if no abundances could be found in previous works, using solar values. For only four objects optical spectra were available enabling the determination of the H/He-abundance ratio. Thus for most objects H and He abundances were taken from the literature and kept unchanged. By comparing the calculated models SEDs with the observations, abundances are adjusted by either fitting a

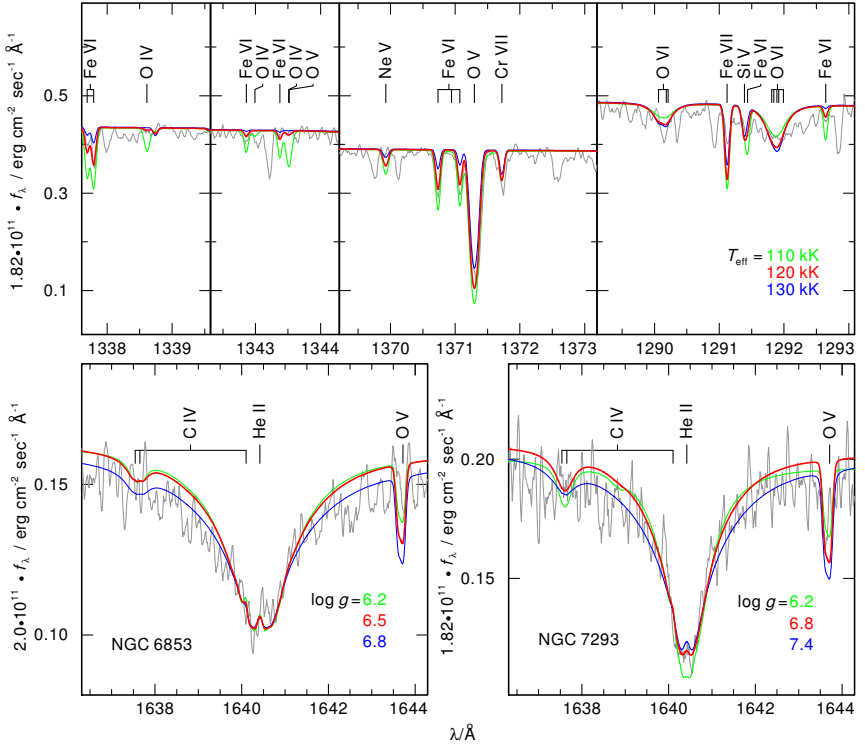


Figure 5.5: Top: Sections of the *STIS* spectrum of NGC 7293 ($\log g = 6.8$) containing ionization equilibria of O IV – VI and Fe VI – VII lines. Bottom: Determination of $\log g$ for NGC 6853 ($T_{\text{eff}} = 126 \text{ kK}$) and NGC 7293 ($T_{\text{eff}} = 120 \text{ kK}$) using He II $\lambda 1640.42 \text{\AA}$.

line that can be seen in the observed spectrum or by the determination of an upper abundance limit if no line is visible. A flow diagram of the abundance determination is shown in Fig. 5.6. In a first step a model is calculated to derive the temperature structure of the model atmosphere. For this purpose the atomic data is kept small to shorten the computing time. In the second step the full atomic data is used for a lineformation calculation, in which the temperature correction is switched off. In a third and fourth step model SEDs are calculated and the abundances are adjusted. With these new parameters a new temperature structure is calculated and the cycle begins anew. The abundance determination is depending on T_{eff} and $\log g$ and, thus, these parameters have to be cross-checked

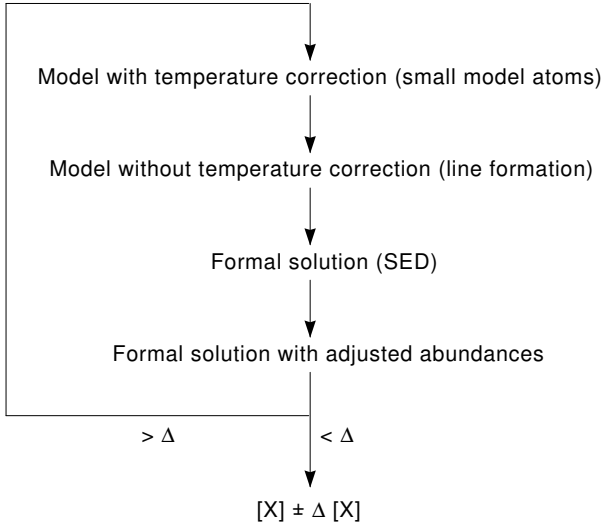


Figure 5.6: Flow diagram of abundance determination.

to derive the best-fitting parameter set.

5.4.1 Hydrogen and helium

Optical observations are suited best for the determination of the H and He abundances because the H and He lines in the FUV range are often blended by ISM absorption. In the *STIS* range only He II λ 1640.42Å can be analyzed without interstellar influence. Only for four of the sample objects optical spectra were available to cross-check the derived H/He-abundance ratio and to cross-check the values for T_{eff} and $\log g$ determined in the UV and FUV range.

Figure 5.7 displays the optical H and He lines of the CSPN LSS 1362 that allowed to derive $T_{\text{eff}} = 106$ kK and $\log g = 5.6$. This is slightly different compared to the values by Traulsen et al. (2005, $T_{\text{eff}} = 114$ kK, $\log g = 5.7$). In the case of available *STIS* observations He II λ 1640.42Å was used to derive the He abundances as well as $\log g$ taken from the literature and adjust both if necessary.

5.4.2 Carbon, nitrogen, and oxygen

The elements C, N, and O show numerous lines in the UV and FUV range (Tab. 5.1) that could be used for the analysis.

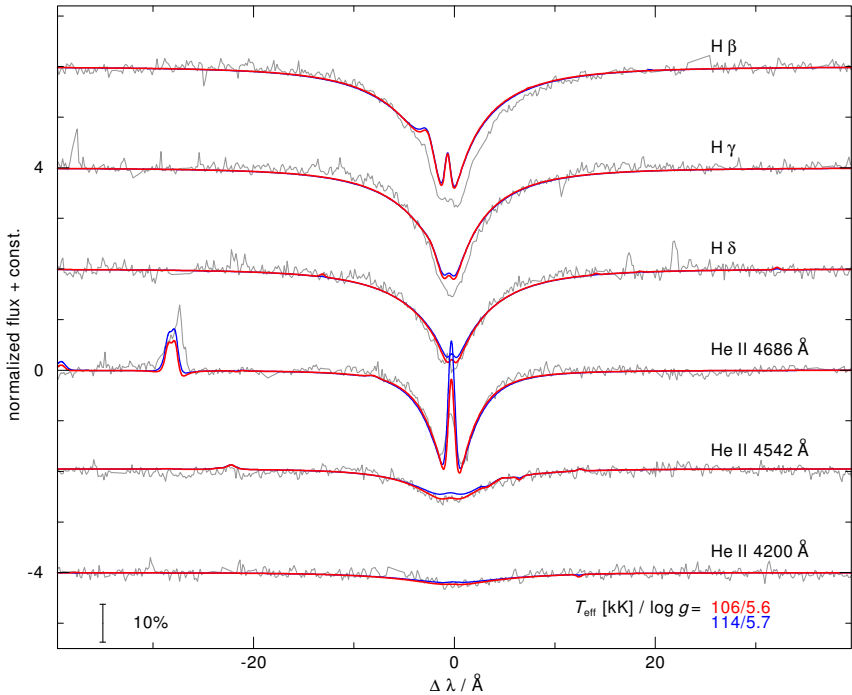


Figure 5.7: Determination of the H/He-abundance ratio, T_{eff} , and $\log g$ using optical H and He lines in LSS 1362. The observation (grey line) is compared with two different model SEDs (red: $T_{\text{eff}} = 106 \text{ kK}$, $\log g = 5.6$; blue: $T_{\text{eff}} = 114 \text{ kK}$, $\log g = 5.7$, H/He = 0.74/0.25).

The C IV, N v, and O VI resonance doublets are mostly contaminated by interstellar line absorption. Only a few objects show no interstellar influence of the N v and O VI resonance doublet.

5.4.3 From fluorine to argon

The elements from F to Ar were only analyzed sparsely for CSPNe so far. The strongest F line in the analyzed wavelength range is F VI $\lambda 1139.5 \text{\AA}$ (Werner et al. 2005). In any of our objects no lines of Mg, Na and Al could be found. Thus, the abundances for these elements were assumed to be solar. All analyzed lines are shown in Tab. 5.2. The Si IV resonance doublet in the *STIS* range is mostly contaminated by ISM absorption.

Table 5.1: Some of the analyzed C, N, and O lines that were used for our analysis whenever available in the observations. “s” denotes singlet, “d” doublet, “t” triplets, “qt” quartets, “q” quintets, “st” septets, and “ISM” often occurring line blends caused by the ISM.

element	ion	wavelength [\AA]	remarks
C	IV	1107.59, 1107.93, 1107.98	t
		1168.85, 1168.99	d
		1198.40, 1198.55, 1198.59	t
		1230.04, 1230.52	d
		1548.19, 1550.77	d; ISM
N	IV	921.99, 922.52, 923.06, 924.28	qt; ISM
		955.34	s; ISM
		1718.55	s
	V	1238.82, 1242.80	d; ISM
		1548.67, 1549.34, 1549.45	t
O	IV	1338.61, 1342.99, 1343.51	t
		1039.66	s
		1040.55	s
		1055.47	s
		1058.14, 1059.01, 1059.95, 1060.36, 1061.22	q
	VI	1371.30	s
		1643.72	s
		1708.00	s
		1031.92, 1037.61	d; ISM
		1171.12	s
	1172.00	s	

5.4.4 Iron-group elements

Model calculations predict numerous lines of iron-group elements in the UV and FUV range in the expected parameter regime. For Ca, Sc, Ti, and V the abundances were set to solar, as no lines were found in the FUV and UV range.

5.5 Mass, luminosity, and distance

In order to derive the stellar mass, luminosity, and distance of a star, the resulting values of T_{eff} and $\log g$ are plotted in a $\log T_{\text{eff}} - \log g$ diagram and are compared

Table 5.2: Some of the analyzed photospheric lines for the elements F, Ne, Mg, Si, P, S, and Ar. Same abbreviations as in Tab. 5.1.

element	ion	wavelength [\AA]	remarks
F	v	1082.31, 1087.82	d
	vi	1139.50	s
Ne	v	1369.93	s
	vi	1645.06, 1645.59, 1666.24, 1667.82, 1679.67	q
	vii	973.33	s; ISM
		1486.10	s
Mg	iv	1679.96, 1683.00, 1685.58, 1698.79	qt
Al	vi	1325.52, 1359.07	
Si	iv	1045.50, 1047.27	t
		1066.61, 1066.64, 1066.64	t
		1122.49, 1122.49, 1122.50, 1128.34,	st
		1128.33, 1128.34, 1128.34	
	v	1393.76, 1393.76, 1402.77	t, ISM
1118.81		s	
P	v	1117.98, 1128.01	d
S	vi	933.38, 944.52	d; ISM
		1117.76, 1117.76, 1117.76	t
Ar	vi	1283.96, 1303.87, 1307.50	t
	vii	1063.63	s; ISM
		1250.15	s

with evolutionary tracks from Miller Bertolami (priv. comm.) for post-AGB stars and with post-EHB evolutionary tracks from Dorman et al. (1993). An example of such a $\log T_{\text{eff}} - \log g$ diagram can be seen in Fig. 5.8. The stellar masses can be interpolated by comparing the star's position with the evolutionary tracks. To derive the spectroscopic distances two methods are used in this thesis, one of them being developed in the framework of this thesis. Both will be demonstrated in the following.

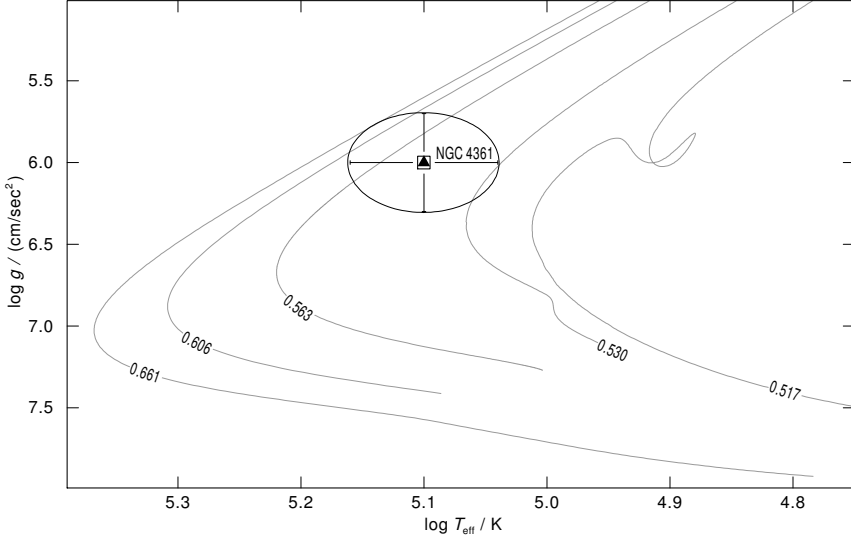


Figure 5.8: Location of the O(H)-type CSPN NGC 4361 in the $\log T_{\text{eff}} - \log g$ diagram to interpolate the stellar mass. The evolutionary tracks are taken from Miller Bertolami (priv. comm., labeled by the stellar mass in M_{\odot}).

Method 1: To derive the spectroscopic distances the flux calibration of Heber et al. (1984),

$$f_V = 3.58 \cdot 10^{-9} \cdot 10^{-0.4m_{V_0}} \text{ erg cm}^{-2} \text{ sec}^{-1} \text{ \AA}^{-1} \quad (5.1)$$

with $m_{V_0} = m_V - 2.175 \cdot c$, $c = 1.47 \cdot E_{B-V}$, and m_V the visual magnitude of the star, is used. The distance can be derived from

$$d = 7.11 \cdot 10^4 \cdot \sqrt{H_V \cdot M \cdot 10^{0.4m_{V_0} - \log g}} \text{ pc} . \quad (5.2)$$

with the Eddington flux H_V at $\lambda_{\text{eff}} = 5454 \text{ \AA}$, the stellar mass M in M_{\odot} , and the surface gravity g .

From Fig. 5.8 a mass of $M = 0.553 \pm 0.05 M_{\odot}$ can be deduced for NGC 4361. With $T_{\text{eff}} = 126 \text{ kK}$, $\log g = 6.0 \pm 0.3$, $E_{B-V} = 0.04 \pm 0.02$, and $H_V = (2.1 \pm 0.2) \cdot 10^{-3} \text{ erg cm}^{-2} \text{ sec}^{-1} \text{ Hz}^{-1}$, a distance of $d = 997_{-0.419}^{+0.300} \text{ pc}$ is calculated. This is in good agreement with the mean distance derived by Bensby & Lundström (2001, $d = 1.44 \text{ kpc}$).

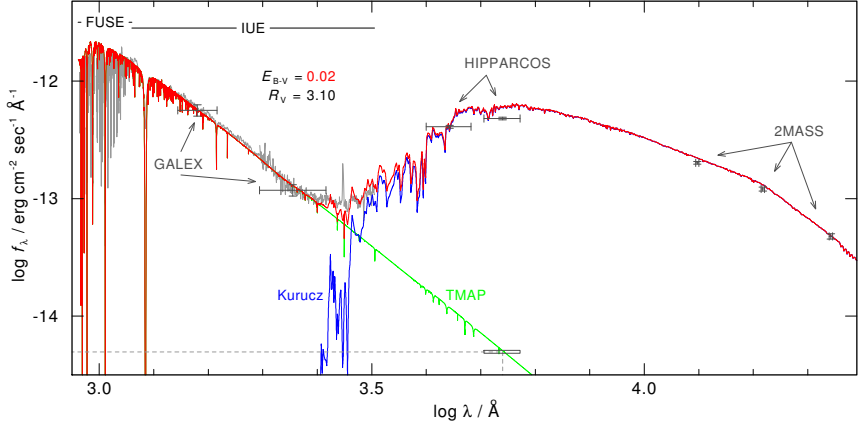


Figure 5.9: Determination of the stellar magnitudes in the V band from SED fits in the case of A 35. The *TMAP* model SED is combined with a Kurucz LTE model atmosphere (blue line, $T_{\text{eff}} = 5$ kK, $\log g = 3.5$, $\log Z = 0.0$) for the companion. The grey dashed line marks the flux value read-off for the middle of the V band. The combined model SED is normalized to the K band measurement from 2MASS.

Method 2: For stars with no existing magnitude measurements (and therefore no value for m_{V_0} that can be found, e.g. in the SIMBAD¹ database) formula 5.2 can not be applied directly. Therefore a new method had to be developed to derive the necessary stellar brightnesses from the final model SEDs. The observed flux, f_{obs} , from the final model SEDs at 4400, 5500, 6400, 12510, 16500, and 22000 Å (the B–K bands) after being corrected for the reddening is read-off. The flux value is then converted to stellar magnitudes via the equation

$$m_v = -2.5 \cdot \log(f_{\text{obs}}/f_H) \quad (5.3)$$

where f_H denotes the flux from Heber et al. (2002) corresponding to the B, V, R, J, H, and K band respectively (see Tab. 5.3). The derived magnitudes were now used to calculate the distance, following Heber et al. (1984) again.

This method had to be used for A 35 (Fig. 5.9). The magnitudes available in the SIMBAD database are dominated by the companion star and, thus, do not allow a distance determination of the ionizing star. For the ionizing star of A 35 a mass of $M = 0.484 \pm 0.05 M_{\odot}$ can be deduced from Fig. 6.2. With $T_{\text{eff}} = 80$ kK, $\log g = 7.2 \pm 0.3$, $E_{B-V} = 0.02 \pm 0.02$, $H_V = (1.16 \pm 0.2) \cdot 10^{-3} \text{ erg cm}^{-2} \text{ sec}^{-1} \text{ Hz}^{-1}$, $f_{\text{obs}} = 4.96 \cdot 10^{-15} \text{ erg cm}^{-2} \text{ sec}^{-1} \text{ Å}^{-1}$ and therefore $m_{V_0} = 14.74$ one derives

¹<http://simbad.u-strasbg.fr/simbad/>

Table 5.3: Flux values for the B, V, R, J, H, and K band from Heber et al. (2002) to determine luminosities from photospheric model SEDs necessary to derive the stellar distances. All flux values are in units of $10^{-10} \text{ erg cm}^{-2} \text{ sec}^{-1} \text{ \AA}^{-1}$.

B	V	R	J	H	K
65.97	36.07	22.54	2.91	1.11	0.383

$d = 351_{-150}^{+109}$ pc for the V band. This is in agreement with the value given by Perryman et al. (1997, $d = 163_{-58}^{+96}$ pc).

This newly developed method allows to derive stellar distances without available magnitude measurements. However, a precise determination of the stellar parameters and thus an accurate modeling of the stellar flux is a prerequisite to apply this method.

5.6 Radial velocity

We determined the radial velocities, v_{rad} , from various lines displayed in Tab. 5.4. If *STIS* and *FUSE* observations were available, the latter was neglected as the wavelength calibration of the different detectors itself are slightly shifted against each other. For each object suitable lines were fitted using a simple Lorentz profile. From these fits v_{rad} and the error was determined.

Table 5.4: Lines used for the determination of v_{rad} . Note that not all lines were suitable for each object.

element	ion	wavelength [\AA]
N	IV	955.33
	V	1238.82, 1242.80
O	IV	1343.51
	V	1040.34, 1055.47, 1058.14, 1059.01, 1059.95, 1060.36, 1371.30
F	VI	1139.50
Ne	V	1369.93
Si	IV	1128.34
	V	1251.39
Ar	V	1371.92
	VI	1283.96
	VII	1063.63
Cr	V	1196.04, 1259.98
	VI	1417.66
Mn	VI	1257.47, 1272.44, 1333.87, 1356.86
Fe	V	1378.56
	VI	1232.48, 1252.77, 1253.68, 1258.02, 1260.32, 1272.07, 1296.73, 1296.87, 1308.64
	VII	1073.95, 1117.58
	VIII	1148.22, 1166.18, 1180.83, 1239.69, 1332.38
Ni	V	1285.09
	VI	1257.16

CHAPTER 6

Results and discussion

In this chapter the results of the spectral analyses will be presented. General results are depicted in Sect. 6.1. The characteristics of individual objects are discussed in Sect. 6.2.1 (DAO-type stars) and Sect. 6.2.3 (O(H)-type stars). The discussion of each star includes a comparison of the derived photospheric abundances of the analyzed stars with previous literature values, predicted abundances from diffusion calculations, AGB nucleosynthesis predictions, as well as PNe abundances if available.

6.1 General results

Ten DAO-type ionizing stars of gaseous nebulae and five of O(H)-type were analyzed using fully line-blanketed NLTE model atmospheres. Some of the main results are displayed in Tab. 6.1. The sample stars span a wide range in T_{eff} with values from 69 – 136 kK and $\log g = 5.4 - 7.4$ and, thus, represent different evolutionary stages. The analyzed DAO and O(H)-type stars do not differ in T_{eff} , but the DAOs show a much higher $\log g$ (6.5 – 7.4) compared to the O(H)-type stars (5.4 – 6.0). The exception is the O(H)-type star Lo 1 with $\log g = 7.0$.

6.1.1 Mean mass

Figure 6.1 shows a $\log T_{\text{eff}} - \log g$ diagram from which masses for 14 of the sample objects were interpolated. The mass of Sh 2–174 was extrapolated as the values for T_{eff} and $\log g$ locate Sh 2–174 in a region of the $\log T_{\text{eff}} - \log g$ diagram for which no evolutionary tracks for H-rich post-AGB stars are available. A 35 and Sh 2–174 are possibly post-EHB stars and, thus, post-AGB tracks as displayed in Fig. 6.1 are not necessarily valid for the mass determination of these two objects. The masses derived for these two stars from post-AGB tracks as displayed in Fig. 6.1 ($M_{\text{Sh 2-174}} = 0.395 \pm 0.05 M_{\odot}$, $M_{\text{A35}} = 0.523 \pm 0.05 M_{\odot}$) are indeed very low for CSPN. At least for Sh 2–174 a post-AGB evolution can be

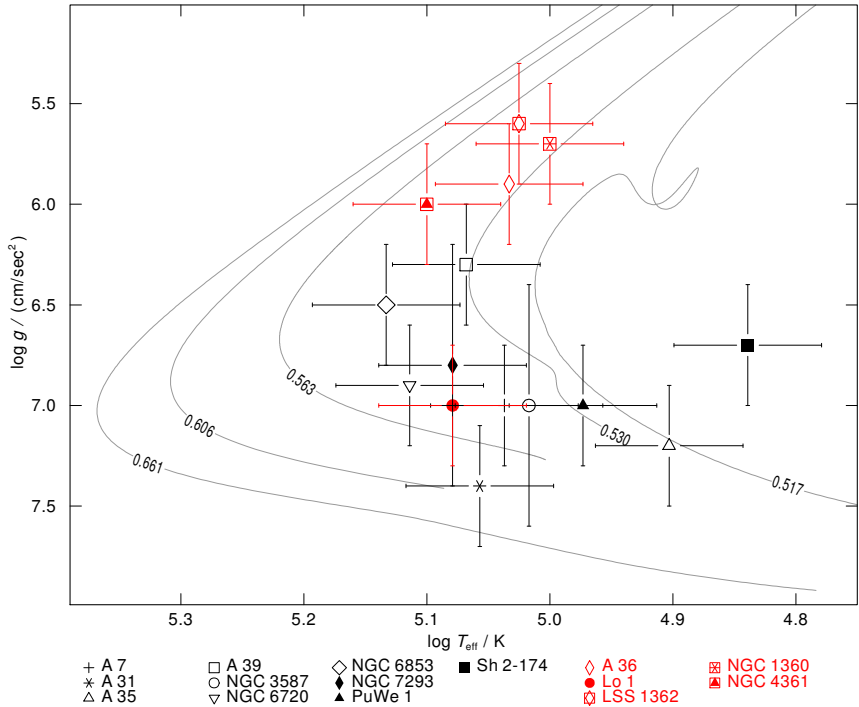


Figure 6.1: Position of all analyzed objects in the $\log T_{\text{eff}} - \log g$ diagram compared to evolutionary tracks taken from Miller Bertolami (priv. comm., labeled by the stellar mass in M_{\odot}). DAO-type CSPNe are displayed in black, O(H)-type CSPNe in red.

ruled out, and a post-EHB evolution is more likely.

Using the post-AGB evolutionary tracks to derive the masses, a mean mass of $\bar{M} = 0.536 \pm 0.023 M_{\odot}$ can be found ($\bar{M}_{\text{DAO}} = 0.531 \pm 0.029 M_{\odot}$ for the DAO and $\bar{M}_{\text{O(H)}} = 0.548 \pm 0.006 M_{\odot}$) including all 15 sample objects. All three mean masses are at the lower end of the expected mean masses for WDs, e.g. Gianninas et al. (2011), who analyzed more than 1300 H-rich WDs (including more than 1100 DA-type WDs) from the catalogue of McCook & Sion (1999). For the latter part of their sample they find a mean mass of $\bar{M}_{\text{DA}} = 0.638 \pm 0.145 M_{\odot}$. Considering the error limits our value agrees with the mean mass of Gianninas et al.

As already mentioned above the nebulae of A 35 and Sh 2–174 are likely “Strömgren spheres in the ambient ISM” (Frew & Parker 2010, cf. Sect. 4.1.3,

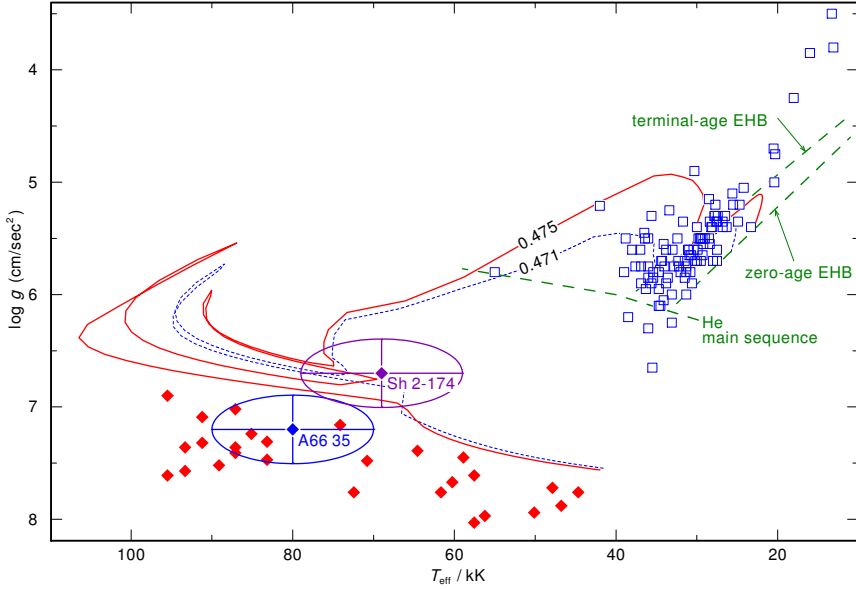


Figure 6.2: Position of A 35 and Sh 2–174 in the $T_{\text{eff}} - \log g$ diagram compared with post-EHB tracks from Dorman et al. (1993, $Y = 0.288 \approx Y_{\odot}$). The labels give the stellar mass in M_{\odot} . The diagram also displays the location of DAO-type WDs from Gianninas et al. (2010, red diamonds) and sd(O)-type stars from Edelman (2003, blue squares).

Sect. 4.1.10), and, therefore, no PNe. In this case both objects would rather be post-EHB stars. Figure 6.2 shows their position in the $\log T_{\text{eff}} - \log g$ diagram compared to post-EHB tracks from Dorman et al. (1993) for a He content of $Y = 0.288 \approx Y_{\odot}$. From Fig. 6.2 masses of $M_{A35} = 0.484 \pm 0.05 M_{\odot}$ and $M_{\text{Sh 2-174}} = 0.477 \pm 0.05 M_{\odot}$ can be deduced. The mean mass for the whole sample in this case is $\bar{M} = 0.539 \pm 0.019 M_{\odot}$.

Both possible mass distributions (A 35 and Sh 2–174 considered as post-AGB and as post-EHB stars) are displayed in Fig. 6.3. The exclusion of A 35 and Sh 2–174 from the overall sample leads to a mean mass of the reduced sample of $\bar{M}_{\text{red}} = 0.548 \pm 0.011 M_{\odot}$. Within the error limits this again agrees with the mean mass for DA-type WDs from Gianninas et al. (2011).

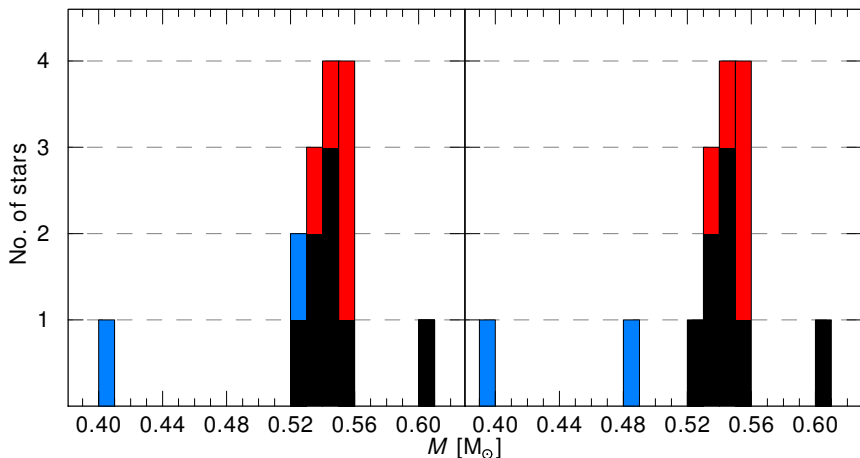


Figure 6.3: Mass distribution of analyzed DAO-type (black) and O(H)-type stars (red). The left panel shows the mass distribution if all masses are derived from post-AGB tracks (cf. Fig. 6.1). The right panel shows the mass distribution if the masses for the two possible DAO-type post-EHB stars (A 35, Sh 2–174, blue) are derived from the post-EHB tracks of Dorman et al. (1993, cf. Fig. 6.2).

6.1.2 Luminosities

The luminosities for each object were interpolated from the evolutionary tracks. The O(H)-type WDs have higher luminosities ($\log L/L_{\odot} \approx 3.4-3.6$) compared to the DAOs ($\log L/L_{\odot} \approx 1.5-3.1$). The exception is again Lo 1 ($\log L/L_{\odot} \approx 2.5$). The typical error for the determination of the luminosity is $\Delta \log L/L_{\odot} \approx \pm 0.40$.

6.1.3 Distances

The distances for all objects were derived with the methods described in Sect. 5.5. A comparison of the distances found in this work with literature values is shown in Fig. 6.4. Within the error limits the spectroscopic distances for the sample stars mostly agree with the literature values. However, for some literature values no error limits were found and, thus, an agreement with these distances is difficult to state.

6.1.4 Chemical abundances

Helium is nearly completely ionized in the parameter regime of the sample stars and is therefore not affected by radiative levitation. Thus, a subsolar He abundance would be a perfect indicator for ongoing gravitational settling if gravity

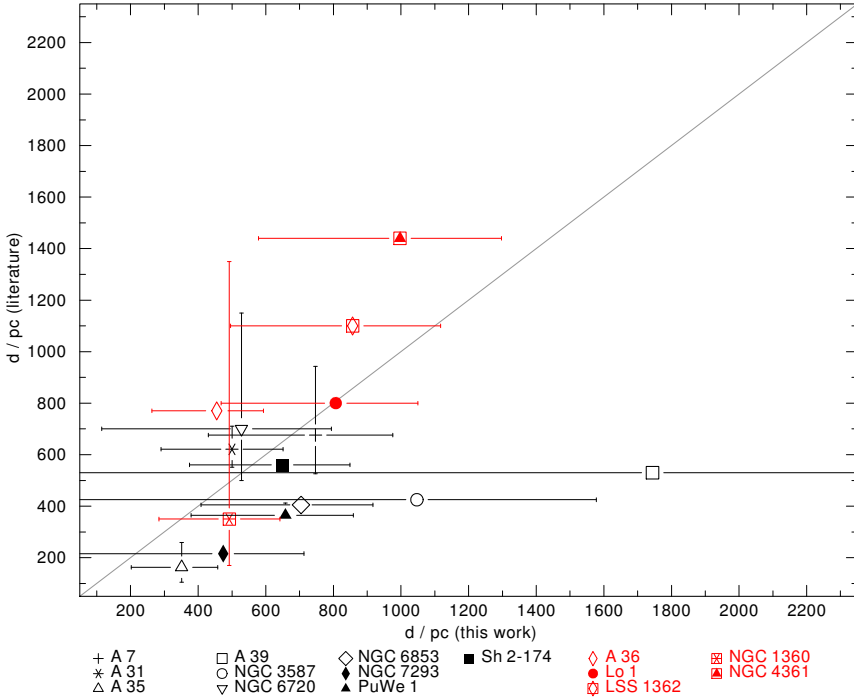


Figure 6.4: Comparison of derived distances with literature values. The literature distances for A 7, A 31, A 35, NGC 1360, NGC 6720, NGC 6853, NGC 7293, and PuWe 1 were determined using trigonometric parallaxes.

and the radiation pressure would be the only forces acting on the atoms in the atmosphere. However, some observations can not be explained by these two effects alone, e.g. the presence of He in DAO-type WDs. A possible solution explaining the He abundances in DAO stars is a weak stellar wind driven by the presence of metals in the atmosphere as discussed by Unglaub & Bues (1998, 2000). Unglaub & Bues found that a mass-loss rate of $\dot{M} \geq 10^{-12} M_{\odot} \text{ yr}^{-1}$ is sufficient to prevent He from being removed from the atmosphere. For a model with solar He, C, N, and O abundances Unglaub & Bues find a transition from DAO to DA-type WDs at $\log g \approx 7$. At $T_{\text{eff}} \leq 80 \text{ kK}$, the so called “wind limit”, the metal-driven wind is no longer strong enough to prevent the onset of gravitational settling. Gianninas et al. (2010) determined the wind limit to be even lower ($T_{\text{eff}} \leq 60 \text{ kK}$). A model including the effects mentioned above in a self consistent manner was not possible with *TMAP*. Therefore no general conclusion

can be made whether gravitational settling is present in the analyzed sample or not.

Although the diffusion calculations of Chayer et al. (1995a,b) did not consider the wind effect discussed above, we compare our abundances with their predicted abundances for C, N, O, Ne, Na, Mg, Al, Si, S, Ar, Ca, and Fe. Figure 6.22 presents our chemical abundances depending on T_{eff} . The calculations of Chayer et al. predict a dip of the Si abundance between $T_{\text{eff}} \approx 50 - 100$ kK for DA-type WDs with a minimum at roughly 70 kK. We find a minimum at $T_{\text{eff}} = 80$ kK (A 35). However, due to the lack of cool objects in our sample this is small number statistics and, thus, we can not confirm nor deny the dip from our analysis. The analyzed sample of Good et al. (2005) better covered the corresponding, cooler parameter range. They analyzed 16 DAO-type WDs using *FUSE* and optical observations. Their sample covered $T_{\text{eff}}^{\text{Balmer}} \approx 46 - 76$ kK and $\log g \approx 6.5 - 7.8$ if T_{eff} and $\log g$ was determined from the optical Balmer line spectra, or, if T_{eff} and $\log g$ was derived from the Lyman line spectra, $T_{\text{eff}}^{\text{Lyman}} \approx 46 - 120$ kK and $\log g \approx 6.5 - 7.9$. However, they did not confirm the dip in the predicted Si abundance of Chayer et al. either, but Good et al. argue that roughly half of their fits were of poor quality. Nearly all of their objects showed a subsolar or roughly solar Si abundance. No stronger Si enhancement was found in their analysis. We confirm this result for our sample that covers hotter stars than the sample of Good et al.. Only for the cool ionizing star of Sh 2-174 we find an enhanced abundance of $[\text{Si}] = +0.96$, while A 35 has a subsolar Si abundance of $[\text{Si}] = -2.12$.

Good et al. (2005) find mostly subsolar C abundances. From our sample all objects below $T_{\text{eff}} \approx 114$ kK have slightly subsolar values, while the hotter ones are C enhanced. NGC 4361 is a Population II object and, therefore, displays a strong C overabundance of $[\text{C}] = +1.43$. We agree with the lower C abundances for cooler stars found by Good et al. No clear trend with T_{eff} is found for N, O, and Fe confirming the results of Good et al. From radiative levitation theory an increase of metal abundances with increasing T_{eff} is expected as the radiation pressure is $\propto T_{\text{eff}}^4$. For C and S a slight increase of the abundances with a rise in T_{eff} can be seen in Fig. 6.22. For none of the other elements we can unambiguously find such a trend in our analysis. On the other hand such a correlation between metal abundances and T_{eff} can not be ruled out either, as for some elements no abundances could be determined.

Neglecting the weak stellar wind stated by Unglaub & Bues (1998, 2000), T_{eff} and g counteract each other. Thus, the dependence of the abundances on $\log(T_{\text{eff}}^4/g)$ is shown in Fig. 6.23. Increasing abundances for C, N, O, Si, P, and S with increasing $\log(T_{\text{eff}}^4/g)$ are obvious. The rise flattens for higher T_{eff}^4/g ratios. More objects especially with lower $\log(T_{\text{eff}}^4/g)$ values are needed to prove or disprove this result, as our objects with the lowest T_{eff}^4/g ratios are Sh 2-174

and A 35, two possible post-EHB stars. Although they show a larger scatter, Ar and Fe follow the contradictory trend. The Ar and Fe abundances of the sample stars decrease with increasing $\log(T_{\text{eff}}^4/g)$. Yet there is no explanation for this decline. The situation looks similar when the abundances are plotted with dependence on the luminosity. However, note that for all abundances a standard error of ≈ 0.3 dex has to be assumed and the errors in T_{eff} and $\log g$ lead to an error in $\log(T_{\text{eff}}^4/g)$ at the order of approximately $\pm 0.4 - 0.5$.

Table 6.1: Main results for the DAO-type (upper part) and Q(H)-type ionizing stars.

object	T_{eff} [kK]	$\log g$ [cm sec ⁻²]	d [pc]	M^\diamond [M_\odot]	$\log L/L_\odot^\diamond$	$E_{\text{B-V}}$ [mag]	m_{V}^\ddagger [mag]	m_{HI} [10 ²⁰ cm ⁻²]	v_{rad} [km sec ⁻¹]
A 7	109	7.0 ± 0.3	747 ⁺²²⁹ ₋₃₁₇	0.546	2.24	0.08 ± 0.04	15.45	4.0 ± 2.5	42 ± 2
A 31	114	7.4 ± 0.3	500 ⁺¹⁵¹ ₋₂₁₀	0.605	1.98	0.11 ± 0.02	15.51	2.0 ^{+3.0} _{-1.8}	82 ± 4
A 35 [‡]	80	7.2 ± 0.3	351 ⁺¹⁰⁹ ₋₁₅₀	0.484	1.40	0.02 ± 0.02	14.66	5.0 ± 1.5	-14 ± 1
A 39	117	6.3 ± 0.6	1744 ⁺⁸⁸¹ ₋₁₇₄₁	0.533	3.06	0.13 ± 0.02	15.60	5.0 ± 2.5	21 ± 10
NGC 3587	104	7.0 ± 0.6	1047 ⁺⁵³¹ ₋₁₀₄₆	0.542	2.17	0.00 ± 0.03	16.04	0.6 ± 0.4	36 ± 1
NGC 6720	130	6.9 ± 0.6	528 ⁺²⁶⁶ ₋₄₁₃	0.552	2.66	0.08 ± 0.02	14.20	4.0 ± 3.0	-13 ± 1
NGC 6853	126	6.5 ± 0.3	704 ⁺³¹³ ₋₅₂₆	0.545	3.14	0.05 ± 0.03	13.70	1.6 ± 0.3	-26 ± 2
NGC 7293	120	6.8 ± 0.6	474 ⁺²³⁹ ₋₄₇₃	0.538	2.63	0.00 ± 0.02	13.52	1.3 ± 0.3	-6 ± 1
PuWe 1	94	7.0 ± 0.3	658 ⁺²⁰¹ ₋₃₇₉	0.526	1.99	0.11 ± 0.02	15.53	5.0 ± 4.0	35 ± 15
Sh 2-174 [♦]	69	6.7 ± 0.3	649 ⁺²⁰³ ₋₂₇₇	0.477	1.70	0.00 ± 0.03	14.74	2.2 ± 0.4	0 ± 2
A 36	108	5.9 ± 0.3	455 ⁺¹³⁸ ₋₁₉₂	0.535	3.38	0.06 ± 0.02	11.57	5.0 ± 1.0	40 ± 10
Lo 1 [‡]	120	7.0 ± 0.3	807 ⁺²⁴³ ₋₃₃₉	0.553	2.45	0.04 ± 0.02	15.26	2.0 ^{+2.0} _{-1.2}	73 ± 6
LSS 1362	106	5.6 ± 0.3	857 ⁺²⁶⁰ ₋₃₆₁	0.553	3.61	0.16 ± 0.02	12.50	6.0 ± 0.5	0 ± 10
NGC 1360	100	5.7 ± 0.3	492 ⁺¹⁵⁰ ₋₂₀₈	0.534	3.40	0.02 ± 0.02	11.20	0.5 ± 0.15	46 ± 2
NGC 4361	126	6.0 ± 0.3	997 ⁺³⁰⁰ ₋₄₁₉	0.553	3.52	0.04 ± 0.02	13.20	2.3 ± 0.3	17 ± 1

[♦] the typical error for the T_{eff} is ±10kK, for the mass determination ±0.05 M_\odot , and for the luminosity ±0.40

[◆] masses derived from post-EHB evolutionary tracks

[‡] taken from the SIMBAD database if not denoted otherwise

[‡] m_{V} derived from SED fits (cf. Sect. 5.5)

6.2 Individual results

This section presents details for each object and illustrates special properties or difficulties connected with the analysis of the individual stars. Figures 6.5–6.21 display the derived abundances for each object compared to solar values from Asplund et al. (2009, Tab. C.1) and PNe abundances (top panels), diffusion calculations for DA and DO-type WDs (Chayer et al. 1995a,b, middle), and nucleosynthesis calculations (Cristallo et al. 2009; Bisterzo et al. 2010, bottom). The standard error for the abundances determined in this thesis is ≈ 0.3 dex. Arrows indicate upper limits.

Comparison with PN abundances

Due to its high luminosity and large radius an AGB star loses a huge amount of its mass which is later ionized to become a PN (cf. Sect. 1.3). The chemical abundance pattern of the PN and the CS should therefore be similar. Note that this connection between the the chemistry of the CS and the PN does not hold for stars with a non-canonical evolution, e.g. PG 1159 stars. The H-deficient PG 1159-stars are mostly surrounded by a H-rich PN, as the PN is ejected during the first AGB phase. The H-deficiency of the CS however, is caused after the ejection of the PN due to a late thermal pulse.

Table 6.2 shows a comparison of the derived CS abundances with abundances of the surrounding nebulae taken from the various literature sources mentioned in the text. No nebula abundances were found for A 7, A 35, Sh 2–174, A 36, Lo 1, and LSS 1362.

Comparison with diffusion calculations

All objects are compared with the predicted abundances for C, N, O, Ne, Na, Mg, Al, Si, S, Ar, Ca, and Fe from the diffusion calculations of Chayer et al. (1995a,b). For some objects the predicted abundances had to be extrapolated as the abundances in Chayer et al. (1995a,b) are calculated only within $T_{\text{eff}} = 20 - 100$ kK, $\log g = 7.0 - 8.5$ (DA-type WDs, blue squares in the abundance plots) and $T_{\text{eff}} = 20 - 130$ kK, $\log g = 7.0 - 8.5$ (DO-type WDs, green triangles). Note the restrictions discussed in Sect. 6.1.4 as the calculations by Chayer et al. (1995a,b) do not include the weak stellar wind stated by Unglaub & Bues (1998, 2000).

Comparison with AGB nucleosynthesis calculations

The enrichment of the stellar atmosphere with s-process elements during the TP-AGB phase determines the atmospheric abundances for post-AGB stars (undergoing a canonical stellar evolution). The abundances found for our sample stars for elements up to Ni are compared with the results of Cristallo et al. (2009) and the respective online-data¹. Cristallo et al. calculated AGB models to derive surface abundances for stars with initial masses $1.5 \leq M/M_{\odot} \leq 3$ and metallicities $1 \cdot 10^{-3} \leq Z \leq 2 \cdot 10^{-2}$.

Using the initial-to-final mass relation from Weidemann (2000) our sample stars should have initial masses of $\approx 1M_{\odot}$ to end up with a final mass of $0.55 M_{\odot}$. However, the nucleosynthesis predictions from Cristallo et al. for all elements of interest are only available for an initial mass of $2 M_{\odot}$. Also the abundances for different metallicities and initial masses available on the FRANEC Repository of Updated Isotopic Tables & Yields (FRUITY) database² are so far incomplete. We therefore use the $2 M_{\odot}$ abundances available online (<http://vizier.cfa.harvard.edu/viz-bin/VizieR-4>). With the initial-to-final mass relation from Weidemann, these stars end up as a $0.60 M_{\odot}$ WDs, which exceeds our mean mass by $\approx 0.04 M_{\odot}$ if the error limits are taken into account. In general stars with a higher initial mass will undergo more TPs before leaving the AGB. This leads to a stronger enhancement of elements synthesized on the AGB. According to the FRUITY database a $1.5 M_{\odot}$ star (with solar metallicity) will end up with a C abundance of $[C/Fe] = +0.31$ after five third dredge-up phases, while a $3 M_{\odot}$ star leaves the AGB after 14 third dredge-up phases with $[C/Fe] = +0.60$. For the Population II object NGC 4361 we compare our results with the final surface abundances of a Carbon enriched metal poor (CEMP) star with an initial mass of $1.3 M_{\odot}$ undergoing s-process nucleosynthesis, and leaving the AGB after five TPs (Bisterzo et al. 2010). For the comparison with the nucleosynthesis abundances the abundances are displayed as $[N_X/N_{Fe}] = \log(n_X/n_{Fe})_{\star} - \log(n_X/n_{Fe})_{\odot}$.

¹<http://vizier.cfa.harvard.edu/viz-bin/VizieR-4>

²<http://fruity.oa-teramo.inaf.it:8080/modelli.pl>

6.2.1 Individual results for DAO-type stars

6.2.1.1 A7

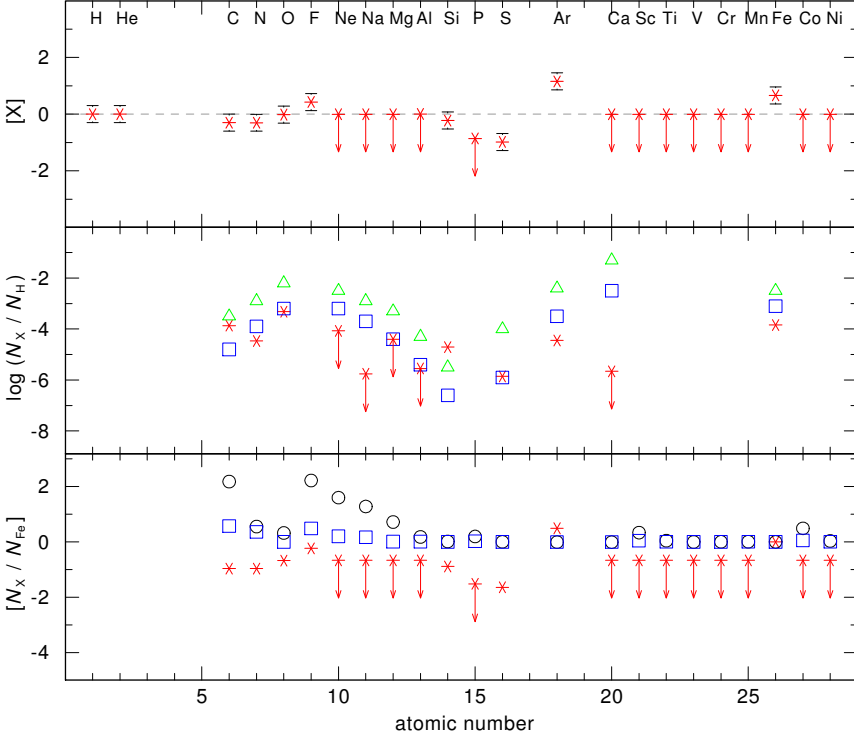


Figure 6.5: Top: Photospheric abundances of A7 compared with solar values (dashed line). $[X]$ denotes \log [mass fraction/solar mass fraction]. Middle: Abundances of A7 compared to the expected photospheric abundances from Chayer et al. (1995a,b) for DA (blue squares) and DO-type WDs (green triangles). Bottom: Photospheric abundances of A7 compared to nucleosynthesis calculations of Cristallo et al. (2009) for different metallicities (blue squares: solar metallicity $Z = 1.38 \cdot 10^{-2}$, black circles: $Z = 1 \cdot 10^{-3}$). For further details see text.

For A7 (Fig. D.1, Fig. E.1–E.3) a slightly higher $T_{\text{eff}} = 109 \pm 10$ kK is derived from the O v–vi and Fe vi–viii ionization equilibria, compared to the literature values from Napiwotzki (1999, $T_{\text{eff}} = 99 \pm 18$ kK) and (Good et al. 2004, $T_{\text{eff}} = 99.2 \pm 2.3$ kK). The values, however, agree within the error limits. We find

$\log g = 7.7 \pm 0.3$, in agreement with $\log g = 7.03 \pm 0.43$ (Napiwotzki 1999) and $\log g = 7.68 \pm 0.06$ (Good et al. 2004). The values for T_{eff} and $\log g$ therefore also agree within the error limits. The derived T_{eff} value does not agree with the value of Gianninas et al. (2010, $T_{\text{eff}} = 82.7 \text{ kK}$, $\log g = 7.47$). The mass derived from our values for T_{eff} and $\log g$ ($M = 0.546 \pm 0.05 M_{\odot}$) agrees within the error limits with the mass from Napiwotzki (1999, $M = 0.57 \pm 0.05 M_{\odot}$).

A7 is one of the few objects of the sample that allowed the determination of the N abundance using N IV $\lambda 955.34 \text{ \AA}$ as the line is not blended by the ISM (Fig. E.1). We find $[\text{N}] = -0.30$. Compared to the value of Good et al. (2005) derived from *FUSE* observations, our value for carbon ($[\text{C}] = +0.30$) is only slightly higher if the error limit is taken into account. The abundances for N, Si, and Fe can be confirmed within the error limits. Good et al. did not derive a O abundance. We find a slightly subsolar abundance. The abundances for O, Mg, Al, and S agree well with the predicted abundances by Chayer et al. (1995a,b, Fig. 6.5) for DA-type WDs. Note that our abundances for Mg and Al are solar as the observations showed no lines to determine a reliable abundance. Besides Ar, which agrees within the error limits, no agreement is found with the predicted nucleosynthesis abundances from Cristallo et al. (2009).

6.2.1.2 A 31

For A 31 (Fig. D.2, Fig. E.4–E.6) we identified lines of C, O, F, Si, P, Ar, and Fe. The photospheric abundances of A 31 for the elements N, O, Ne, Mg, Al, and Fe are consistent with the values from Chayer et al. (1995a,b, Fig. 6.6) for DA-type WDs.

Our T_{eff} derived from metal ionization equilibria (O IV – VI, Fe VI – VIII) yields $T_{\text{eff}} = 114 \pm 10 \text{ kK}$. This value differs from $T_{\text{eff}} = 94 \pm 3 \text{ kK}$ found by Good et al. (2004) analyzing the Lyman line spectra. However, we confirm their value for the surface gravity ($\log g = 7.4$). Within the error limits we can also approve the abundances of C, Si, and Fe found by Good et al. (2005) derived from the *FUSE* observation. For N, and O we find larger abundances by a factor of ≈ 10 compared to the value of Good et al., possibly due to the different values for T_{eff} used. Our T_{eff} and $\log g$ shows a huge disagreement with the values from Napiwotzki (1999, $T_{\text{eff}} = 84.7 \pm 4.7$, $\log g = 6.6 \pm 0.3$). Thus, we also find a much larger mass ($M = 0.605 \pm 0.05 M_{\odot}$) compared to Napiwotzki ($M = 0.48 \pm 0.04 M_{\odot}$).

We find a good agreement for F with the predicted surface abundance for a $2 M_{\odot}$ star with solar metallicity (Cristallo et al. 2009). Although our CS abundances for C, N, and O are too low compared to the nucleosynthesis predictions, they follow the decreasing trend of Cristallo et al.. We find a large unexplained

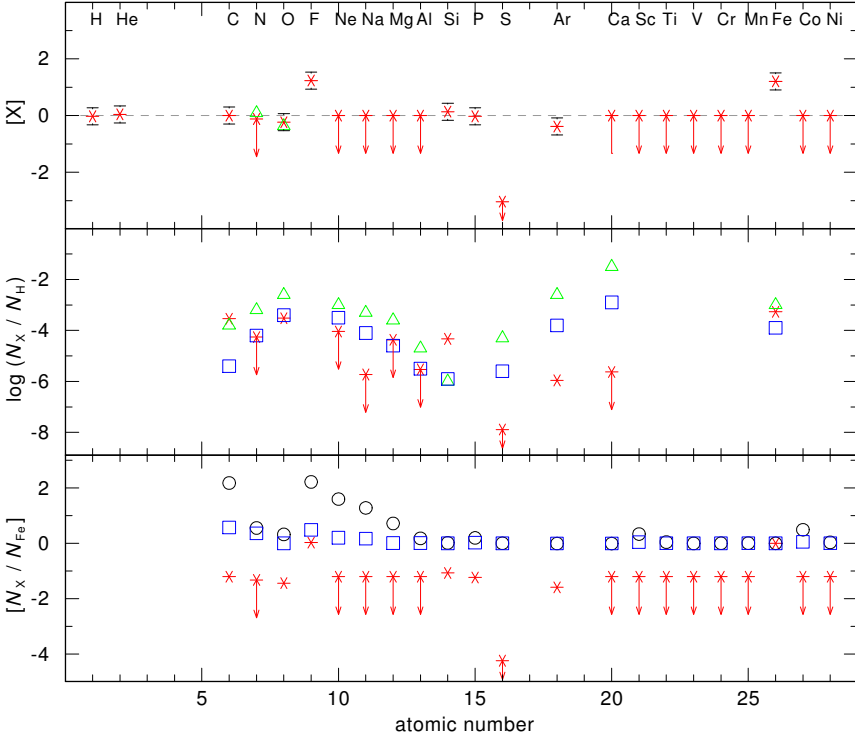


Figure 6.6: Same as Fig. 6.5 for A31. In the top panel additional abundances of the PN are displayed as green triangles.

deviation for S of ≈ 4 dex. The N and O abundances are consistent with the PN abundances from Kaler et al. (1990).

6.2.1.3 A35

For A35 (Fig. D.3, Fig. E.7–E.12) $T_{\text{eff}} = 80$ kK from Herald & Bianchi (2002) can be confirmed, while $\log g = 7.7$ (taken from the same work) is too large to fit He II $\lambda 1640.42\text{\AA}$. We adopt $\log g = 7.2 \pm 0.3$.

No photometric magnitudes could be used for the determination of E_{B-V} as the flux of the cool companion star dominates the spectrum longward of $\approx 2800\text{\AA}$. The final model for the main component was therefore combined with a Kurucz model ($T_{\text{eff}} = 5$ kK, $\log g = 3.5$) and normalized to the H band magnitude of the

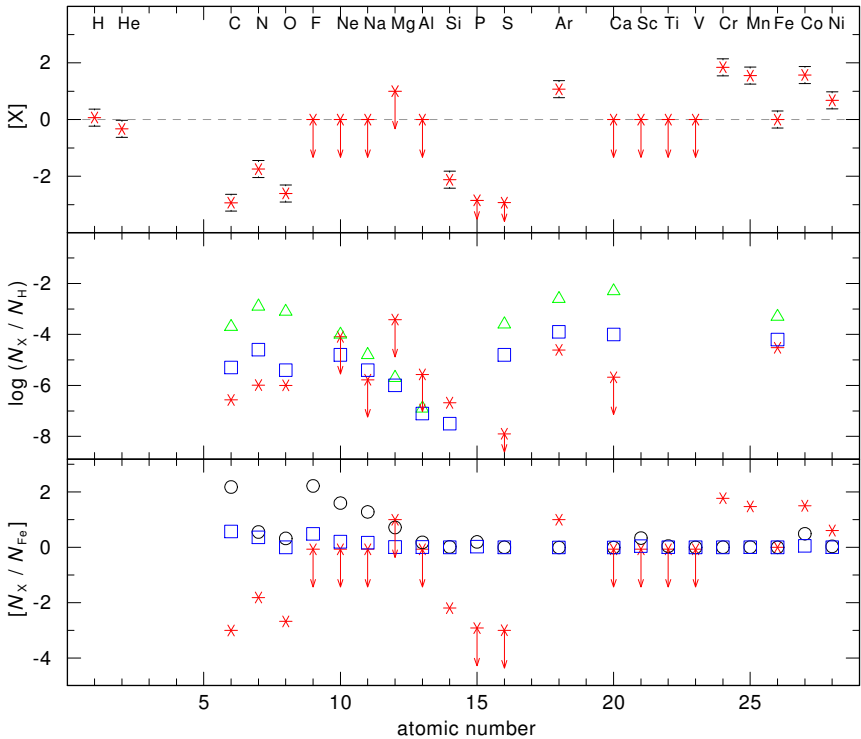


Figure 6.7: Same as Fig. 6.5 for A 35.

2MASS measurements. A reddening of $E_{B-V} = 0.02 \pm 0.02$ could be derived analyzing *FUSE* and *IUE* observations (Fig. D.3). Within the error limits this value is in agreement with Herald & Bianchi (2002, $E_{B-V} = 0.04 \pm 0.01$) using *FUSE* observations only. We find a best fit for $n_{\text{HI}} = (5.0 \pm 1.5) \cdot 10^{20} \text{ cm}^{-2}$ also in agreement with Herald & Bianchi (2002). A 35 is one of the few sample objects for which the N v resonance doublet at $\lambda\lambda$ 1238.82, 1240.80 Å shows no influence of the ISM. Hence an abundance of $[\text{N}] = -1.75$ could be derived. For the first time the Ar, Cr, Mn, Co, and Ni abundances are determined for A 35 (Fig. 6.8). Similar to LS V +46°21, the CS of the PN Sh 2–216 (cf. Rauch et al. 2007), Ar vi lines are identified in the *STIS* observation of A 35. Argon is enhanced to $[\text{Ar}] = +1.07$. No lines of F, Ne, Na, Mg, Al, Ca, Sc, Ti, and V were identified. Compared with the abundances of Herald & Bianchi (2002) He, O, Si, and Fe

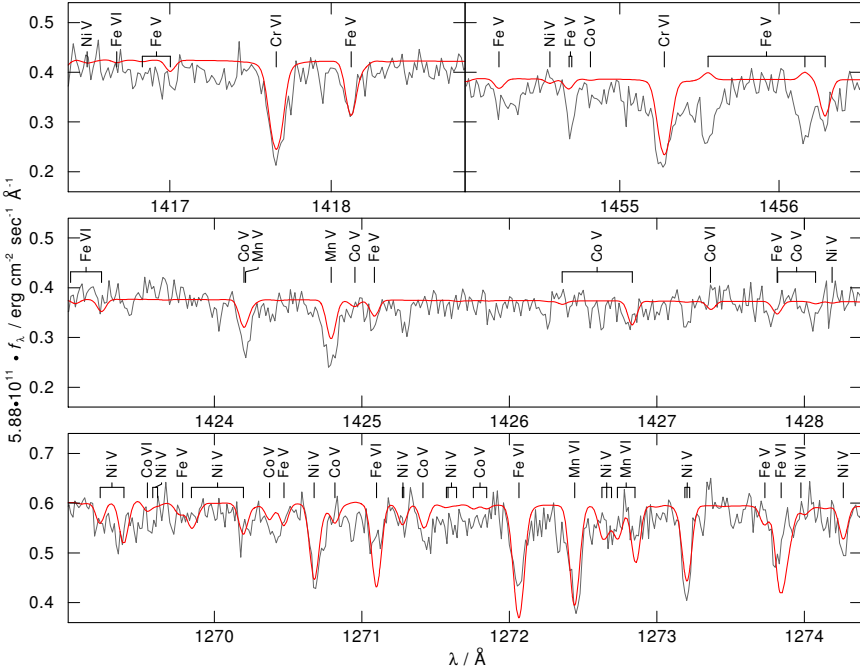


Figure 6.8: Sections of the *STIS* spectrum of A 35 containing Cr, Mn, Co, and Ni lines.

are in agreement. The derived abundance for C is smaller by a factor of ≈ 0.1 in comparison to the value by Herald & Bianchi, N is larger by ≈ 15 . Due to its position in the $\log T_{\text{eff}} - \log g$ diagram and the classification of the nebula as an ionized H II region (and thus not as a PN), the CS of A 35 is more likely a post-EHB star ionizing the surrounding ISM. For more details on A 35 see Ziegler et al. (2012, in preparation).

Our abundances for O, Ne, Na, Ar, and Fe are (within the error limits) roughly in agreement with the predicted abundances from diffusion calculations for DA-type WDs (Chayer et al. 1995a,b, Fig. 6.7). The CS abundances for F, Ne, Na, Al, as well as the iron-group elements Ca, Sc, Ti, and V agree with the predicted nucleosynthesis abundances for a $2 M_{\odot}$ star with solar metallicity from Cristallo et al. (2009), while Mg fits better for a metallicity of $Z = 1 \cdot 10^{-3}$. However, for Mg only an upper limit could be derived and the abundances of Ca, Sc, Ti, and V were considered solar as no lines were found in the UV and FUV ranges.

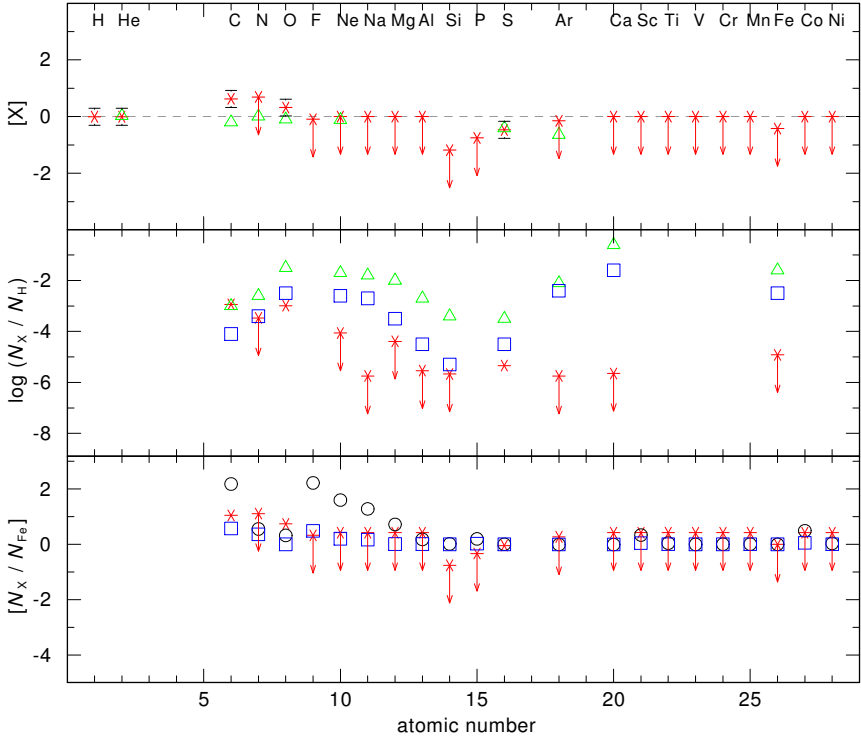


Figure 6.9: Same as Fig. 6.6 for A 39.

6.2.1.4 A 39

The *FUSE* observation of A 39 (Fig. D.4, Fig. E.13–E.15) has a rather low S/N-ratio. Therefore only upper limits could be derived except for the elements C, O, and S.

Our T_{eff} and $\log g$ ($T_{\text{eff}} = 117 \pm 10$ kK, $\log g = 6.3 \pm 0.6$) confirm the values of Napiwotzki (1999). The derived masses also agree within the error limits ($M = 0.533 \pm 0.05 M_{\odot}$, and $M = 0.57 \pm 0.02 M_{\odot}$, respectively). While $\log g$ coincides with the value found by Good et al. (2004, $\log g = 7.0 \pm 0.2$), the effective temperature disagrees as Good et al. find $T_{\text{eff}} = 88 \pm 5$ kK. Our abundance for C is ≈ 700 larger than the one of Good et al., N by a factor of roughly 10, while we can confirm their Si and Fe abundances, as well as $E_{B-V} = 0.13$ (Good et al. 2004). The large deviations for the abundances might be due to the bad quality

of the observation leading to large uncertainty in the derived values.

Only the abundances of N, O, and Si are in good agreement with the diffusion calculations for DA-type WDs (Chayer et al. 1995a,b). Within the error limits the abundances of O, F, Ne, P, S, Ar and the iron-group elements agree with the nucleosynthesis predictions for a $2 M_{\odot}$ star with solar metallicity (Cristallo et al. 2009). Note that most of our abundances are upper limits only. Our CS abundances of He, N, O, Ne, S, and Ar are in agreement (within the error limits) with the PN abundances from Jacoby et al. (2001). However, we find a larger C abundance by ≈ 0.8 dex.

The spectroscopic distance ($d = 1744^{+881}_{-1741}$ pc) is much larger than the distance of Phillips (2005, $d = 530$ pc). However, the error of the derived spectroscopic value is large and therefore the distance highly uncertain.

6.2.1.5 NGC 3587

The *FUSE* observation of NGC 3587 (Fig. D.5, Fig. E.16–E.18) does not show any interstellar H_2 lines. The ISM fit with *OWENS* yields $n_{H I} \approx 0.6 \cdot 10^{20} \text{ cm}^{-2}$ based on the numerous $H I$ lines from 911 \AA towards longer wavelengths. This value, however, is too strong if $Ly\alpha$ in the *IUE* range is taken into account (Fig. D.5), which is barely visible. A possible reason could be a geocoronal H line blending $Ly\alpha$.

Our analysis yields $T_{\text{eff}} = 104 \pm 10 \text{ kK}$, $\log g = 7.0 \pm 0.3$, and a stellar mass of $M = 0.542 \pm 0.05 M_{\odot}$. These values confirm the results of Napiwotzki (1999, $T_{\text{eff}} = 94 \pm 6 \text{ kK}$, $\log g = 6.9 \pm 0.3$, $M = 0.55 \pm 0.03 M_{\odot}$) from optical observations.

NGC 3587 exhibits lines of C, O, F, Si, P, S, Ar, and Fe. The abundances determined for O, Mg, Al, and S are in agreement with the calculations by Chayer et al. (1995a,b, Fig. 6.10) for DA-type WDs. The CS abundances for the elements O, Ne, Na, Mg, Al, Si, and the iron-group elements match the predicted surface abundances derived from nucleosynthesis calculations (Cristallo et al. 2009). An agreement is also found for the stellar He, O, Ne, and S abundances compared to PN abundances from Stanghellini et al. (2006). Nitrogen and iron (the PN value for the latter is taken from Delgado Inglada et al. (2009)) disagree by > 1 dex.

6.2.1.6 NGC 6720

The *FUSE* observation of NGC 6720 (Fig. D.6, Fig. E.19–E.21) exhibits some emission features. They are most likely of geocoronal origin. One of these broad features ($\approx 1168.5 - 1169.2 \text{ \AA}$) blends the $C IV \lambda\lambda 1168.4, 1168.9 \text{ \AA}$ lines used for the determination of the C abundance in the FUV range. Therefore the $C IV \lambda\lambda 1107.59, 1107.93, 1107.98 \text{ \AA}$ is used and an abundance of $[C] = +0.39$ is derived. The abundances for N, O, Mg, P, and S agree within the error limits with

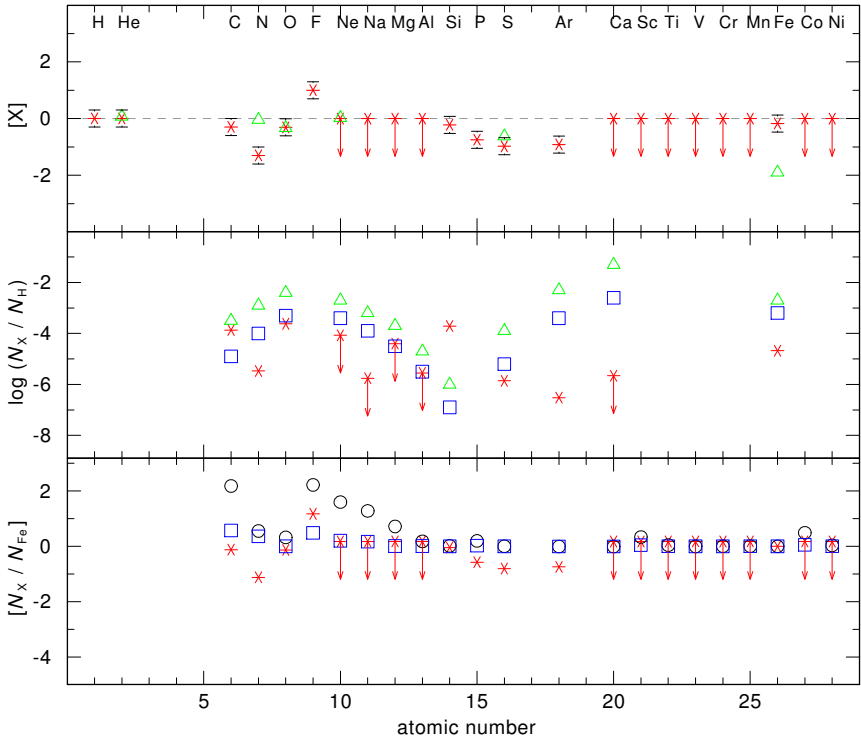


Figure 6.10: Same as Fig. 6.6 for NGC 3587.

the predictions for DA and DO-type WDs (Chayer et al. 1995a,b). Compared to predictions from nucleosynthesis calculations (Cristallo et al. 2009) most abundances agree within the error limits. However, the vast majority of the CS abundances are upper limits and, thus, the compliance is rather uncertain. PN abundances are taken from various sources. Stanghellini et al. (2006) determined the He, N, O, Ne, and Ar abundance of the nebula. Only He, O, Ne and S are in agreement with the abundances determined for the CS if the errors are taken into account. Our N abundance is lower than the value of Stanghellini et al., while our C and S abundances are consistent with the nebula abundances from Milanova & Kholtygin (2009) and Henry et al. (2004), respectively.

We find a much larger T_{eff} (130 ± 10 kK) compared to Napiwotzki (1999, $T_{\text{eff}} = 101 \pm 5$ kK), but confirm their value for $\log g$ (6.9 ± 0.3). The different ef-

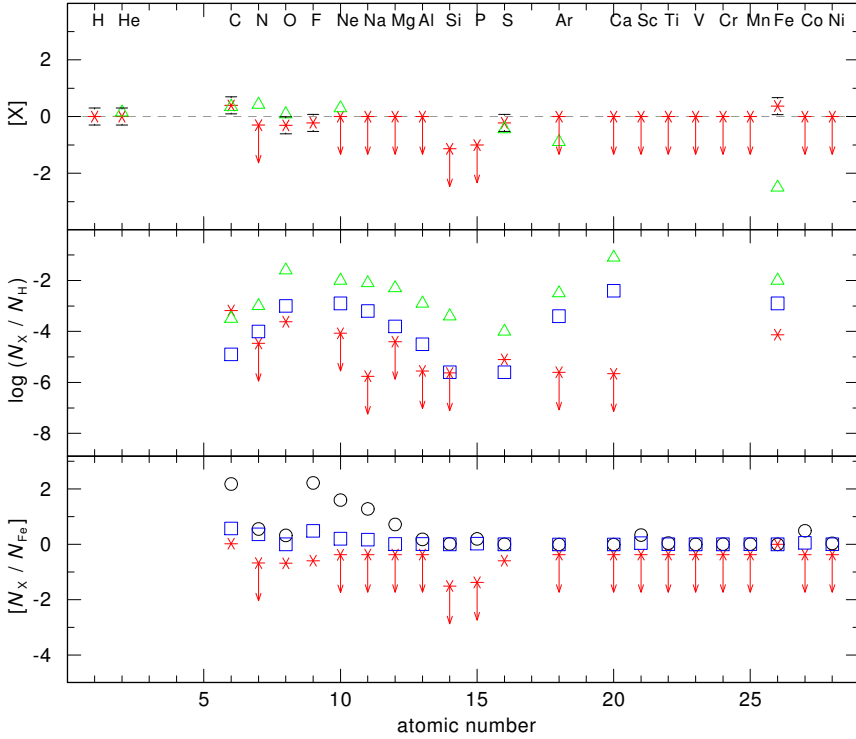


Figure 6.11: Same as Fig. 6.6 for NGC 6720.

fective temperatures might be explained by the different methods they have been determined. While we analyzed ionization equilibria to derive T_{eff} , Napiwotzki analyzed optical H lines using NLTE model atmospheres containing only H and He. However, our mass for NGC 6720 ($M = 0.552 \pm 0.05 M_{\odot}$) confirms the value of Napiwotzki ($M = 0.56 \pm 0.02 M_{\odot}$).

6.2.1.7 NGC 6853

The analysis of the *FUSE* observation of NGC 6853 (Fig. D.7, Fig. E.22–E.28) was hampered by interstellar H_2 lines up to a rotational state higher than nine, which is the upper limit of the *OWENS* program. Thus, a large number of observed lines in the FUV range remain unidentified.

In the *STIS* observation C, O, Ne, Si lines can be identified. No lines of iron-

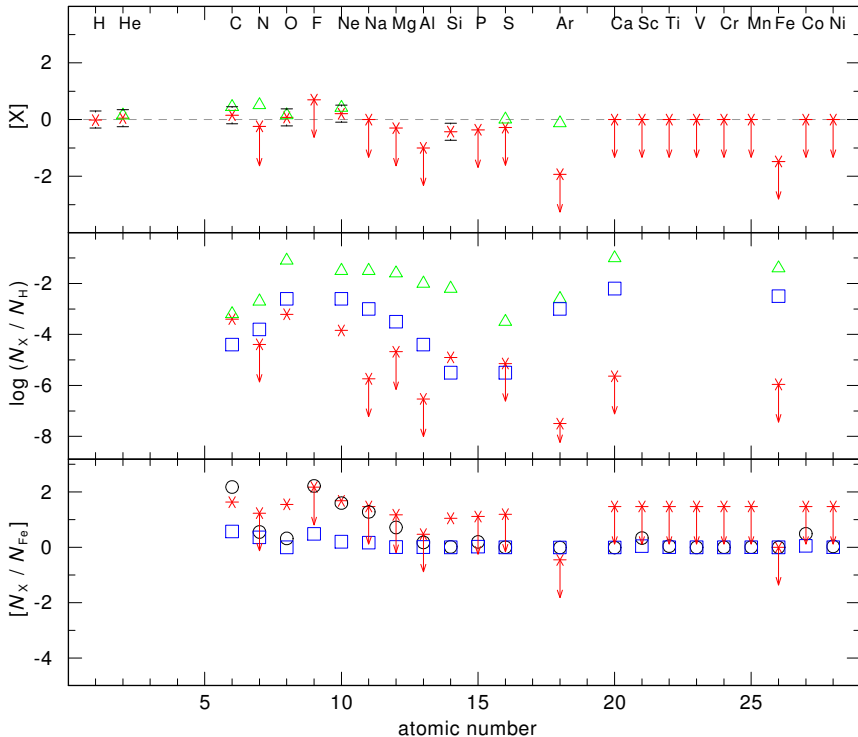


Figure 6.12: Same as Fig. 6.6 for NGC 6853.

group elements are visible in the UV range. Fe VII and VIII lines in the FUV range are not suitable for an abundance determination due to unknown blends of interstellar H₂ lines. However, using *STIS* an upper limit of [Fe] = -1.47 can be found. Our abundances agree within the error limits with the values of Traulsen et al. (2005, cf. Sect. 4.1.7). Using the parameters of Traulsen et al. a F abundance of log F < -6.4 (in mass fraction) has been determined by Werner et al. (2005). We confirm this value and find log F < -6.6. We also confirm T_{eff} , log g , the stellar mass, as well as the C, N, and O abundances from Traulsen et al. ($T_{\text{eff}} = 126 \pm 6 \text{ kK}$, log $g = 6.5 \pm 0.2$, $M = 0.58 M_{\odot}$), but we find a larger Si abundance by roughly one dex. The derived abundances for N, O, Si, and S agree within the error limits with the abundances predicted by the diffusion calculations for DA-type WDs from Chayer et al. (1995a,b). We also find an

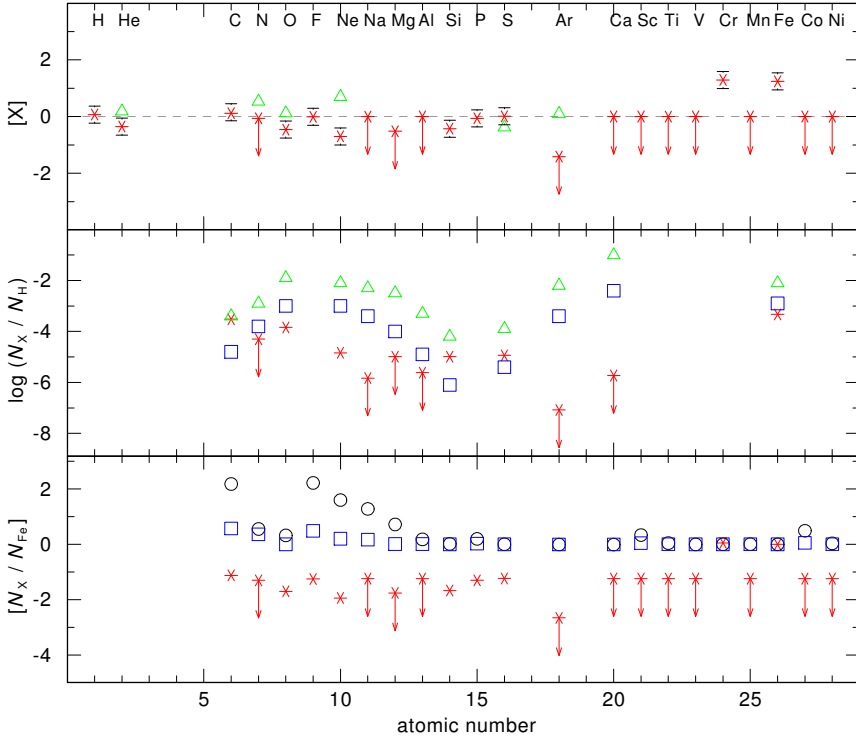


Figure 6.13: Same as Fig. 6.6 for NGC 7293.

agreement for F, Ne, Na, Mg, and Al with the predicted surface abundances from nucleosynthesis calculations from Cristallo et al. (2009) for a star with an initial mass of $2 M_{\odot}$ and a metallicity of $Z = 1 \cdot 10^{-3}$. The nebula abundances of He, O, and Ne determined by Stanghellini et al. (2006) agree with our values for the CS, while we disagree with their N and Ar abundance. The C abundance determined for the nebula (Barker 1984) is consistent with our abundance for the CS, while we find a slightly lower S abundance than Holovatyy & Havrilova (2005) found for the PN.

6.2.1.8 NGC 7293

Besides NGC 1360, NGC 7293 (Fig. D.8, Fig. E.29–E.35) is one of only two objects of the sample showing the Ne VII $\lambda 973.3 \text{ \AA}$ line. Iron and chromium are

enhanced by a factor of ≈ 18 compared to solar. The Fe VI and VII lines in the *FUSE* and *STIS* observations can be fitted with this enhanced abundance. Also the Fe VIII lines in the *FUSE* range support this value, while Fe VIII in the *STIS* range seems to impose a smaller Fe abundance. Besides Fe and Cr, lines of C, O, F, Si, P, and S can be found. Within the error limits the abundances of He, C, N, O, and Si, as well as T_{eff} , $\log g$, and the mass determined by Traulsen et al. (2005, $T_{\text{eff}} = 126 \pm 6$ kK, $\log g = 6.3 \pm 0.2$, $M = 0.56 M_{\odot}$) can be confirmed. The F abundance ($[F] = -0.01$) agrees with the value of Werner et al. (2005), who used T_{eff} and $\log g$ from Traulsen et al.. Also the Ar underabundance of a factor of roughly 50 (Werner et al. 2007) can be confirmed. Compared to the abundances for DA-type WDs predicted by diffusion calculations (Chayer et al. 1995a,b), the values of N, S, and Fe agree within the error limits. The rest of the abundances, however, show larger deviations up to almost four dex (Ar and Ca). Compared with the nucleosynthesis calculations of Cristallo et al. (2009) only Cr matches the predicted surface abundances, while all other abundances from our analysis are too small by more than one dex. Only the CS abundance for S coincides with the value determined for the PN (Henry et al. 2004). For He, N, O, Ne, and Ar we find lower abundances.

6.2.1.9 PuWe 1

The S/N-ratio of the *FUSE* spectrum of PuWe 1 (Fig. D.9, Fig. E.36–E.38) is very low. The observation exhibits a geocoronal emission feature at 1168.2 – 1168.7 Å. Our results confirm T_{eff} , $\log g$, as well as the stellar mass determined by Napiwotzki (1999, $T_{\text{eff}} = 94 \pm 6$ kK, $\log g = 7.0 \pm 0.2$, $M = 0.56 \pm 0.03 M_{\odot}$).

No photospheric line could be identified unambiguously. The abundances therefore have a high uncertainty and are only upper limits. However, for the elements C, N, O, Ne, Mg, and Al they agree well with predictions for DA-type WDs from Chayer et al. (1995a,b, Fig. 6.14). The applied abundances for our model atmosphere calculations match most of the surface abundances predicted from the AGB nucleosynthesis models from Cristallo et al. (2009). All of our values, however, are upper limits. Only nebula abundances for N and O were found (Kaler et al. 1990). Our upper limit determined for O agrees with the value for the nebula while we find a lower N abundance by almost one dex.

The model SEDs that are displayed in Fig. E.36–Fig. E.38 show emission features of iron-group elements possibly due to the not fully converged model.

6.2.1.10 Sh 2–174

Sh 2–174 (Fig. D.10, Fig. E.39–E.44) exhibits numerous metal lines in the UV and FUV range. Lines of C, N, O, Si, P, Ar, Cr, Mn, Fe, Co, and Ni were

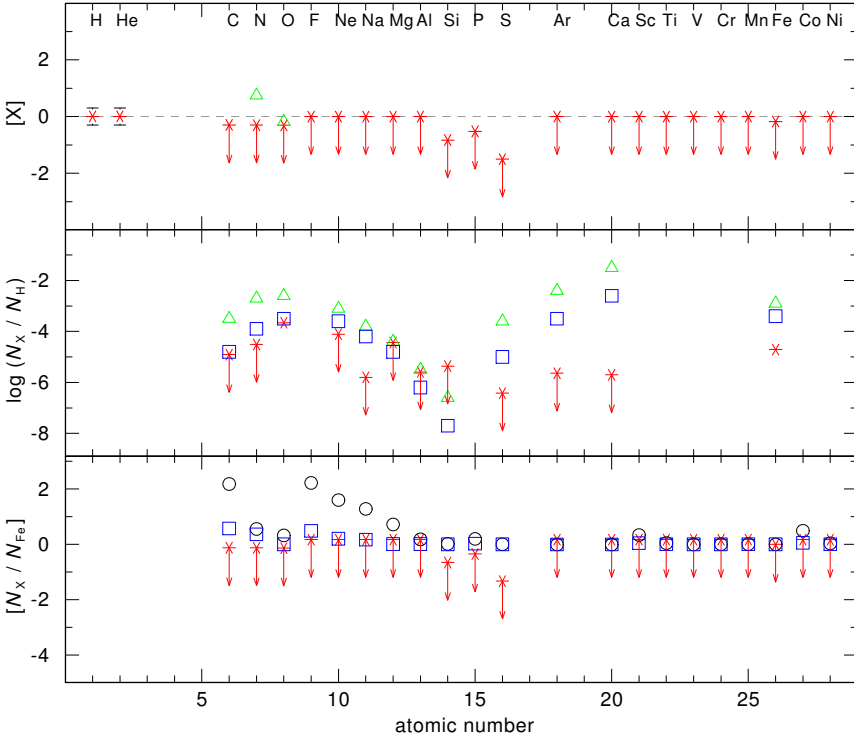


Figure 6.14: Same as Fig. 6.6 for PuWe 1.

identified. The iron-group elements Cr, Mn, Fe, Co, and Ni are enhanced to ≈ 10 times solar. The derived abundances do not agree with the abundances predicted for DA-type WDs (Chayer et al. 1995a,b), besides C, O, and Fe. For Si, as well as for the iron-group elements Cr, Mn, and Ni the determined abundances are consistent with predicted nucleosynthesis abundances (Cristallo et al. 2009).

Sh 2–174 is one of the sample objects for which the N v resonance doublet in the *STIS* range is not superposed by interstellar absorption. It is the only object of the sample for which C III lines are visible. Ionization equilibria of C III – IV, N IV – v, O IV – VI, Fe v – VI enabled to determine T_{eff} precisely. Our value of $T_{\text{eff}} = 69 \pm 10$ kK and $\log g = 6.7 \pm 0.3$ confirms the results of Napiwotzki (1999, $T_{\text{eff}} = 69 \pm 3$ kK, $\log g = 6.7 \pm 0.2$), and is also in good agreement with $T_{\text{eff}} = 74$ kK and $\log g = 7.2$ from Gianninas et al. (2010).

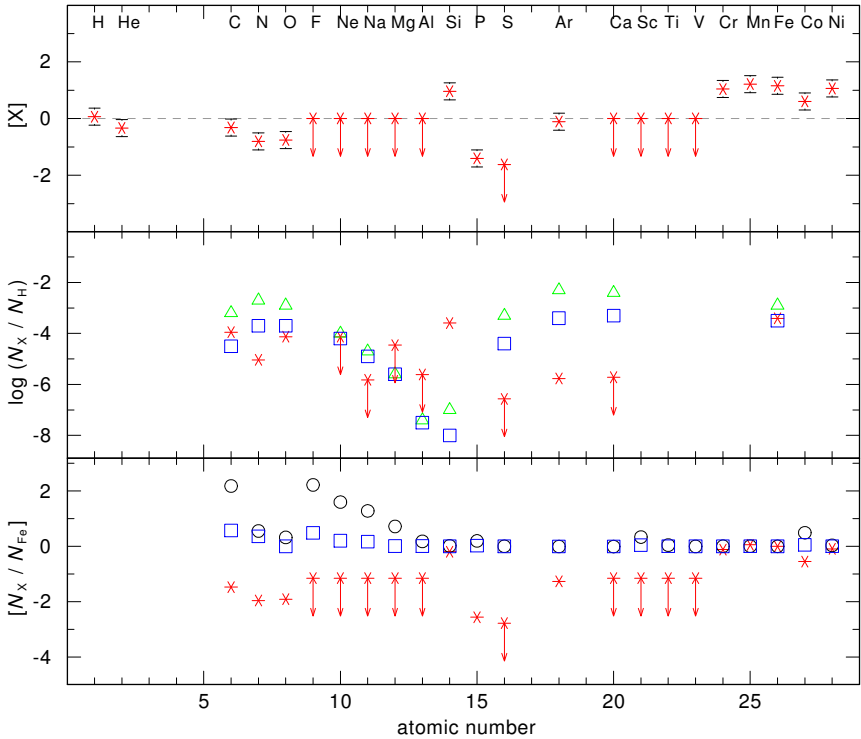


Figure 6.15: Same as Fig. 6.5 for Sh 2–174.

Our low stellar mass ($M = 0.477 \pm 0.05 M_{\odot}$) coincides with the mass determined by Napiwotzki (1999) who find $M = 0.43 \pm 0.03 M_{\odot}$. The low mass of Sh 2–174 as well as the classification of the surrounding nebula as an ionized low-mass H II region (Frew & Parker 2010, Sect. 4.1.10) supports the scenario of the ionizing star being a post-EHB star rather than a post-AGB star.

6.2.2 Summary for the DAO-type WDs

From the ten analyzed DAO-type stars two are possible post-EHB stars (A 35, Sh 2–174) due to their low masses and the classification of their surrounding nebulae as ionized H II nebulae and not as PNe. In the $\log T_{\text{eff}} - \log g$ diagram the DAO-type stars of the analyzed sample are all located either at or after the “knee” (cf. Fig. 6.1), marking the transition between post-AGB evolution and the

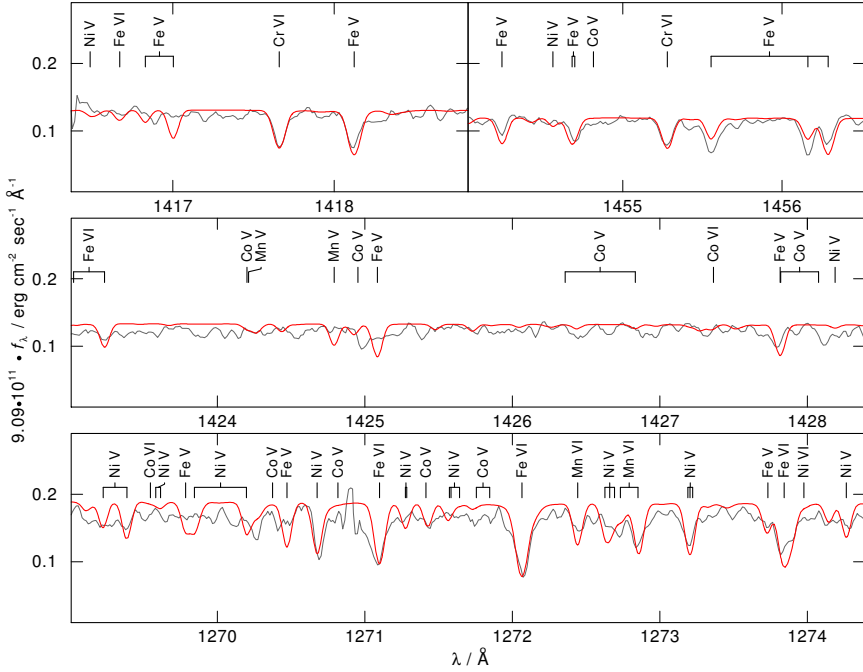


Figure 6.16: Sections of the *STIS* spectrum of Sh2–174 containing Cr, Mn, Co, and Ni lines.

WD cooling sequence. The DAO-type WDs show heterogeneous abundance patterns. They show the same correlations between $\log(T_{\text{eff}}^4/g)$ and the abundances as depicted in Sect. 6.1.4 for the whole sample, i.e. an increase for C, N, O, Si, P, and S with increasing $\log(T_{\text{eff}}^4/g)$, and a decrease for Ar and Fe.

6.2.3 Individual results for O(H)-type stars

6.2.3.1 A 36

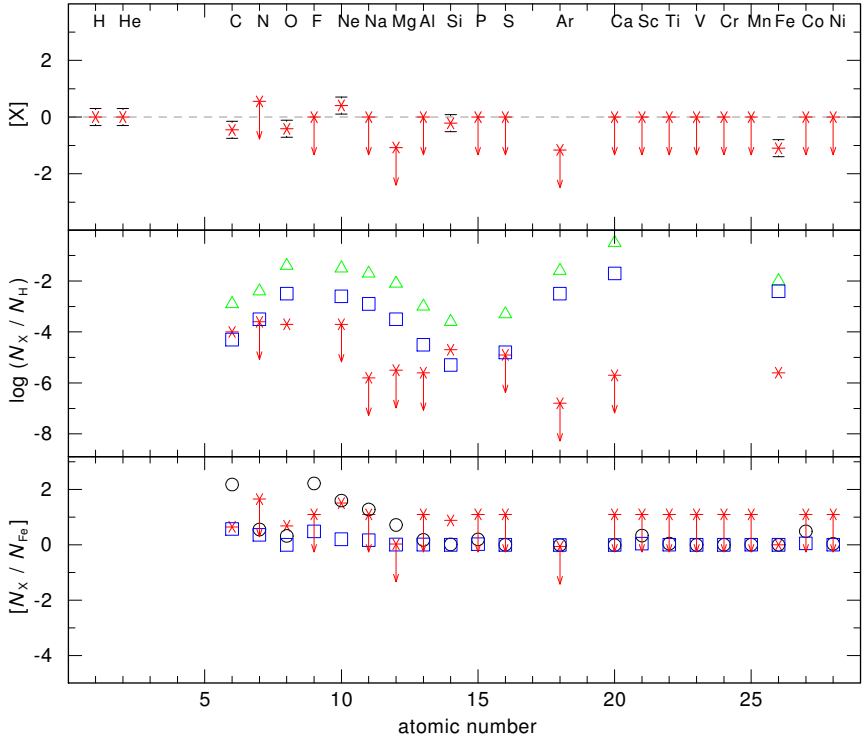


Figure 6.17: Same as Fig. 6.5 but for A 36.

The *STIS* observation of A 36 (Fig. D.11, Fig. E.45–E.47) exhibits a metal poor spectrum, with only a few metal lines of C, N, O, Ne, Si, and Fe.

Within the error limits the derived abundances for C, N, and O confirm the values of Traulsen et al. (2005), while we find a larger Si abundance by roughly 0.7 dex. Our analysis confirms the subsolar Fe abundance determined by Deetjen (1999). A 36 exhibits lines of Ne v and vi that are fitted at $[\text{Ne}] = +0.41$.

While the ionization equilibrium of O IV – VI seems to favour $T_{\text{eff}} = 118$ kK in order to fit He II λ 1640.42Å a lower T_{eff} is necessary. The best fit is achieved for $T_{\text{eff}} = 108$ kK and $\log g = 5.9$, although O v λ 1643.72Å is too strong. The derived values are higher than the ones of Deetjen (1999, $T_{\text{eff}} = 95$ kK, $\log g = 5.5$) but

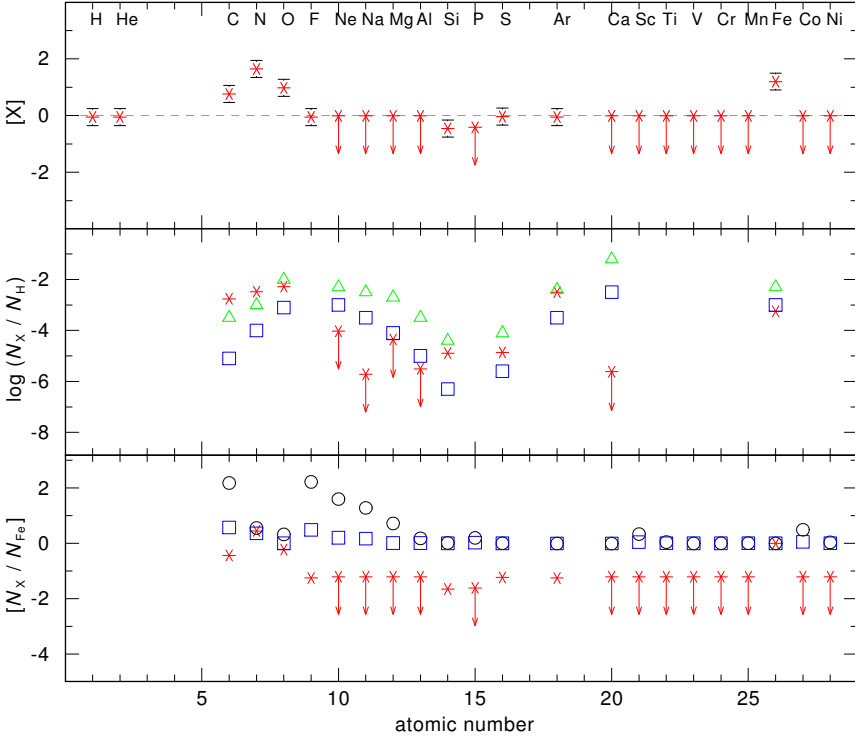


Figure 6.18: Same as Fig. 6.5 but for Lo 1.

agree within the error limits with the values found by Traulsen et al. (2005, $T_{\text{eff}} = 113 \pm 6$ kK, $\log g = 5.6 \pm 0.2$). We find a much smaller stellar mass ($M = 0.535 \pm 0.05 M_{\odot}$) compared to $M = 0.65 M_{\odot}$ from Traulsen et al. The disagreement is due to the different post-AGB tracks used for the mass determination.

The abundances of C, N, O, Al, Si, and Ar reasonably fit the predicted abundances for DA-type WDs from Chayer et al. (1995a,b). Compared to the nucleosynthesis abundances from Cristallo et al. (2009) for solar metallicity, the abundances for C, Mg, and Ar agree within the error limits. However, the abundances for O, Ne and Si for the CS are too high compared to the nucleosynthesis predictions for solar metallicity and favour $Z = 1 \cdot 10^{-3}$.

The derived spectroscopic distance ($d = 463_{-195}^{+140}$ pc) does not agree with the value of Phillips (2005, $d = 770$ pc) within the error limits.

6.2.3.2 *Lo 1*

Lo 1 (Fig. D.12, Fig. E.48–E.50) exhibits C, N, O, F, Si, S, Ar, and Fe lines. Carbon, nitrogen, and oxygen are strongly enhanced ($[C] = +0.76$, $[N] = +1.64$, $[O] = +0.98$). Herald & Bianchi (2004) already reported a O abundance of roughly five times solar. Our O abundance is ≈ 10 times solar. According to Herald & Bianchi oxygen rich atmospheres in CSPNe are often associated with He-rich stars (i.e. helium burners), that often also exhibit a C enrichment. While their analysis did not find the other abundances (besides O) significantly different from the solar values, our abundances for C, N, and O point at Lo 1 being a He-rich object. However, we do not find He enrichment. We confirm T_{eff} , $\log g$, and the stellar mass from Herald & Bianchi (2004, $T_{\text{eff}} = 120 \pm 10$ kK, $\log g = 6.7^{+0.3}_{-0.7}$, $M \simeq 0.60 M_{\odot}$) within the error limits.

The abundances for N, O, Si, and Ar agree well with the predicted photospheric abundances for DO-type WDs Chayer et al. (1995a). The abundances of C, N, O, Si, and Ar accord within the error limits with the abundances predicted from diffusion calculations for DO-type WDs from Chayer et al. (1995a,b). Compared with the abundances from AGB nucleosynthesis calculations (Cristallo et al. 2009) only N and O agree with the predicted abundances for a star with an initial mass of $2 M_{\odot}$ at solar metallicity.

6.2.3.3 *LSS 1362*

With $T_{\text{eff}} = 106 \pm 10$ kK and $\log g = 5.6 \pm 0.3$ LSS 1362 (Fig. D.13, Fig. E.52–E.57) is close to the Eddington limit. Thus, LSS 1362 experiences a mass loss due to a radiation-driven wind (cf. Pauldrach et al. 1988). It is the only object of the sample that exhibits P Cygni profiles of Ne VII $\lambda 973.3 \text{ \AA}$ and the O VI resonance lines at 1031.91, 1037.61 \AA .

The determination of T_{eff} does show contradictions between the Fe VI–VII ionization equilibrium for the *FUSE* and the *STIS* range. While a higher T_{eff} would better fit the Fe VIII lines in the FUV range, the Fe VIII lines in the *STIS* range tend towards a lower T_{eff} or a lower Fe abundance of roughly 0.2 dex. No Fe VI lines can be found in the observation. Within the error limits our value ($T_{\text{eff}} = 106 \pm 10$ kK) confirms T_{eff} determined by Traulsen et al. (2005, $T_{\text{eff}} = 114 \pm 6$ kK). Using the optical H and He lines (Fig. E.57) $\log g = 5.6 \pm 0.3$ can be derived in agreement with $\log g = 5.7 \pm 0.2$ from Traulsen et al.. While their abundances for He, C, and Si can be confirmed, we find lower abundances for N and O of about one dex. Our F abundance ($[F] = -0.80$) confirms the abundance of Werner et al. (2005), who used T_{eff} and $\log g$ from Traulsen et al. (2005). Our mass for LSS 1362 ($M = 0.553 \pm 0.05 M_{\odot}$) is consistent within the error limits with the mass derived by Traulsen et al. (2005) who give $M = 0.60 M_{\odot}$.

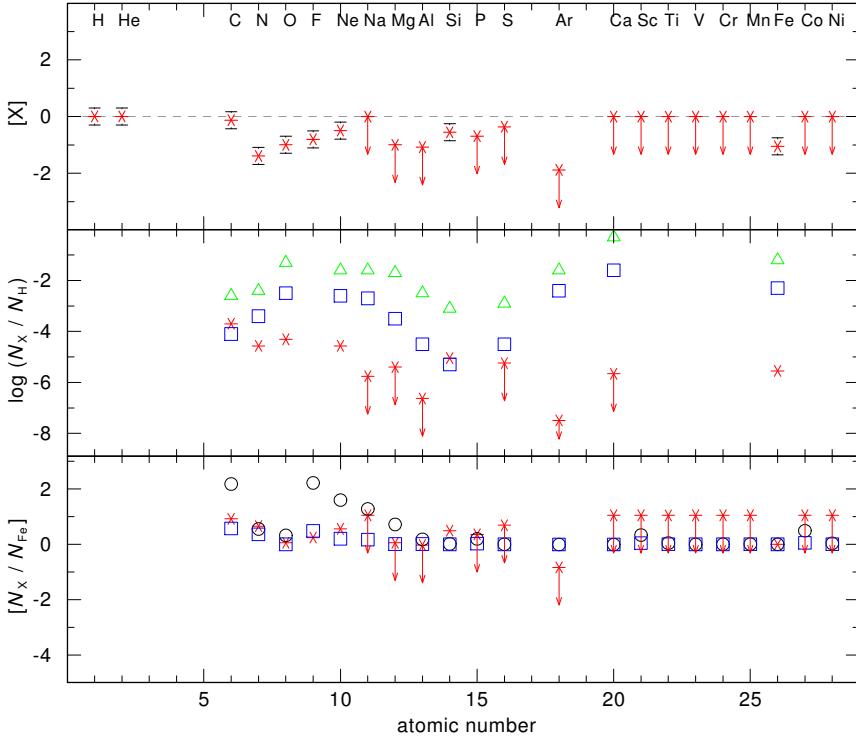


Figure 6.19: Same as Fig. 6.5 but for LSS 1362.

The abundances derived from diffusion calculations for DA-type WDs from Chayer et al. (1995a,b) are not in agreement with the abundances determined from our spectral analysis. Only C and Si match within the error limits. Compared to the predicted abundances from AGB nucleosynthesis calculations (Cristallo et al. 2009), we find an agreement for C, N, O, F, Ne, Mg, Al, and P within the error limits.

6.2.3.4 NGC 1360

The *FUSE* spectrum of NGC 1360 (Fig. D.14, Fig. E.58–E.64) is only sparsely affected by interstellar absorption compared to most other objects of the sample. Lines of C, N, O, F, Ne, P, S, and Ar can be found in the spectrum. From the iron-group elements only lines of Fe VI–VIII are visible.

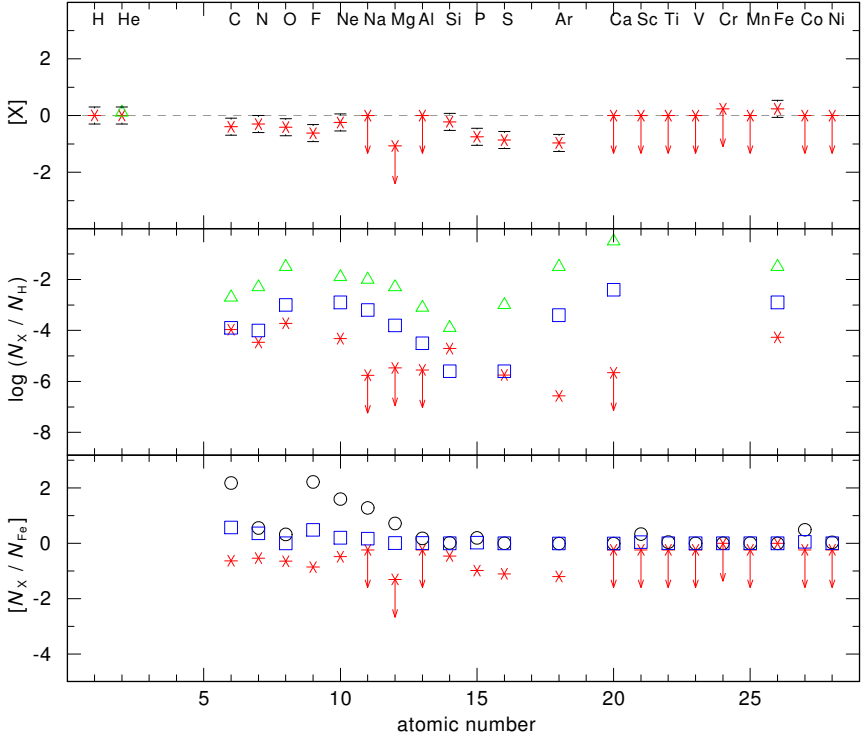


Figure 6.20: Same as Fig. 6.6 but for NGC 1360.

Though the final model SED fits the observation well, we were not able to fit several O v lines. The lines at 933 \AA , 943.5 \AA , as well as the lines between $\approx 1055.5 - 1061.3 \text{ \AA}$ require a higher O abundance. However, the fit to all other O lines (including the O IV – VI lines in the *STIS* range) would fall off in quality with a higher O abundance.

The literature values by Traulsen et al. (2005) for C, N, O, and Si can be confirmed. The He abundance, however, had to be decreased from $n_{\text{He}}/n_{\text{H}} = 0.25$ of Traulsen et al. to $n_{\text{He}}/n_{\text{H}} \approx 0.09$ in order to fit the optical He lines (Fig. E.64). We also find a much smaller stellar mass ($M = 0.534 \pm 0.05 M_{\odot}$) compared to Traulsen et al. who find $M = 0.65 M_{\odot}$. The reason for this huge difference are the evolutionary tracks used for the mass determination. Traulsen et al. used post-AGB tracks from Schönberner (1983) and Blöcker & Schönberner (1990),

while we used recent evolutionary tracks of Miller-Bertolami (priv. comm.).

Compared to the solar Ne abundance found by Werner et al. (2004) we find a subsolar abundance of $[\text{Ne}] = -0.25$. The different values are possibly due to the different T_{eff} , $\log g$, and He values used for the analyses. Werner et al. applied the parameters determined by Hoare et al. (1996, $T_{\text{eff}} = 110$ kK, $\log g = 5.6$), while our analysis yields $T_{\text{eff}} = 100 \pm 10$ kK and $\log g = 5.7 \pm 0.3$, which is in agreement with the results of Traulsen et al. (2005, $T_{\text{eff}} = 97 \pm 5$ kK, $\log g = 5.3 \pm 0.2$). For our T_{eff} and $\log g$ we can exclude a higher Ne abundance due to the Ne lines in the *STIS* observation (Fig. E.61). We can not confirm the supersolar Ar abundance Werner et al. (2007). Instead we derive $[\text{Ar}] = -0.96$. The F abundance found in this thesis ($[\text{F}] = -0.62$) is in agreement with the value found by Werner et al. (2005). However, Werner et al. find F $\nu \lambda \lambda 1087.82, 1088.39 \text{ \AA}$ to be too weak to fit the observation with their abundance derived from F $\nu \lambda 1139.50 \text{ \AA}$. We find the two observed F ν lines to be possibly Fe νII and O ν lines (Fig. E.60). The He abundance for the PN (Maciel & Chiappini 1994, and references therein) agrees with our value for the CS.

6.2.3.5 NGC 4361

NGC 4361 (Fig. D.15, Fig. E.65–E.67) is a CEMP Population II object of the outer halo of the Milky Way. A best fit to the C IV lines in the *STIS* range is achieved for $[\text{C}] = +1.43$. Besides C, only O ν , Si ν , and Ne ν lines can be found in the spectrum. The observation does not show any lines of iron-group elements besides Fe, from which an abundance of $[\text{Fe}] = -1.12$ is derived. Within the error limits our analysis confirms T_{eff} , $\log g$, the stellar mass, as well as the abundances of He, C, O, and Si determined by Traulsen et al. (2005). However, we find a lower N abundance of roughly one dex.

Our abundances do not match the abundances predicted from diffusion calculations for DA and DO-type WDs from Chayer et al. (1995a,b). Only Si and S agree within the error limits with the predictions for DA-type WDs. To match the high C abundance a nucleosynthesis model with $[\text{Fe}/\text{H}] = -2.0$ for a $1.3 M_{\odot}$ star is necessary. Compared to the abundances of this model from Bisterzo et al. (2010), He, O, Ne, Mg, Si, Cr, and Fe agree well within the error limits. Compared with the PN abundances of Torres-Peimbert et al. (1990) we find an accordance for He, Ne, and Ar, while C, N, and O disagree. The PN abundance of F determined by Liu (1998) complies with our solar value applied for the model calculation. Note that in our model atmosphere the solar value has been used due to the lack of F lines in the *STIS* observation. Therefore the compliance between the CS and the PN F abundance has to be regarded with reservation.

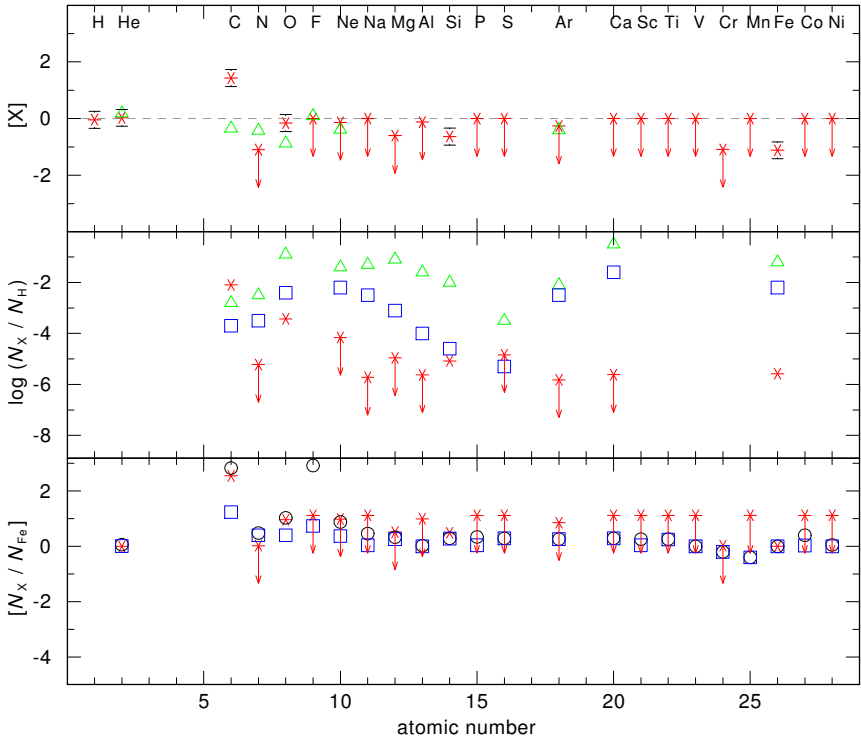


Figure 6.21: Top and middle: Same as Fig. 6.6 but for NGC 4361. Bottom: Photospheric abundances of NGC 4361 compared to nucleosynthesis calculations of Bisterzo et al. (2010) for different metallicities (blue squares: $[\text{Fe}/\text{H}] = -1.0$, black circles: $[\text{Fe}/\text{H}] = -2.0$).

6.2.4 Summary for the O(H)-type WDs

The four O(H)-type CS A 36, LSS 1362, NGC 1360, and NGC 4361 are all located before the “knee” of the stellar evolution. The fifth O(H)-type star of the sample, Lo 1, does not fit well into this picture. It is the only O(H)-type star of the sample that is located after the “knee” in the $\log T_{\text{eff}} - \log g$ diagram, and also its $\log(T_{\text{eff}}^4/g)$ value (13.32) is rather of the order of the DAO-type stars (12.41–13.97, cf. Fig. 6.23) than that of the other O(H)-type stars (14.23–14.50). It is also the only object of the the O(H)-type stars showing enhanced C, N, and O abundances.

Table 6.2: Comparison of CS abundances derived in this thesis with PN abundances from the literature. Top row for each object: PN abundances, bottom: CS abundances.

	$n_{\text{He}}/n_{\text{H}}$	$n_{\text{C}}/n_{\text{H}}$	$n_{\text{N}}/n_{\text{H}}$	$n_{\text{O}}/n_{\text{H}}$	$n_{\text{F}}/n_{\text{H}}$	$n_{\text{Ne}}/n_{\text{H}}$	$n_{\text{S}}/n_{\text{H}}$	$n_{\text{Ar}}/n_{\text{H}}$	$n_{\text{Fe}}/n_{\text{H}}$
A 31	—	—	$0.84 \cdot 10^{-4}$	$2.10 \cdot 10^{-4}$	—	—	—	—	—
	0.10	$2.86 \cdot 10^{-4}$	$2.86 \cdot 10^{-4}$	$3.04 \cdot 10^{-4}$	$6.59 \cdot 10^{-7}$	$9.06 \cdot 10^{-5}$	$1.29 \cdot 10^{-8}$	$1.10 \cdot 10^{-6}$	$5.39 \cdot 10^{-4}$
A 39	0.09	$0.17 \cdot 10^{-3}$	$0.69 \cdot 10^{-4}$	$0.39 \cdot 10^{-3}$	—	$6.50 \cdot 10^{-5}$	$5.20 \cdot 10^{-6}$	$0.58 \cdot 10^{-6}$	—
	0.09	$1.15 \cdot 10^{-3}$	$3.36 \cdot 10^{-4}$	$1.03 \cdot 10^{-3}$	$2.96 \cdot 10^{-8}$	$8.64 \cdot 10^{-5}$	$4.55 \cdot 10^{-6}$	$1.80 \cdot 10^{-6}$	$1.21 \cdot 10^{-5}$
NGC 3587	0.10	—	$2.90 \cdot 10^{-5}$	$2.30 \cdot 10^{-4}$	—	$9.00 \cdot 10^{-5}$	$3.13 \cdot 10^{-6}$	—	$0.04 \cdot 10^{-5}$
	0.09	$1.35 \cdot 10^{-4}$	$0.34 \cdot 10^{-5}$	$2.39 \cdot 10^{-4}$	$3.61 \cdot 10^{-7}$	$8.46 \cdot 10^{-5}$	$1.38 \cdot 10^{-6}$	$3.02 \cdot 10^{-7}$	$2.10 \cdot 10^{-5}$
NGC 6720	0.12	$6.02 \cdot 10^{-4}$	$1.80 \cdot 10^{-4}$	$6.00 \cdot 10^{-4}$	—	$1.70 \cdot 10^{-4}$	$4.80 \cdot 10^{-6}$	$0.32 \cdot 10^{-6}$	$0.01 \cdot 10^{-5}$
	0.09	$6.67 \cdot 10^{-4}$	$0.34 \cdot 10^{-4}$	$2.39 \cdot 10^{-4}$	$2.20 \cdot 10^{-8}$	$0.85 \cdot 10^{-4}$	$7.93 \cdot 10^{-6}$	$2.52 \cdot 10^{-6}$	$7.46 \cdot 10^{-5}$
NGC 6853	0.12	$7.60 \cdot 10^{-4}$	$2.20 \cdot 10^{-4}$	$7.00 \cdot 10^{-4}$	—	$2.24 \cdot 10^{-4}$	$1.34 \cdot 10^{-5}$	$1.88 \cdot 10^{-6}$	—
	0.10	$4.03 \cdot 10^{-4}$	$0.41 \cdot 10^{-4}$	$6.12 \cdot 10^{-4}$	$1.90 \cdot 10^{-8}$	$1.43 \cdot 10^{-4}$	$0.72 \cdot 10^{-5}$	$0.16 \cdot 10^{-6}$	$1.10 \cdot 10^{-6}$
NGC 7293	0.13	—	$2.32 \cdot 10^{-4}$	$6.47 \cdot 10^{-4}$	—	$4.23 \cdot 10^{-4}$	$0.55 \cdot 10^{-5}$	$3.13 \cdot 10^{-6}$	—
	0.03	$3.00 \cdot 10^{-4}$	$0.50 \cdot 10^{-4}$	$1.45 \cdot 10^{-4}$	$3.02 \cdot 10^{-8}$	$0.14 \cdot 10^{-4}$	$1.15 \cdot 10^{-5}$	$1.17 \cdot 10^{-6}$	$4.69 \cdot 10^{-4}$
PuWe 1	—	—	$3.79 \cdot 10^{-4}$	$3.27 \cdot 10^{-4}$	—	—	—	—	—
	0.09	$1.35 \cdot 10^{-4}$	$0.34 \cdot 10^{-4}$	$2.39 \cdot 10^{-4}$	$3.61 \cdot 10^{-8}$	$8.46 \cdot 10^{-5}$	$4.12 \cdot 10^{-7}$	$2.50 \cdot 10^{-6}$	$2.11 \cdot 10^{-5}$
NGC 1360	0.11	—	—	—	—	—	—	—	—
	0.09	$1.08 \cdot 10^{-4}$	$3.38 \cdot 10^{-5}$	$1.90 \cdot 10^{-4}$	$8.69 \cdot 10^{-9}$	$4.81 \cdot 10^{-6}$	$1.79 \cdot 10^{-6}$	$2.71 \cdot 10^{-7}$	$5.43 \cdot 10^{-5}$
NGC 4361	0.13	$0.12 \cdot 10^{-3}$	$2.57 \cdot 10^{-5}$	$0.66 \cdot 10^{-4}$	$4.50 \cdot 10^{-8}$	$3.47 \cdot 10^{-5}$	—	$1.00 \cdot 10^{-6}$	—
	0.10	$8.00 \cdot 10^{-3}$	$0.60 \cdot 10^{-5}$	$3.75 \cdot 10^{-4}$	$4.00 \cdot 10^{-8}$	$6.92 \cdot 10^{-5}$	$1.46 \cdot 10^{-5}$	$1.52 \cdot 10^{-6}$	$2.66 \cdot 10^{-6}$

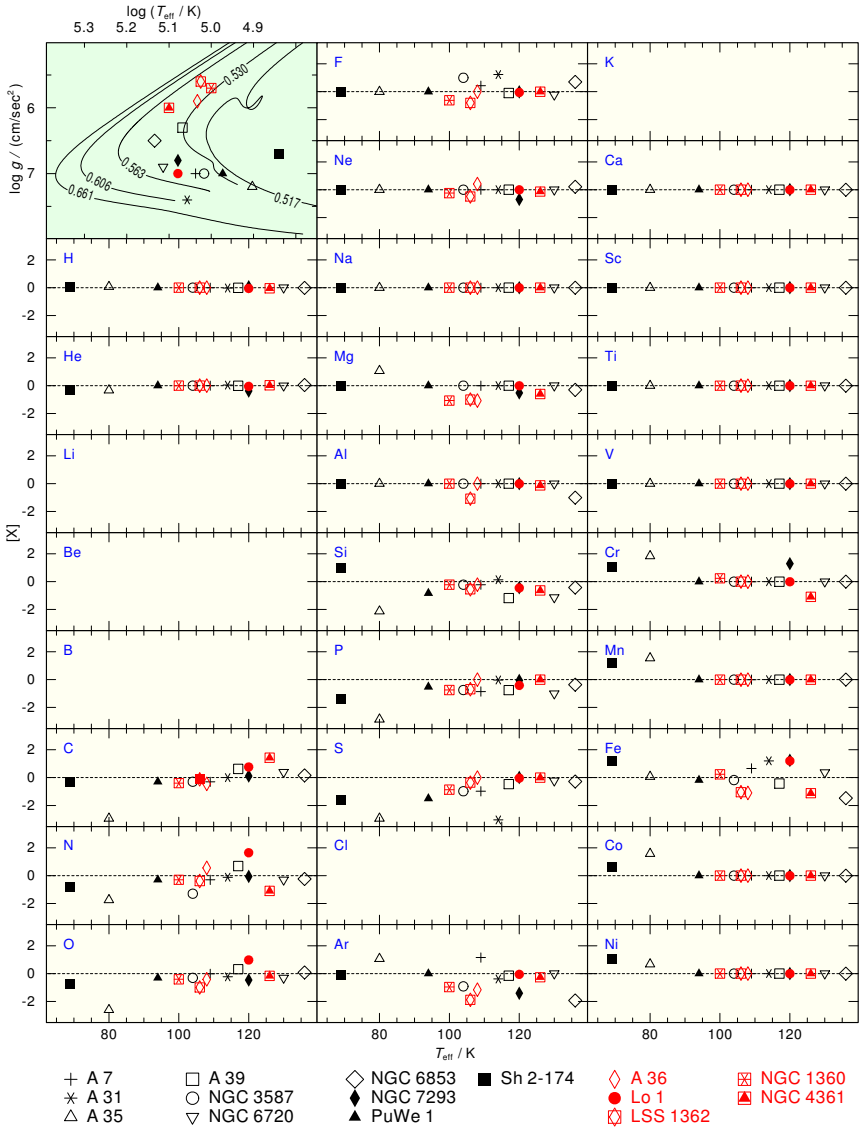


Figure 6.22: Abundances for all elements and all objects as a function of T_{eff} . The abundances for the DAO-type ionizing stars are displayed in black, the abundances for the O(H)-type ionizing stars in red.

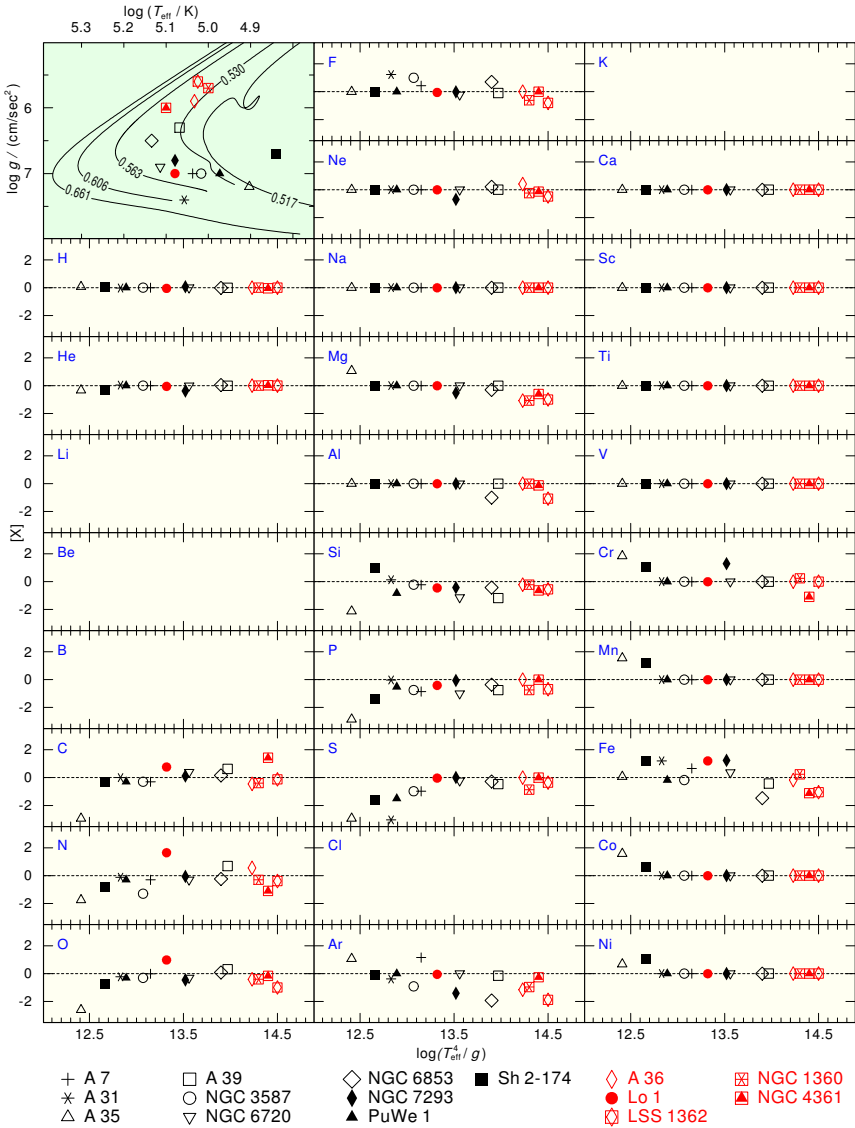


Figure 6.23: Same as Fig. 6.22. Dependence on $\log(T_{\text{eff}}^4/g)$.

CHAPTER 7

Conclusions

UV and FUV spectra of 15 ionizing stars of gaseous nebulae of DAO (A 7, A 31, A 35, A 39, NGC 3587, NGC 6720, NGC 6853, NGC 7293, PuWe 1, Sh 2–174) and O(H)-type (A 36, Lo 1, LSS 1362, NGC 1360, NGC 4361) were analyzed, and the stellar parameters T_{eff} , $\log g$, mass, distance, luminosity, radial velocity, and the chemical composition were determined. For this purpose fully line-blanketed NLTE model atmospheres including almost all elements from H–Ni were calculated. As the desired photospheric informations were superimposed by interstellar absorption lines, ISM models have been calculated with the program *OWENS* and combined with the photospheric model SEDs. Especially the analysis of the FUV range was hampered by the ISM.

The sample, introduced in Chapt. 4, spread a wide range of parameters ($T_{\text{eff}} = 69–130$ kK, $\log g = 5.4–7.4$) and therefore covered different stellar evolutionary stages. The flux maximum at these high effective temperatures is located in the UV and FUV range only accessible from satellites like *FUSE* and *HST*. In these wavelength ranges numerous strategic metal lines can be found. Especially for metals previously unknown abundances were determined and compared to PNe abundances, abundances derived from diffusion calculations, as well as abundances predicted from AGB nucleosynthesis calculations (Sect. 6.2). The findings were of mixed quality. This may be the result of some restrictions that had to be made, e.g. a comparison with AGB nucleosynthesis abundances was only possible for stars with initial masses of $2 M_{\odot}$. With the initial-to-final-mass relation of Weidemann (2000) the progenitors of our sample stars should have had initial masses of $\approx 1 M_{\odot}$. The agreement between abundances of post-AGB stars and AGB nucleosynthesis calculations could improve when AGB nucleosynthesis predictions for stars with lower initial masses will become available.

No clear dependence of the derived abundances with T_{eff} or $\log g$ was found. A correlation between $\log(T_{\text{eff}}^4/g)$ and the element abundances for C, N, O, Si, P, and S was detected. An increasing $\log(T_{\text{eff}}^4/g)$ leads to an increase for the C, N, O, Si, P, and S abundances. For Ar and Fe the abundances decrease unexpectedly

for increasing $\log(T_{\text{eff}}^4/g)$. No lines of Ca, Sc, Ti, and V have been found in any of our objects, and only a few objects showed lines of iron-group elements besides Fe itself.

As results for T_{eff} , $\log g$, and the chemical abundances become more reliable if they are cross-checked in different wavelength ranges, future analyses of post-AGB and post-EHB stars (and astronomical objects in general) should make use of all observations available. In the case of hot and evolved stars some strategic lines are rather located in the UV (e.g. Cr, Mn, Co lines) and some in the FUV range (e.g. F VI, P V, Ar VII). Both ranges are therefore a useful completion to each other. In addition high-resolution, high-S/N observations in the optical enable to cross-check the H/He-abundance ratio, T_{eff} , and $\log g$ derived from the UV and FUV ranges, and, thus, help to constrain the stellar parameters. For most objects analyzed in this thesis this cross-check was not possible as optical observations were lacking, or only *FUSE* or *STIS* observations were available.

Further investigations of post-AGB and post-EHB stars are highly desirable to improve the statistical situation. Especially analyses of cooler DAO-type stars with state-of-the-art model calculations of fully line-blanketed model atmospheres using the latest atomic data will give further insights into stellar evolution. As there are numerous observations available in the *FUSE* archive more interesting results in the field of post-AGB stars and pre-WDs are likely.

Bibliography

- Abell, G. O. 1955, *PASP*, 67, 258
- Abell, G. O. 1966, *ApJ*, 144, 259
- Acker, A., Chopinet, M., Pottasch, S. R., & Stenholm, B. 1987, *A&AS*, 71, 163
- Acker, A., Fresneau, A., Pottasch, S. R., & Jasiewicz, G. 1998, *A&A*, 337, 253
- Allamandola, L. J., Tielens, A. G. G. M., & Barker, J. R. 1985, *ApJ*, 290, L25
- Aller, L. H. 1968, *Planetary Nebulae*, University of Chicago Press, 34, 339
- Amuel, P. R., Guseinov, O. K., & Rustamov, I. S. 1989, *Ap&SS*, 154, 21
- Anderson, L. S. 1989, *ApJ*, 339, 558
- Anderson, L. 1991, *NATO ASIC Proc. 341: Stellar Atmospheres - Beyond Classical Models*, 29
- Apparao, K. M. V., & Tarafdar, S. P. 1989, *ApJ*, 344, 826
- Asplund, M., Grevesse, N., Sauval, A. J., & Scott, P. 2009, *ARA&A*, 47, 481
- Barker, T. 1984, *ApJ*, 284, 589
- Batten, A. H. 1995, *Reports on Progress in Physics*, 58, 885
- Bauer, F., & Husfeld, D. 1995, *A&A*, 300, 481
- Benedict, G. F., et al. 2003, *AJ*, 126, 2549
- Benedict, G. F., et al. 2009, *AJ*, 138, 1969
- Bensby, T., & Lundström, I. 2001, *A&A*, 374, 599
- Bergeron, P., Saffer, R. A., & Liebert, J. 1992, *ApJ*, 394, 228
- Bergeron, P., Wesemael, F., Beauchamp, A., et al. 1994, *ApJ*, 432, 305
- Bisterzo, S., Gallino, R., Straniero, O., Cristallo, S., Käppeler, F. 2010, *MNRAS*, 404, 1529
- Blöcker, T. 1995, *A&A*, 297, 727
- Blöcker, T. 1995, *A&A*, 299, 755
- Blöcker, T., & Schönberner, D. 1990, *A&A*, 240, L11
- Bohlin, R. C., Harrington, J. P., & Stecher, T. P. 1982, *ApJ*, 252, 635
- Bohuski, T. J., & Smith, M. G. 1974, *ApJ*, 193, 197
- Borkowski, K. J., Sarazin, C. L., & Soker, N. 1990, *ApJ*, 360, 173
- Cannon, C. J. 1973, *ApJ*, 185, 621

- Chayer, P., Fontaine, G., & Wesemael, F. 1995, *ApJS*, 99, 189
- Chayer, P., Vennes, S., Pradhan, A. K., et al. 1995, *ApJ*, 454, 429
- Chu, Y.-H., Gruendl, R. A., & Conway, G. M. 1998, *AJ*, 116, 1882
- Ciardullo, R., Bond, H. E., Sipior, M. S., Fullton, L. K., Zhang, C.-Y., & Schaefer, K. G. 1999, *AJ*, 118, 488
- Cristallo, S., Straniero, O., Gallino, R., et al. 2009, *ApJ*, 696, 797
- Cudworth, K. M. 1973, *PASP*, 85, 401
- Cudworth, K. M. 1977, *PASP*, 89, 139
- Curtis, H. D. 1918, *Publications of Lick Observatory*, 13, 55
- de Freitas Pacheco, J. A., Codina, S. J., & Viadana, L. 1986, *MNRAS*, 220, 107
- de Korte, P. A. J., Claas, J. J., Jansen, F. A., & McKechnie, S. P. 1985, *Advances in Space Research*, 5, 57
- Deetjen, J. L. 1999, *Die Eisenhäufigkeit in wasserstoffreichen Zentralsternen Planetarischer Nebel*, *Diploma thesis, University of Tübingen, Germany*
- Delgado Inglada, G., Rodríguez, M., Mampaso, A., & Viironen, K. 2009, *ApJ*, 694, 1335
- de Marco, O. 2009, *PASP*, 121, 316
- D'Odorico, S., Enard, D., Lizon, J. L., Ljung, B., Nees, W., Ponz, D., Raffi, G., & Tanne, J. F. 1983, *The Messenger*, 33, 2
- Dorman, B., Rood, R. T., & O'Connell, R. W. 1993, *ApJ*, 419, 596
- Drilling, J. S. 1983, *ApJ*, 270, L13
- Durand, S., Acker, A., & Zijlstra, A. 1998, *A&AS*, 132, 13
- Edelmann, H. 2003, *Ph.D thesis, University Erlangen-Nuremberg, Germany*
- Feibelman, W. A. 1994, *PASP*, 106, 756
- Feibelman, W. A., & Bruhweiler, F. C. 1990, *ApJ*, 357, 548
- Fich, M., & Blitz, L. 1984, *ApJ*, 279, 125
- Fitzpatrick, E. L. 1999, *PASP*, 111, 63
- Frew, D. J., & Parker, Q. A. 2010, *PASA*, 27, 129
- Gatti, A. A., Drew, J. E., Oudmaijer, R. D., Marsh, T. R., & Lynas-Gray, A. E. 1998, *MNRAS*, 301, L33
- Gianninas, A., Bergeron, P., Dupuis, J., & Ruiz, M. T. 2010, *ApJ*, 720, 581
- Gianninas, A., Bergeron, P., & Ruiz, M. T. 2011, *ApJ*, 743, 138
- Giesecking, F., Hippelein, H., & Weinberger, R. 1986, *A&A*, 156, 101

- Good, S. A., Barstow, M. A., Holberg, J. B., Sing, D. K., Burleigh, M. R., & Dobbie, P. D. 2004, *MNRAS*, 355, 1031
- Good, S. A., Barstow, M. A., Burleigh, M. R., Dobbie, P. D., Holberg, J. B., & Hubeny, I. 2005, *MNRAS*, 363, 183
- Goriely, S., & Mowlavi, N. 2000, *A&A*, 362, 599
- Greggio, L., & Renzini, A. 1990, *ApJ*, 364, 35
- Guerrero, M. A., Chu, Y.-H., & Gruendl, R. A. 2000, *ApJS*, 129, 295
- Guerrero, M. A., Chu, Y.-H., Gruendl, R. A., Williams, R. M., & Kaler, J. B. 2001, *ApJ*, 553, L55
- Guinan, E., Garlow, K., & Theokas, A. 1984, *BAAS*, 16, 994
- Haas, S. 1997, *PhD thesis*, University Erlangen-Nürnberg, Germany
- Haro, G., & Luyten, W. J. 1962, *Boletín de los Observatorios Tonantzintla y Tacubaya*, 3, 37
- Harris, H. C., Dahn, C. C., Monet, D. G., & Pier, J. R. 1997, *Planetary Nebulae*, *IAUS*, 180, 40
- Harris, H. C., et al. 2007, *AJ*, 133, 631
- Heap, S. R. 1986, *New Insights in Astrophysics. Eight Years of UV Astronomy with IUE*, *ESA Proceedings*, 263, 291
- Heber, U., Hunger, K., Jonas, G., & Kudritzki, R. P. 1984, *A&A*, 130, 119
- Heber, U., & Drilling, J. S. 1984, *Mitteilungen der Astronomischen Gesellschaft Hamburg*, 62, 252
- Heber, U., Hunger, K., & Werner, K. 1988, *The Impact of Very High S/N Spectroscopy on Stellar Physics*, *IAUS*, 132, 389
- Heber, U., Werner, K., & Drilling, J. S. 1988, *A&A*, 194, 223
- Heber, U., Moehler, S., Napiwotzki, R., Thejll, P., & Green, E. M. 2002, *A&A*, 383, 938
- Hébrard, G., & Moos, H. W. 2003, *ApJ*, 599, 297
- Henry, R. B. C., Kwitter, K. B., & Balick, B. 2004, *AJ*, 127, 2284
- Herald, J. E., & Bianchi, L. 2002, *ApJ*, 580, 434
- Herald, J. E., & Bianchi, L. 2004, *PASP*, 116, 391
- Herald, J. E., & Bianchi, L. 2011, *MNRAS*, 417, 2440
- Herwig, F. 2005, *ARA&A*, 43, 435
- Herwig, F. 2006, *International Symposium on Nuclear Astrophysics - Nuclei in the Cosmos IX*, 206
- Hoare, M. G., Drake, J. J., Werner, K., & Dreizler, S. 1996, *MNRAS*, 283, 830

- Holovaty, V. V., & Havrilova, N. V. 2005, *Astronomy Reports*, 49, 390
- Hummer, D. G., Berrington, K. A., Eissner, W., Pradhan, A. K., Saraph, H. E., & Tully, J. A. 1993, *A&A*, 279, 298
- Iben, I., Jr., Kaler, J. B., Truran, J. W., & Renzini, A. 1983, *ApJ*, 264, 605
- Ishida, K., & Weinberger, R. 1987, *A&A*, 178, 227
- Jacoby, G. H. 1981, *ApJ*, 244, 903
- Jacoby, G. H., Ferland, G. J., & Korista, K. T. 2001, *ApJ*, 560, 272
- Jahn, D. 2005, *Diploma thesis, University Tübingen, Germany*
- Jordan, S., Werner, K., & O'Toole, S. J. 2005, *14th European Workshop on White Dwarfs, ASP Conference Series*, 334, 257
- Kaler, J. B. 1980, *ApJ*, 239, 78
- Kaler, J. B. 1983, *ApJ*, 271, 188
- Kaler, J. B., & Feibelman, W. A. 1985, *ApJ*, 297, 724
- Kaler, J. B., & Jacoby, G. H. 1989, *ApJ*, 345, 871
- Kaler, J. B., Shaw, R. A., & Kwitter, K. B. 1990, *ApJ*, 359, 392
- Kepler, S. O., Kleinman, S. J., Nitta, A., Koester, D., Castanheira, B. G., Giovannini, O., & Althaus, L. 2007, *15th European Workshop on White Dwarfs, ASP Conference Series*, 372, 35
- Kerber, F., Mignani, R. P., Pauli, E.-M., Wicenec, A., & Guglielmetti, F. 2004, *A&A*, 420, 207
- Kippenhahn, R., & Weigert, A. 1990, *Stellar Structure and Evolution, XVI, Springer-Verlag Berlin Heidelberg New York*
- Kitsikis, A., & Weiss, A. 2007, *Why Galaxies Care About AGB Stars: Their Importance as Actors and Probes, ASP Conference Series*, 378, 99
- Kohoutek, L. 2001, *A&A*, 378, 843
- Kreysing, H. C., Diesch, C., Zweigle, J., Staubert, R., Grewing, M., & Hasinger, G. 1992, *A&A*, 264, 623
- Kudritzki, R. P., Méndez, R. H., & Simon, K. P. 1984, *Observational Tests of the Stellar Evolution Theory, IAUS*, 105, 205
- Kurucz, R. L. 1991, *NATO ASIC Proc. 341: Stellar Atmospheres - Beyond Classical Models*, 441
- Kurucz, R. L. 2009, *American Institute of Physics Conference Series*, 1171, 43
- Lasker, B. M., & Hesser, J. E. 1971, *ApJ*, 164, 303
- Leahy, D. A., Zhang, C. Y., Volk, K., & Kwok, S. 1996, *ApJ*, 466, 352
- Lemoine, M., et al. 2002, *ApJS*, 140, 67
- Leone, F., Martínez González, M. J., Corradi, R. L. M., Privitera, G., & Manso Sainz, R. 2011, *ApJ*, 731, L33

- Liu, X.-W. 1998, *MNRAS*, 295, 699
- Longmore, A. J. 1977, *MNRAS*, 178, 251
- Maciel, W. J., & Chiappini, C. 1994, *Ap&SS*, 219, 231
- Maciel, W. J., & Cazetta, J. O. 1997, *Ap&SS*, 249, 341
- McCarthy, J. K., Mendez, R. H., & Kudritzki, R.-P. 1997, *Planetary Nebulae*, IAUS, 180, 120
- McCook, G. P., & Sion, E. M. 1999, *ApJS*, 121, 1
- Meatheringham, S. J., Wood, P. R., & Faulkner, D. J. 1988, *ApJ*, 334, 862
- Méndez, R. H., & Niemelä, V. S. 1977, *MNRAS*, 178, 409
- Méndez, R. H., Kudritzki, R. P., Gruschinske, J., & Simon, K. P. 1981, *A&A*, 101, 323
- Méndez, R. H., Kudritzki, R. P., & Simon, K. P. 1985, *A&A*, 142, 289
- Méndez, R. H. 1991, *Evolution of Stars: the Photospheric Abundance Connection*, IAUS, 145, 375
- Méndez, R. H., Kudritzki, R. P., & Herrero, A. 1992, *A&A*, 260, 329
- Milanova, Y. V., & Kholtygin, A. F. 2009, *Astronomy Letters*, 35, 518
- Napiwotzki, R. 1999, *A&A*, 350, 101
- Napiwotzki, R. 2003, *Planetary Nebulae: Their Evolution and Role in the Universe*, IAUS, 209, 211
- Napiwotzki, R., & Schönberner, D. 1993, *Planetary Nebulae*, IAUS, 155, 495
- O'Dell, C. R., Sabbadin, F., & Henney, W. J. 2007, *AJ*, 134, 1679
- Oegerle, W., Murphy, E., & Kriss, J. 2000, *User's Guide, Far Ultraviolet Spectroscopic Explorer*, 4 February 2000. Baltimore: Johns Hopkins University
- Padmanabhan, T. 2001, *Theoretical Astrophysics Volume 2: Stars and Stellar Systems*, Cambridge University Press
- Patriarchi, P., & Perinotto, M. 1991, *A&AS*, 91, 325
- Pauldrach, A., Puls, J., Kudritzki, R. P., Méndez, R. H., & Heap, S. R. 1988, *A&A*, 207, 123
- Perryman, M. A. C., et al. 1997, *A&A*, 323, L49
- Phillips, J. P. 2003, *MNRAS*, 344, 501
- Phillips, J. P. 2004, *MNRAS*, 353, 589
- Phillips, J. P. 2005, *MNRAS*, 357, 619
- Pottasch, S. R. 1996, *A&A*, 307, 561
- Pottasch, S. R., Wesselius, P. R., Wu, C.-C., Fieten, H., & van Duinen, R. J. 1978, *A&A*, 62, 95
- Pottasch, S. R., & Bernard-Salas, J. 2010, *A&A*, 517, A95
- Purgathofer, A., & Weinberger, R. 1980, *A&A*, 87, L5

- Rauch, T. 1997, *A&A*, 320, 237
- Rauch, T. 2006, *Planetary Nebulae in our Galaxy and Beyond*, IAUS, 234, 131
- Rauch, T., & Deetjen, J. L. 2003, *Stellar Atmosphere Modeling*, ASP Conference Series, 288, 103
- Rauch, T., Ziegler, M., Werner, K., Kruk, J. W., Oliveira, C. M., Vande Putte, D., Mignani, R. P., & Kerber, F. 2007, *A&A*, 470, 317
- Savitzky, A., & Golay, M. J. E. 1964, *Analytical Chemistry*, 36, 1627
- Scharmer, G. B. 1981, *ApJ*, 249, 720
- Schneider, S. E., Terzian, Y., Purgathofer, A., & Perinotto, M. 1983, *ApJS*, 52, 399
- Schönberner, D. 1979, *A&A*, 79, 108
- Schönberner, D. 1983, *ApJ*, 272, 708
- Schönberner, D., & Drilling, J. S. 1984, *ApJ*, 278, 702
- Seaton, M. J., Yan, Y., Mihalas, D., & Pradhan, A. K. 1994, *MNRAS*, 266, 805
- Sharpless, S. 1959, *ApJS*, 4, 257
- Stanghellini, L., Guerrero, M. A., Cunha, K., Machado, A., & Villaver, E. 2006, *ApJ*, 651, 898
- Taresch, G., Kudritzki, R. P., Hurwitz, M., et al. 1997, *A&A*, 321, 531
- Torres-Peimbert, S., Peimbert, M., & Pena, M. 1990, *A&A*, 233, 540
- Traulsen, I., Hoffmann, A. I. D., Rauch, T., Werner, K., Dreizler, S., & Kruk, J. W. 2005, *14th European Workshop on White Dwarfs*, ASP Conference Series, 334, 325
- Tweedy, R. W. 1993, *MNRAS*, 260, 855
- Unglaub, K., & Bues, I. 1998, *A&A*, 338, 75
- Unglaub, K., & Bues, I. 2000, *A&A*, 359, 1042
- Wehmeyer, R., & Kohoutek, L. 1979, *A&A*, 78, 39
- Weidemann, V. 2000, *A&A*, 363, 647
- Weidmann, W. A., & Gamen, R. 2011, *A&A*, 531, A172
- Weigert, A. 1966, *ZAp*, 64, 395
- Werner, K., & Husfeld, D. 1985, *A&A*, 148, 417
- Werner, K., Deetjen, J. L., Dreizler, S., Rauch, T., & Kruk, J. W. 2003, *Planetary Nebulae: Their Evolution and Role in the Universe*, IAUS, 209, 169
- Werner, K., Rauch, T., Reiff, E., Kruk, J. W., & Napiwotzki, R. 2004, *A&A*, 427, 685
- Werner, K., Rauch, T., & Kruk, J. W. 2005, *A&A*, 433, 641
- Werner, K., Rauch, T., & Kruk, J. W. 2007, *A&A*, 466, 317

Wesemael, F., Green, R. F., & Liebert, J. 1985, ApJS, 58, 379

Wood, M. A. 1995, White Dwarfs, 443, 41

Zanstra, H. 1927, ApJ, 65, 50

Zhang, C. Y. 1993, ApJ, 410, 239

Zuckerman, B., & Aller, L. H. 1986, ApJ, 301, 772

APPENDIX A

Atomic-data statistics

The following two tables give an overview of the statistics of the atomic data used for the analysis. Note that the atomic data had to be adjusted for each sample object to avoid numerical problems and to adopt to the individual parameter ranges. Table A.1 gives the statistics for the “classical” treated atomic data (H–Ar), Tab. A.2 shows the details for the iron-group elements (Ca–Ni) treated with *IrOnIc* (cf. 2.3.1).

Table A.1: Statistics of H–Ar model atoms used in our calculations.

ion	levels			ion	levels		
	NLTE	LTE	lines		NLTE	LTE	lines
H I	12	4	66	Na v	8	42	9
H II	0	1	0	Na VI	43	10	130
He I	5	98	3	Na VII	1	0	0
He II	16	16	120	Mg III	1	34	0
He III	1	0	0	Mg IV	31	0	93
C III	6	61	12	Mg v	15	37	18
C IV	54	4	295	Mg VI	1	0	0
C v	1	0	0	Al III	1	6	0
N III	1	65	0	Al IV	15	2	0
N IV	16	78	30	Al v	1	16	0
N v	54	8	297	Al VI	14	24	16
N VI	1	0	0	Al VII	1	0	0
O III	3	69	0	Si III	3	31	1
O IV	18	67	39	Si IV	16	7	44
O v	90	36	610	Si v	25	0	59
O VI	54	8	291	Si VI	1	0	0
O VII	1	0	0	P III	1	9	0
F III	1	6	0	P IV	15	36	9
F IV	1	10	0	P v	18	7	12
F v	15	91	31	P VI	1	0	0
F VI	12	115	16	S IV	6	94	4
F VII	1	0	0	S v	21	89	37
Ne II	1	33	0	S VI	18	19	48
Ne III	3	43	0	S VII	1	0	0
Ne IV	3	37	0	Ar IV	1	349	0
Ne v	20	74	35	Ar v	32	329	38
Ne VI	1	0	0	Ar VI	16	168	21
Na III	1	186	0	Ar VII	40	112	130
Na IV	1	237	0	Ar VIII	1	0	0
				total	741	2837	2514

Table A.2: Same as Tab. A.1 for Ca – Ni. The so-called sample lines are combined to super lines by *IrOnIc*.

ion	super levels	super lines	sample lines	ion	super levels	super lines	sample lines
Ca IV	6	16	20291	Cr VII	6	19	37070
Ca V	6	21	141956	Cr VIII	6	20	132221
Ca VI	6	19	114545	Cr IX	1	0	0
Ca VII	6	21	71608	Mn IV	6	20	719387
Ca VIII	6	20	9124	Mn V	6	20	285376
Ca IX	1	0	0	Mn VI	6	20	70116
Sc IV	6	20	15024	Mn VII	6	20	8277
Sc V	6	21	261235	Mn VIII	6	20	37168
Sc VI	6	19	237271	Mn IX	1	0	0
Sc VII	6	20	176143	Fe IV	6	20	3102371
Sc VIII	6	21	91935	Fe V	6	20	3266247
Sc IX	1	0	0	Fe VI	6	20	991935
Ti IV	6	19	1000	Fe VII	6	20	200455
Ti V	6	20	26654	Fe VIII	6	18	19587
Ti VI	6	19	95448	Fe IX	1	0	0
Ti VII	6	20	230618	Co IV	6	20	552916
Ti VIII	6	21	182699	Co V	6	20	1469717
Ti IX	1	0	0	Co VI	6	18	898484
V IV	6	19	37130	Co VII	6	19	492913
V V	6	20	2123	Co VIII	6	20	88548
V VI	6	19	35251	Co IX	1	0	0
V VII	6	19	112883	Ni IV	6	20	2512561
V VIII	6	20	345089	Ni V	6	20	2766664
V IX	1	0	0	Ni VI	6	18	7408657
Cr IV	6	20	234170	Ni VII	6	18	4195381
Cr V	6	20	43860	Ni VIII	6	20	1473122
Cr VI	6	20	4406	Ni IX	1	0	0
				total	279	884	33219636

APPENDIX B

Observational details

Tables Tab. B.1 and Tab. B.2 give some observational details for all (F)UV observations analyzed. Further details can also be found in the MAST database.

Table B.1: Log of analyzed observations for the O(H)-type ionizing stars of gaseous nebulae. The characters at the end of the *IUE* ObsIds denote the dispersion (“L” - low) and the aperture (“L” - large).

Object	Instrument	ObsId	Start time (UT)	Exp. time (s)
A 36	<i>STIS</i>	O64D06010	2001-02-12	2336
	<i>IUE</i>	SWP47001LL	1993-02-19	180
		LWP03692LL	1984-07-01	300
Lo 1	<i>FUSE</i>	P1330601000	2000-12-11	5848
	<i>IUE</i>	SWP21421LL	1983-11-01	900
		LWP11432LL	1987-08-19	1020
LSS 1362	<i>FUSE</i>	P3020701000	2003-12-11	28703
	<i>STIS</i>	O64D02010	2001-04-17	2469
		O64D02020	2001-04-18	3054
	<i>IUE</i>	LWR14242LL	1982-09-24	420
		SWP37797LL	1989-12-11	240
NGC 1360	<i>FUSE</i>	D1800102000	2004-09-08	9016
	<i>STIS</i>	O64D01010	2001-09-02	2366
	<i>IUE</i>	LWR05680LL	1979-09-24	140
NGC 4361	<i>STIS</i>	O64D08010	2002-01-07	2300
		O64D08020	2002-01-07	2897
	<i>IUE</i>	LWP23365LL	1992-06-23	420
		SWP44989LL	1992-06-23	300

Table B.2: Same as Tab. B.1 but for DAO-type ionizing stars of gaseous nebulae

Object	Instrument	ObsId	Start time (UT)	Exp. time (s)
A 7	<i>FUSE</i>	B0520901000	2001-10-05	11123
	<i>IUE</i>	SWP40248LL	1990-12-02	3000
		LWP19340LL	1990-12-02	4800
A 31	<i>FUSE</i>	B0521001000	2001-04-25	8432
	<i>IUE</i>	LWR13237LL	1982-05-13	1800
		SWP16970LL	1982-05-15	1800
A 35	<i>FUSE</i>	P1330101000	2000-05-20	4416
	<i>STIS</i>	O4GT02010	1999-04-17	2050
	<i>IUE</i>	SWP44121LL	1992-03-06	1440
		LWP22518LL	1992-03-06	1440
A 39	<i>FUSE</i>	B0520301000	2001-07-26	6879
	<i>IUE</i>	SWP16937LL	1982-05-09	4200
		LWR15846LL	1983-04-30	4920
NGC 3587	<i>FUSE</i>	B0520501000	2001-03-23	9910
	<i>IUE</i>	SWP04920LL	1979-04-12	1800
		LWR12579LL	1982-02-14	3600
NGC 6720	<i>FUSE</i>	B0690201000	2001-06-08	28312
	<i>IUE</i>	SWP06463LL	1979-09-10	3600
		LWR06239LL	1979-11-27	5400
NGC 6853	<i>FUSE</i>	M1070301000	2000-09-23	15933
	<i>STIS</i>	O64D07010	2001-04-22	2261
		O64D07020	2001-04-22	2906
	<i>IUE</i>	LWR05515LL	1979-09-06	1800
NGC 7293	<i>FUSE</i>	C1770401000	2002-10-02	8747
	<i>STIS</i>	O64D05010	2000-11-18	2265
		O64D05020	2000-11-18	2900
	<i>IUE</i>	LWR15828LL	1983-04-28	840
PuWe 1	<i>FUSE</i>	U1020601000	2007-02-11	9219
	<i>IUE</i>	SWP15894LL	1981-12-28	2700
		LWR12231LL	1981-12-28	9000
Sh 2-174	<i>FUSE</i>	B0520401000	2001-09-08	5289
		G0030307000	2006-08-29	17811
	<i>STIS</i>	O5F201010	1999-10-12	2788
		O5F201020	1999-10-12	3271
		O5F202010	1999-10-13	2788
	<i>IUE</i>	SWP52696LL	1994-10-31	960
		LWR16162LL	1983-06-14	2400

APPENDIX C

Solar abundances

Table C.1: Solar abundances for H to Ni used in our calculations, taken from Asplund et al. (2009). “A” denotes the atomic number, “ATW” the atomic weight, and $\log \epsilon = \log(N_X/N_H) + 12.00$ for the element X.

Atom (X)	A	ATW	$\log \epsilon$	n(X)/n(H) (by number)	n(X)/n(He) (by number)	mass fraction
H	1	1.0079	12.00	1.000E+00	1.175E+01	7.374E-01
He	2	4.0026	10.93	8.511E-02	1.000E+00	2.492E-01
C	6	12.0107	8.43	2.692E-04	3.162E-03	2.365E-03
N	7	14.0067	7.83	6.761E-05	7.943E-04	6.928E-04
O	8	15.9994	8.69	4.898E-04	5.754E-03	5.733E-03
F	9	18.9984	4.56	3.631E-08	4.266E-07	5.046E-07
Ne	10	20.1797	7.93	8.511E-05	1.000E-03	1.257E-03
Na	11	22.9898	6.24	1.738E-06	2.042E-05	2.923E-05
Mg	12	24.3050	7.60	3.981E-05	4.677E-04	7.079E-04
Al	13	26.9815	6.45	2.818E-06	3.311E-05	5.563E-05
Si	14	28.0855	7.51	3.236E-05	3.802E-04	6.649E-04
P	15	30.9738	5.41	2.570E-07	3.020E-06	5.825E-06
S	16	32.0650	7.12	1.318E-05	1.549E-04	3.092E-04
Ar	18	39.9480	6.40	2.512E-06	2.951E-05	7.341E-05
Ca	20	40.0780	6.34	2.188E-06	2.570E-05	6.415E-05
Sc	21	44.9559	3.15	1.413E-09	1.660E-08	4.646E-08
Ti	22	47.8670	4.95	8.913E-08	1.047E-06	3.121E-06
V	23	50.9415	3.93	8.511E-09	1.000E-07	3.172E-07
Cr	24	51.9961	5.64	4.365E-07	5.129E-06	1.660E-05
Mn	25	54.9380	5.43	2.692E-07	3.162E-06	1.082E-05
Fe	26	55.8450	7.50	3.162E-05	3.715E-04	1.292E-03
Co	27	58.9332	4.99	9.772E-08	1.148E-06	4.213E-06
Ni	28	58.6934	6.22	1.660E-06	1.950E-05	7.126E-05

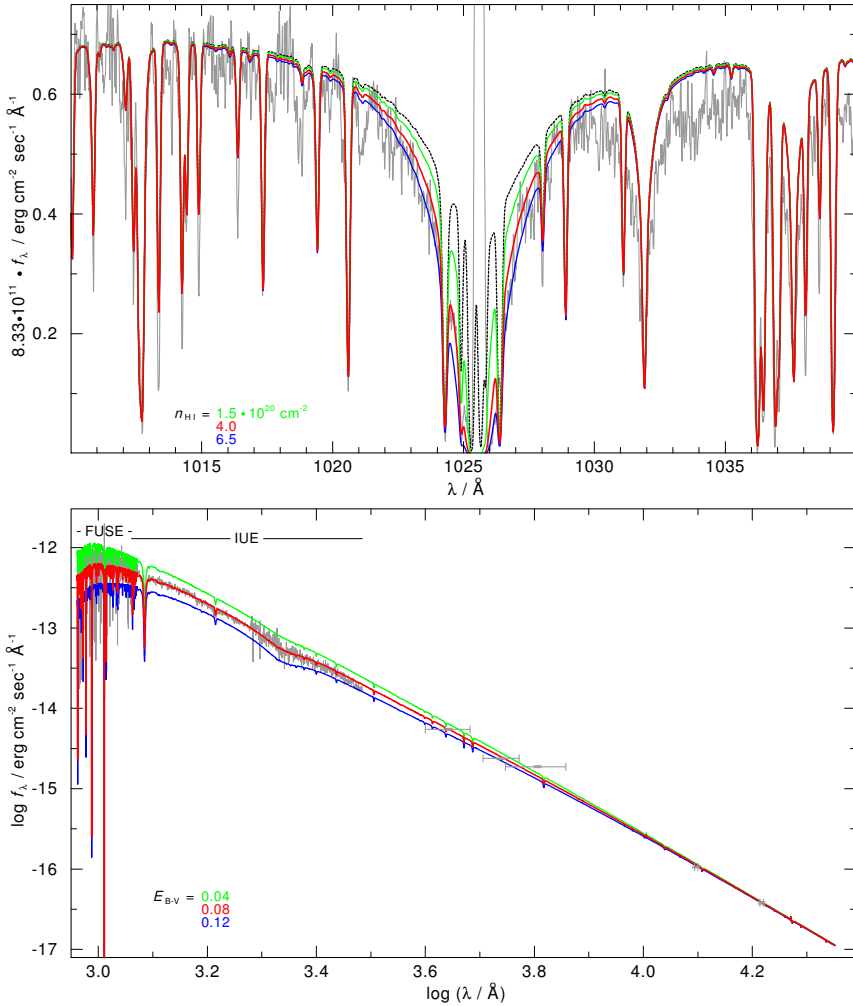
APPENDIX D

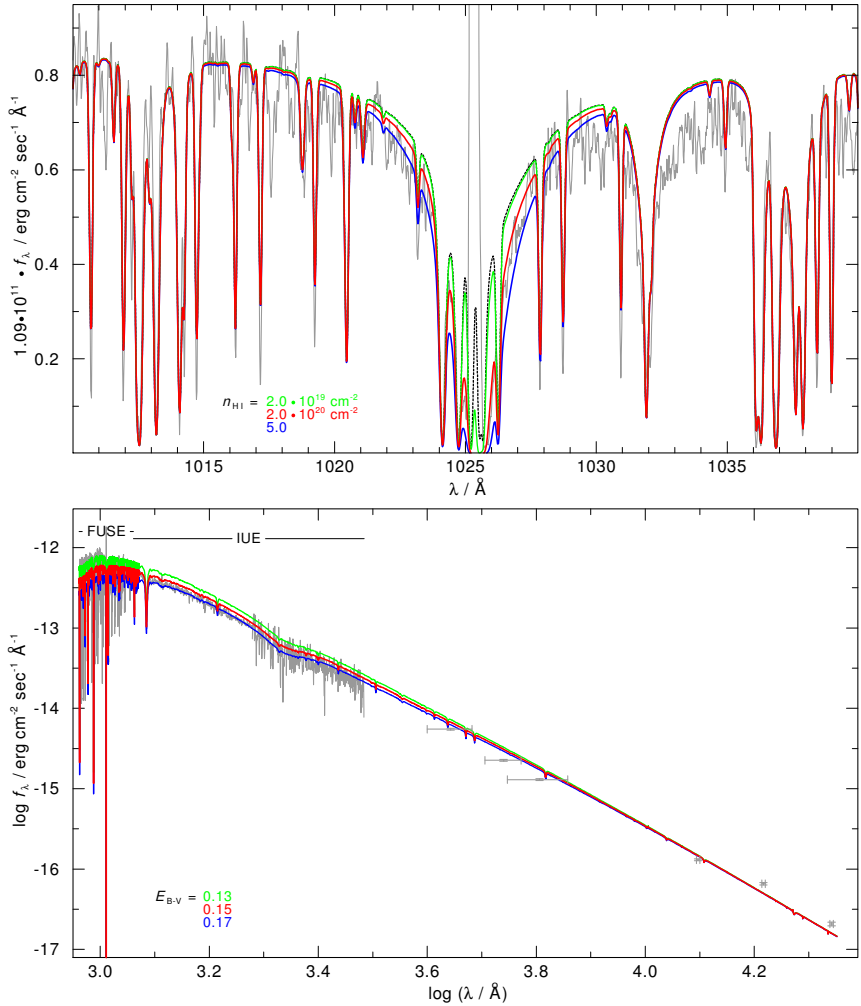
Determination of n_{HI} and $E_{\text{B-V}}$

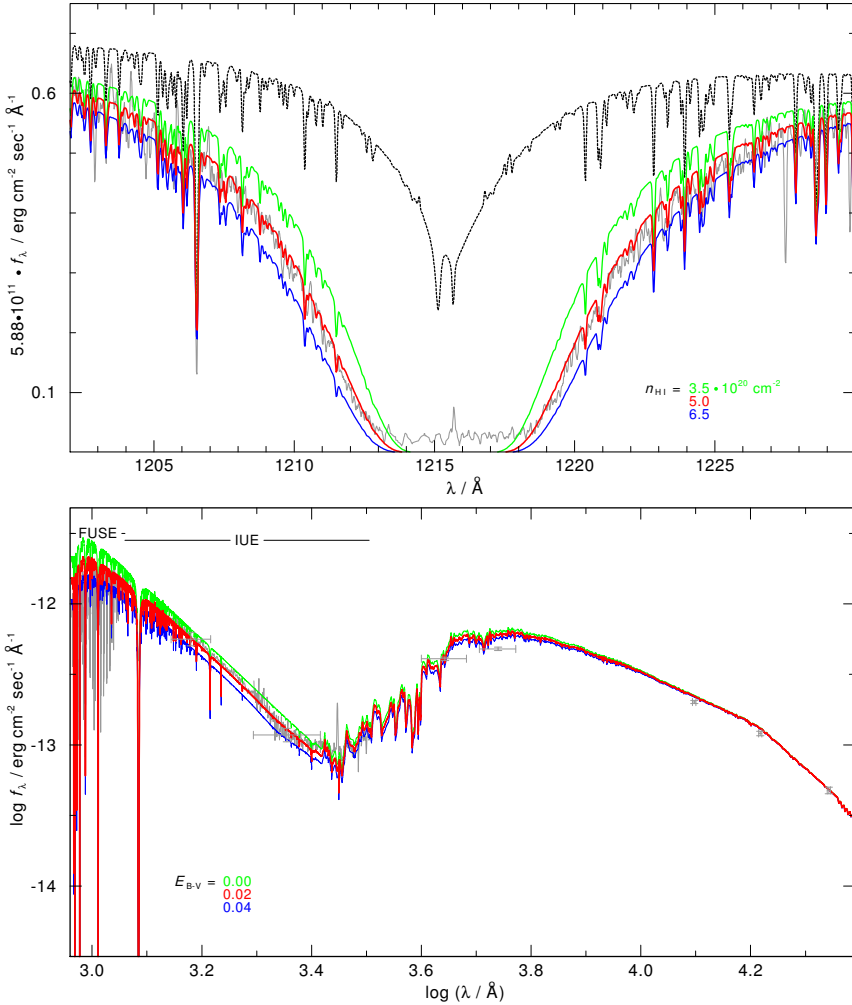
For each sample object plots for the determination of n_{HI} (top) and $E_{\text{B-V}}$ (bottom) are presented. All observations are coloured grey, the best fit value in red, upper limits in blue, lower limits in green. For n_{HI} an additional black dashed line shows the pure photospheric model SED without n_{HI} absorption.

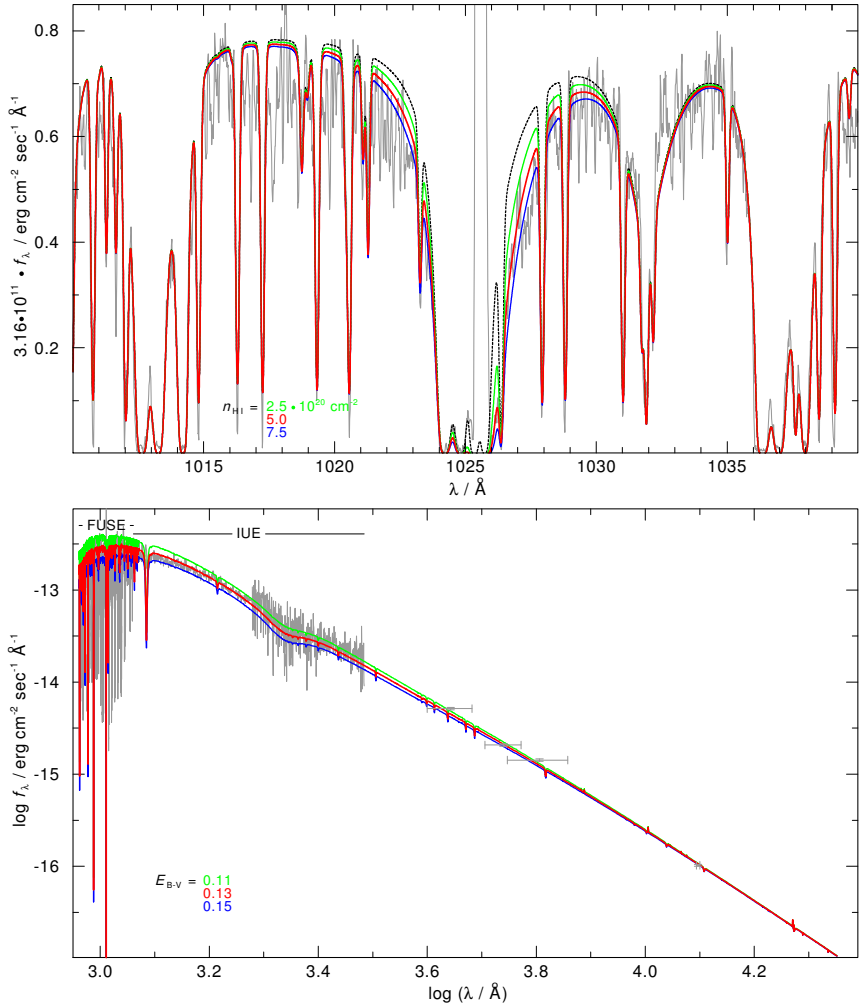
For clarity the model SEDs in the plots for the determination of $E_{\text{B-V}}$ are smoothed with a Gaussian of 0.1 and 7 Å for the *FUSE* and *IUE* observations, respectively. Photometric data was taken from the SIMBAD database. To normalize the model SEDs the photometric magnitudes with the longest wavelength was used as these are the least influenced by the reddening. However, for A 31 a normalization using the photometric magnitudes leads to bad fit of the flux of the *FUSE* range. In this case the necessary value for $E_{\text{B-V}}$ to match the flux in the *IUE* range is 0.15 ± 0.2 , which is too large for the FUV range. Therefore the flux is “normalized” in such a manner, that the FUV, UV and the photometric magnitudes are matched best.

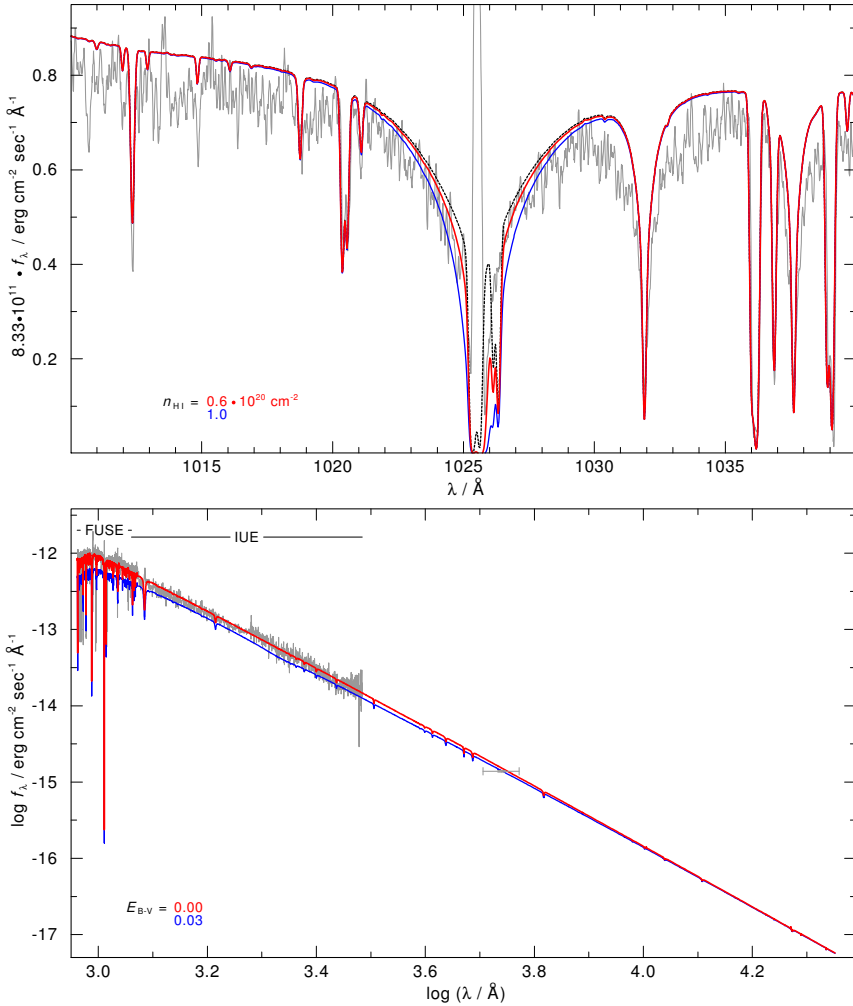
Some of the magnitudes for NGC 6720, NGC 6853, and PuWe 1 taken from the SIMBAD database display a strong deviation from the stellar flux. These measurements have not been centered on the CS but are rather targeted at the PN.

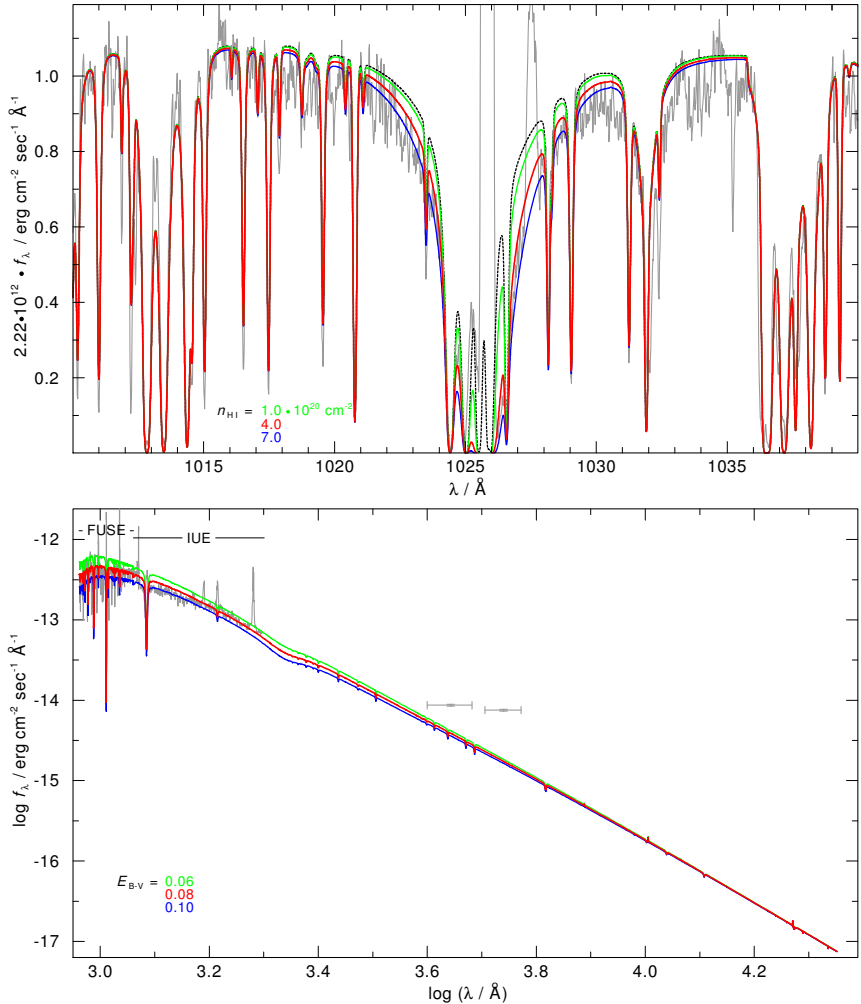
D.1 A 7, $T_{\text{eff}} = 109 \text{ kK}$, $\log g = 7.0$ Figure D.1: Top: Determination of n_{HI} ; bottom: $E_{\text{B-V}}$ for A 7.

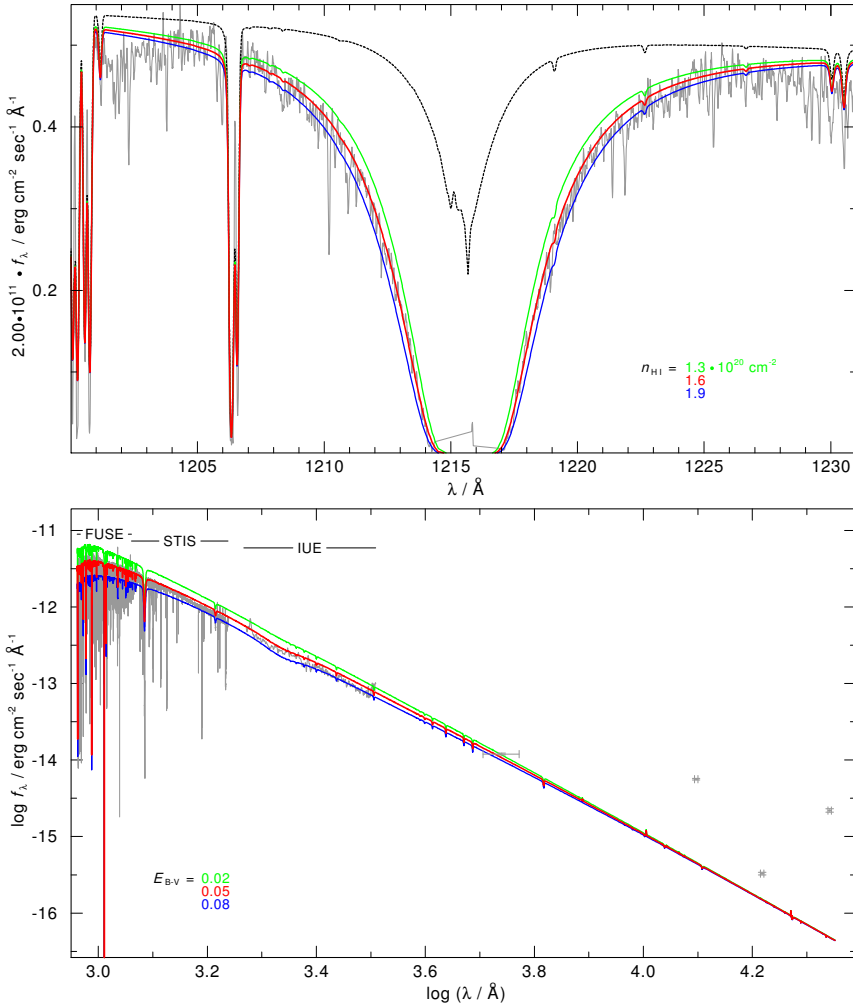
D.2 A 31, $T_{\text{eff}} = 114 \text{ kK}$, $\log g = 7.4$ Figure D.2: Top: Determination of n_{HI} ; bottom: $E_{\text{B-V}}$ for A 31.

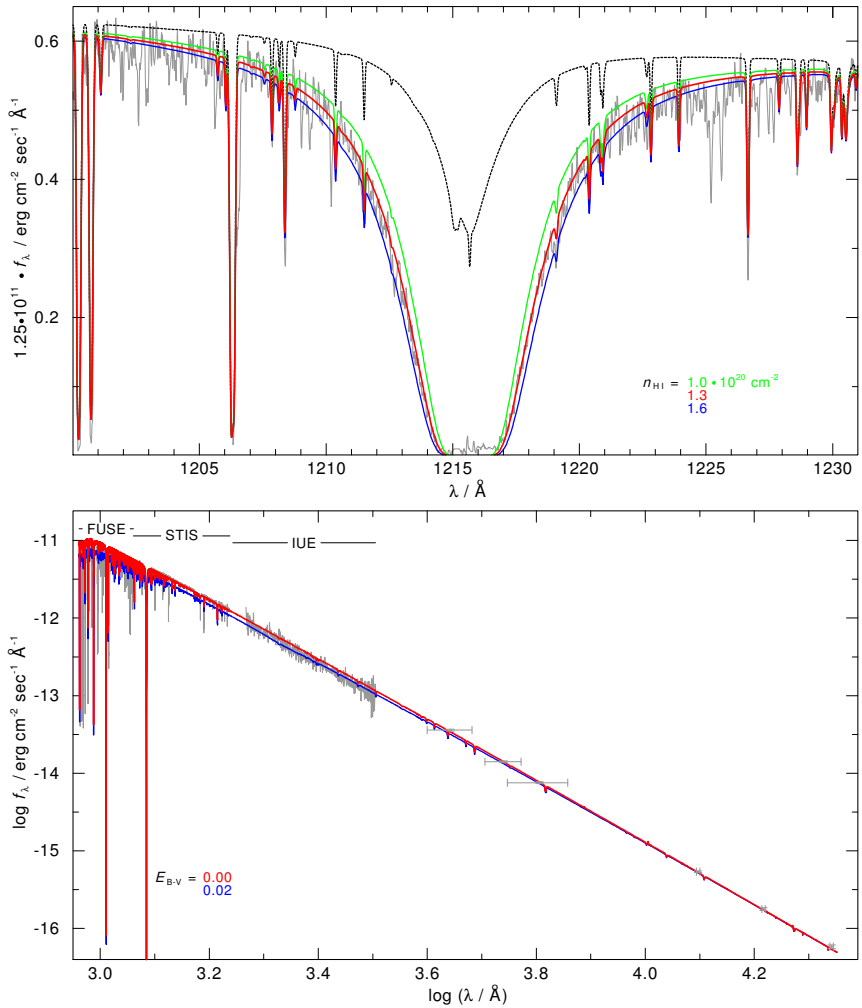
D.3 A 35, $T_{\text{eff}} = 80 \text{ kK}$, $\log g = 7.2$ Figure D.3: Top: Determination of n_{HI} ; bottom: $E_{\text{B-V}}$ for A 35.

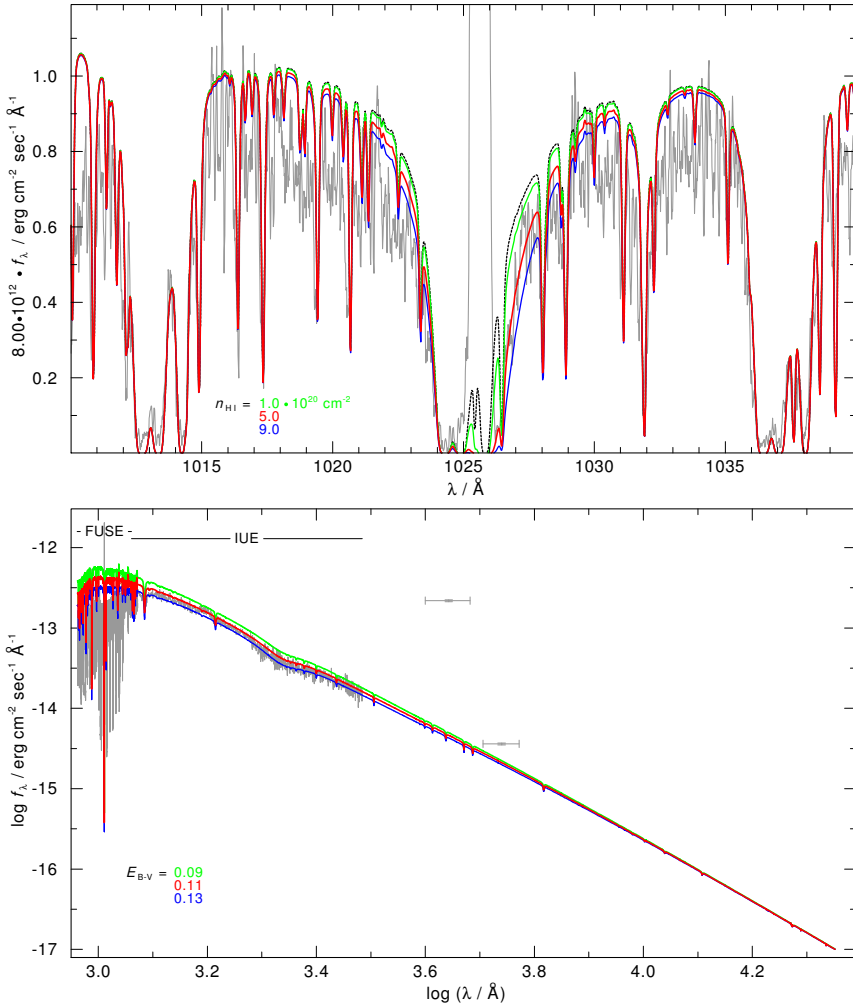
D.4 A 39, $T_{\text{eff}} = 117 \text{ kK}$, $\log g = 6.3$ Figure D.4: Top: Determination of n_{HI} ; bottom: $E_{\text{B-V}}$ for A 39.

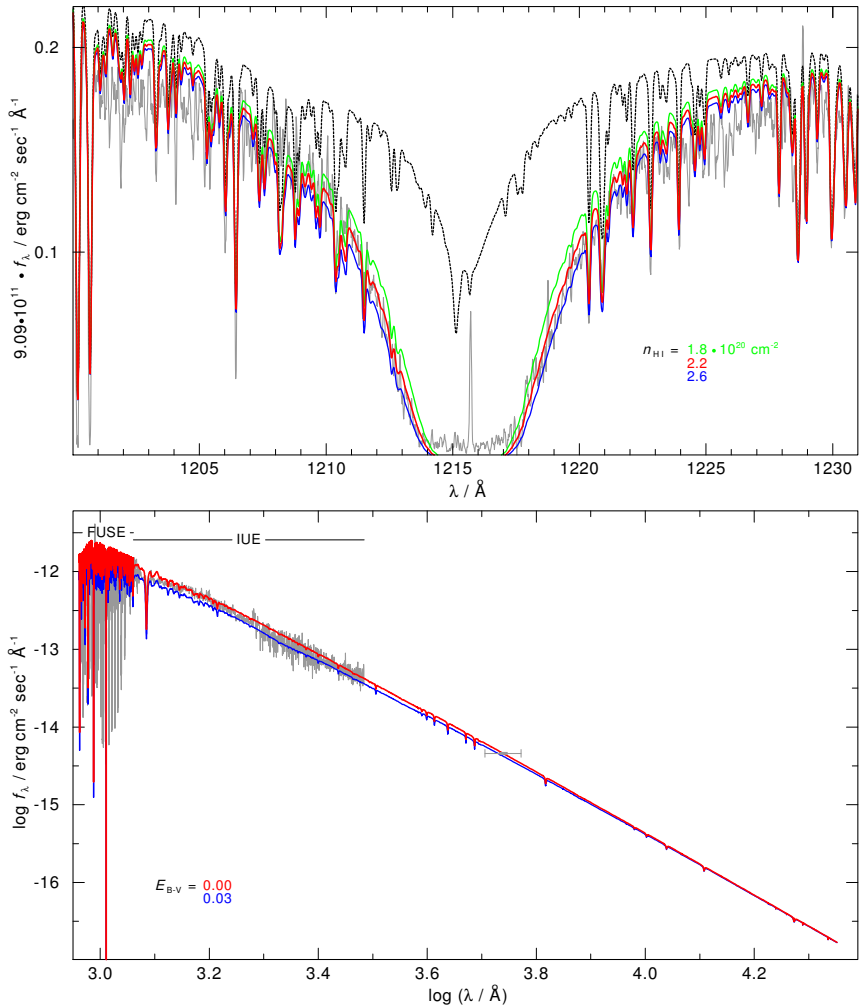
D.5 NGC 3587, $T_{\text{eff}} = 104 \text{ kK}$, $\log g = 7.0$ Figure D.5: Top: Determination of $n_{\text{H I}}$; bottom: $E_{\text{B-V}}$ for NGC 3587.

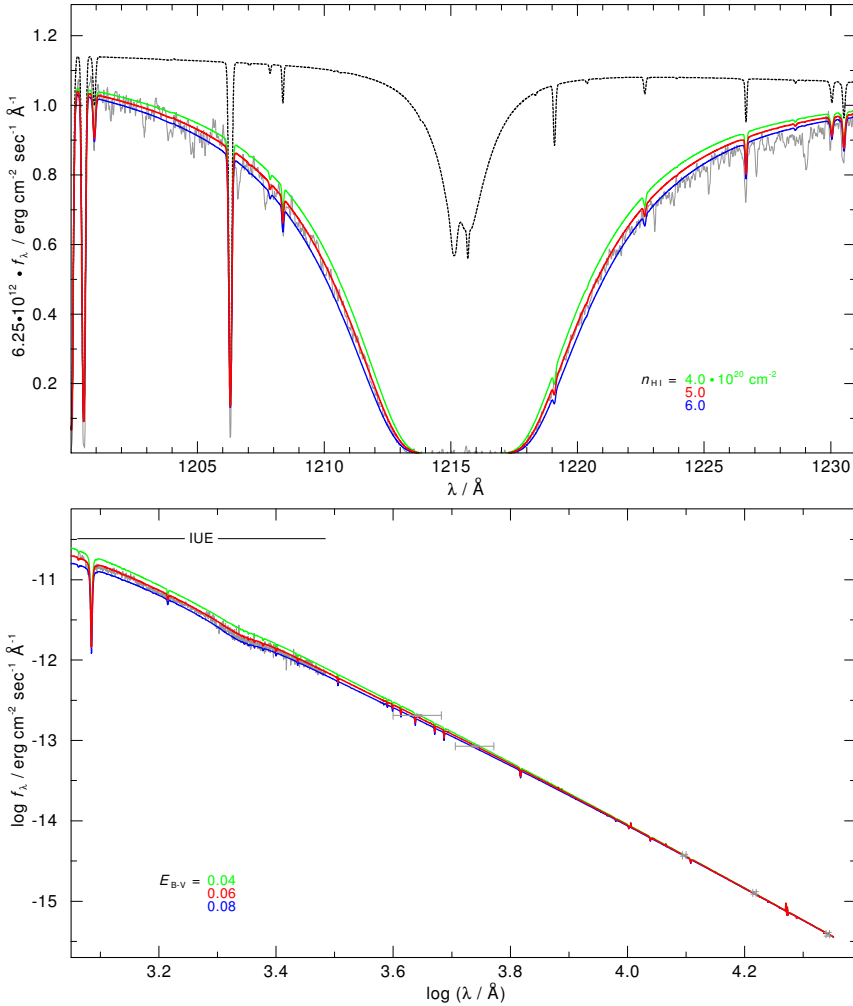
D.6 NGC 6720, $T_{\text{eff}} = 130 \text{ kK}$, $\log g = 6.9$ Figure D.6: Top: Determination of n_{HI} ; bottom: $E_{\text{B-V}}$ for NGC 6720.

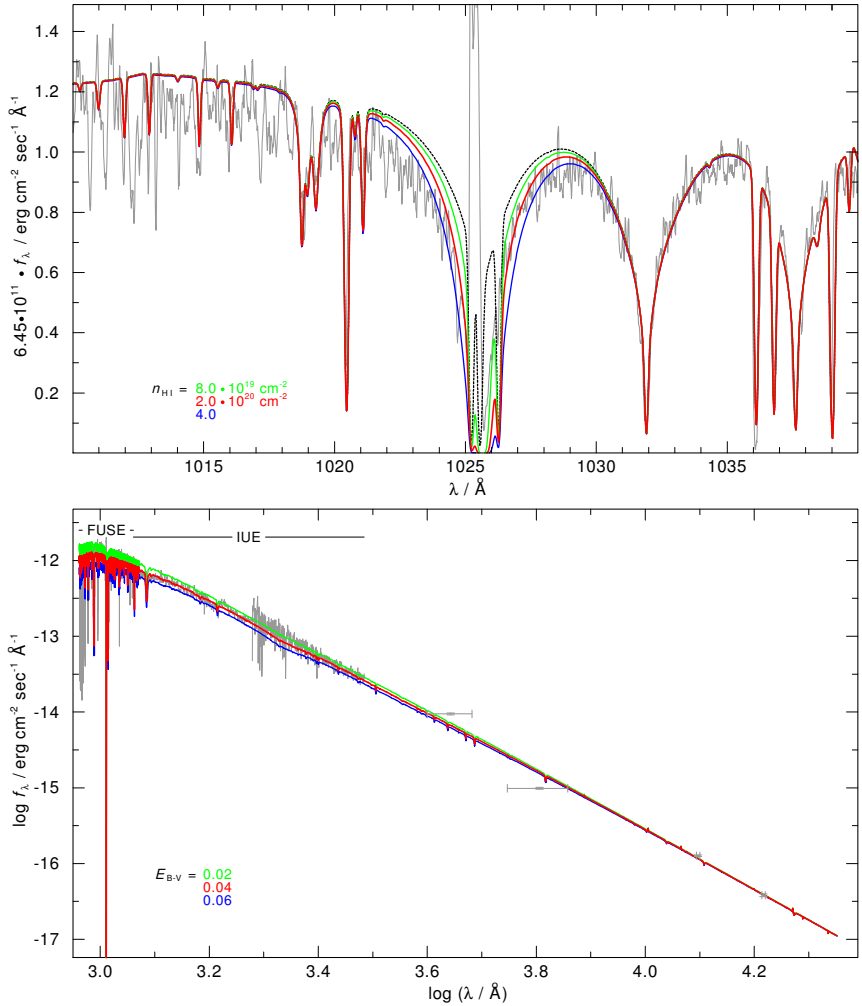
D.7 NGC 6853, $T_{\text{eff}} = 136 \text{ kK}$, $\log g = 6.5$ Figure D.7: Top: Determination of n_{HI} ; bottom: E_{B-V} for NGC 6853.

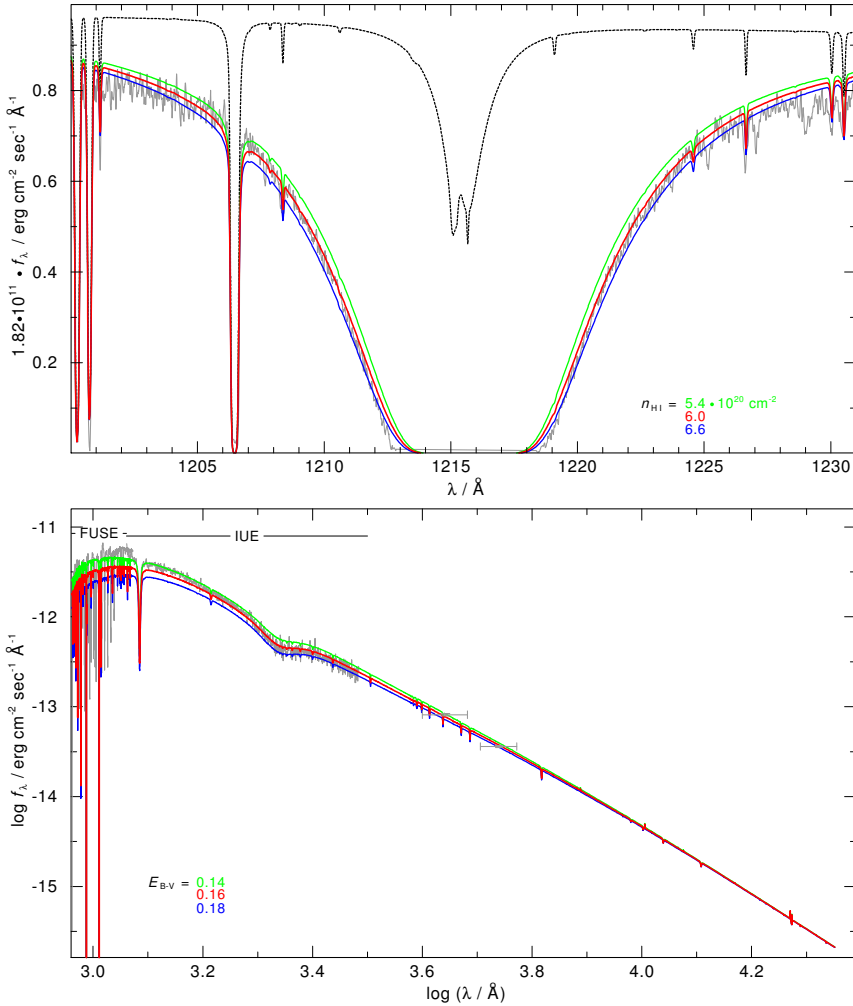
D.8 NGC 7293, $T_{\text{eff}} = 120 \text{ kK}$, $\log g = 6.8$ Figure D.8: Top: Determination of n_{HI} ; bottom: $E_{\text{B-V}}$ for NGC 7293.

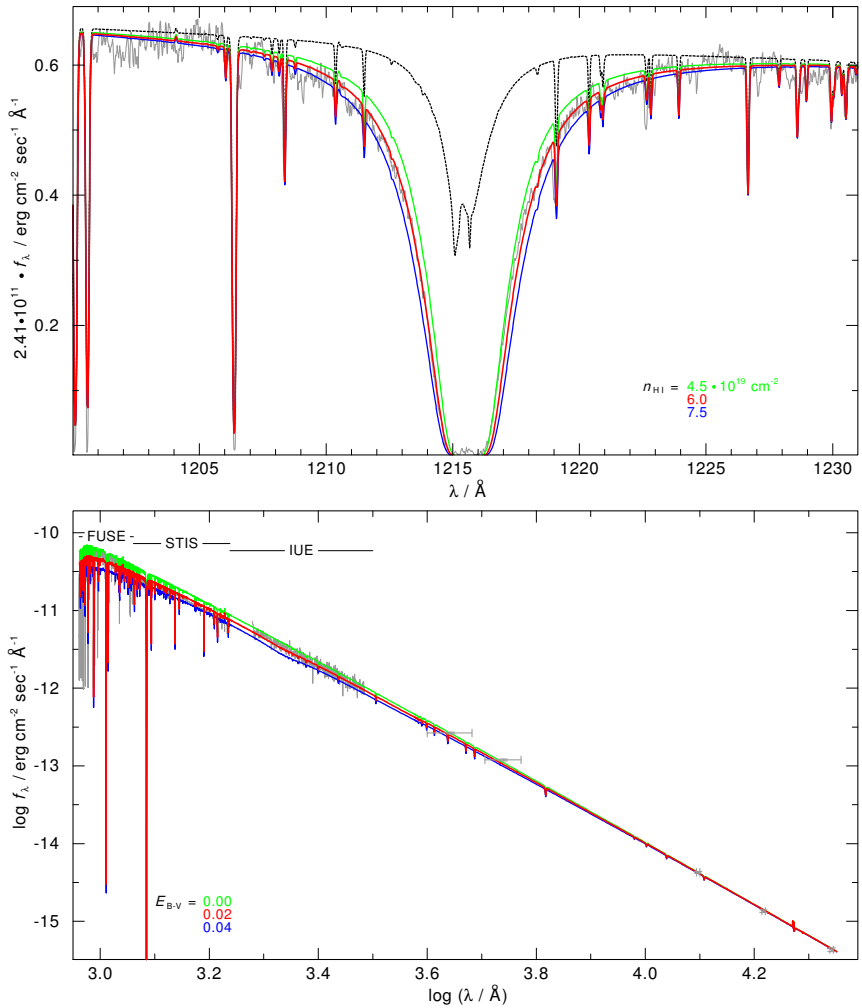
D.9 PuWe 1, $T_{\text{eff}} = 94 \text{ kK}$, $\log g = 7.0$ Figure D.9: Top: Determination of n_{HI} ; bottom: $E_{\text{B-V}}$ for PuWe 1.

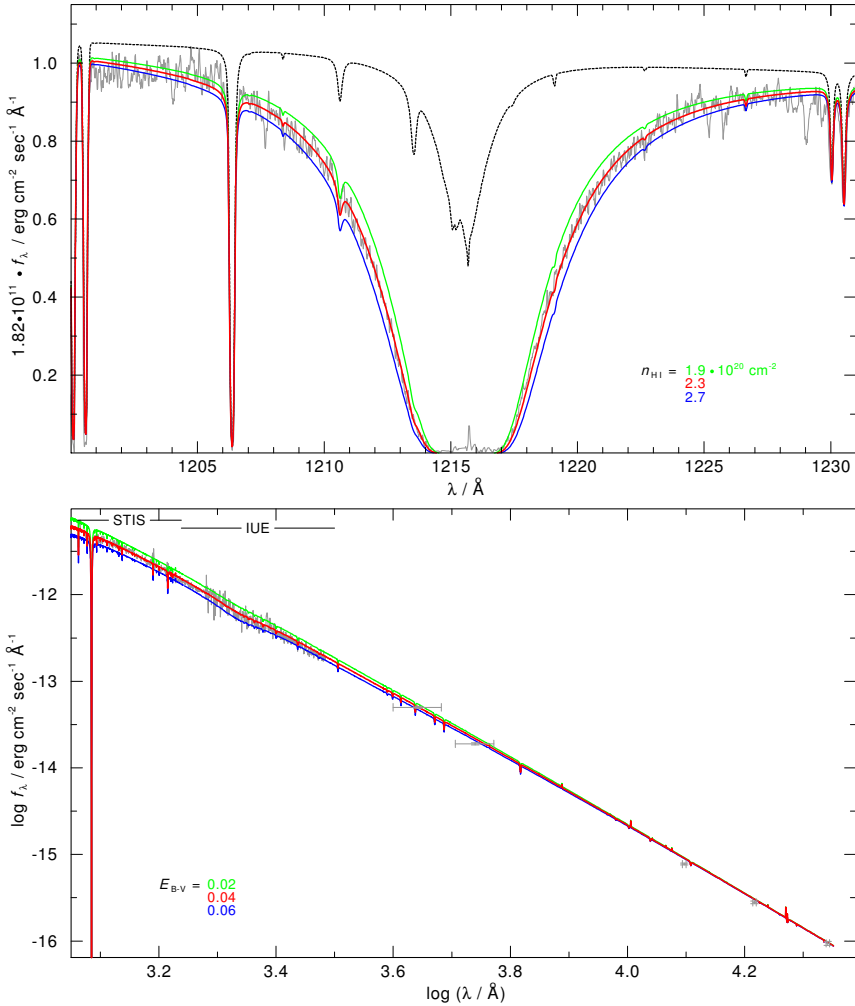
D.10 Sh 2 – 174, $T_{\text{eff}} = 69 \text{ kK}$, $\log g = 6.7$ Figure D.10: Top: Determination of n_{HI} ; bottom: $E_{\text{B-V}}$ for Sh 2 – 174.

D.11 A 36, $T_{\text{eff}} = 108 \text{ kK}$, $\log g = 5.9$ Figure D.11: Top: Determination of $n_{\text{H I}}$; bottom: $E_{\text{B-V}}$ for A 36.

D.12 Lo 1, $T_{\text{eff}} = 120 \text{ kK}$, $\log g = 7.0$ Figure D.12: Top: Determination of n_{HI} ; bottom: $E_{\text{B-V}}$ for Lo 1.

D.13 LSS 1362, $T_{\text{eff}} = 106 \text{ kK}$, $\log g = 5.6$ Figure D.13: Top: Determination of $n_{\text{H I}}$; bottom: $E_{\text{B-V}}$ for LSS 1362.

D.14 NGC 1360, $T_{\text{eff}} = 100 \text{ kK}$, $\log g = 5.7$ Figure D.14: Top: Determination of n_{HI} ; bottom: $E_{\text{B-V}}$ for NGC 1360.

D.15 NGC 4361, $T_{\text{eff}} = 126 \text{ kK}$, $\log g = 6.0$ Figure D.15: Top: Determination of n_{HI} ; bottom: $E_{\text{B-V}}$ for NGC 4361.

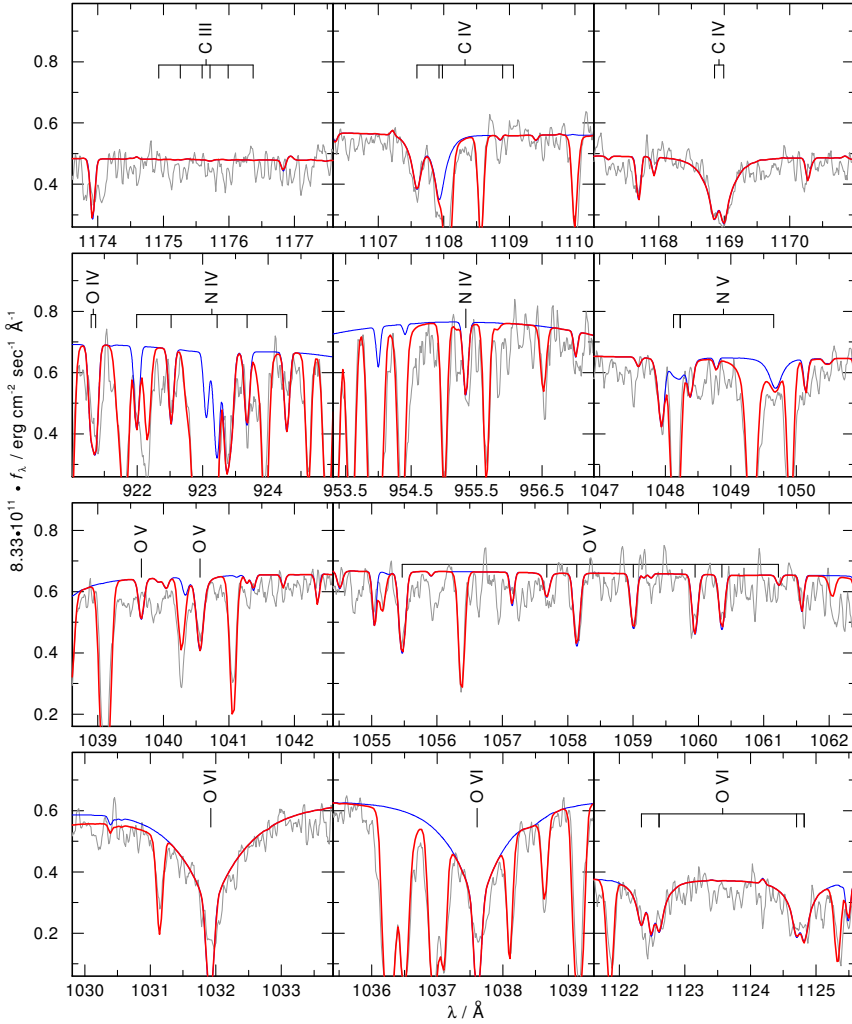
APPENDIX E

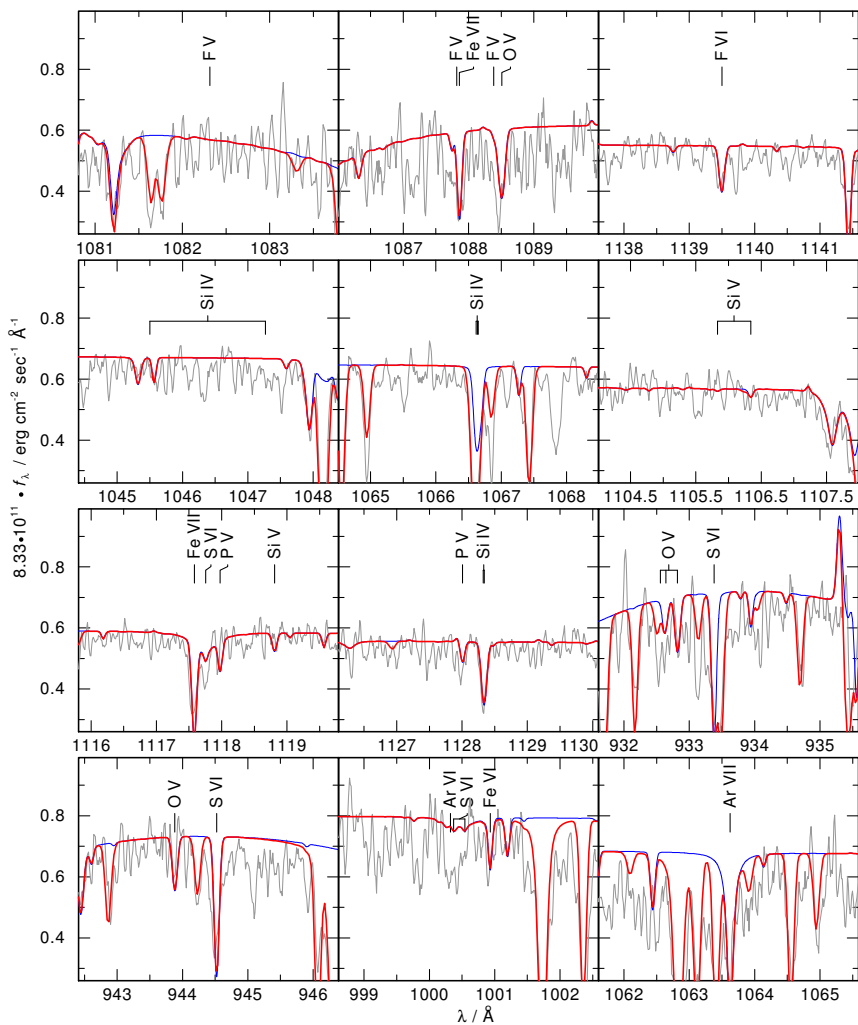
Line fits for individual elements and abundances

This chapter presents fits for individual lines for all objects. In all plots the observations are displayed in grey, the pure photospheric model SEDs in blue, and the combined photospheric + ISM models SEDs in red.

The first page of an object with available *FUSE* data shows a selection of C, N, and O lines for different ionization stages. If *STIS* data was available the He II λ 1640.42Å line is shown in addition to the C, N, and O lines in the *STIS* range. The metal elements from F – Ar are presented on the second page. For the *FUSE* range F, Si, P, S, and Ar lines are presented. A sample of Ne, Mg, Al, Si, and Ar lines is shown for the *STIS* wavelength range. For some elements (Mg, Al) only upper limits can be determined. For the iron-group elements we show lines of three successive ionizations stages for Fe. Most objects did not exhibit lines of other iron-group elements.

For each object the final abundances (Tab. E.1 – Tab. E.15) are given in mass fraction, number fraction, $\log \epsilon = \log(N_X/N_H) + 12.00$ for the element X as well as [X]. The latter is defined as $[X] = \log [\text{mass fraction}/\text{solar mass fraction}]$ for species X. The solar values are taken from Asplund et al. (2009) and are displayed in Tab. C.1. Abundances that were obtained by individual line fitting are marked with “*”. Note that only lines of interest are labeled in the according sections due to clarity.

E.1 A 7, $T_{\text{eff}} = 109 \text{ kK}$, $\log g = 7.0$ Figure E.1: C, N, and O lines in the *FUSE* observation of A 7.

Figure E.2: F, Si, P, S, and Ar lines in the $FUSE$ observation of A 7.

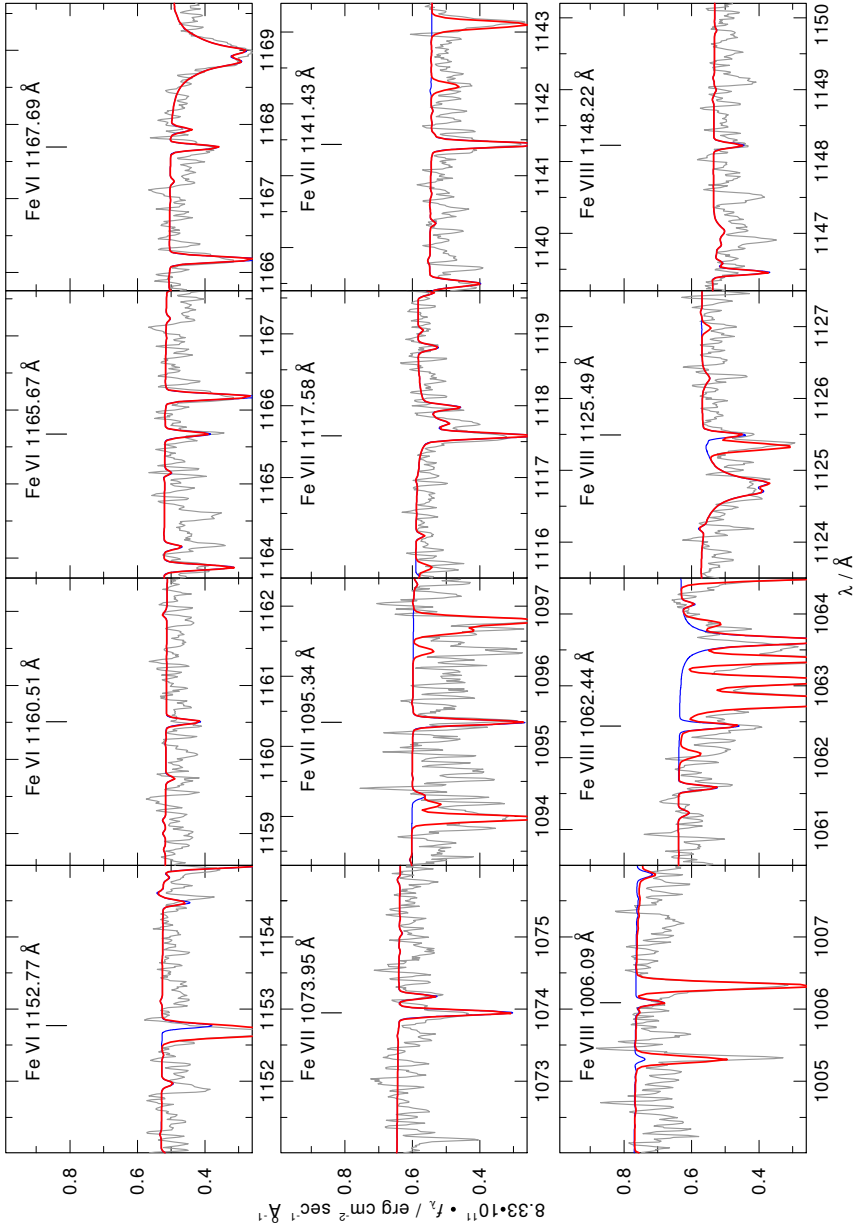
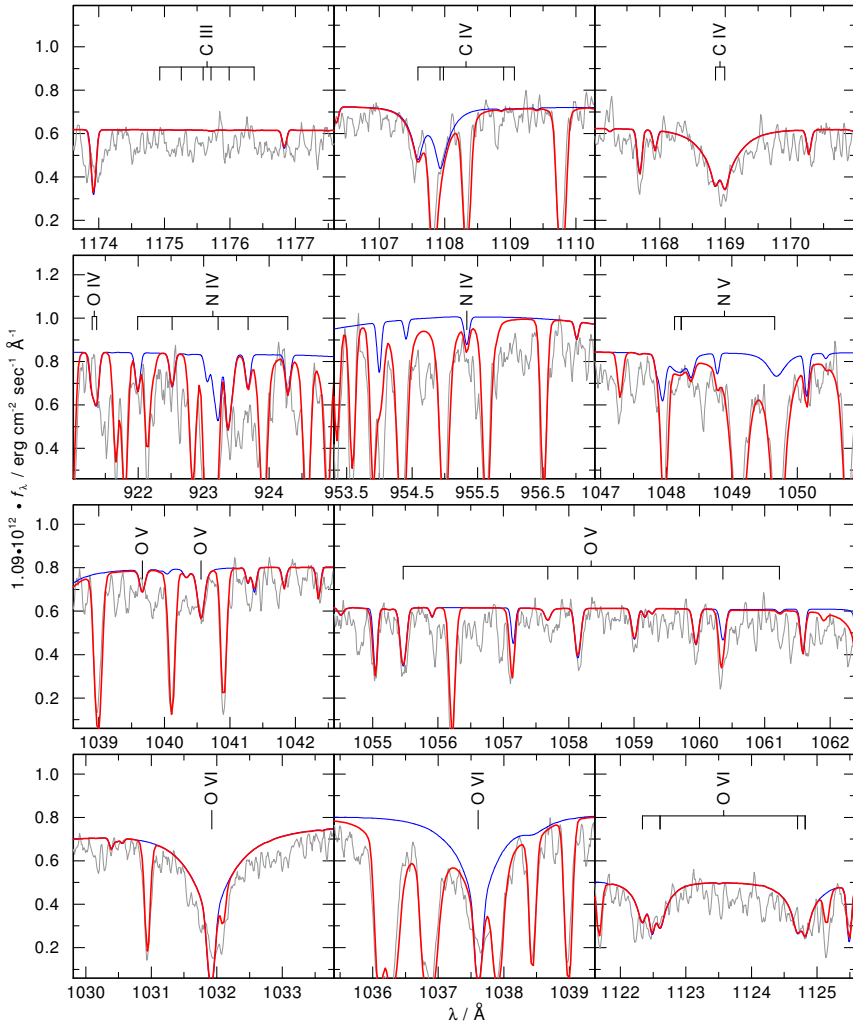
Figure E.3: Fe VI–VIII lines in the *FUSE* observation of A 7.

Table E.1: Abundances of A 7

element (X)	mass fraction	number fraction	$\log \epsilon$	[X]	
H	7.3498E-01	9.2074E-01	12.013	-0.001	
He	2.4838E-01	7.8356E-02	10.943	-0.001	
C	1.1823E-03	1.2430E-04	8.143	-0.301	*
N	3.4467E-04	3.1072E-05	7.541	-0.303	*
O	5.5299E-03	4.3643E-04	8.689	-0.016	*
F	1.3541E-06	8.9997E-08	5.003	0.429	*
Ne	1.2447E-03	7.7886E-05	7.940	-0.004	
Na	2.8945E-05	1.5898E-06	6.250	-0.004	
Mg	7.0099E-04	3.6418E-05	7.610	-0.004	
Al	5.5090E-05	2.5781E-06	6.460	-0.004	
Si	3.9666E-04	1.7834E-05	7.300	-0.224	*
P	8.0922E-07	3.2989E-08	4.567	-0.857	
S	3.2197E-05	1.2679E-06	6.152	-0.982	*
Ar	1.0436E-03	3.2987E-05	7.567	1.153	
Ca	6.3524E-05	2.0013E-06	6.350	-0.004	
Sc	4.6002E-08	1.2921E-09	3.160	-0.004	
Ti	3.0884E-06	8.1470E-08	4.960	-0.005	
V	3.1411E-07	7.7860E-09	3.940	-0.004	
Cr	1.6437E-05	3.9916E-07	5.650	-0.004	
Mn	1.0714E-05	2.4625E-07	5.440	-0.004	
Fe	5.9153E-03	1.3374E-04	8.175	0.661	*
Co	4.1721E-06	8.9391E-08	5.000	-0.004	
Ni	7.0564E-05	1.5177E-06	6.230	-0.004	

E.2 A 31, $T_{\text{eff}} = 114 \text{ kK}$, $\log g = 7.4$ Figure E.4: C, N, and O lines in the *FUSE* observation of A 31.

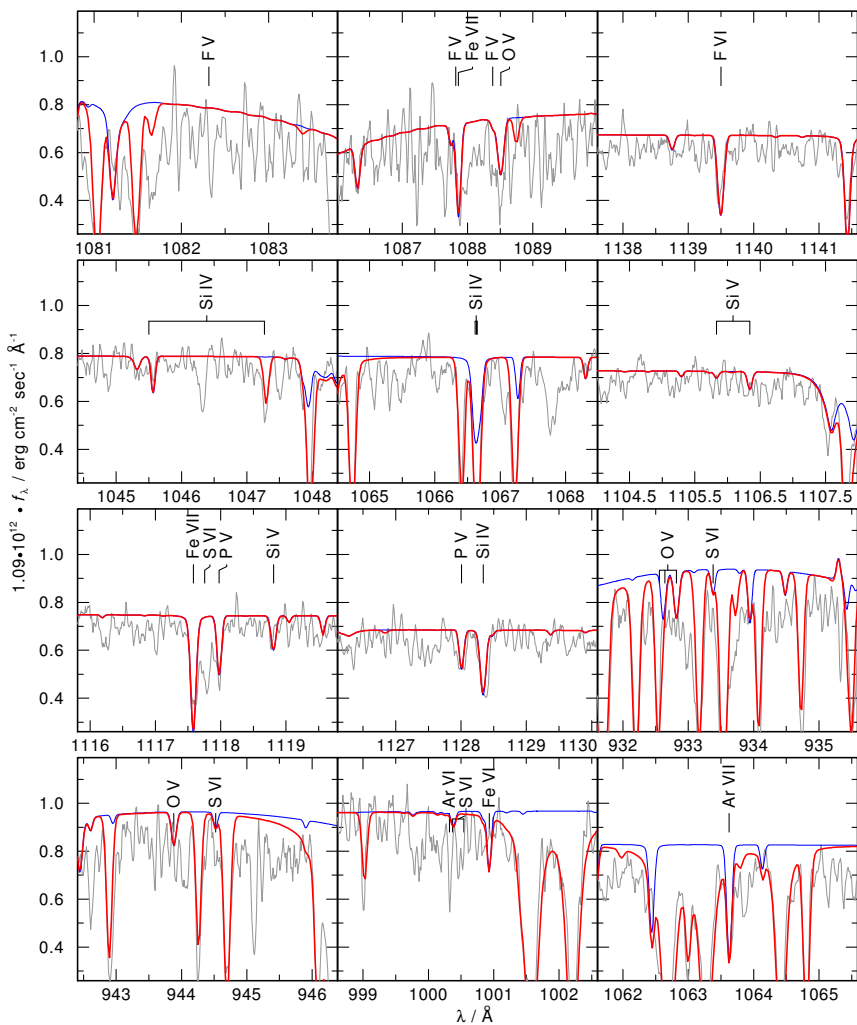


Figure E.5: F, Si, P, S, and Ar lines in the *FUSE* observation of A 31.

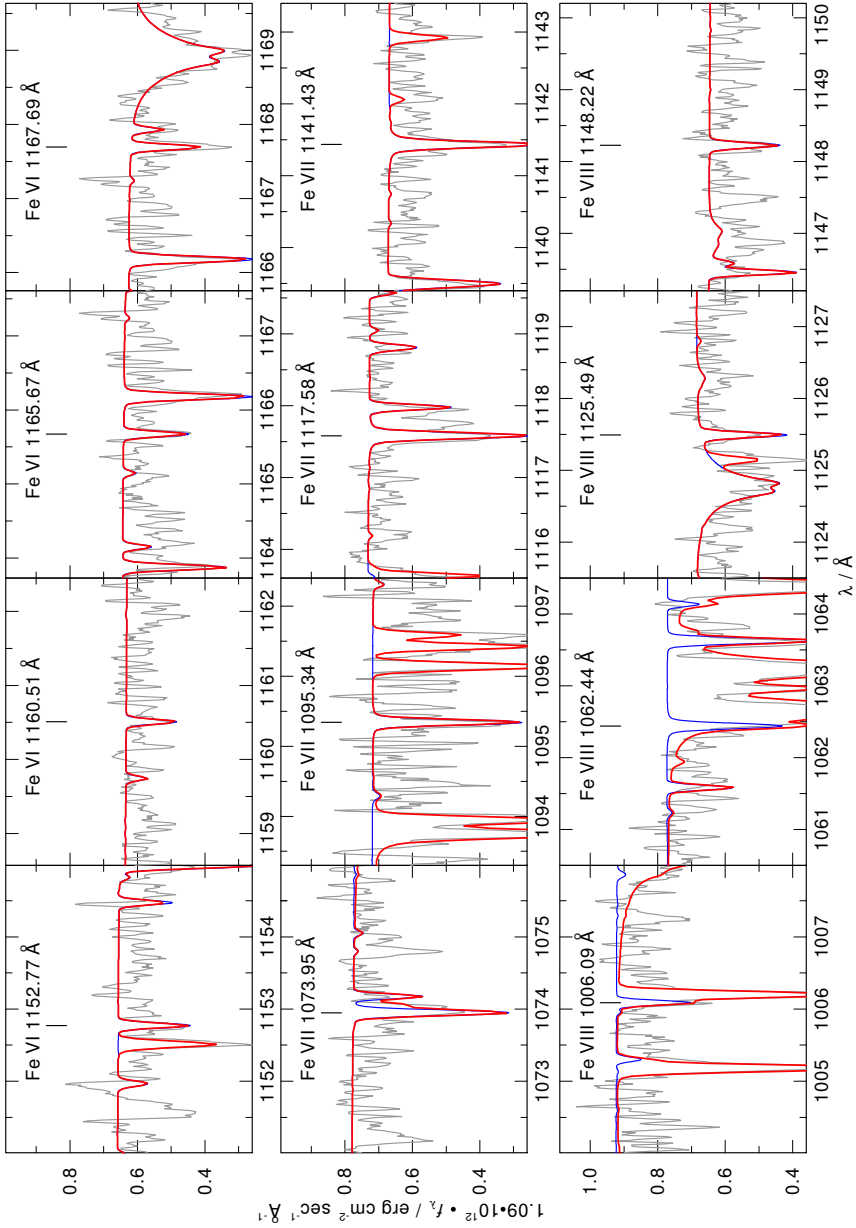
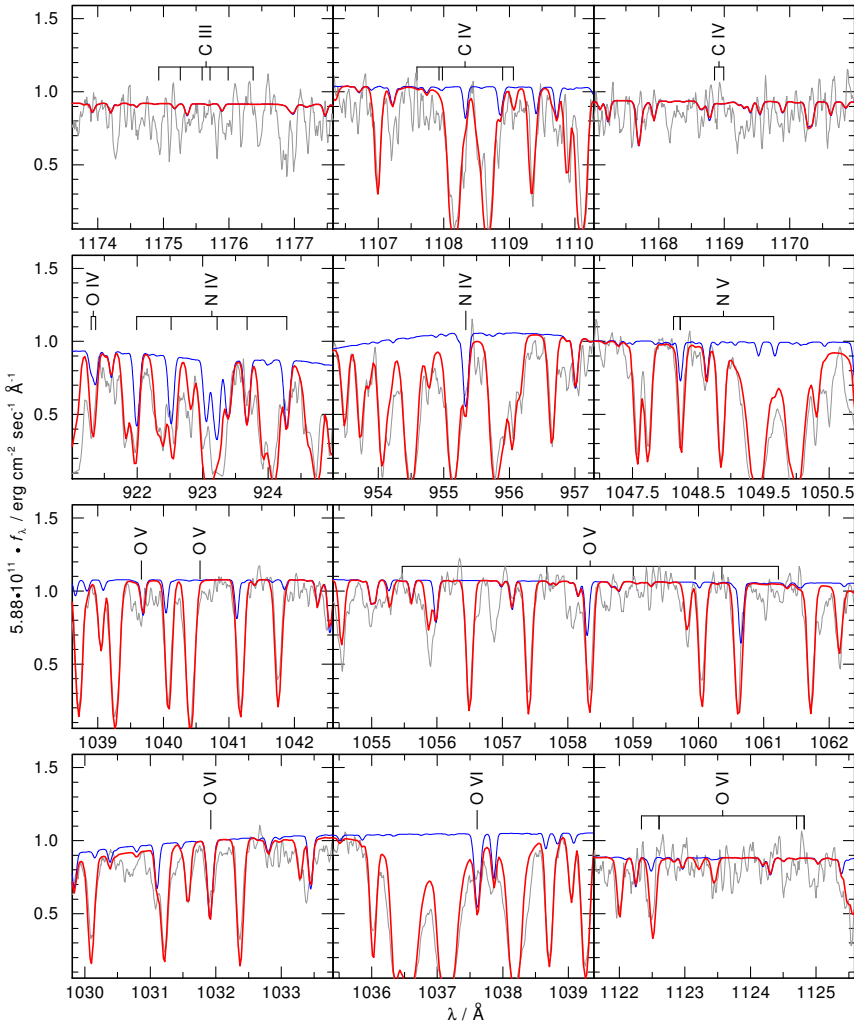
Figure E.6: Fe VI– VIII lines in the *FUSE* observation of A 31.

Table E.2: Abundances of A 31

element (X)	mass fraction	number fraction	$\log \epsilon$	[X]	
H	6.9419E-01	9.0796E-01	11.988	-0.026	
He	2.7567E-01	9.0796E-02	10.988	0.044	
C	2.3637E-03	2.5945E-04	8.444	0.000	*
N	5.2589E-04	4.9498E-05	7.725	-0.120	
O	3.3498E-03	2.7602E-04	8.471	-0.233	*
F	8.6282E-06	5.9873E-07	5.807	1.233	*
Ne	1.2594E-03	8.2276E-05	7.945	0.001	
Na	2.9286E-05	1.6794E-06	6.255	0.001	
Mg	7.0925E-04	3.8471E-05	7.615	0.001	
Al	5.5739E-05	2.7235E-06	6.465	0.001	
Si	9.0973E-04	4.2702E-05	7.660	0.136	*
P	5.4868E-06	2.3353E-07	5.398	-0.026	*
S	2.8397E-07	1.1675E-08	4.097	-3.037	
Ar	3.0237E-05	9.9787E-07	6.029	-0.385	*
Ca	6.4273E-05	2.1141E-06	6.355	0.001	
Sc	4.6545E-08	1.3649E-09	3.165	0.001	
Ti	3.1248E-06	8.6062E-08	4.965	0.001	
V	3.1782E-07	8.2248E-09	3.945	0.001	
Cr	1.6630E-05	4.2166E-07	5.655	0.001	
Mn	1.0840E-05	2.6013E-07	5.445	0.001	
Fe	2.0731E-02	4.8935E-04	8.720	1.205	*
Co	4.2213E-06	9.4435E-08	5.005	0.001	
Ni	7.1396E-05	1.6032E-06	6.235	0.001	

E.3 A 35, $T_{\text{eff}} = 80 \text{ kK}$, $\log g = 7.2$ Figure E.7: C, N, and O lines in the *FUSE* observation of A 35.

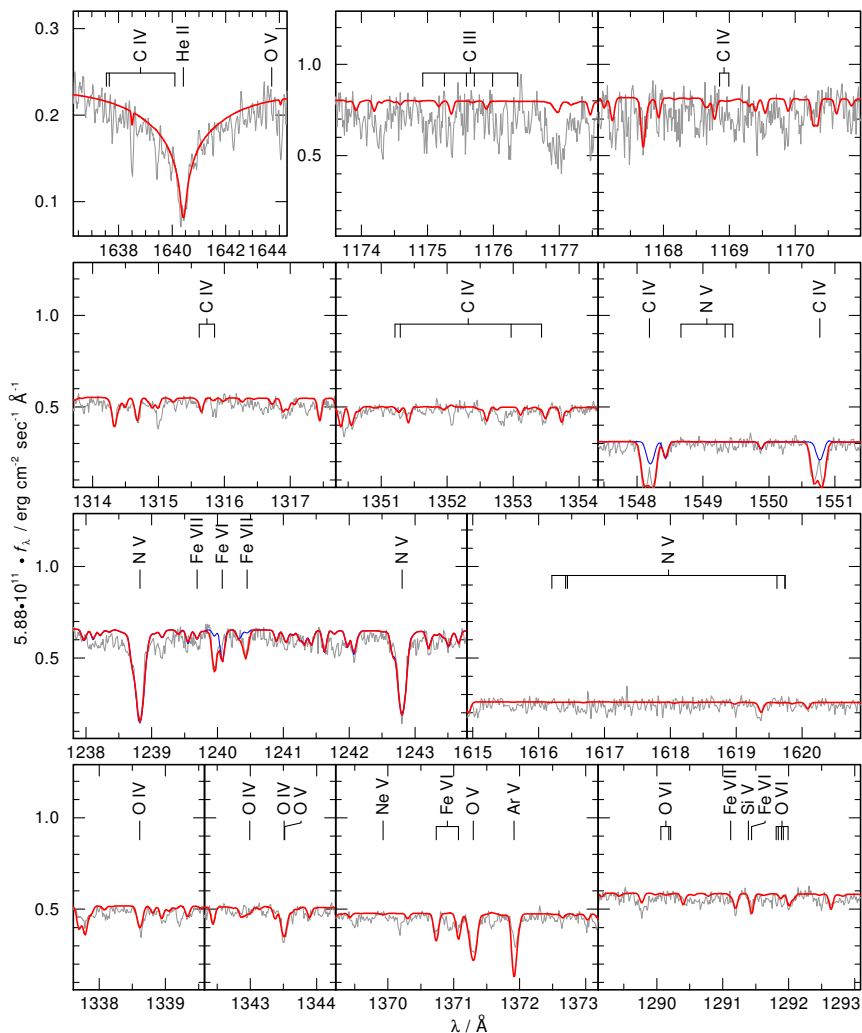


Figure E.8: He, C, N, and O lines in the STIS observation of A 35.

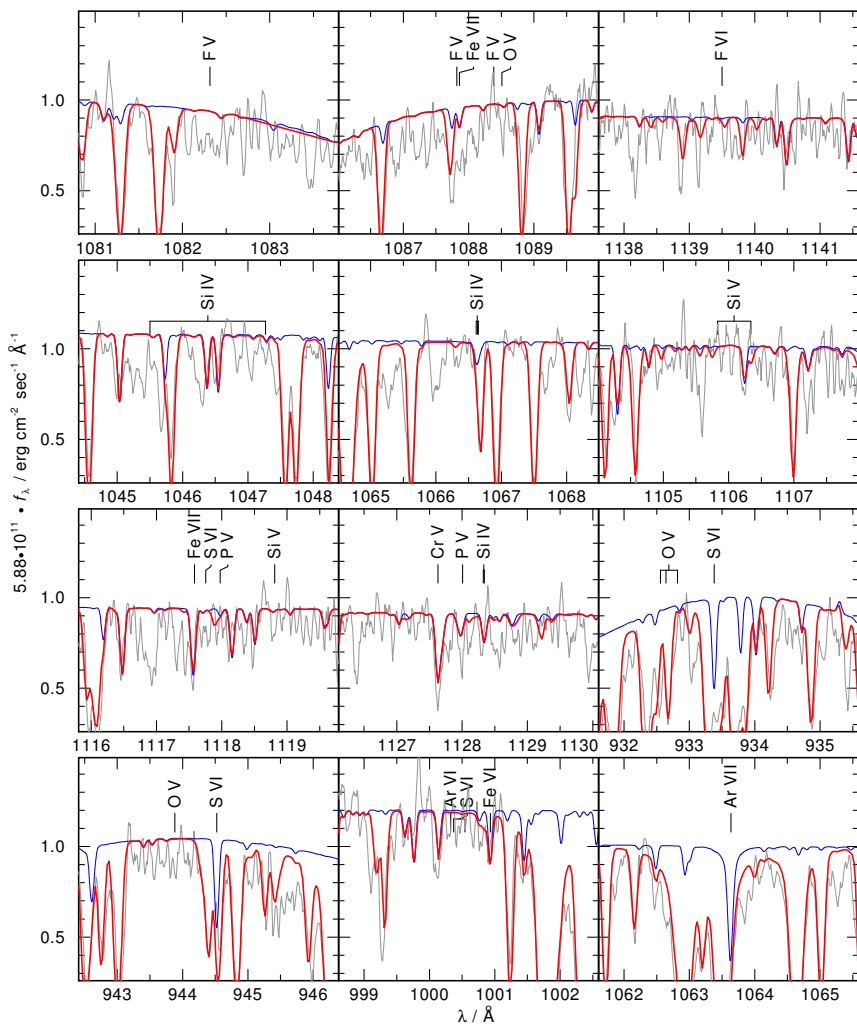


Figure E.9: F, Si, P, S, and Ar lines in the *FUSE* observation of A 35.

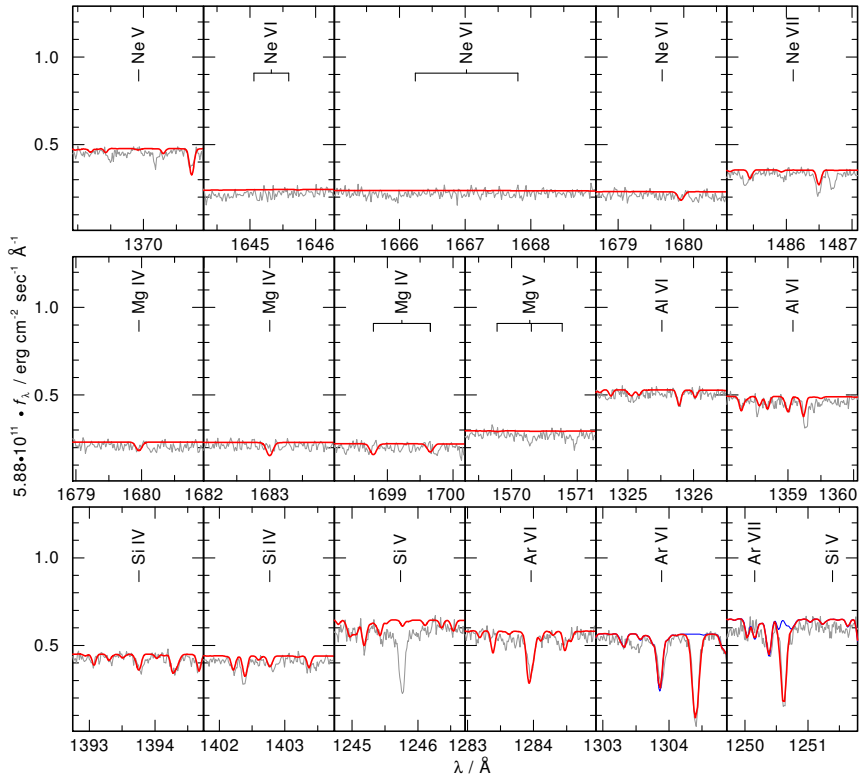


Figure E.10: Ne, Mg, Al, Si, and Ar lines in the *STIS* observation of A 35.

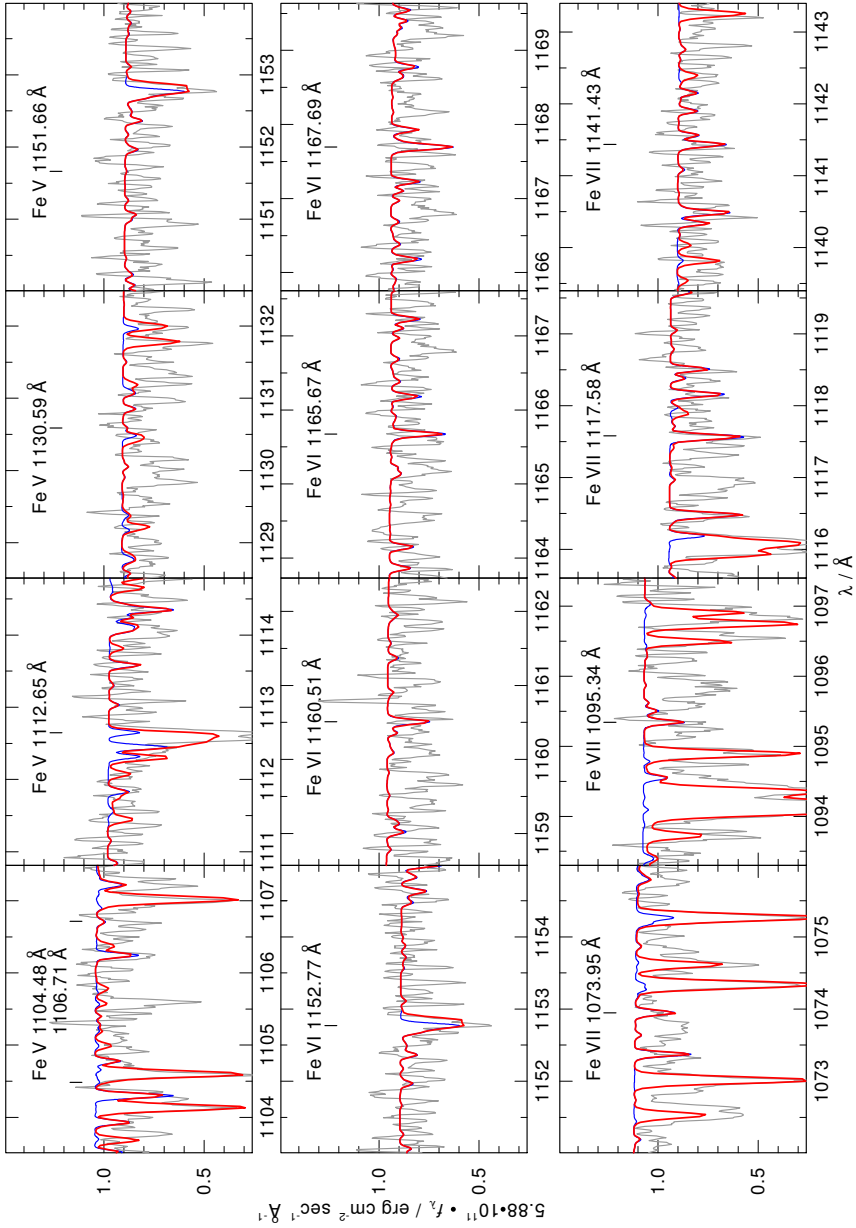


Figure E.11: Fe v – vii lines in the *FUSE* observation of A 35.

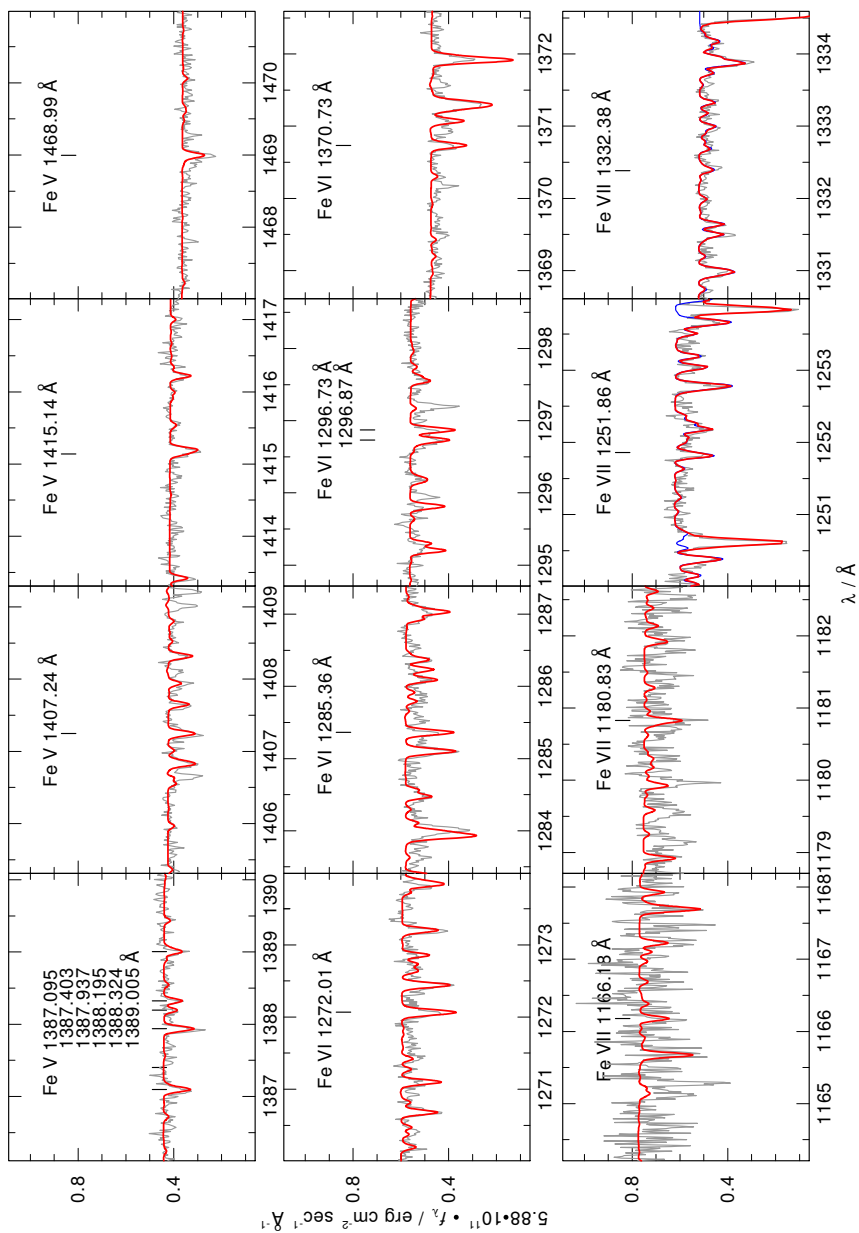
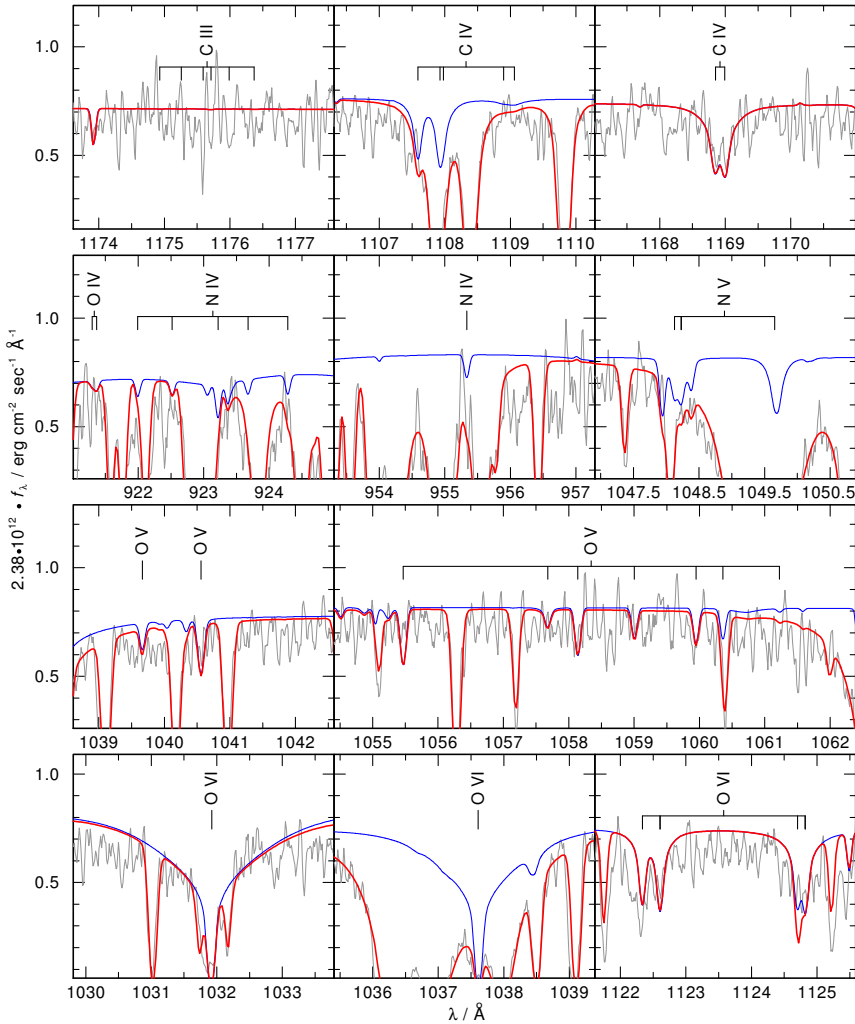
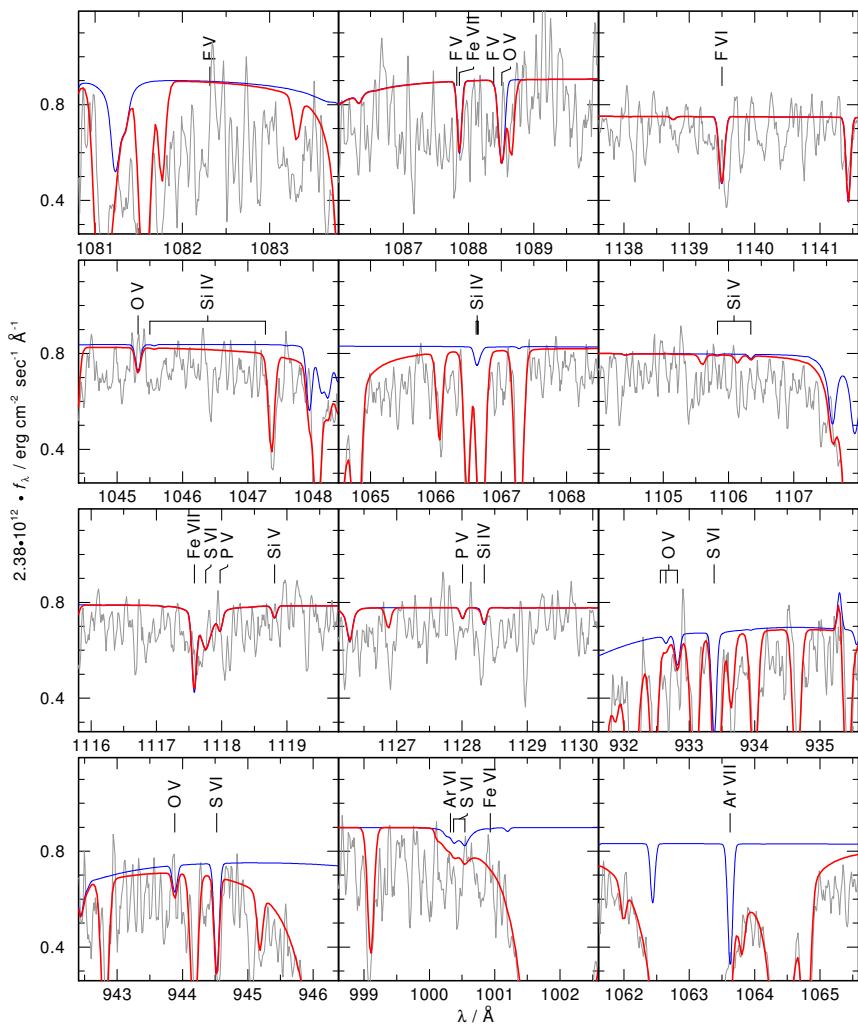


Figure E.12: Fe v – vii lines in the STIS observation of A 35.

Table E.3: Abundances of A 35

element (X)	mass fraction	number fraction	$\log \epsilon$	[X]	
H	8.6842E-01	9.6654E-01	12.085	0.071	
He	1.1739E-01	3.2901E-02	10.617	-0.327	*
C	2.7750E-06	2.5919E-07	5.514	-2.931	
N	1.2468E-05	9.9860E-07	6.099	-1.745	*
O	1.4242E-05	9.9859E-07	6.099	-2.605	*
F	5.0473E-07	2.9803E-08	4.574	0.000	
Ne	1.2573E-03	6.9896E-05	7.945	0.000	
Na	2.9237E-05	1.4267E-06	6.254	0.000	
Mg	8.3269E-03	3.8434E-04	8.685	1.071	
Al	5.5647E-05	2.3137E-06	6.464	0.000	
Si	5.0046E-06	1.9990E-07	5.401	-2.123	*
P	8.2725E-09	2.9962E-10	2.577	-2.848	*
S	3.6412E-07	1.2739E-08	4.205	-2.929	
Ar	8.6611E-04	2.4322E-05	7.486	1.072	*
Ca	6.4166E-05	1.7960E-06	6.354	0.000	
Sc	4.6467E-08	1.1595E-09	3.164	0.000	
Ti	3.1196E-06	7.3113E-08	4.964	0.000	
V	3.1729E-07	6.9873E-09	3.944	0.000	
Cr	1.1571E-03	2.4964E-05	7.497	1.843	*
Mn	3.8186E-04	7.7976E-06	6.992	1.548	*
Fe	1.5216E-03	3.0563E-05	7.585	0.071	*
Co	1.5755E-04	2.9991E-06	6.577	1.573	*
Ni	3.3970E-04	6.4910E-06	6.912	0.678	*

E.4 A 39, $T_{\text{eff}} = 117 \text{ kK}$, $\log g = 6.3$ Figure E.13: C, N, and O lines in the *FUSE* observation of A 39.

Figure E.14: F, Si, P, S, and Ar lines in the *FUSE* observation of A 39.

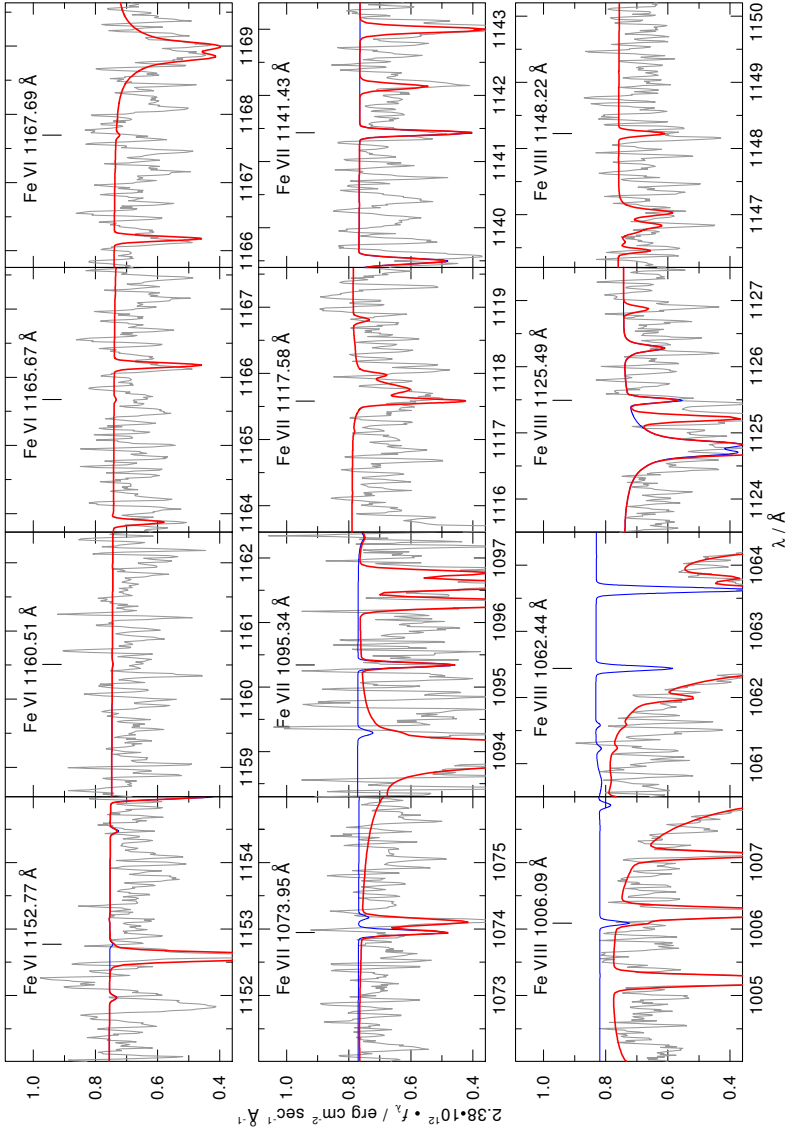
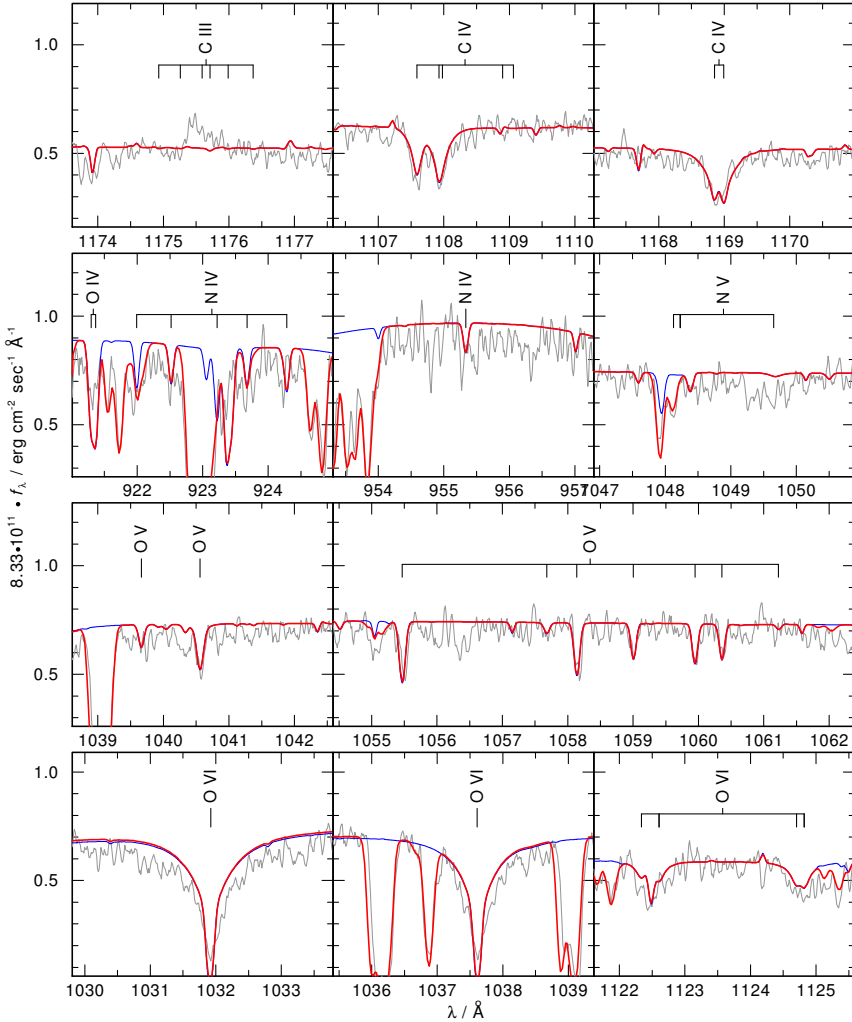


Figure E.15: Fe VI–VIII lines in the *FUSE* observation of A 39.

Table E.4: Abundances of A 39

element (X)	mass fraction	number fraction	$\log \epsilon$	[X]	
H	7.2638E-01	9.1931E-01	12.008	-0.007	
He	2.4548E-01	7.8234E-02	10.938	-0.007	
C	9.9648E-03	1.0584E-03	9.069	0.625	*
N	3.3888E-03	3.0864E-04	8.534	0.689	
O	1.1882E-02	9.4738E-04	9.021	0.317	*
F	4.0454E-07	2.7163E-08	4.478	-0.096	
Ne	1.2568E-03	7.9450E-05	7.944	0.000	
Na	2.9226E-05	1.6217E-06	6.254	0.000	
Mg	7.0780E-04	3.7149E-05	7.614	0.000	
Al	5.5626E-05	2.6299E-06	6.464	0.000	
Si	4.3772E-05	1.9881E-06	6.343	-1.182	
P	1.0275E-06	4.2319E-08	4.671	-0.753	
S	1.0507E-04	4.1795E-06	6.665	-0.469	*
Ar	5.1676E-05	1.6502E-06	6.262	-0.152	
Ca	6.4141E-05	2.0415E-06	6.354	0.000	
Sc	4.6449E-08	1.3180E-09	3.164	0.000	
Ti	3.1184E-06	8.3106E-08	4.964	0.000	
V	3.1716E-07	7.9423E-09	3.944	0.000	
Cr	1.6596E-05	4.0717E-07	5.654	0.000	
Mn	1.0818E-05	2.5120E-07	5.444	0.000	
Fe	4.8797E-04	1.1145E-05	7.091	-0.423	*
Co	4.2127E-06	9.1186E-08	5.004	0.000	
Ni	7.1250E-05	1.5481E-06	6.234	0.000	

E.5 NGC 3587, $T_{\text{eff}} = 104 \text{ kK}$, $\log g = 7.0$ Figure E.16: C, N, and O lines in the *FUSE* observation of NGC 3587.

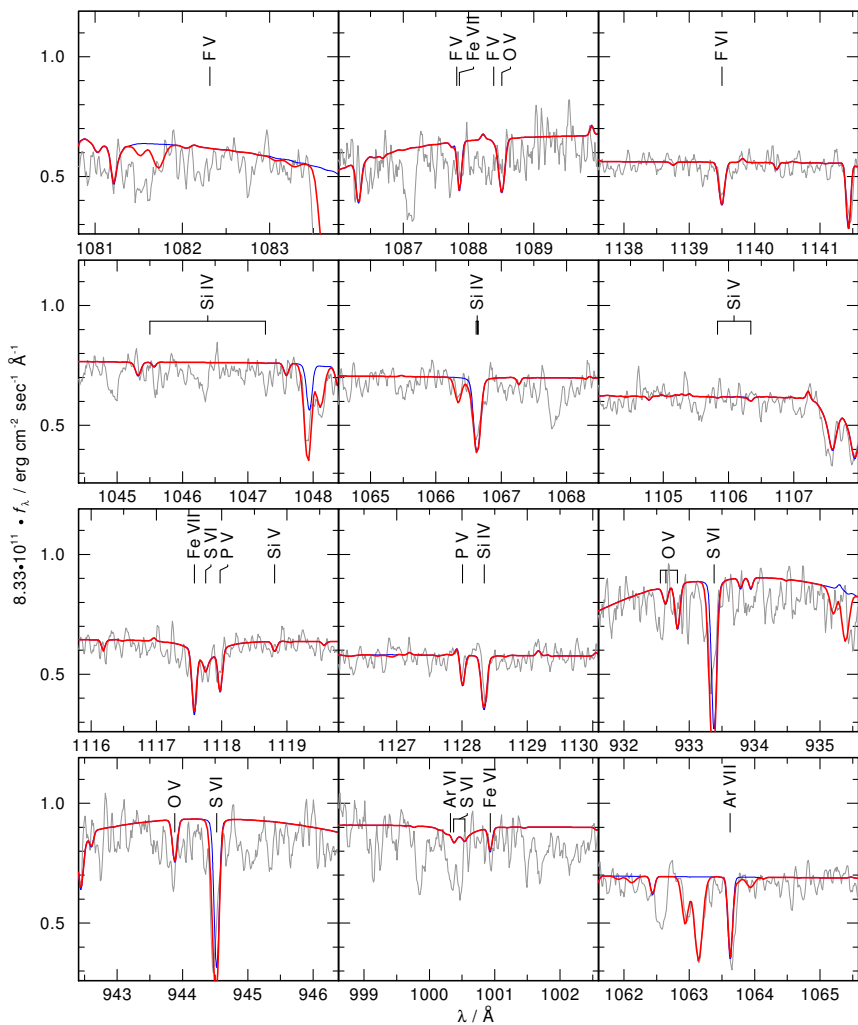


Figure E.17: F, Si, P, S, and Ar lines in the *FUSE* observation of NGC 3587.

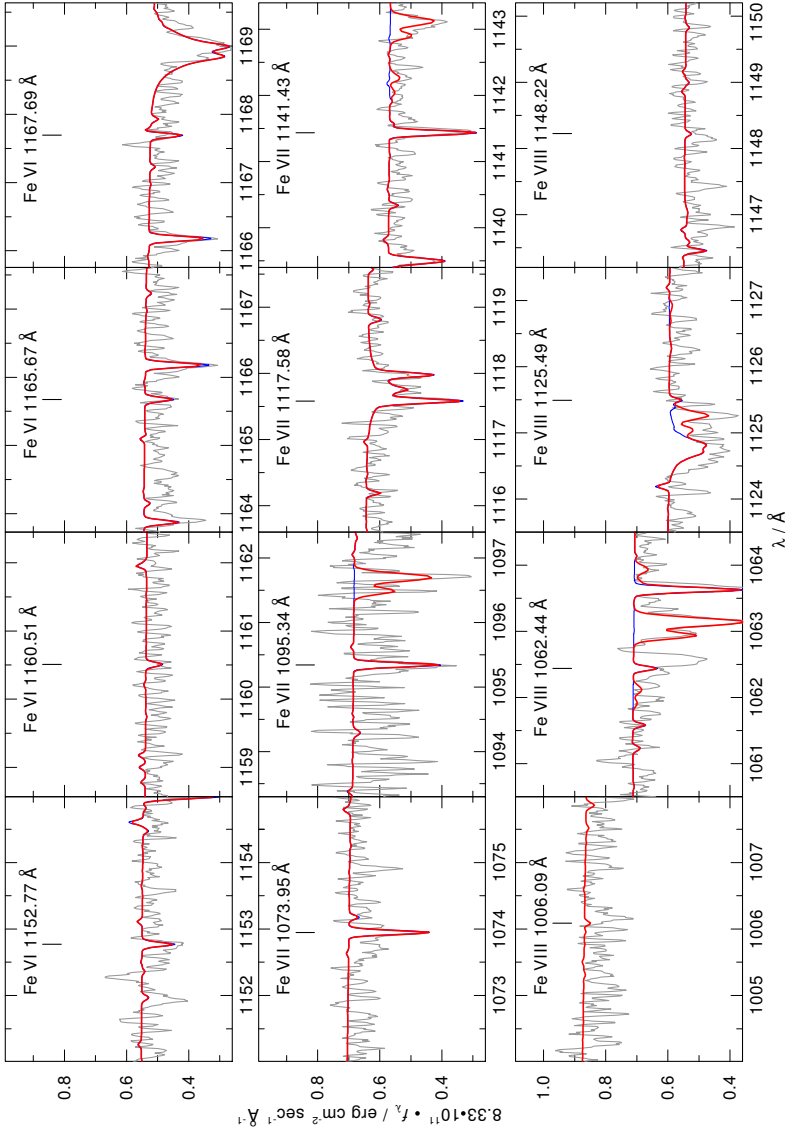
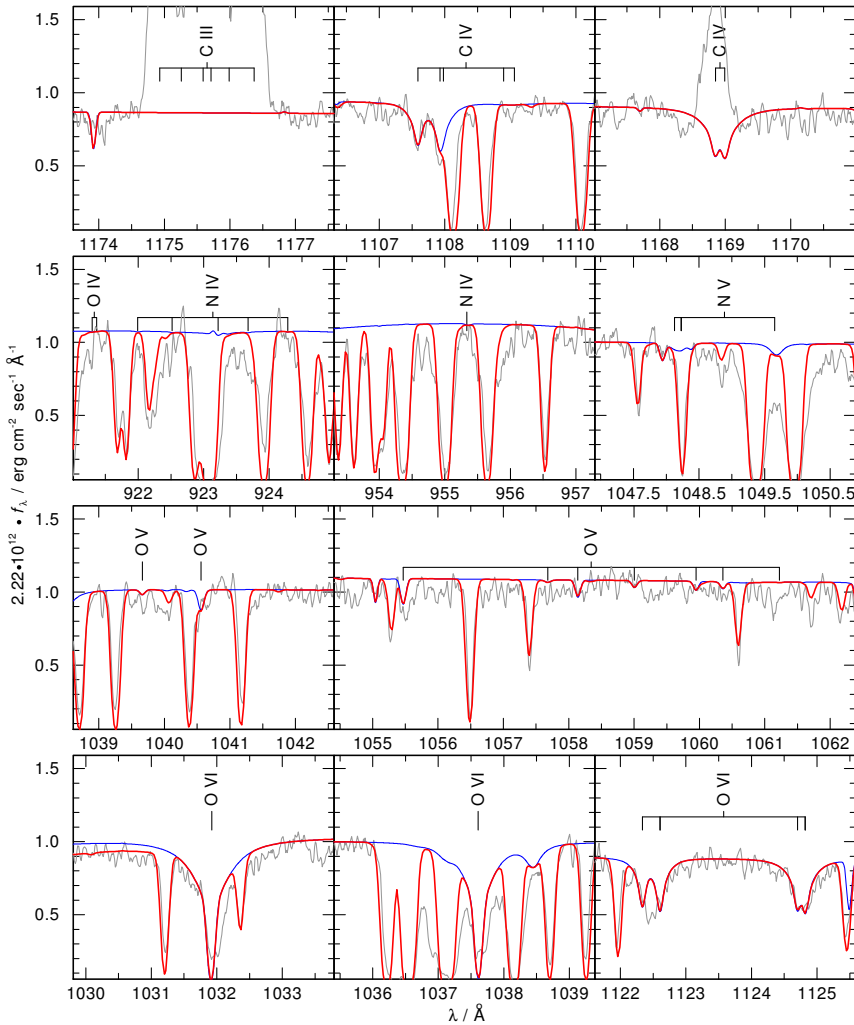
Figure E.18: Fe VI–VIII lines in the *FUSE* observation (black) of NGC 3587.

Table E.5: Abundances of NGC 3587

element (X)	mass fraction	number fraction	$\log \epsilon$	[X]	
H	7.4176E-01	9.2111E-01	12.017	0.003	
He	2.5067E-01	7.8386E-02	10.947	0.003	
C	1.1932E-03	1.2434E-04	8.148	-0.297	*
N	3.4785E-05	3.1084E-06	6.545	-1.299	
O	2.8192E-03	2.2055E-04	8.396	-0.308	*
F	5.0429E-06	3.3223E-07	5.574	1.000	*
Ne	1.2558E-03	7.7891E-05	7.944	0.000	
Na	2.9202E-05	1.5899E-06	6.254	0.000	
Mg	7.0723E-04	3.6420E-05	7.614	0.000	
Al	5.5577E-05	2.5783E-06	6.464	0.000	
Si	4.0040E-04	1.7841E-05	7.304	-0.220	*
P	1.0429E-06	4.2147E-08	4.677	-0.747	*
S	3.2492E-05	1.2683E-06	6.156	-0.978	*
Ar	8.8860E-06	2.7842E-07	5.497	-0.917	*
Ca	6.4089E-05	2.0014E-06	6.354	0.000	
Sc	4.6416E-08	1.2922E-09	3.164	0.000	
Ti	3.1180E-06	8.1476E-08	4.964	0.000	
V	3.1690E-07	7.7865E-09	3.944	0.000	
Cr	1.6584E-05	3.9918E-07	5.654	0.000	
Mn	1.0810E-05	2.4627E-07	5.444	0.000	
Fe	8.6360E-04	1.9354E-05	7.339	-0.175	*
Co	4.2090E-06	8.9397E-08	5.004	0.000	
Ni	7.1192E-05	1.5178E-06	6.234	0.000	

E.6 NGC 6720, $T_{\text{eff}} = 130 \text{ kK}$, $\log g = 6.9$ Figure E.19: C, N, and O lines in the *FUSE* observation of NGC 6720.

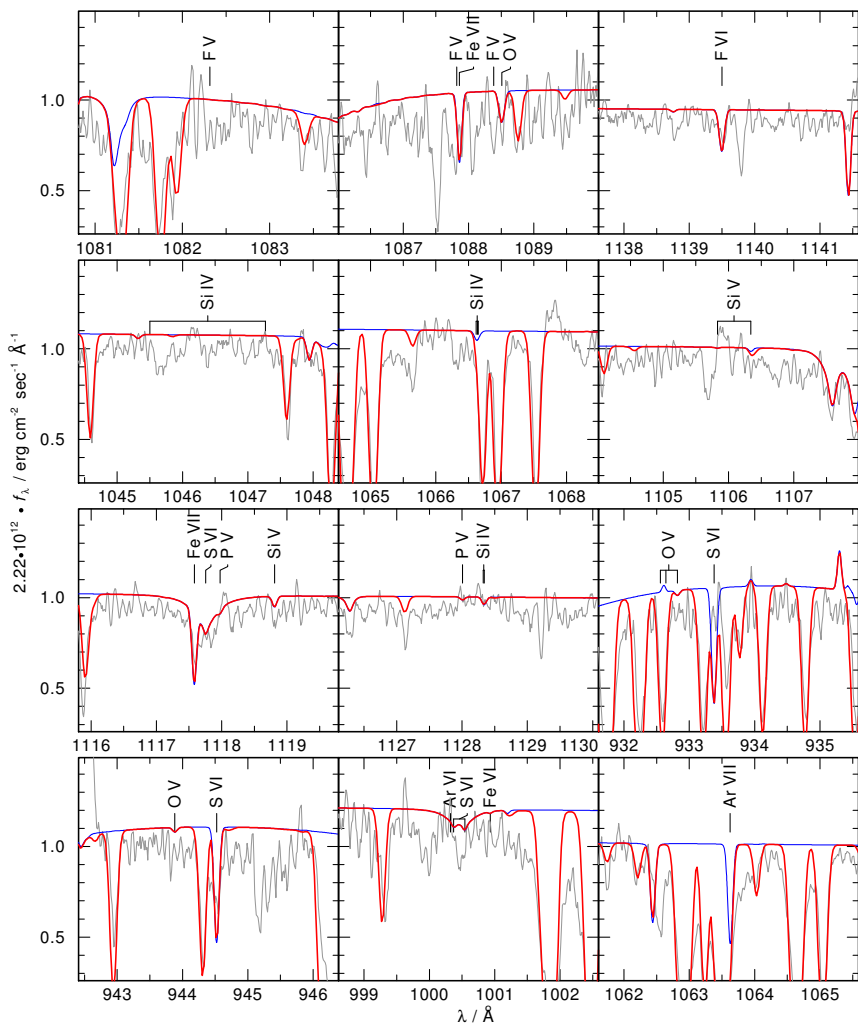


Figure E.20: F, Si, P, S, and Ar lines in the *FUSE* observation of NGC 6720.

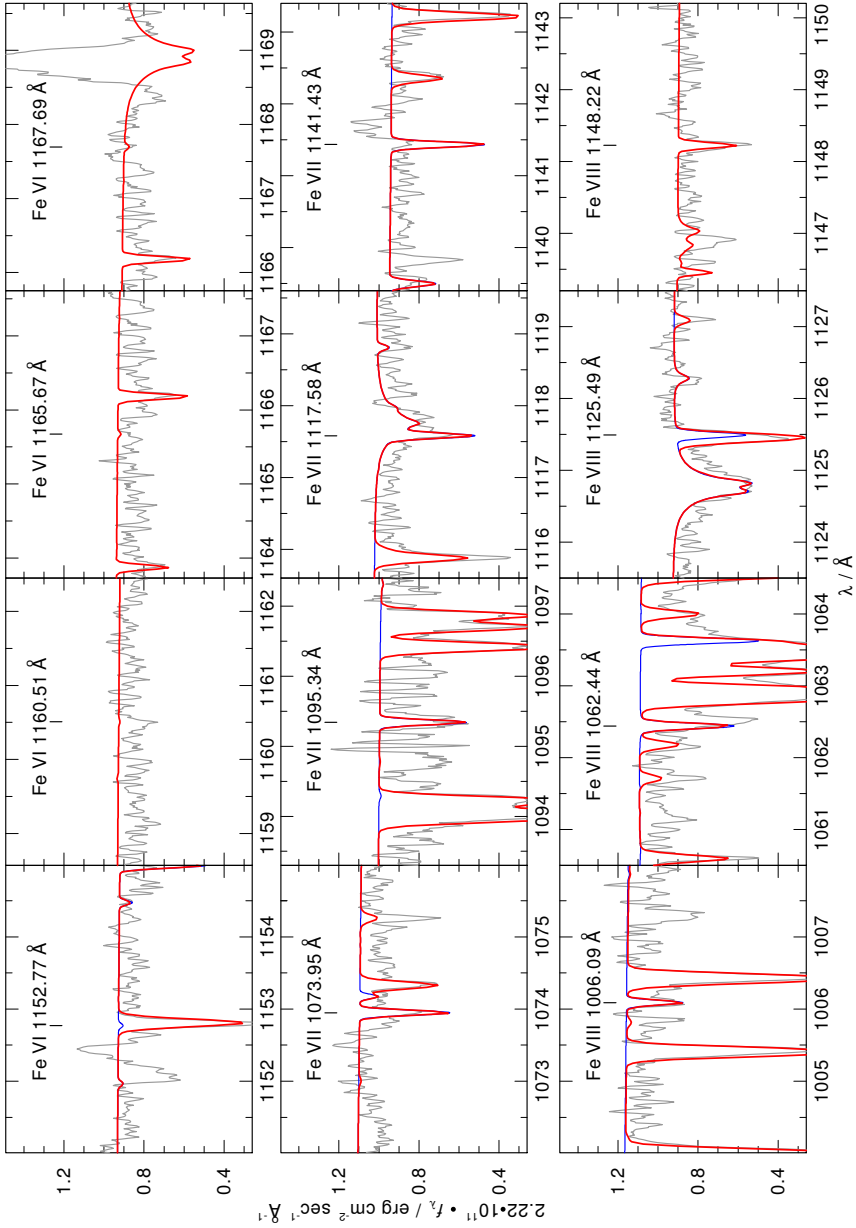
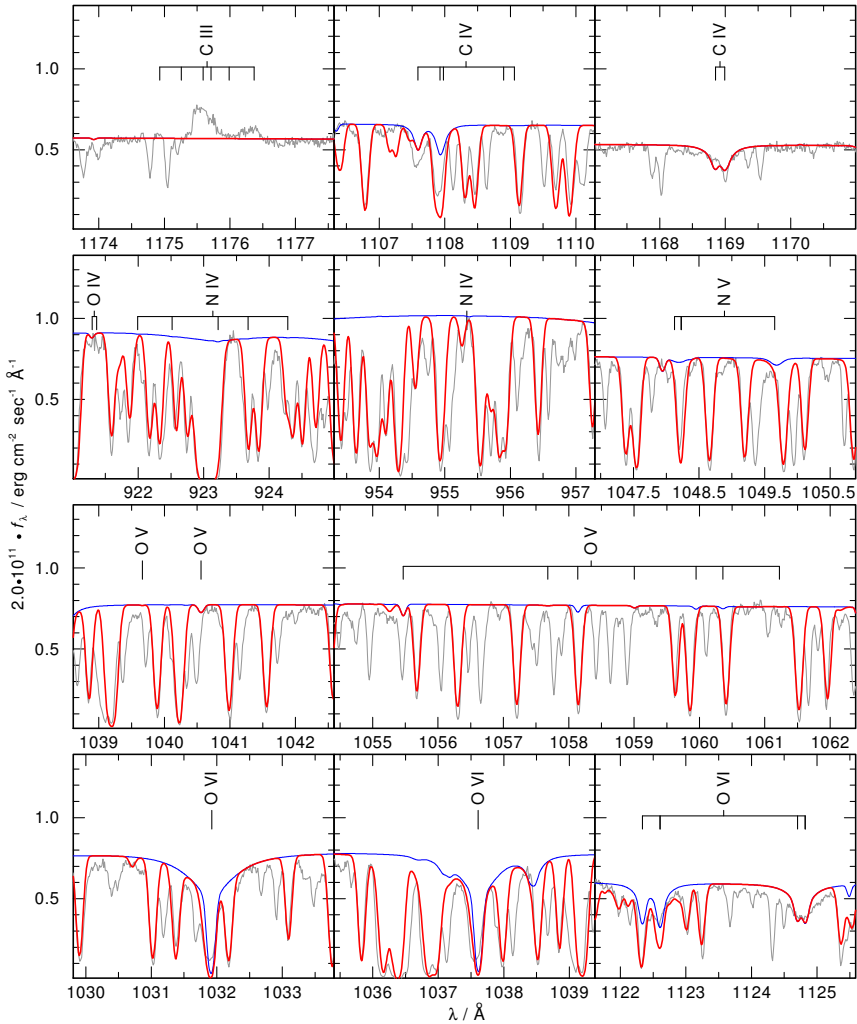
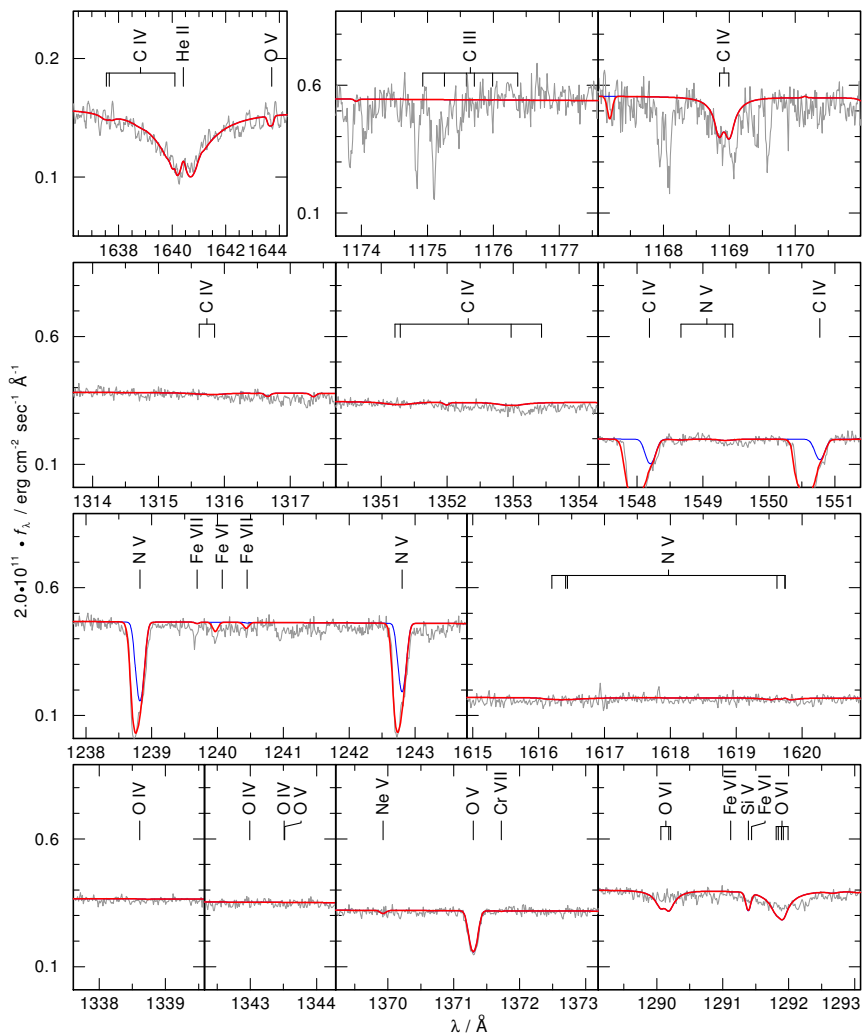
Figure E.21: Fe VI – VIII lines in the *FUSE* observation of NGC 6720.

Table E.6: Abundances of NGC 6720

element (X)	mass fraction	number fraction	$\log \epsilon$	[X]	
H	7.3651E-01	9.2059E-01	12.014	-0.001	
He	2.4890E-01	7.8344E-02	10.944	-0.001	
C	5.8568E-03	6.1434E-04	8.838	0.394	*
N	3.4539E-04	3.1066E-05	7.542	-0.302	
O	2.7992E-03	2.2042E-04	8.393	-0.311	*
F	3.0495E-07	2.0222E-08	4.356	-0.219	*
Ne	1.2601E-03	7.7869E-05	7.945	0.001	
Na	2.9302E-05	1.6057E-06	6.255	0.001	
Mg	7.0964E-04	3.6784E-05	7.615	0.001	
Al	5.5770E-05	2.6041E-06	6.465	0.001	
Si	4.8589E-05	2.1796E-06	6.388	-1.136	
P	5.7875E-07	2.3540E-08	4.421	-1.003	
S	1.8587E-04	7.3028E-06	6.913	-0.221	*
Ar	7.3590E-05	2.3208E-06	6.415	0.001	
Ca	6.4308E-05	2.0214E-06	6.355	0.001	
Sc	4.6570E-08	1.3051E-09	3.165	0.001	
Ti	3.1265E-06	8.2289E-08	4.965	0.001	
V	3.1798E-07	7.8642E-09	3.945	0.001	
Cr	1.6640E-05	4.0317E-07	5.655	0.001	
Mn	1.0846E-05	2.4873E-07	5.445	0.001	
Fe	3.0457E-03	6.8703E-05	7.887	0.372	*
Co	4.2236E-06	9.0290E-08	5.005	0.001	
Ni	7.1435E-05	1.5329E-06	6.235	0.001	

E.7 NGC 6853, $T_{\text{eff}} = 136 \text{ kK}$, $\log g = 6.5$ Figure E.22: C, N, and O lines in the *FUSE* observation of NGC 6853.

Figure E.23: He, C, N, and O lines in the *STIS* observation of NGC 6853.

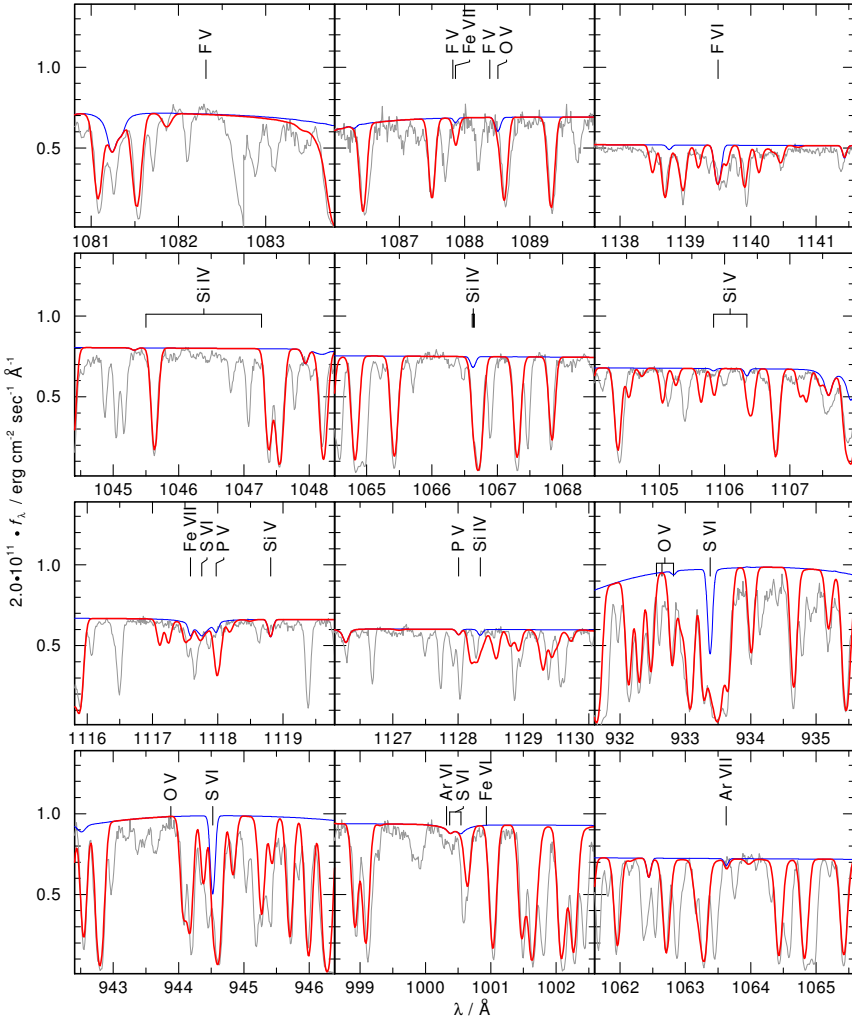
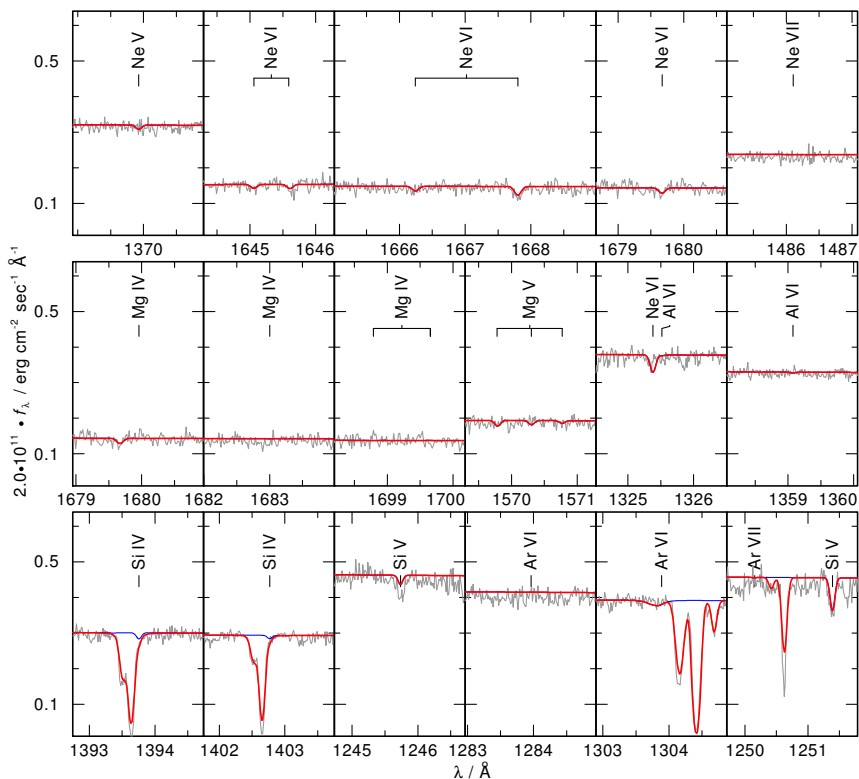
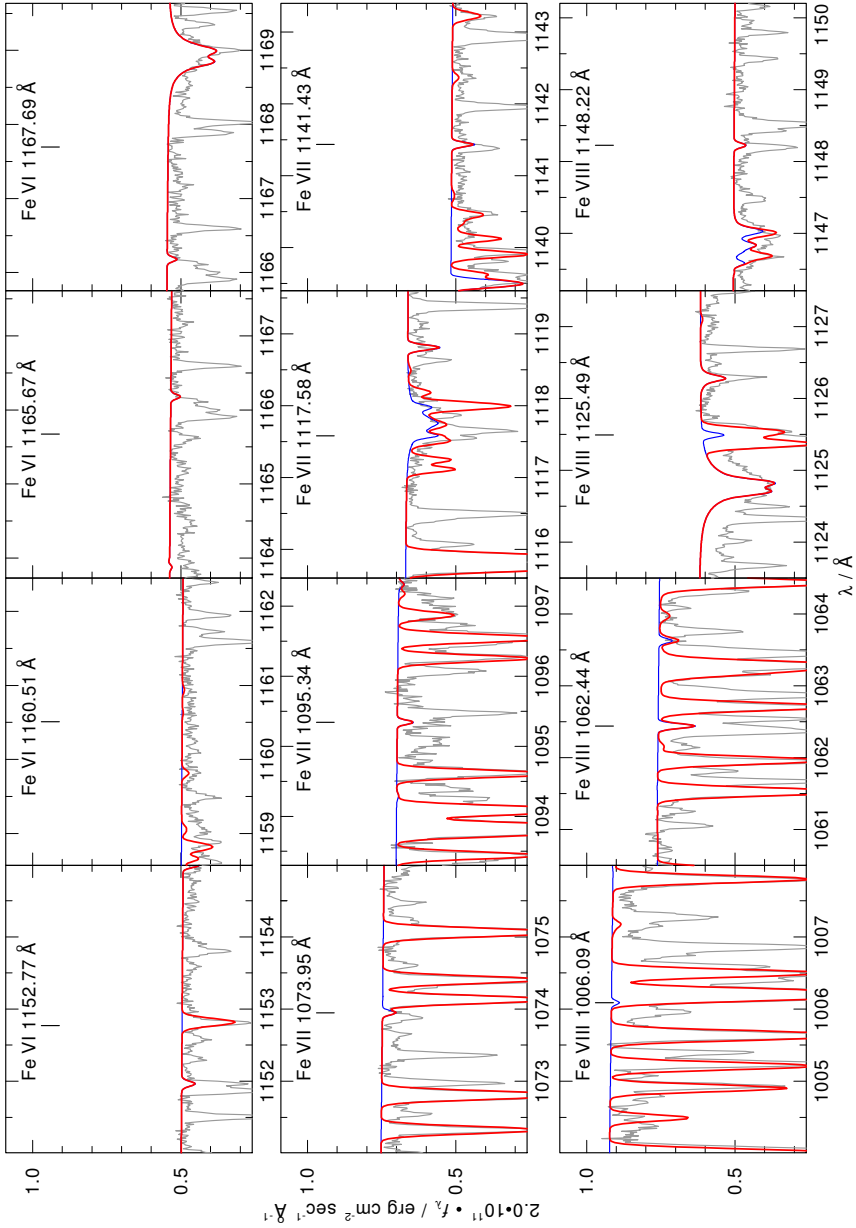
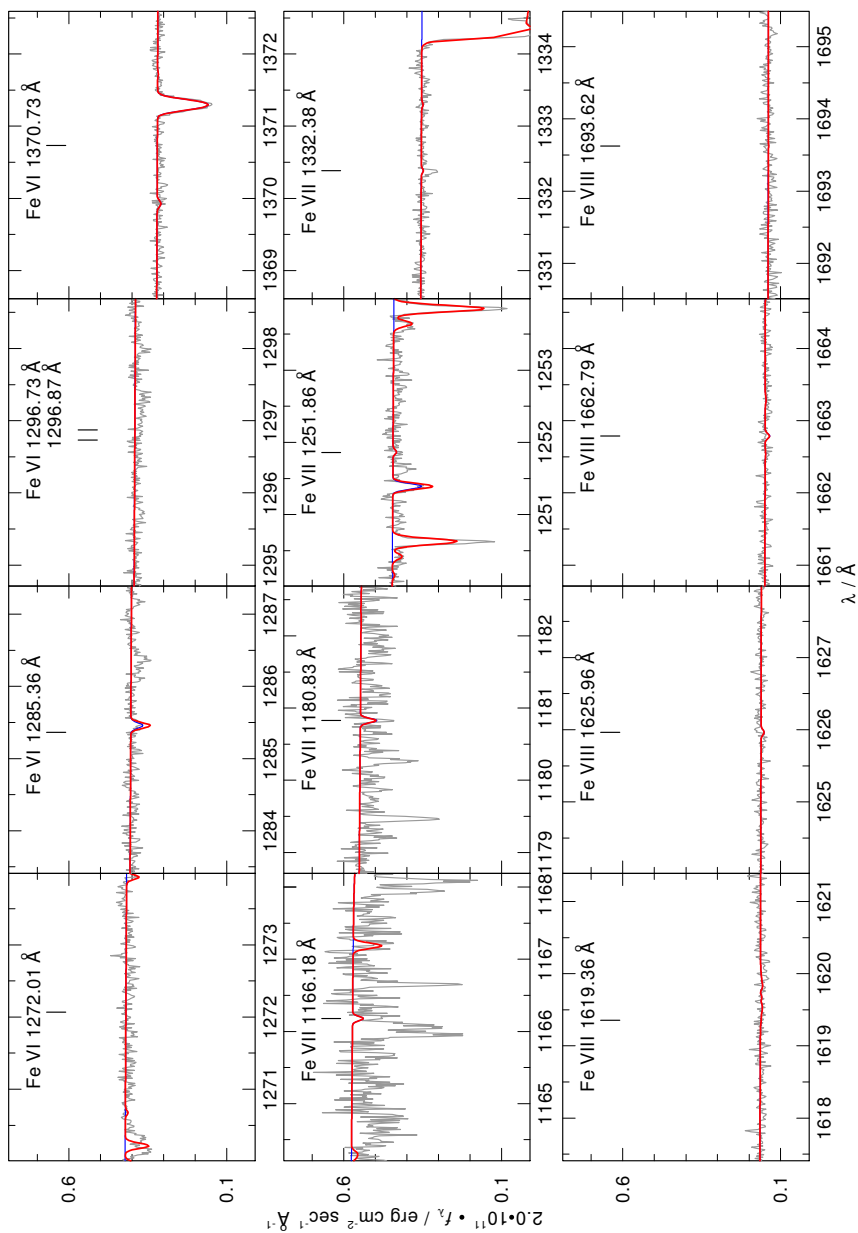


Figure E.24: F, Si, P, S, and Ar lines in the *FUSE* observation of NGC 6853.

Figure E.25: Ne, Mg, Al, Si, and Ar lines in the *STIS* observation of NGC 6853.

Figure E.26: Fe VI – VIII lines in the *FUSE* observation of NGC 6853.

Figure E.27: Fe VI– VIII lines in the *STIS* observation of NGC 6853.

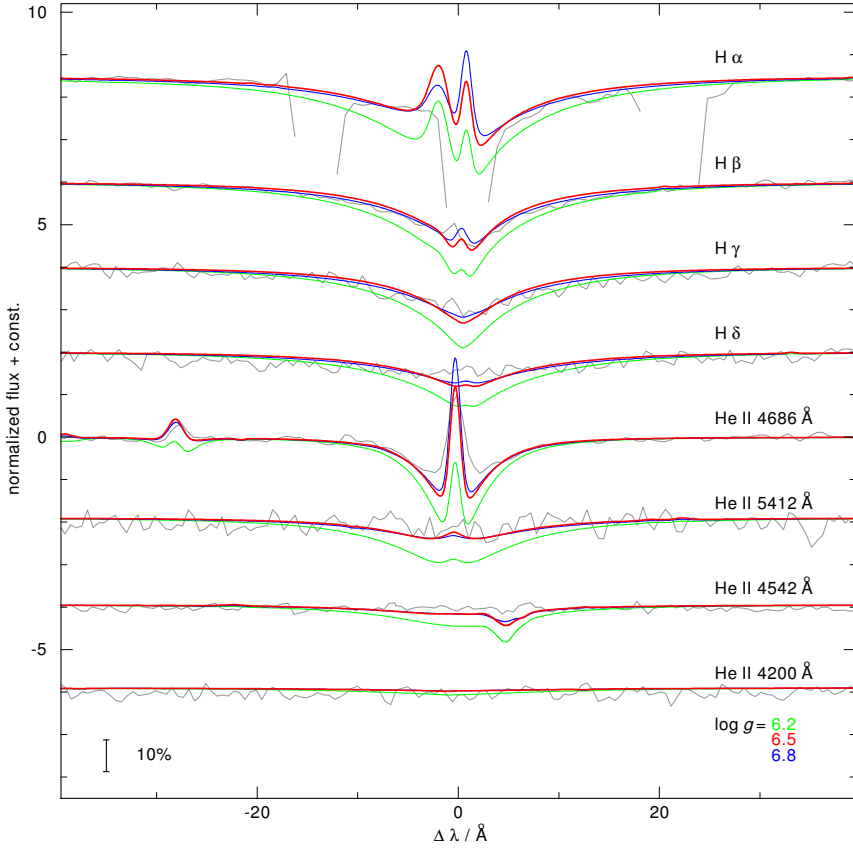
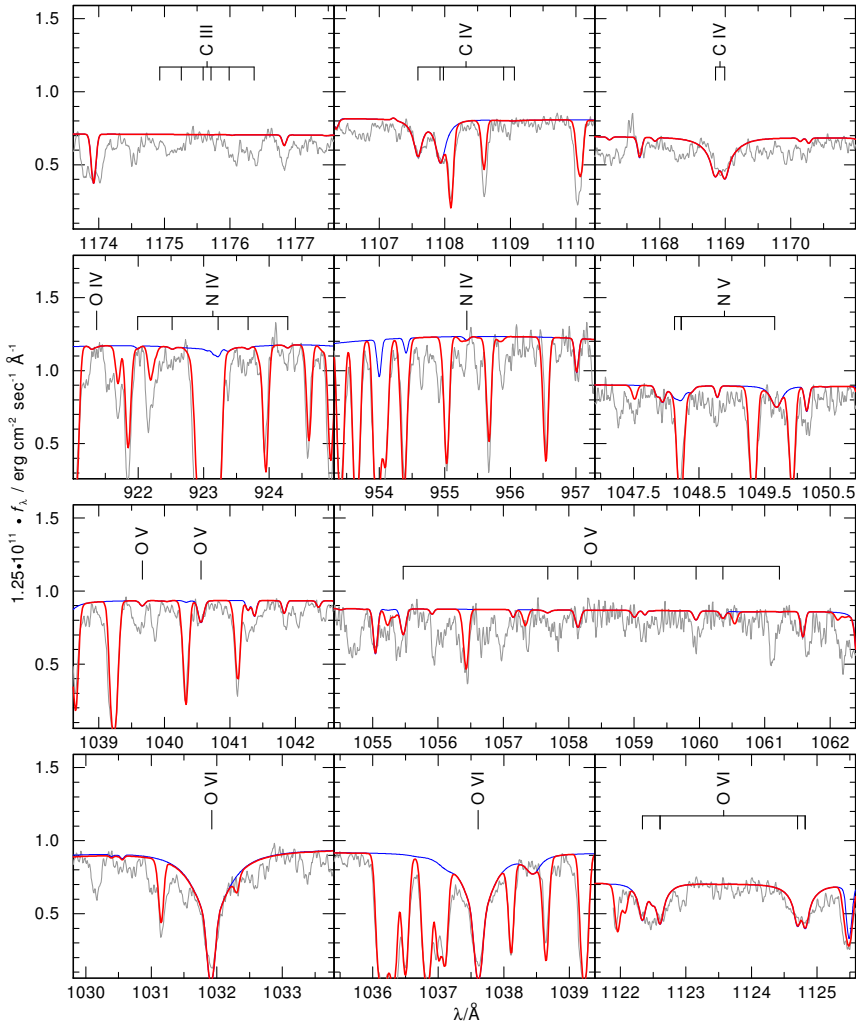
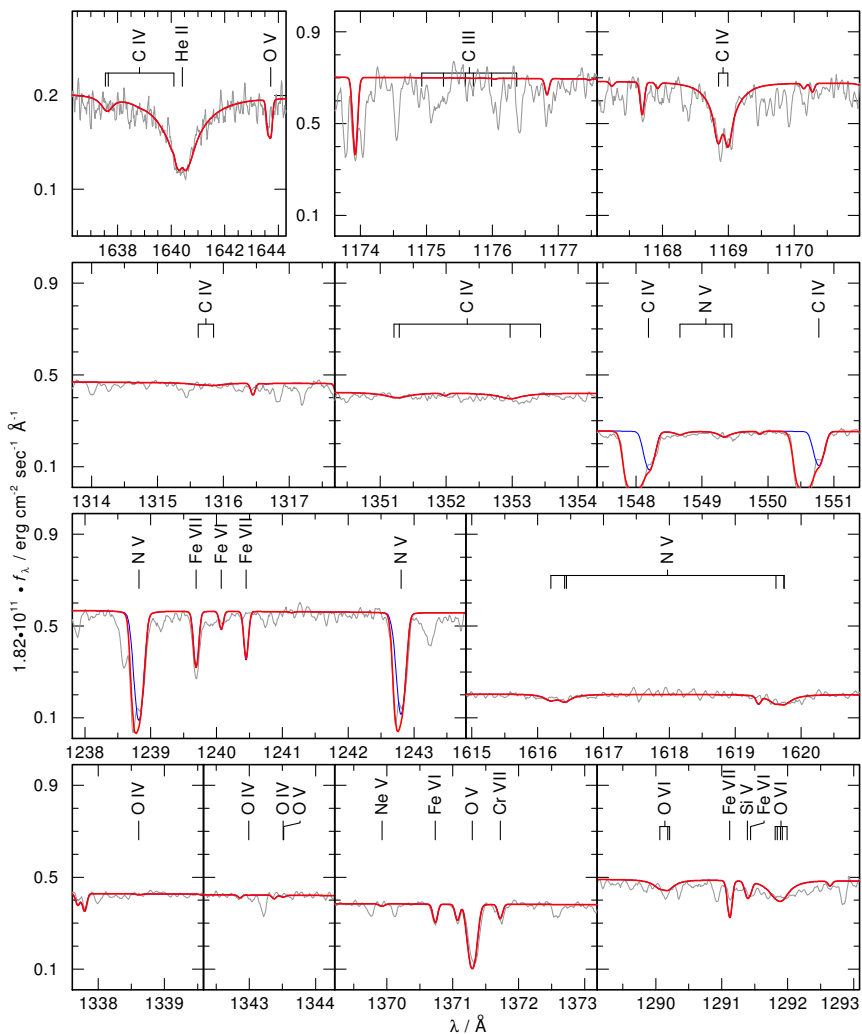


Figure E.28: H and He lines in the optical observation of NGC 6853.

Table E.7: Abundances of NGC 6853

element (X)	mass fraction	number fraction	$\log \epsilon$	[X]	
H	7.0579E-01	9.0806E-01	11.995	-0.019	*
He	2.8035E-01	9.0807E-02	10.995	0.051	*
C	3.3896E-03	3.6588E-04	8.601	0.156	*
N	3.9797E-04	3.6837E-05	7.604	-0.241	
O	6.8530E-03	5.5532E-04	8.782	0.077	*
F	2.5289E-06	1.7257E-07	5.274	0.700	
Ne	2.0246E-03	1.3007E-04	8.151	0.207	*
Na	2.9240E-05	1.6490E-06	6.254	0.000	
Mg	3.5362E-04	1.8863E-05	7.313	-0.301	
Al	5.5653E-06	2.6741E-07	5.464	-1.000	
Si	2.4913E-04	1.1500E-05	7.098	-0.426	*
P	2.5354E-06	1.0613E-07	5.063	-0.361	
S	1.6229E-04	6.5617E-06	6.854	-0.280	
Ar	8.6277E-07	2.8000E-08	4.484	-1.930	
Ca	6.4172E-05	2.0758E-06	6.354	0.000	
Sc	4.6472E-08	1.3402E-09	3.164	0.000	
Ti	3.1199E-06	8.4503E-08	4.964	0.000	
V	3.1732E-07	8.0759E-09	3.944	0.000	
Cr	1.6605E-05	4.1402E-07	5.654	0.000	
Mn	1.0823E-05	2.5542E-07	5.444	0.000	
Fe	4.3103E-05	1.0006E-06	6.037	-1.477	
Co	4.2147E-06	9.2719E-08	5.004	0.000	
Ni	7.1285E-05	1.5742E-06	6.234	0.000	

E.8 NGC 7293, $T_{\text{eff}} = 120 \text{ kK}$, $\log g = 6.8$ Figure E.29: C, N, and O lines in the $FUSE$ observation of NGC 7293.

Figure E.30: He, C, N, and O lines in the *STIS* observation of NGC 7293.

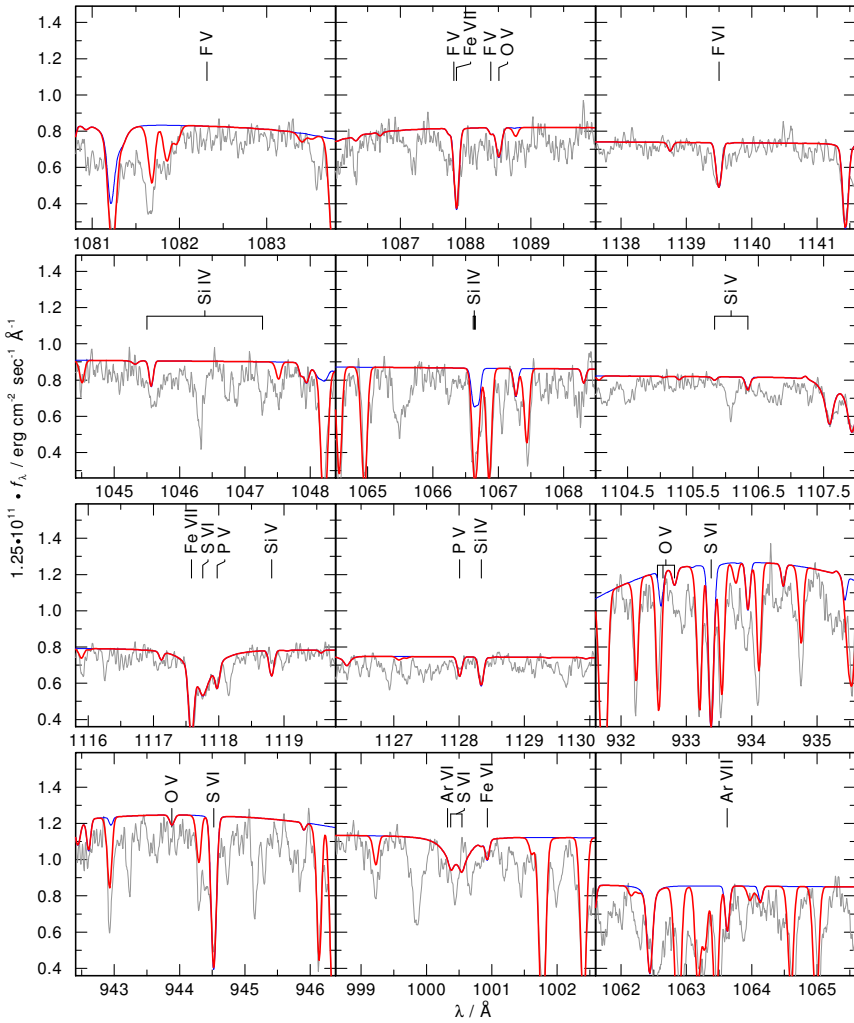


Figure E.31: F, Si, P, S, and Ar lines in the *FUSE* observation of NGC 7293.

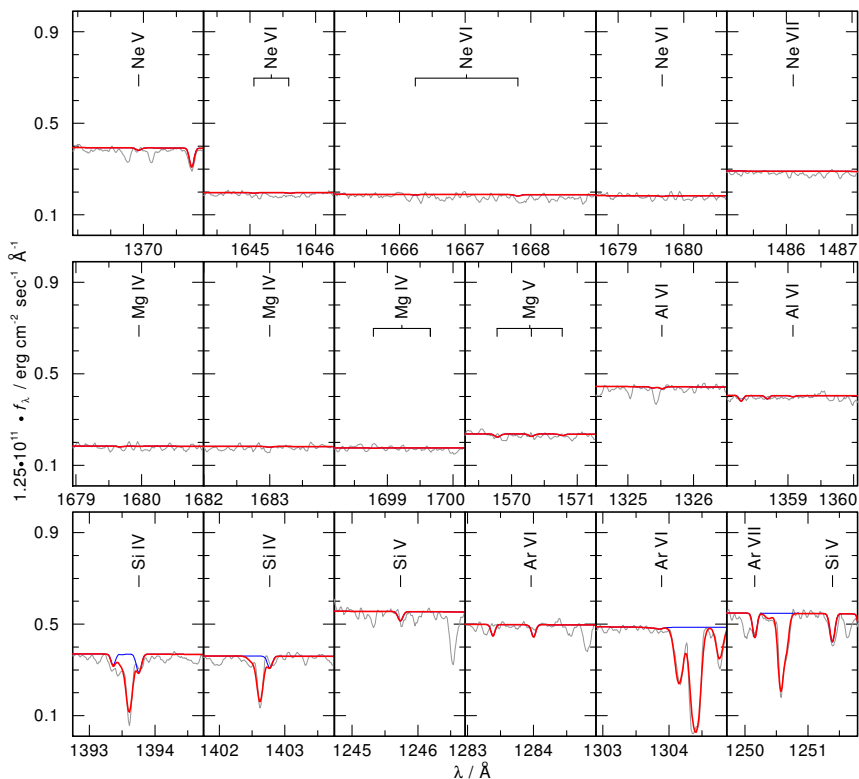
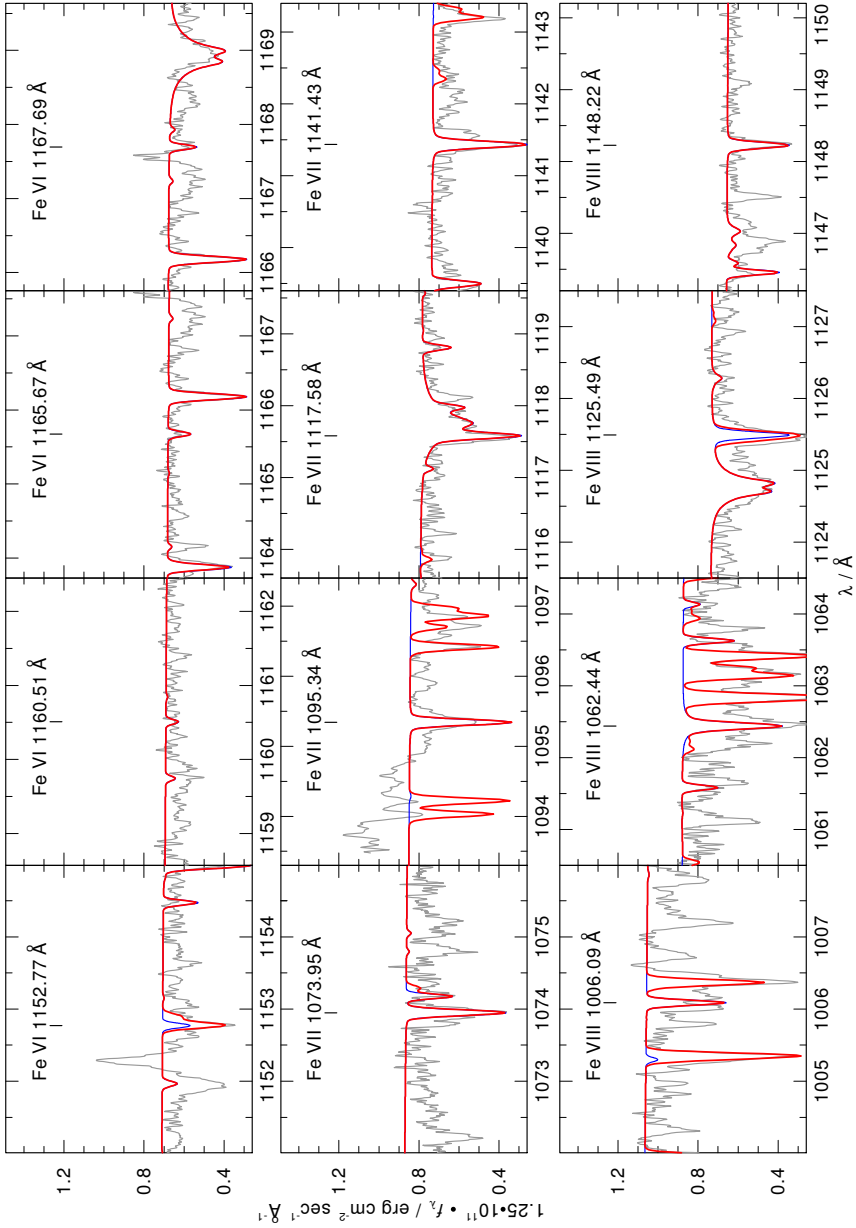
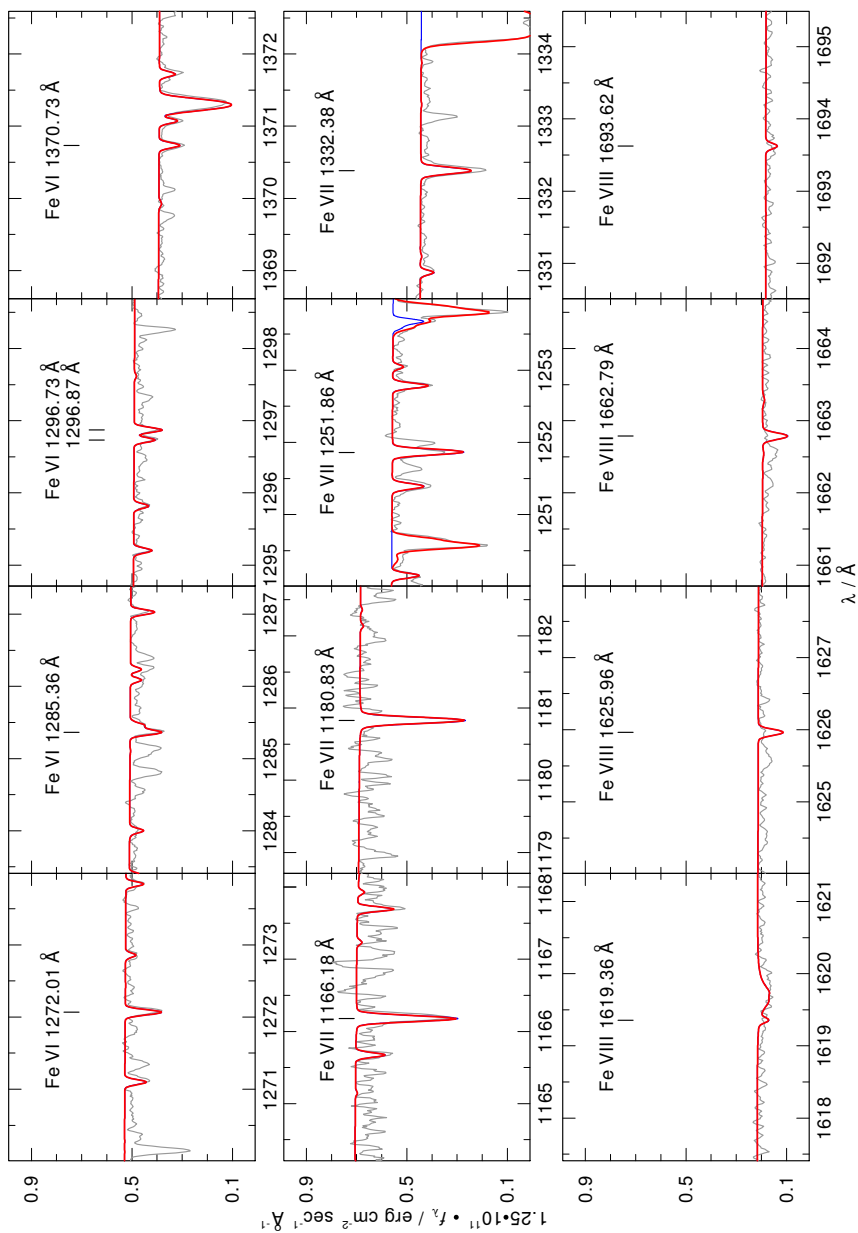


Figure E.32: Ne, Mg, Al, Si, and Ar lines in the *STIS* observation of NGC 7293.

Figure E.33: Fe VI – VIII lines in the *FUSE* observation of NGC 7293.

Figure E.34: Fe VI– VIII lines in the *STIS* observation of NGC 7293.

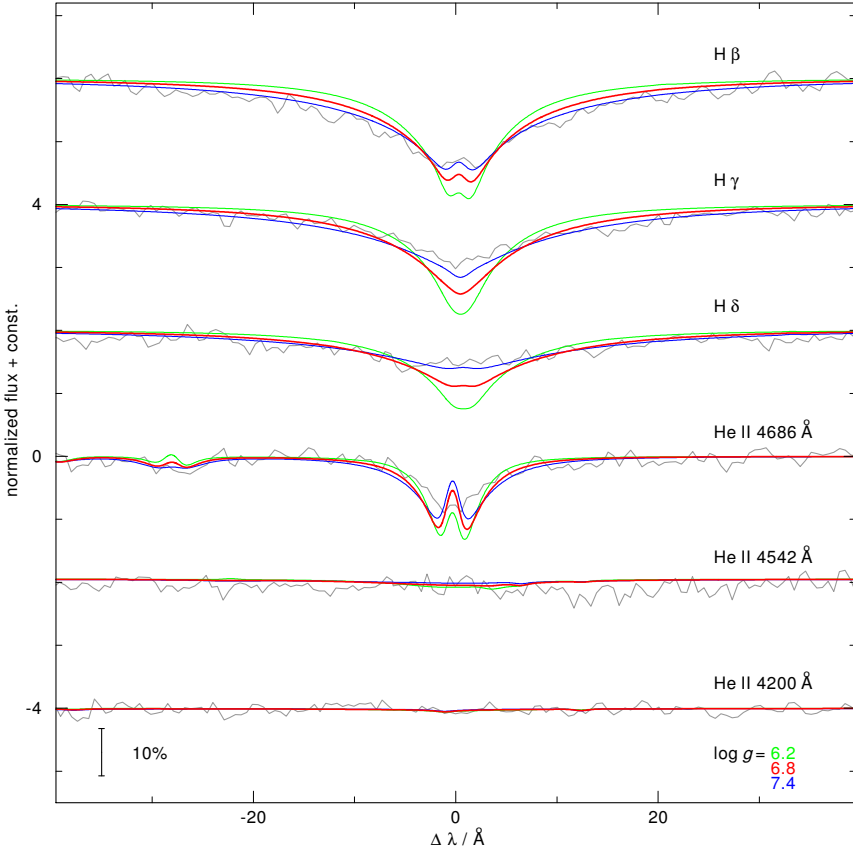
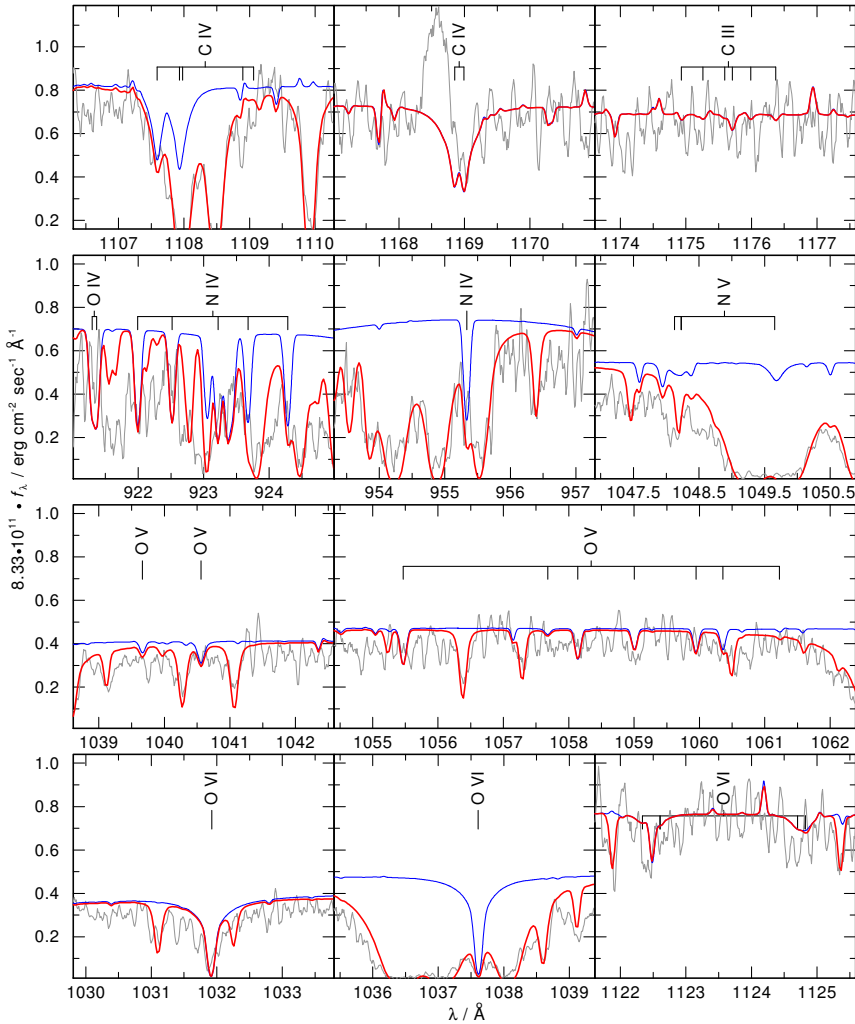


Figure E.35: H and He lines in the optical observation of NGC 7293.

Table E.8: Abundances of NGC 7293

element (X)	mass fraction	number fraction	$\log \epsilon$	[X]	
H	8.6691E-01	9.6991E-01	12.085	0.070	*
He	1.0327E-01	2.9094E-02	10.562	-0.383	*
C	3.0992E-03	2.9098E-04	8.562	0.117	*
N	6.0233E-04	4.8495E-05	7.783	-0.061	
O	1.9914E-03	1.4036E-04	8.245	-0.459	*
F	4.9304E-07	2.9265E-08	4.564	-0.010	*
Ne	2.5054E-04	1.4001E-05	7.244	-0.700	
Na	2.9345E-05	1.4395E-06	6.256	-0.002	
Mg	2.1554E-04	1.0001E-05	7.098	-0.516	
Al	5.5853E-05	2.3344E-06	6.466	0.002	
Si	2.4839E-04	9.9736E-06	7.097	-0.428	*
P	5.0715E-06	1.8464E-07	5.364	-0.060	*
S	3.1642E-04	1.1128E-05	7.144	0.010	*
Ar	2.8342E-06	8.0006E-08	5.001	-1.413	
Ca	6.4403E-05	1.8121E-06	6.356	0.002	
Sc	4.6639E-08	1.1699E-09	3.166	0.002	
Ti	3.1312E-06	7.3767E-08	4.966	0.001	
V	3.1846E-07	7.0498E-09	3.946	0.002	
Cr	3.2505E-04	7.0497E-06	6.946	1.292	*
Mn	1.0862E-05	2.2297E-07	5.446	0.002	
Fe	2.2529E-02	4.5490E-04	8.756	1.241	*
Co	4.2299E-06	8.0939E-08	5.006	0.002	
Ni	7.1541E-05	1.3742E-06	6.236	0.002	

E.9 PuWe 1, $T_{\text{eff}} = 94 \text{ kK}$, $\log g = 7.0$ Figure E.36: C, N, and O lines in the *FUSE* observation of PuWe 1.

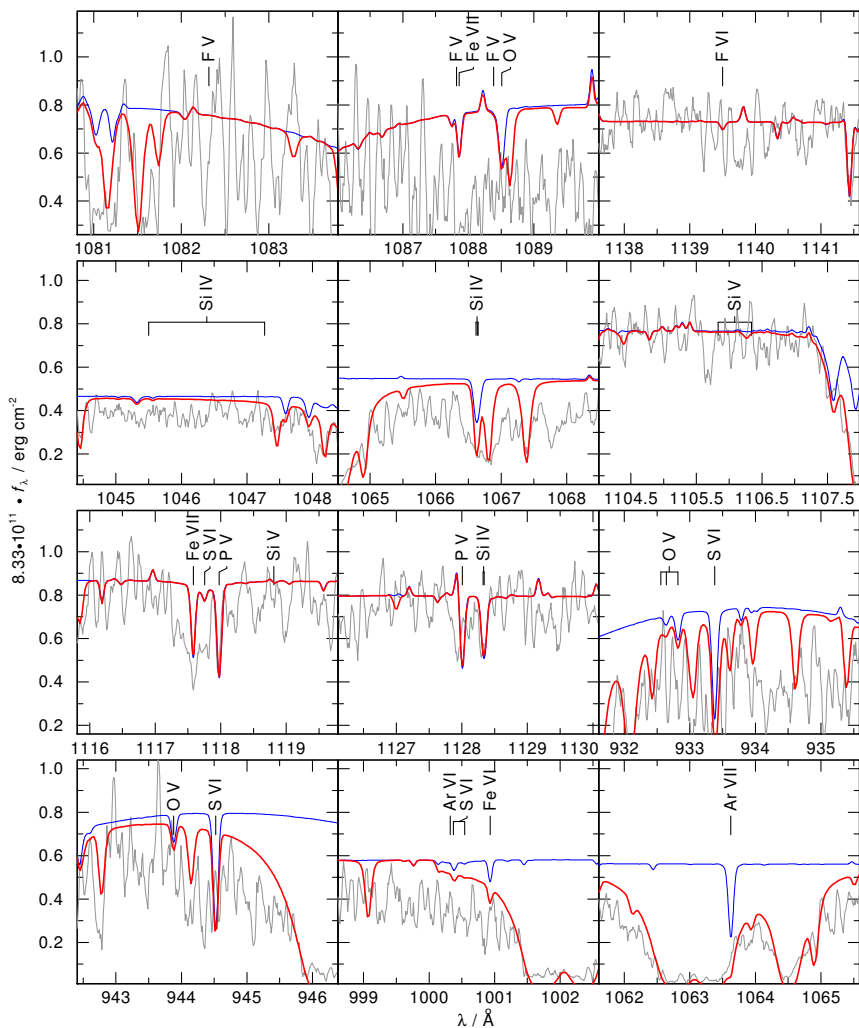


Figure E.37: F, Si, P, S, and Ar lines in the *FUSE* observation of PuWe 1.

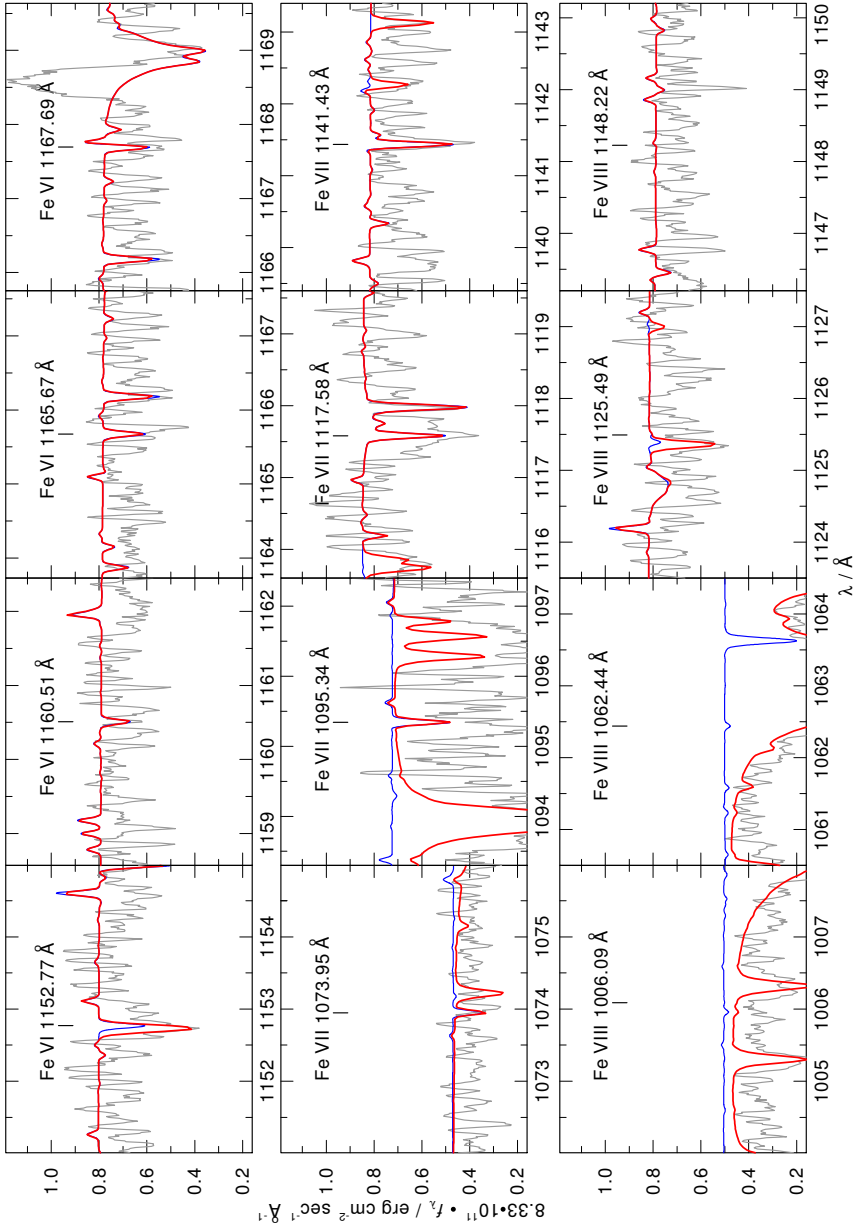
Figure E.38: Fe VI – VIII lines in the *FUSE* observation of PuWe 1.

Table E.9: Abundances of PuWe 1

element (X)	mass fraction	number fraction	$\log \epsilon$	[X]
H	7.4171E-01	9.2109E-01	12.017	0.003
He	2.5066E-01	7.8386E-02	10.947	0.003
C	1.1932E-03	1.2435E-04	8.147	-0.297
N	3.4783E-04	3.1084E-05	7.545	-0.299
O	2.8190E-03	2.2054E-04	8.396	-0.308
F	5.0425E-07	3.3223E-08	4.574	0.000
Ne	1.2561E-03	7.7915E-05	7.944	0.000
Na	2.9210E-05	1.5904E-06	6.254	0.000
Mg	7.0742E-04	3.6432E-05	7.614	0.000
Al	5.5595E-05	2.5791E-06	6.464	0.000
Si	9.8627E-05	4.3955E-06	6.696	-0.829
P	1.7462E-06	7.0565E-08	4.901	-0.523
S	9.7197E-06	3.7942E-07	5.632	-1.503
Ar	7.3360E-05	2.2986E-06	6.414	0.000
Ca	6.4148E-05	2.0033E-06	6.354	0.000
Sc	4.6454E-08	1.2934E-09	3.164	0.000
Ti	3.1188E-06	8.1554E-08	4.964	0.000
V	3.1720E-07	7.7940E-09	3.944	0.000
Cr	1.6598E-05	3.9957E-07	5.654	0.000
Mn	1.0819E-05	2.4651E-07	5.444	0.000
Fe	8.6674E-04	1.9425E-05	7.341	-0.173
Co	4.2131E-06	8.9483E-08	5.004	0.000
Ni	7.1258E-05	1.5192E-06	6.234	0.000

E.10 Sh 2 – 174, $T_{\text{eff}} = 69 \text{ kK}$, $\log g = 6.7$

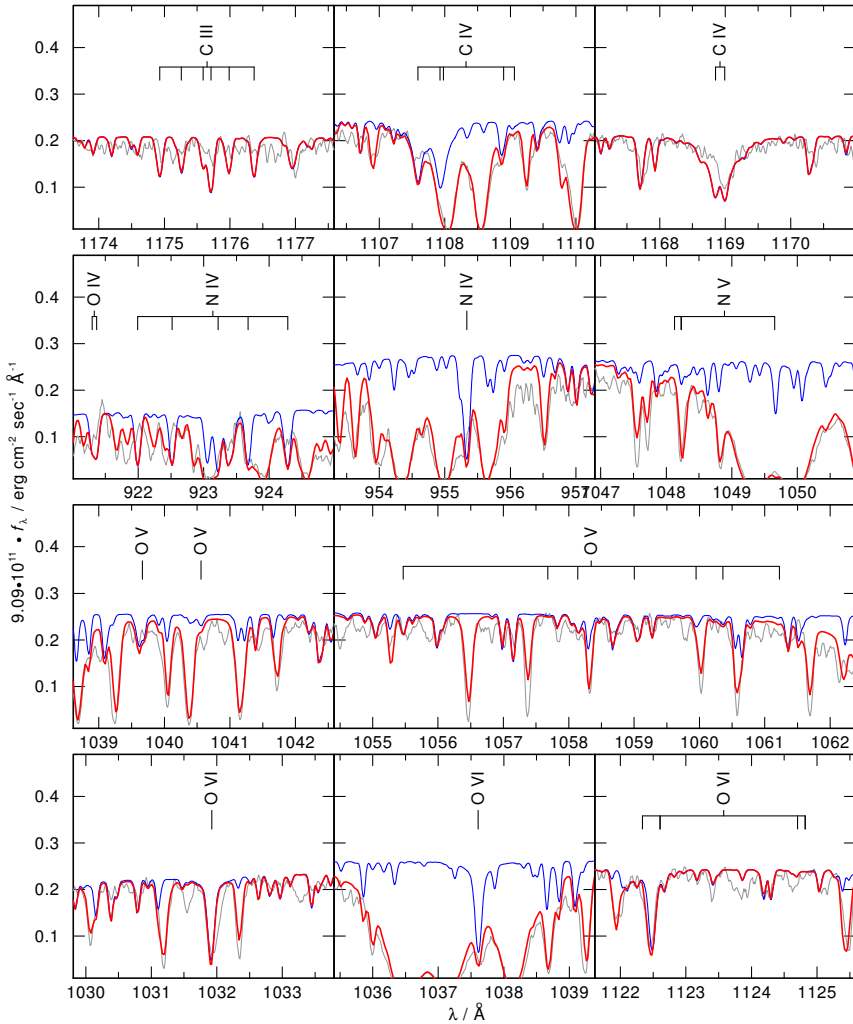
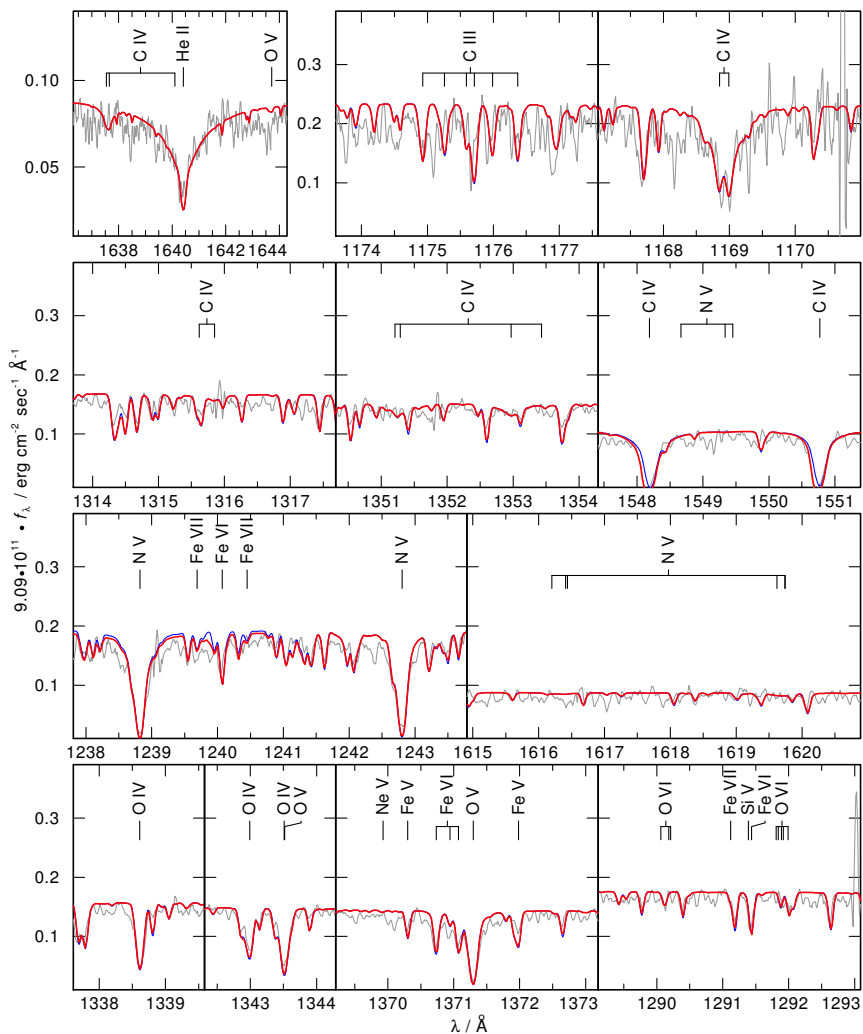


Figure E.39: C, N, and O lines in the *FUSE* observation of Sh 2 – 174.

Figure E.40: He, C, N, and O lines in the *STIS* observation of Sh 2 - 174.

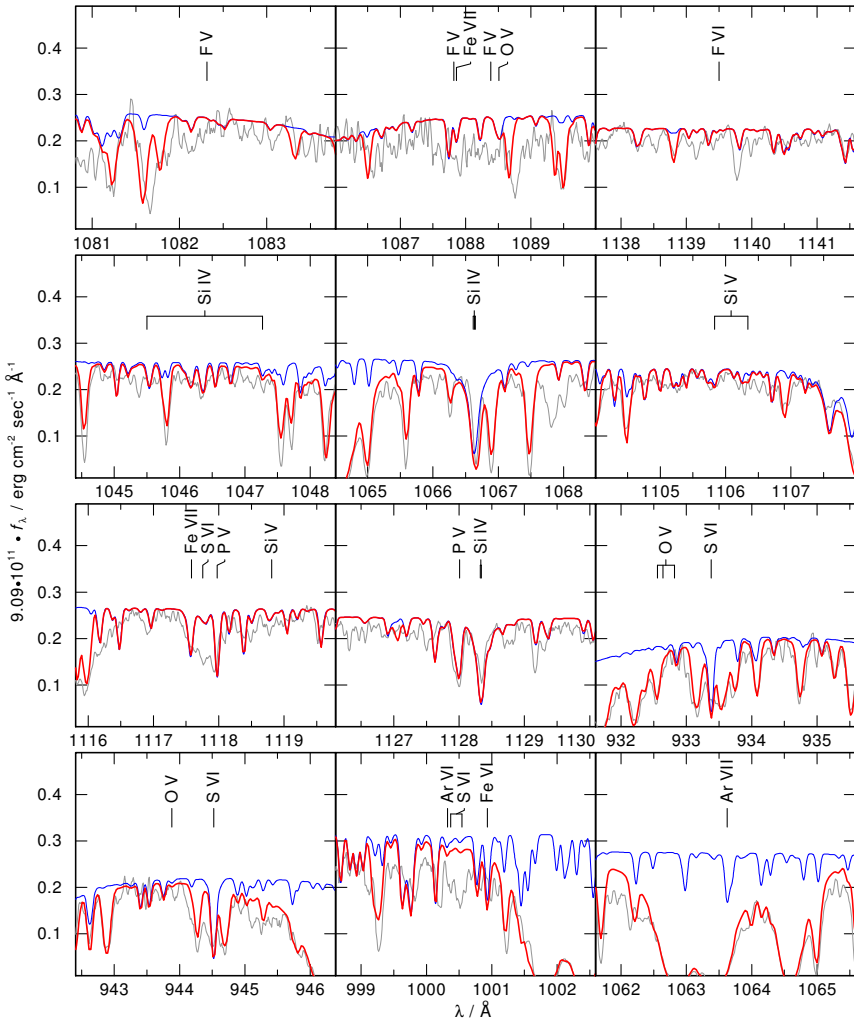


Figure E.41: F, Si, P, S, and Ar lines in the *FUSE* observation of Sh 2 – 174.

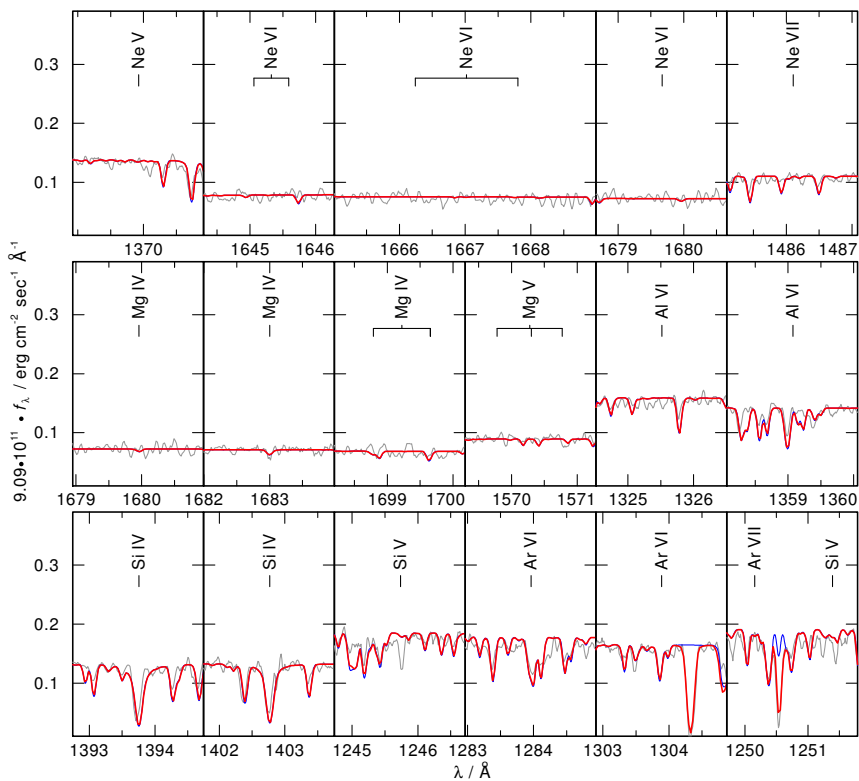


Figure E.42: Ne, Mg, Al, Si, and Ar lines in the *STIS* observation of Sh 2 – 174.

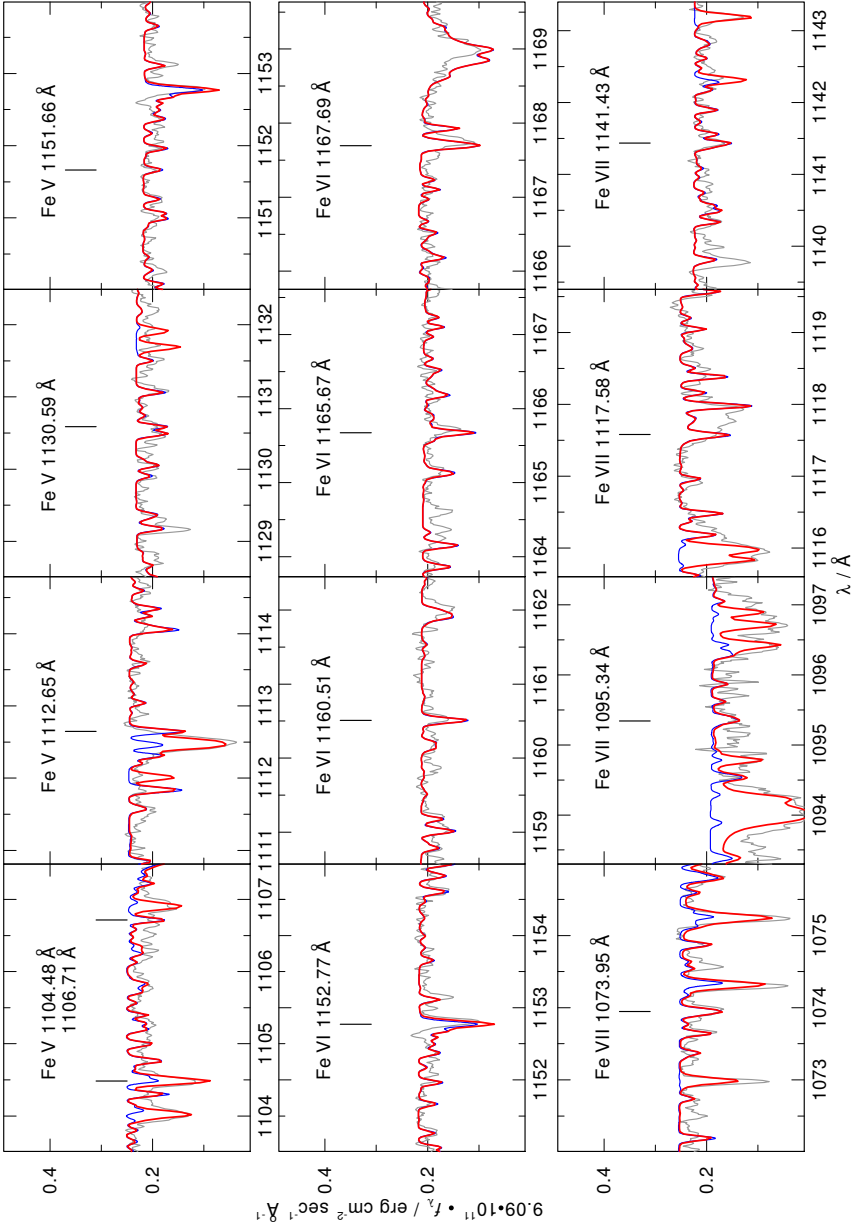


Figure E.43: Fe v – vii lines in the *FUSE* observation of Sh 2 – 174.

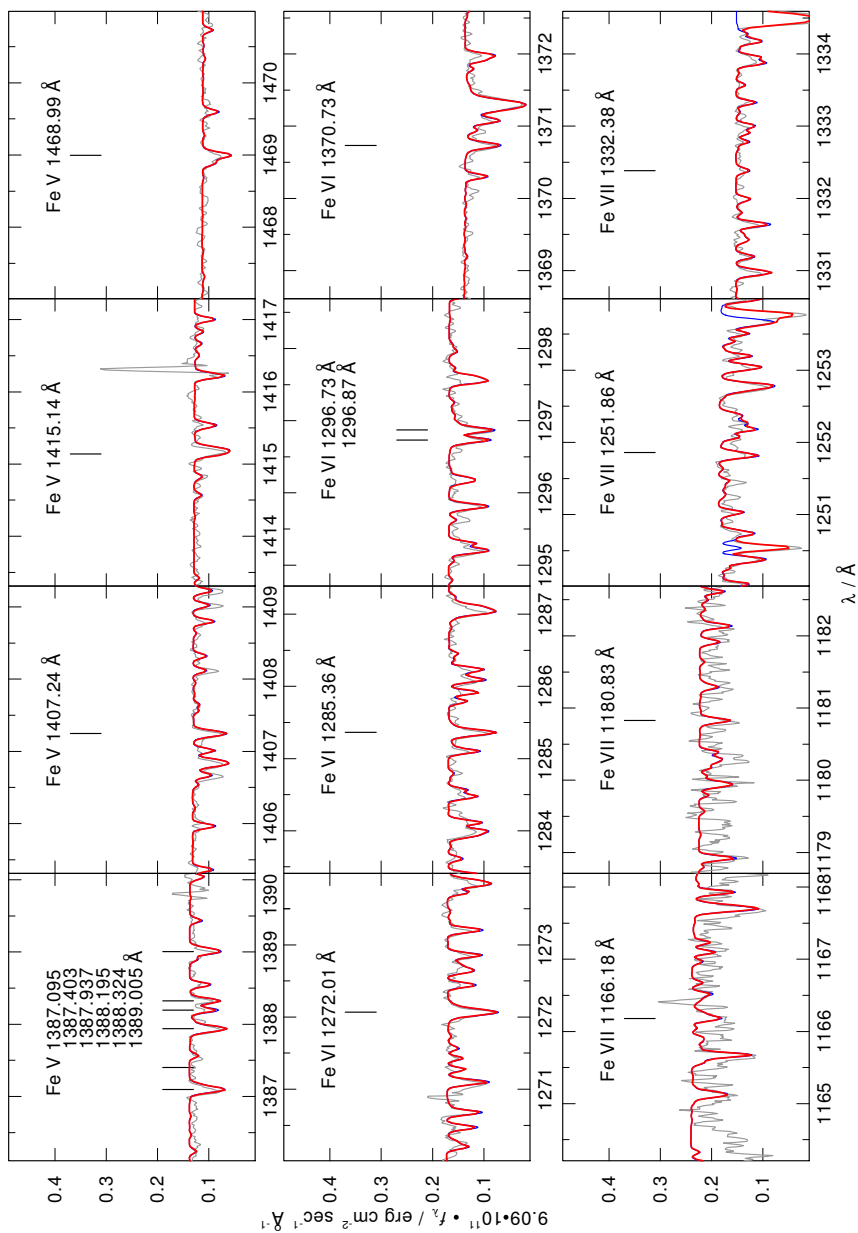


Figure E.44: Fe v – vii lines in the STIS observation of Sh 2 – 174.

Table E.10: Abundances of Sh 2 – 174

element (X)	mass fraction	number fraction	$\log \epsilon$	[X]	
H	8.5422E-01	9.6616E-01	12.078	0.064	
He	1.1547E-01	3.2886E-02	10.610	-0.334	*
C	1.1393E-03	1.0814E-04	8.127	-0.317	*
N	1.0940E-04	8.9041E-06	7.043	-0.802	*
O	1.0072E-03	7.1769E-05	7.949	-0.755	*
F	5.0971E-07	3.0586E-08	4.579	0.004	
Ne	1.2697E-03	7.1732E-05	7.949	0.004	
Na	2.9526E-05	1.4641E-06	6.259	0.004	
Mg	7.1507E-04	3.3540E-05	7.619	0.004	
Al	5.6197E-05	2.3744E-06	6.469	0.004	
Si	6.1264E-03	2.4868E-04	8.489	0.964	*
P	2.3065E-07	8.4892E-09	4.022	-1.402	*
S	7.3949E-06	2.6291E-07	5.513	-1.621	
Ar	5.7128E-05	1.6303E-06	6.305	-0.109	*
Ca	6.4800E-05	1.8431E-06	6.359	0.004	
Sc	4.6927E-08	1.1900E-09	3.169	0.004	
Ti	3.1505E-06	7.5033E-08	4.968	0.004	
V	3.2041E-07	7.1708E-09	3.949	0.004	
Cr	1.8247E-04	4.0007E-06	6.965	1.041	*
Mn	1.7737E-04	3.6807E-06	6.659	1.215	*
Fe	1.8522E-02	3.7807E-04	8.671	1.156	*
Co	1.7062E-05	3.3006E-07	5.612	0.607	*
Ni	8.2414E-04	1.6003E-05	7.297	1.063	*

E.11 A 36, $T_{\text{eff}} = 108 \text{ kK}$, $\log g = 5.9$

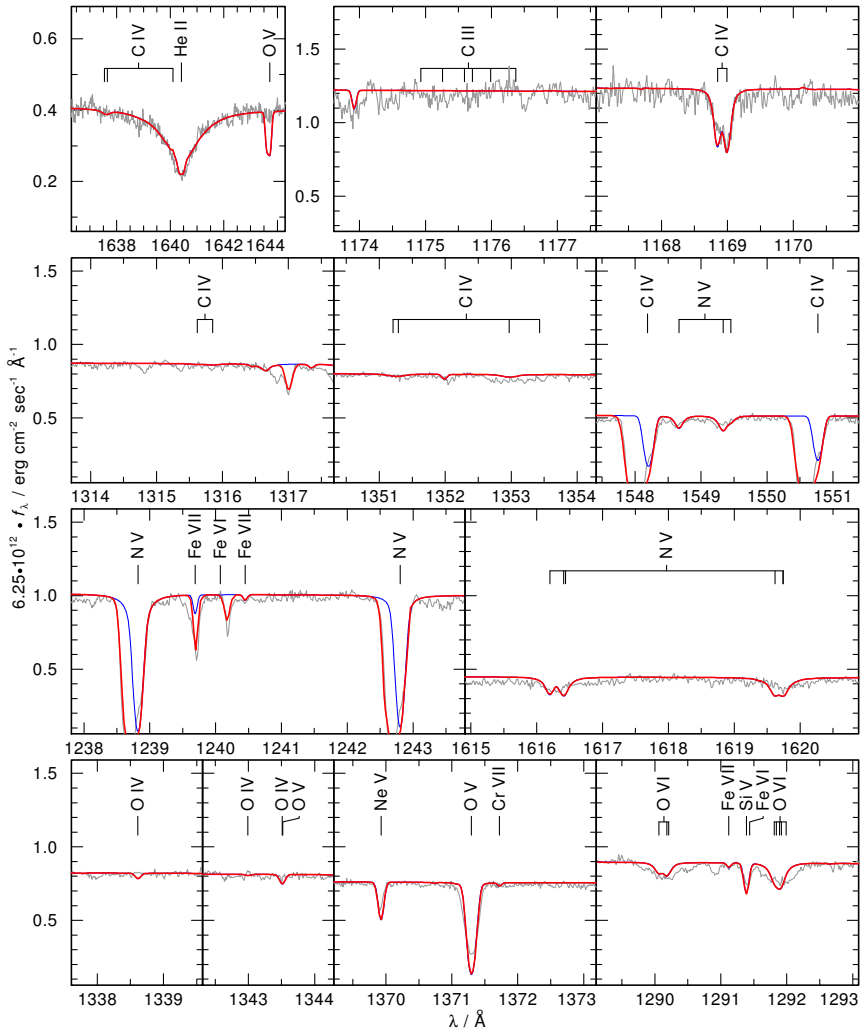
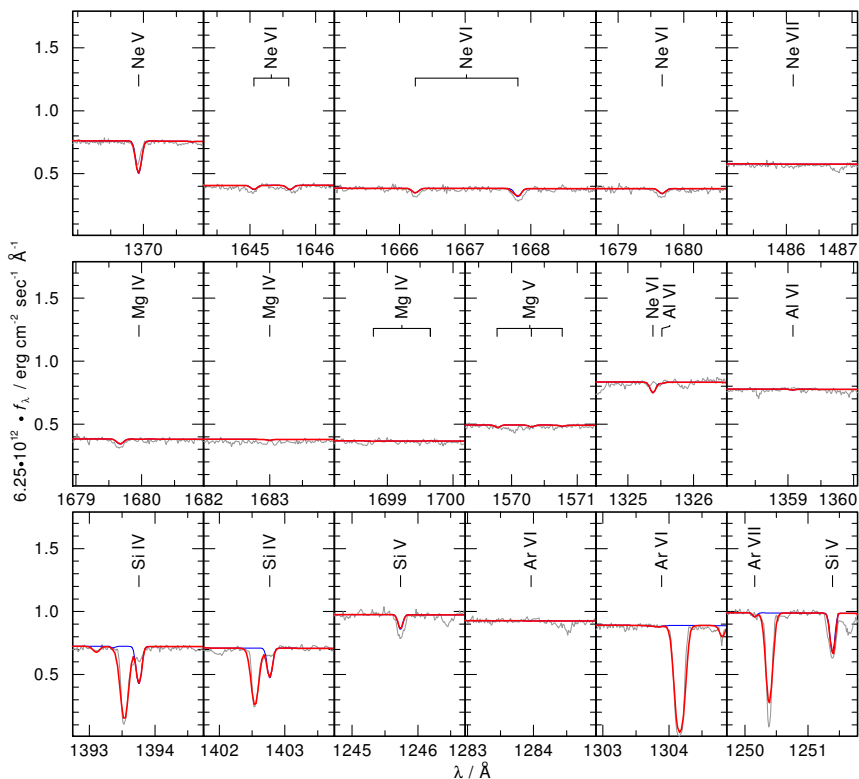


Figure E.45: He, C, N, and O lines in the *STIS* observation of A 36.

Figure E.46: Ne, Mg, Al, Si, and Ar lines in the *STIS* observation of A 36.

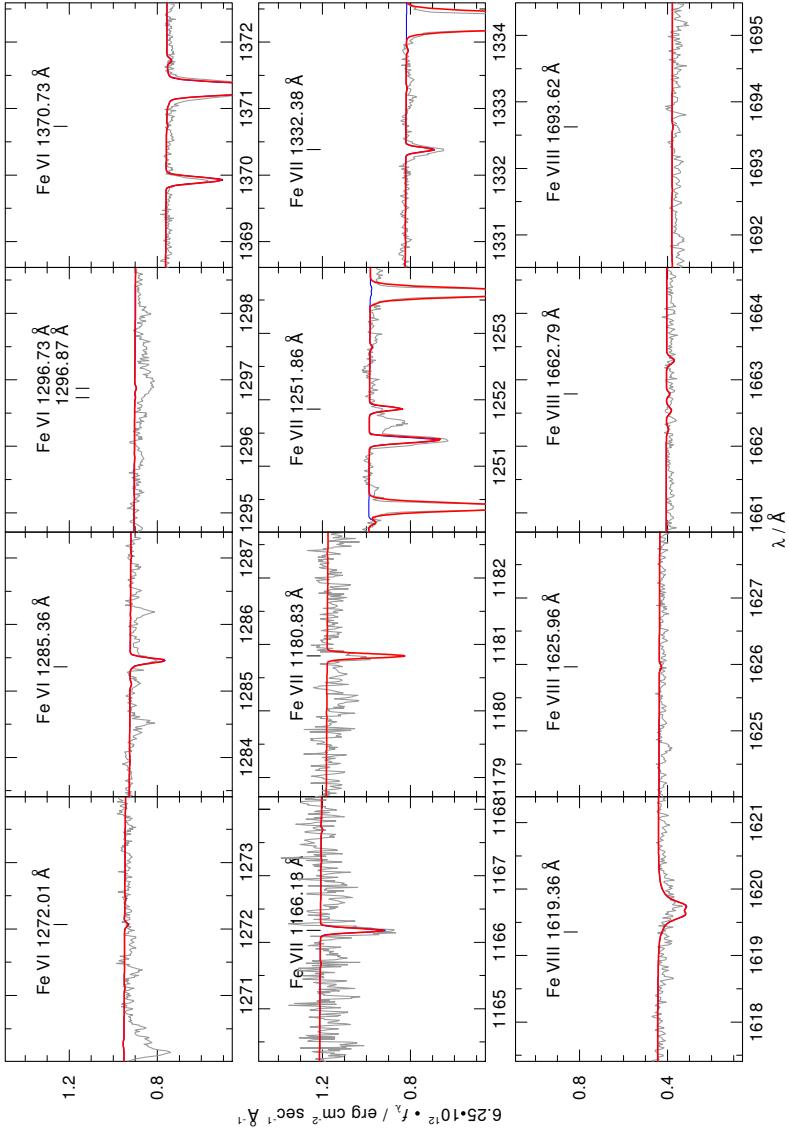
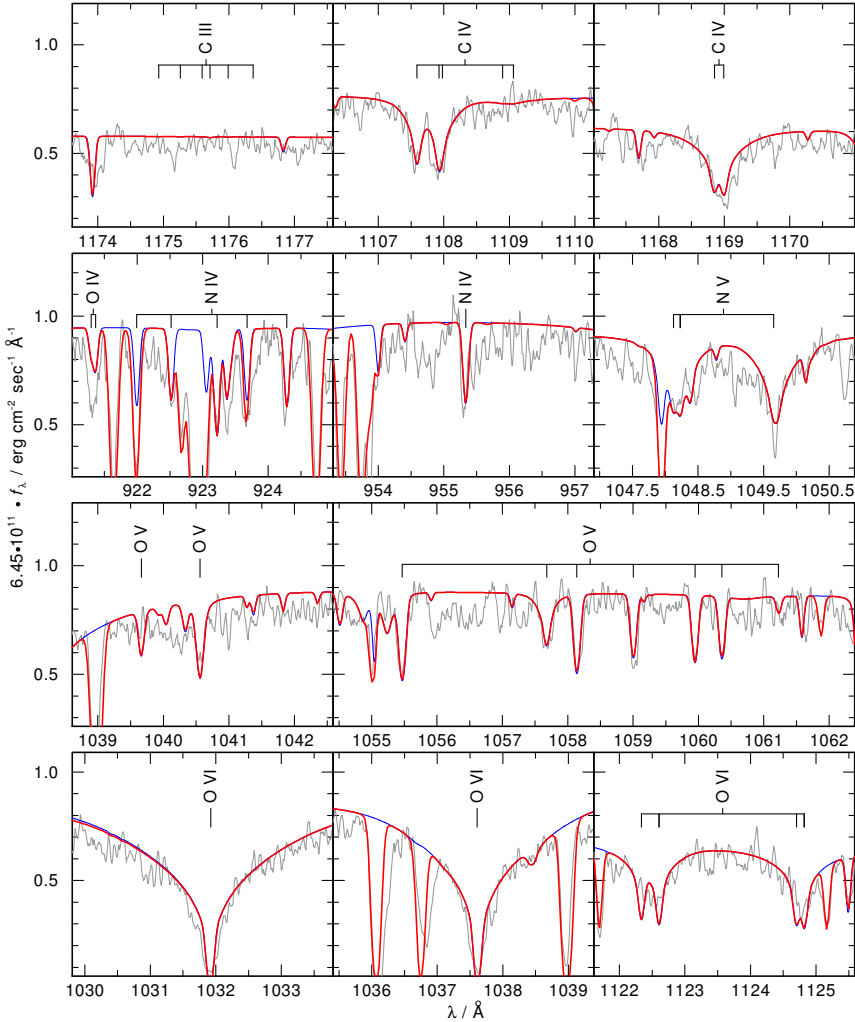
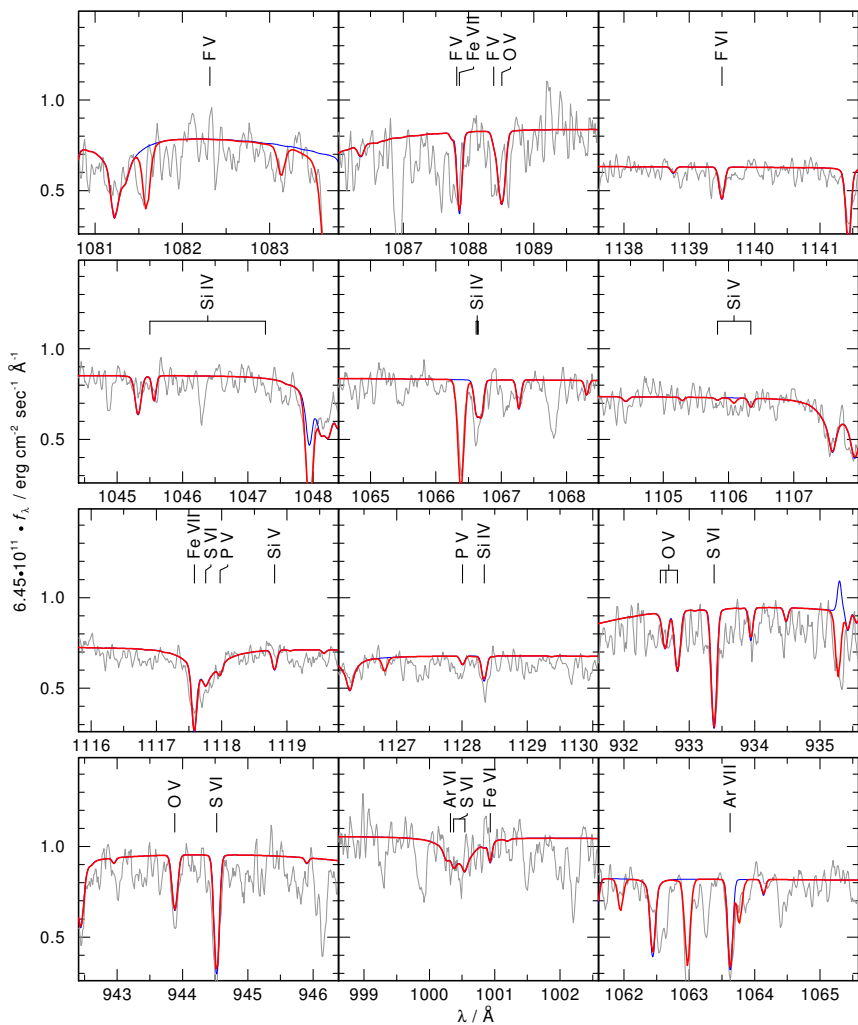


Figure E.47: Fe VI–VIII lines in the STIS observation of A 36.

Table E.11: Abundances of A 36

element (X)	mass fraction	number fraction	$\log \epsilon$	[X]	
H	7.4002E-01	9.2090E-01	12.016	0.002	
He	2.5008E-01	7.8370E-02	10.946	0.002	*
C	8.3562E-04	8.7265E-05	7.992	-0.452	*
N	2.4868E-03	2.2270E-04	8.399	0.555	
O	2.2203E-03	1.7406E-04	8.292	-0.412	*
F	5.0499E-07	3.3340E-08	4.575	0.000	
Ne	3.2076E-03	1.9937E-04	8.351	0.407	*
Na	2.9252E-05	1.5960E-06	6.255	0.000	
Mg	5.9866E-05	3.0895E-06	6.541	-1.073	
Al	5.5676E-05	2.5882E-06	6.465	0.000	
Si	4.0304E-04	1.8000E-05	7.307	-0.217	*
P	5.8302E-06	2.3610E-07	5.425	0.000	
S	3.0944E-04	1.2104E-05	7.135	0.000	
Ar	5.0958E-06	1.6000E-07	5.256	-1.159	
Ca	6.4199E-05	2.0091E-06	6.355	0.000	
Sc	4.6491E-08	1.2971E-09	3.156	0.000	
Ti	3.1212E-06	8.1789E-08	4.964	0.000	
V	3.1212E-07	7.8164E-09	3.945	0.000	
Cr	1.6611E-05	4.0072E-07	5.654	0.000	
Mn	1.0828E-05	2.4721E-07	5.445	0.000	
Fe	1.0254E-04	2.3029E-06	6.414	-1.100	*
Co	4.2164E-06	8.9741E-08	5.005	0.000	
Ni	7.1314E-05	1.5236E-06	6.234	0.000	

E.12 Lo 1, $T_{\text{eff}} = 120 \text{ kK}$, $\log g = 7.0$ Figure E.48: C, N, and O lines in the *FUSE* observation of Lo 1.

Figure E.49: F, Si, P, S, and Ar lines in the *FUSE* observation of Lo 1.

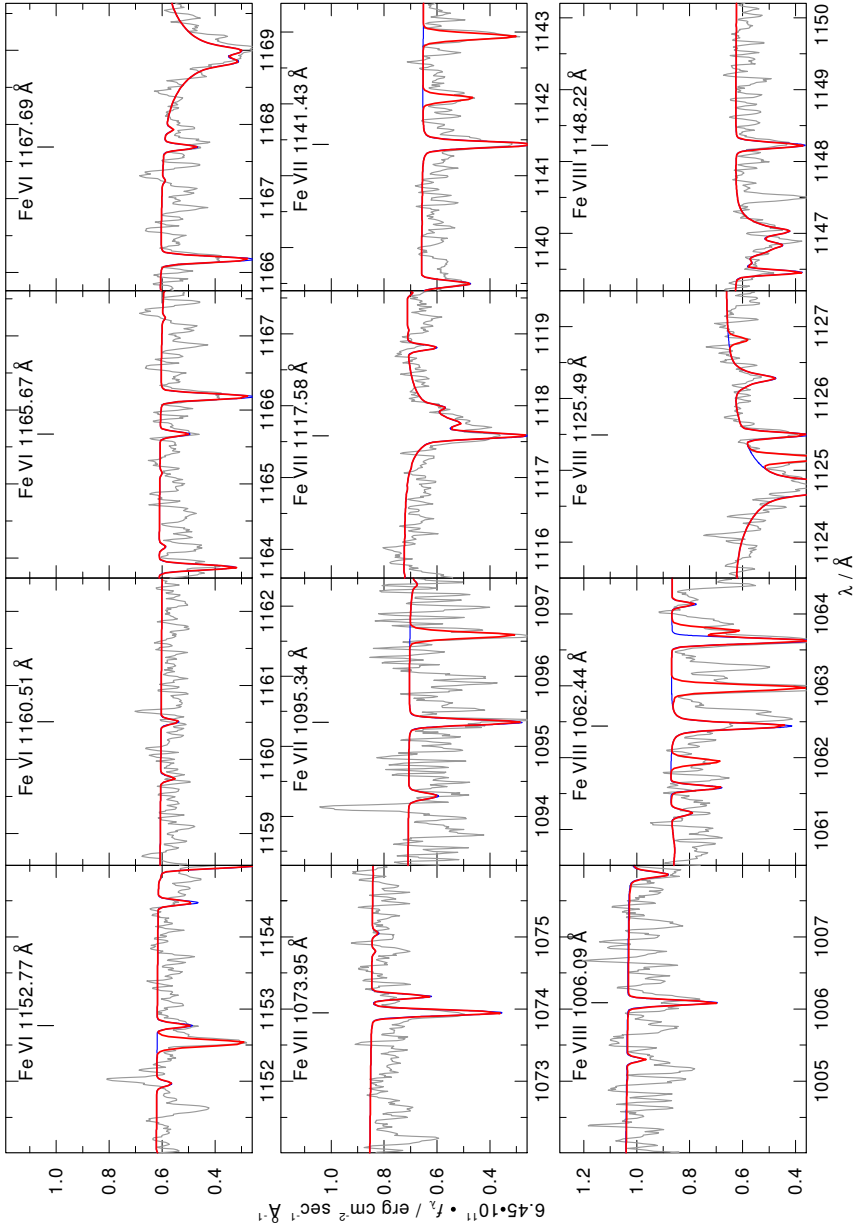
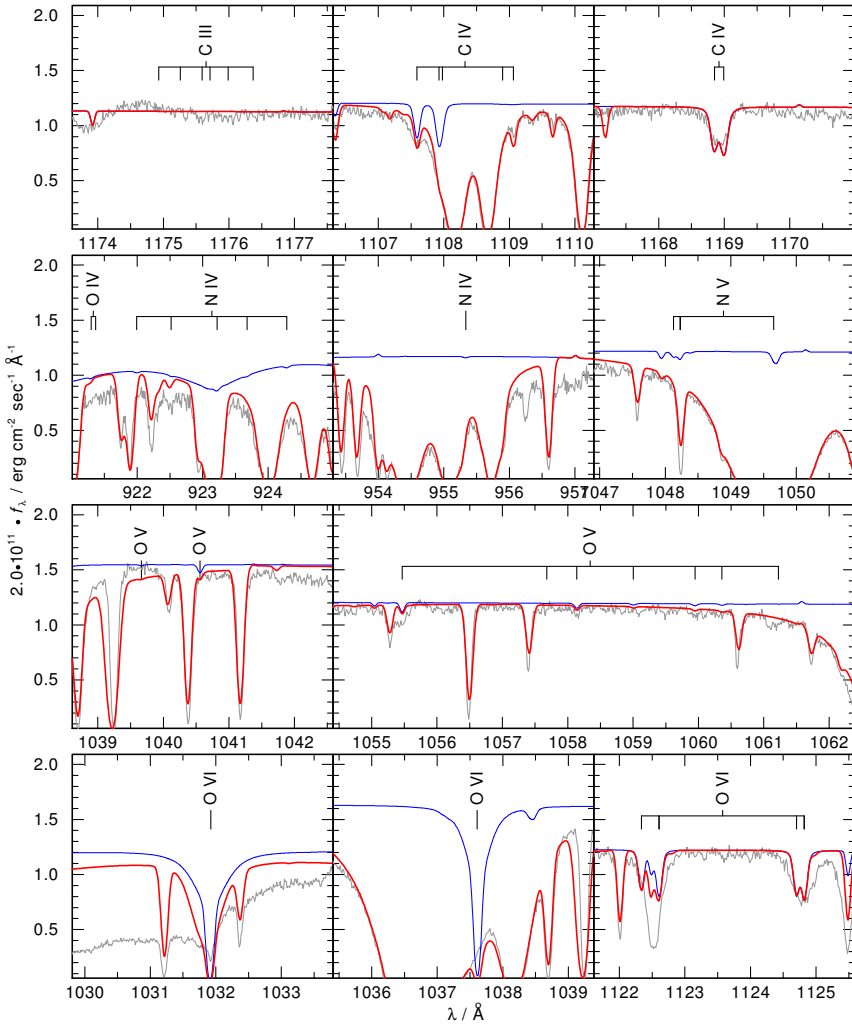
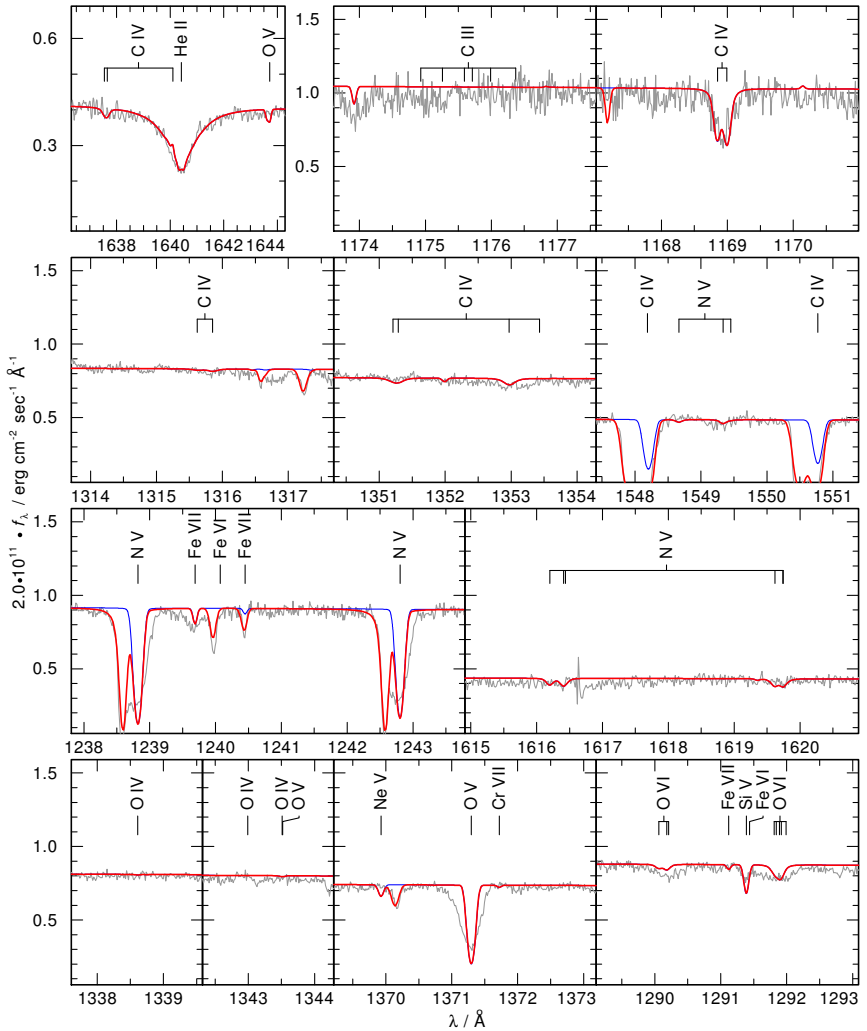


Figure E.50: Fe VI – VIII lines in the *FUSE* observation of Lo 1.

Table E.12: Abundances of Lo 1

element (X)	mass fraction	number fraction	$\log \epsilon$	[X]	
H	6.5630E-01	9.1227E-01	11.964	-0.051	
He	2.2179E-01	7.7636E-02	10.894	-0.051	
C	1.3643E-02	1.5915E-03	9.205	0.761	*
N	3.0530E-02	3.0539E-03	9.488	1.644	*
O	5.4521E-02	4.7744E-03	9.682	0.978	*
F	4.4614E-07	3.2901E-08	4.521	-0.053	*
Ne	1.2345E-03	8.5712E-05	7.937	-0.008	
Na	2.8707E-05	1.7495E-06	6.246	-0.008	
Mg	6.9525E-04	4.0077E-05	7.606	-0.008	
Al	5.4639E-05	2.8372E-06	6.456	-0.008	
Si	2.3392E-04	1.1669E-05	7.071	-0.454	*
P	2.2481E-06	1.0169E-07	5.011	-0.413	
S	2.8551E-04	1.2475E-05	7.100	-0.035	*
Ar	6.4910E-05	2.2765E-06	6.361	-0.053	*
Ca	6.3003E-05	2.2024E-06	6.346	-0.008	
Sc	4.5625E-08	1.4219E-09	3.156	-0.008	
Ti	3.0631E-06	8.9656E-08	4.956	-0.008	
V	3.1153E-07	8.5683E-09	3.936	-0.008	
Cr	1.6302E-05	4.3926E-07	5.646	-0.008	
Mn	1.0626E-05	2.7099E-07	5.437	-0.008	
Fe	2.0442E-02	5.1281E-04	8.714	1.199	*
Co	4.1379E-06	9.8373E-08	4.996	-0.008	
Ni	6.9986E-05	1.6701E-06	6.226	-0.008	

E.13 LSS 1362, $T_{\text{eff}} = 106 \text{ kK}$, $\log g = 5.6$ Figure E.51: C, N, and O lines in the *FUSE* observation of LSS 1362.

Figure E.52: He, C, N, and O lines in the *STIS* observation of LSS 1362.

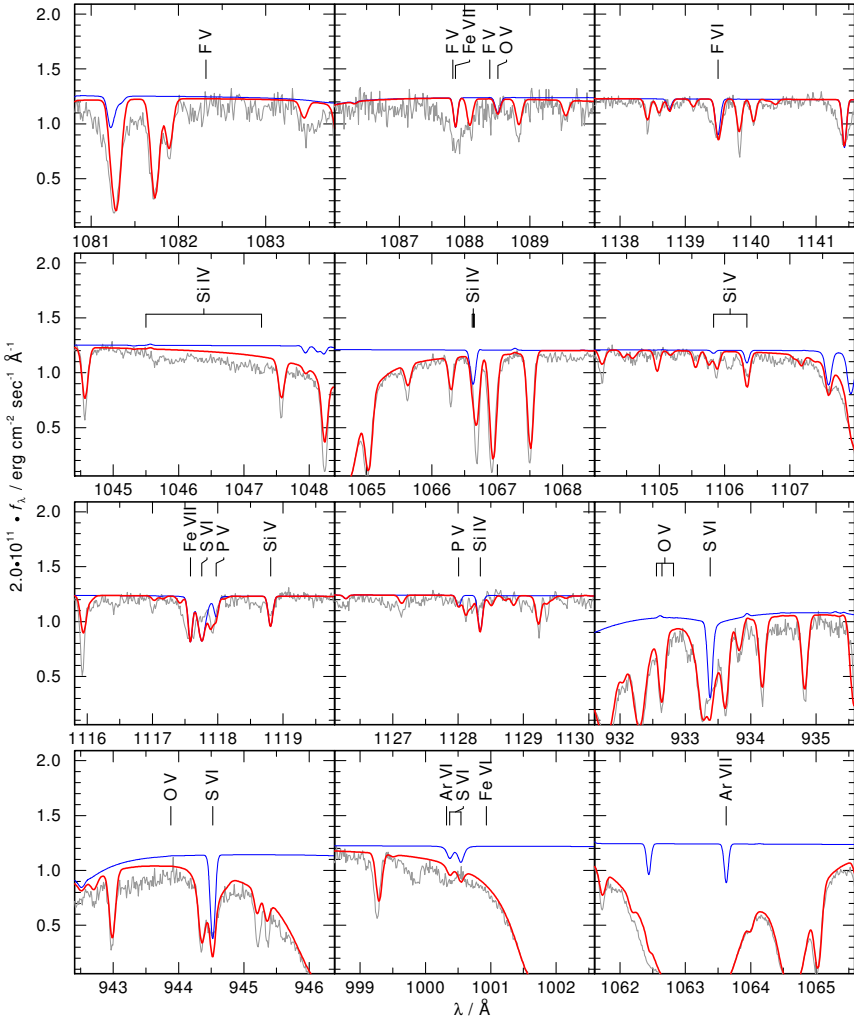
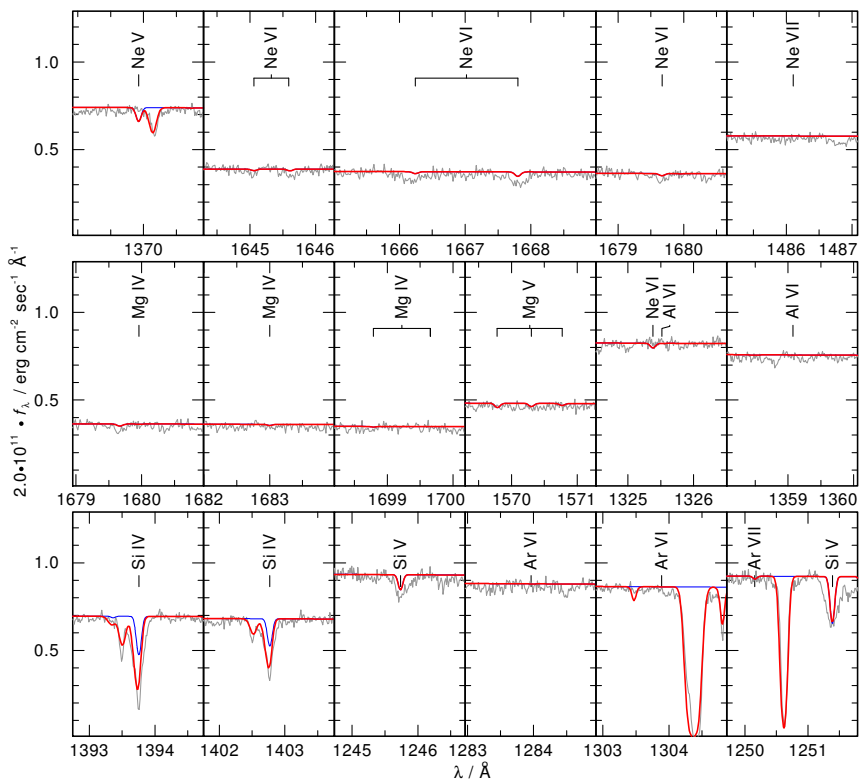
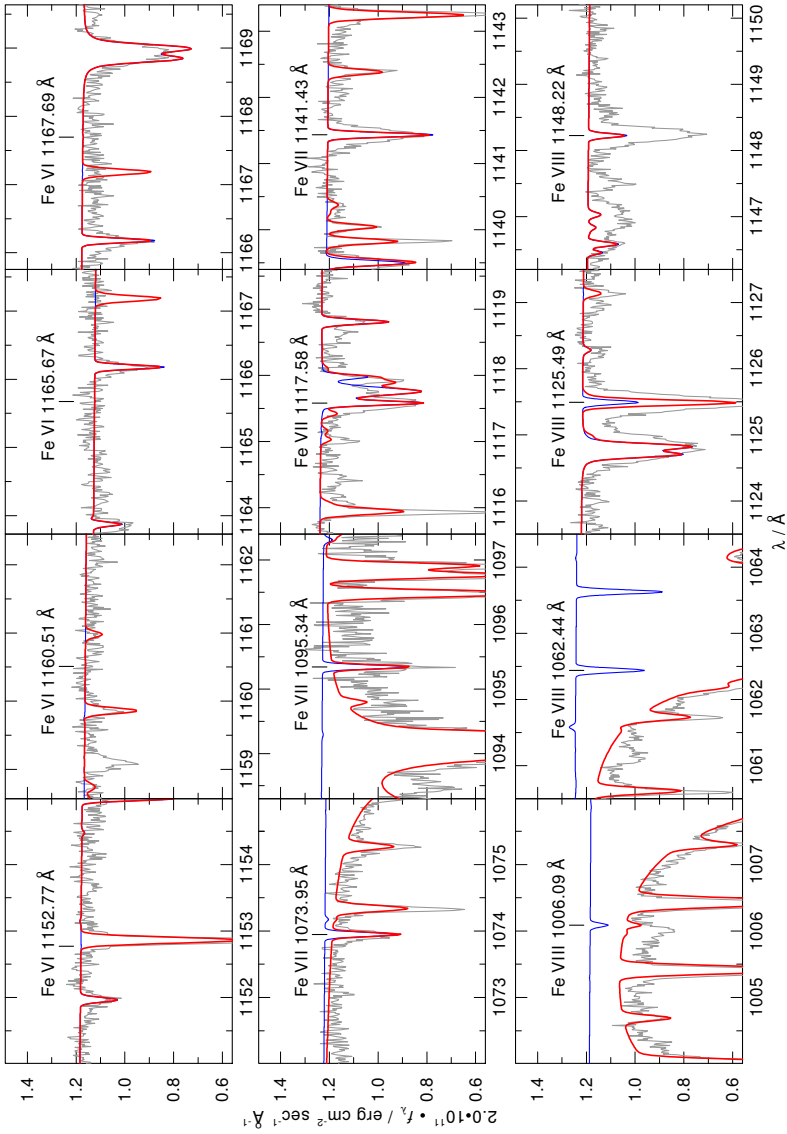
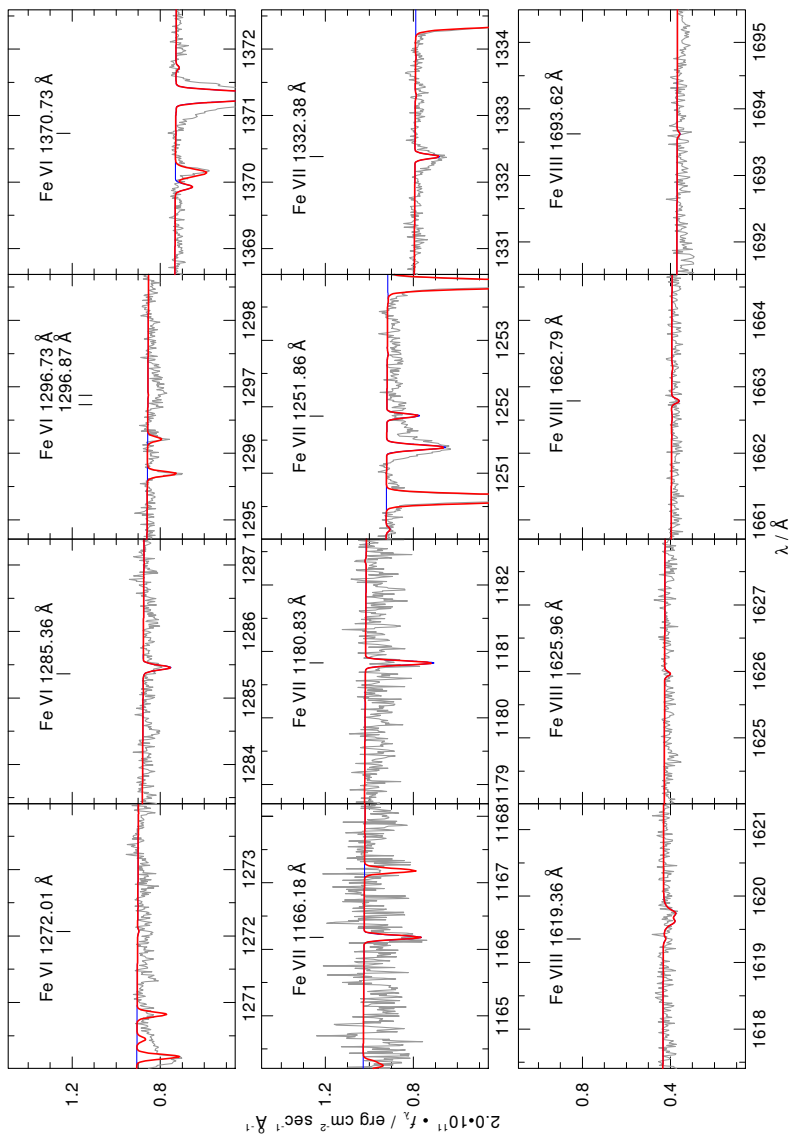


Figure E.53: F, Si, P, S, and Ar lines in the *FUSE* observation of LSS 1362.

Figure E.54: Ne, Mg, Al, Si, and Ar lines in the *STIS* observation of LSS 1362.

Figure E.55: Fe VI–VIII lines in the *FUSE* observation of LSS 1362.

Figure E.56: Fe VI – VIII lines in the *STIS* observation of LSS 1362.

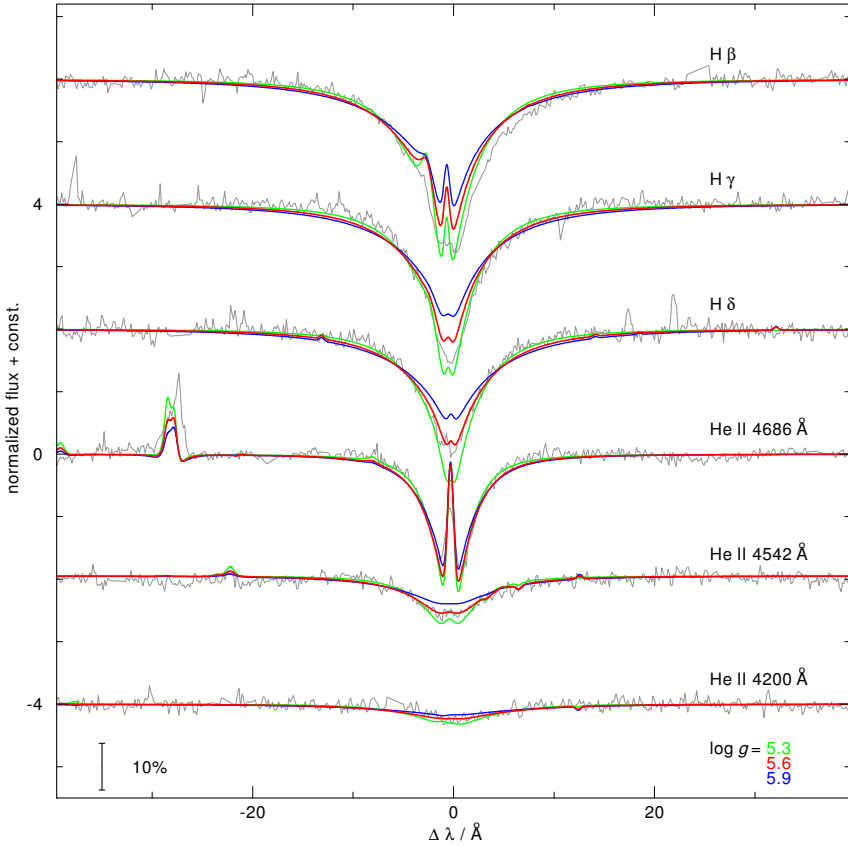
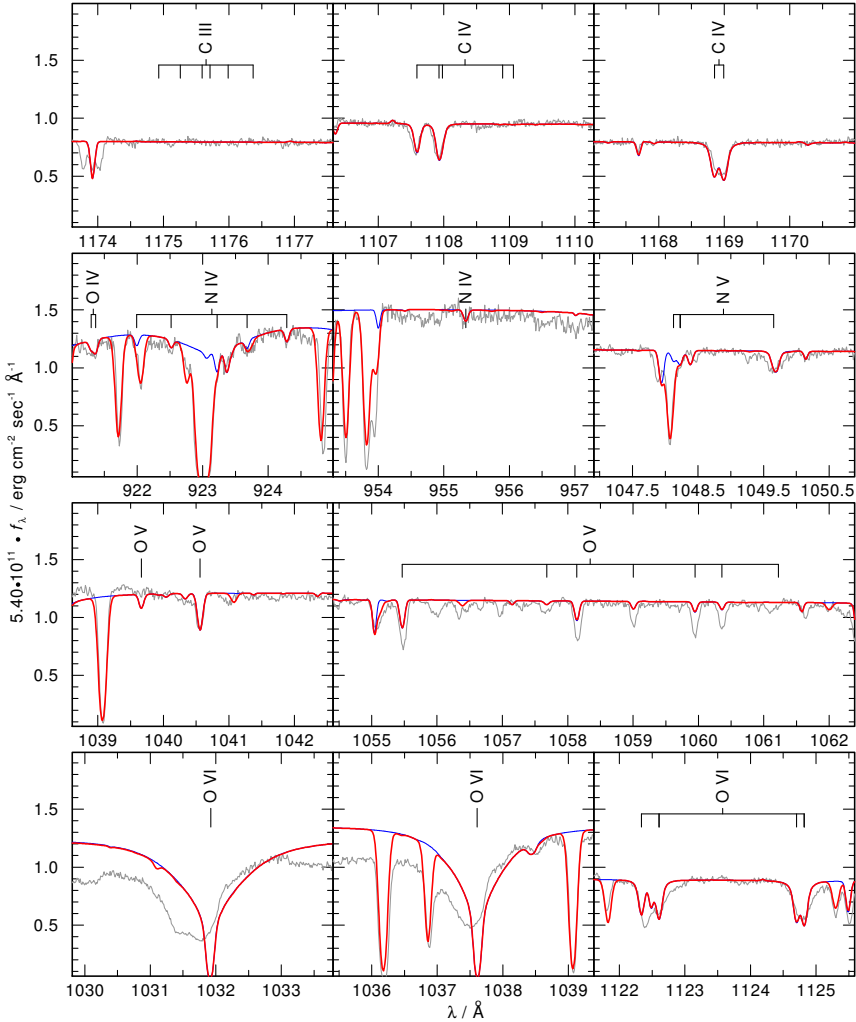
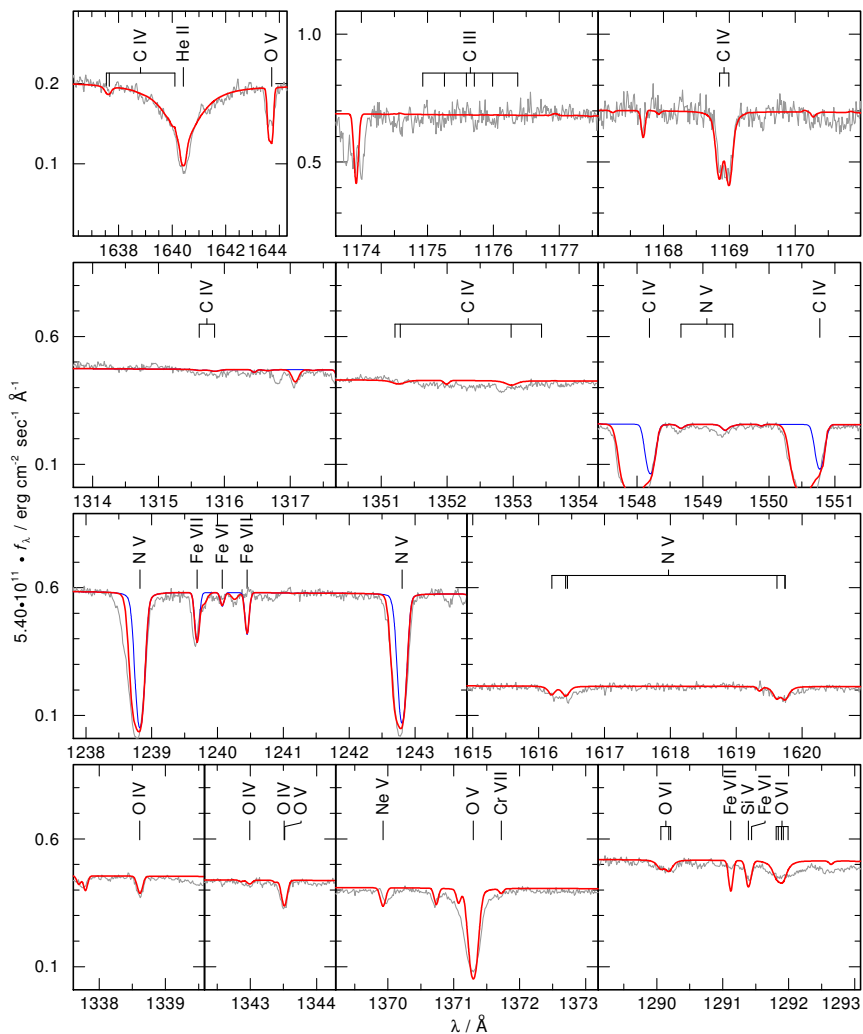


Figure E.57: H and He lines in the optical observation of LSS 1362.

Table E.13: Abundances of LSS 1362

element (X)	mass fraction	number fraction	$\log \epsilon$	[X]	
H	7.4459E-01	9.2128E-01	12.018	0.004	*
He	2.5165E-01	7.8410E-02	10.948	0.004	*
C	1.7746E-03	1.8426E-04	8.320	-0.125	*
N	2.8176E-04	2.5087E-05	7.454	-0.391	*
O	5.7913E-04	4.5143E-05	7.709	-0.996	*
F	7.9222E-08	5.2004E-09	3.770	-0.804	*
Ne	4.0624E-04	2.5106E-05	7.454	-0.491	*
Na	2.9267E-05	1.5877E-06	6.255	0.001	
Mg	7.1691E-05	3.6786E-06	6.620	-0.995	
Al	4.6592E-06	2.1536E-07	5.387	-1.077	
Si	1.8612E-04	8.2645E-06	6.971	-0.553	*
P	1.1922E-06	4.8004E-08	4.735	-0.689	
S	1.3499E-04	5.2504E-06	6.774	-0.360	
Ar	9.6104E-07	3.0002E-08	4.531	-1.883	
Ca	6.4232E-05	1.9986E-06	6.355	0.001	
Sc	4.6515E-08	1.2904E-09	3.165	0.001	
Ti	3.1228E-06	8.1362E-08	4.965	0.001	
V	3.1760E-07	7.7757E-09	3.945	0.001	
Cr	1.6620E-05	3.9863E-07	5.655	0.001	
Mn	1.0833E-05	2.4593E-07	5.445	0.001	
Fe	1.1534E-04	2.5756E-06	6.465	-1.049	*
Co	4.2186E-06	8.9273E-08	5.005	0.001	
Ni	7.1351E-05	1.5157E-06	6.235	0.001	

E.14 NGC 1360, $T_{\text{eff}} = 100 \text{ kK}$, $\log g = 5.7$ Figure E.58: C, N, and O lines in the *FUSE* observation of NGC 1360.

Figure E.59: He, C, N, and O lines in the *STIS* observation of NGC 1360.

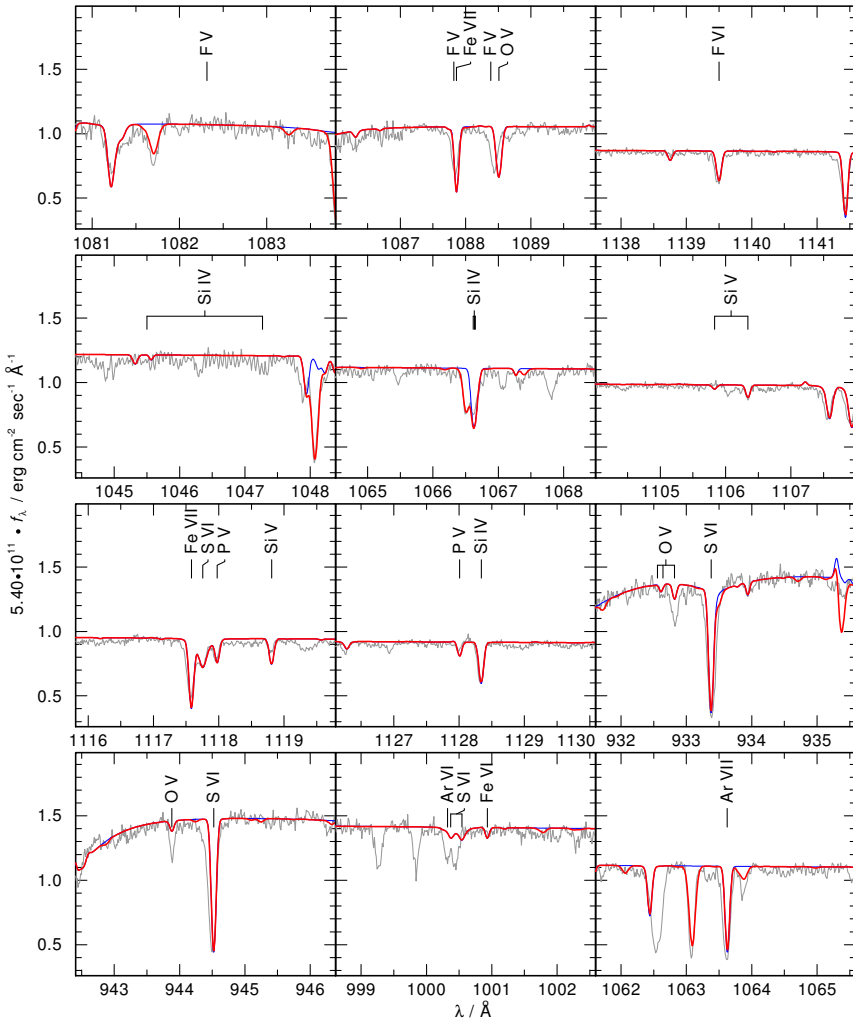


Figure E.60: F, Si, P, S, and Ar lines in the *FUSE* observation of NGC 1360.

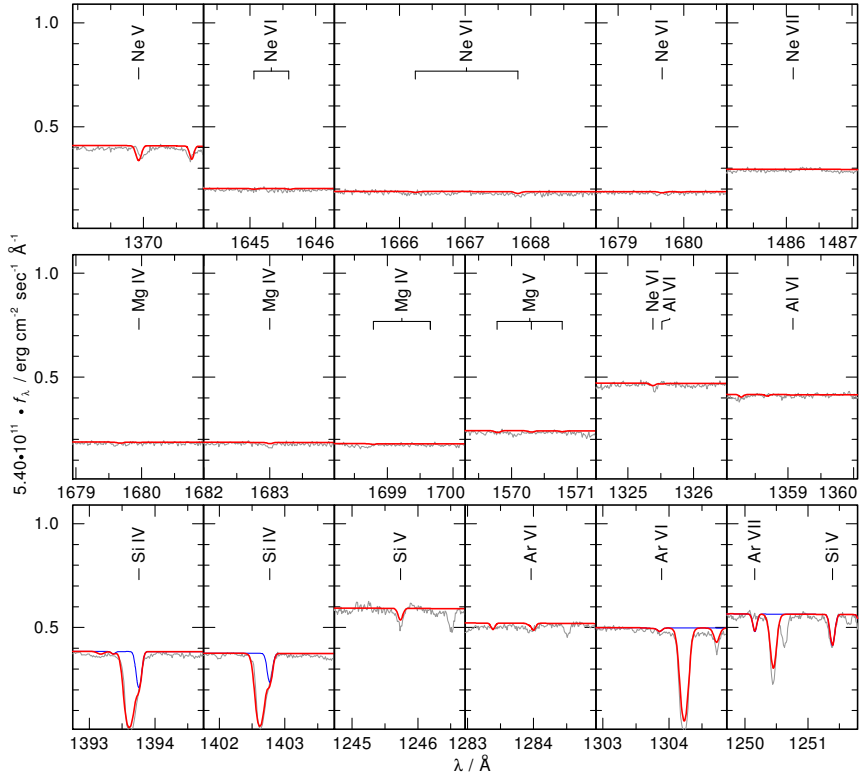


Figure E.61: Ne, Mg, Al, Si, and Ar lines in the *STIS* observation of NGC 1360.

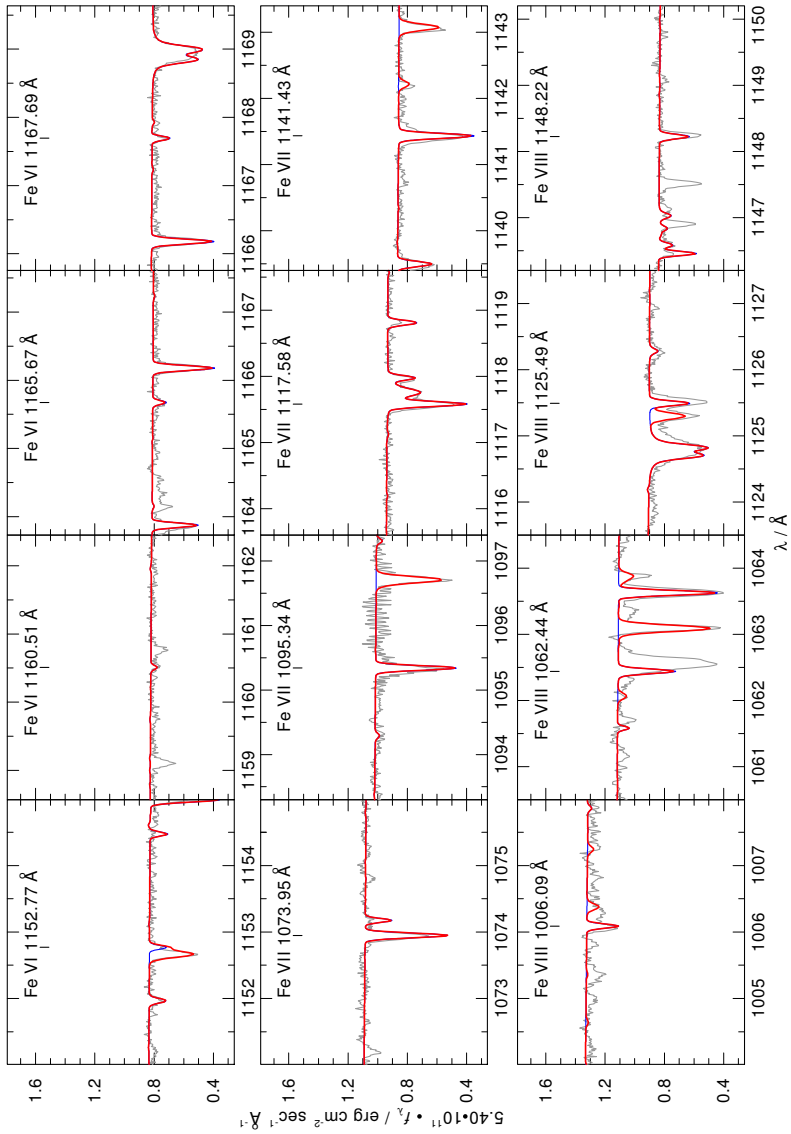


Figure E.62: Fe VI – VIII lines in the *FUSE* observation of NGC 1360.

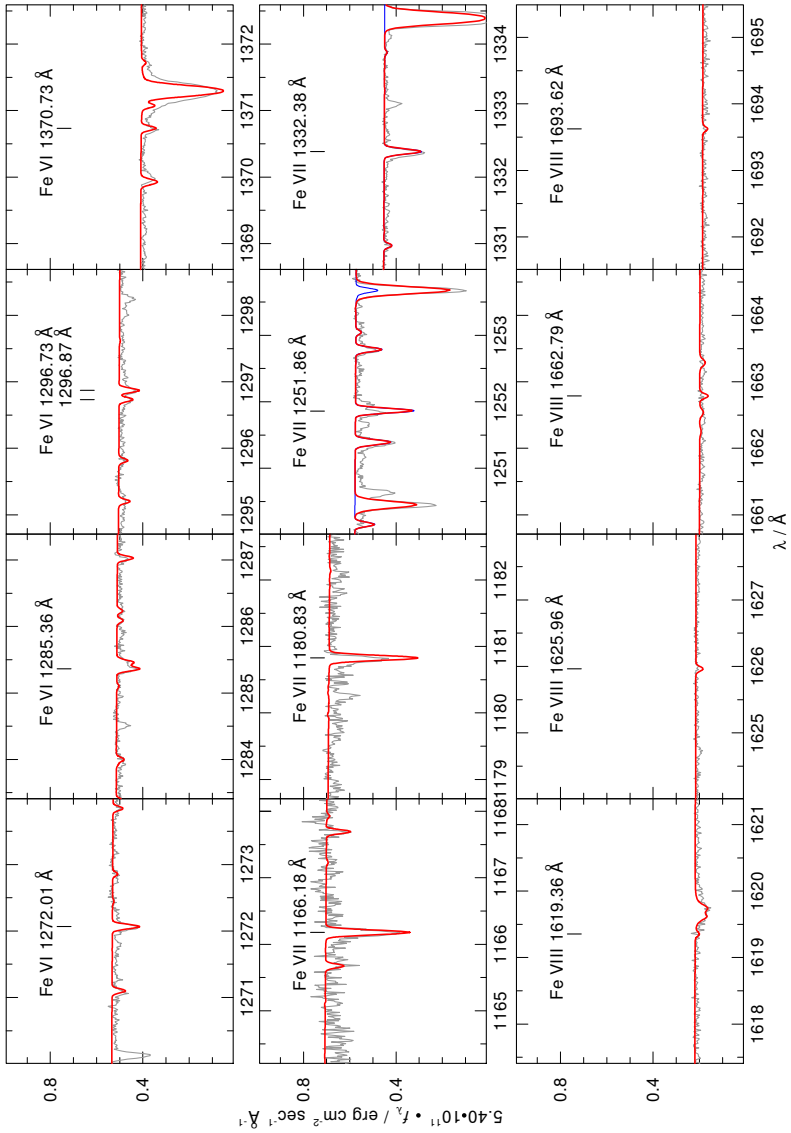


Figure E.63: Fe VI–VIII lines in the STIS observation of NGC 1360.

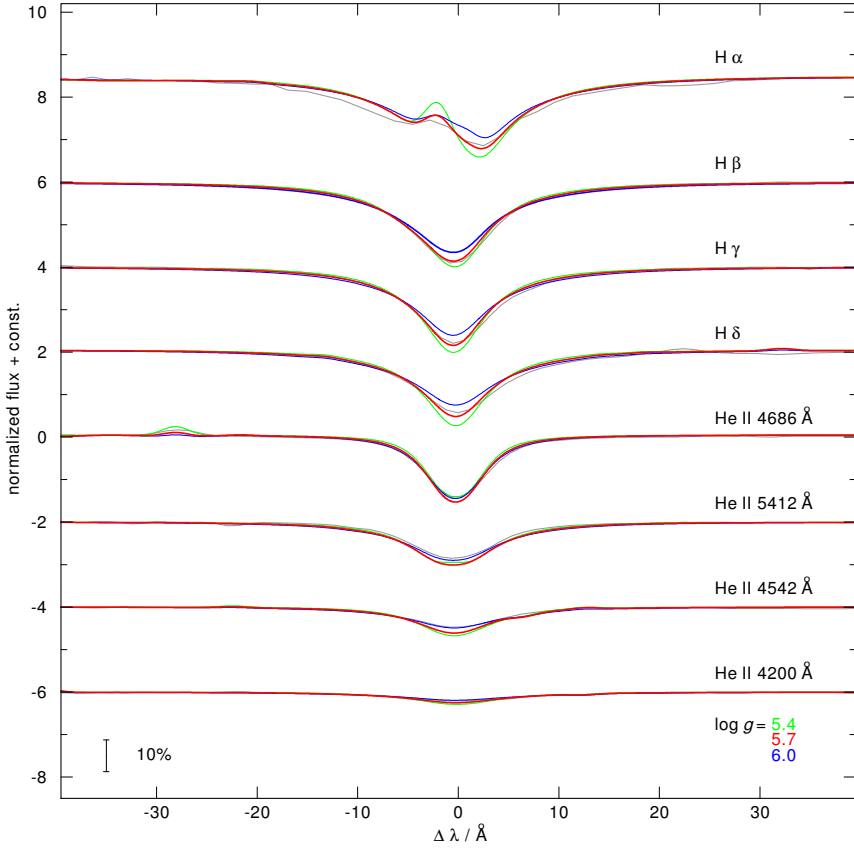


Figure E.64: H and He lines in the optical observation of NGC 1360.

Table E.14: Abundances of NGC 1360

element (X)	mass fraction	number fraction	$\log \epsilon$	[X]	
H	7.4199E-01	9.2118E-01	12.017	0.003	*
He	2.5075E-01	7.8393E-02	10.947	0.003	*
C	9.5168E-04	9.9152E-05	8.049	-0.395	*
N	3.4796E-04	3.1087E-05	7.545	-0.299	*
O	2.2364E-03	1.7491E-04	8.295	-0.409	*
F	1.2146E-07	8.0001E-09	3.956	-0.619	*
Ne	7.1441E-04	4.4301E-05	7.699	-0.245	*
Na	2.9242E-05	1.5916E-06	6.254	0.000	
Mg	6.0211E-05	3.1000E-06	6.544	-1.070	
Al	5.5655E-05	2.5812E-06	6.464	0.000	
Si	4.0045E-04	1.7842E-05	7.304	-0.220	*
P	1.0433E-06	4.2151E-08	4.677	-0.747	*
S	4.2281E-05	1.6500E-06	6.270	-0.864	*
Ar	7.9771E-06	2.4988E-07	5.450	-0.964	*
Ca	6.4175E-05	2.0036E-06	6.354	0.000	
Sc	4.6474E-08	1.2936E-09	3.164	0.000	
Ti	3.1201E-06	8.1566E-08	4.964	0.000	
V	3.1733E-07	7.7952E-09	3.944	0.000	
Cr	2.8654E-05	6.8960E-07	5.891	0.237	
Mn	1.0824E-05	2.4654E-07	5.445	0.000	
Fe	2.2305E-03	4.9976E-05	7.751	0.237	*
Co	4.2149E-06	8.9496E-08	5.004	0.000	
Ni	7.1288E-05	1.5194E-06	6.234	0.000	

E.15 NGC 4361, $T_{\text{eff}} = 126 \text{ kK}$, $\log g = 6.0$

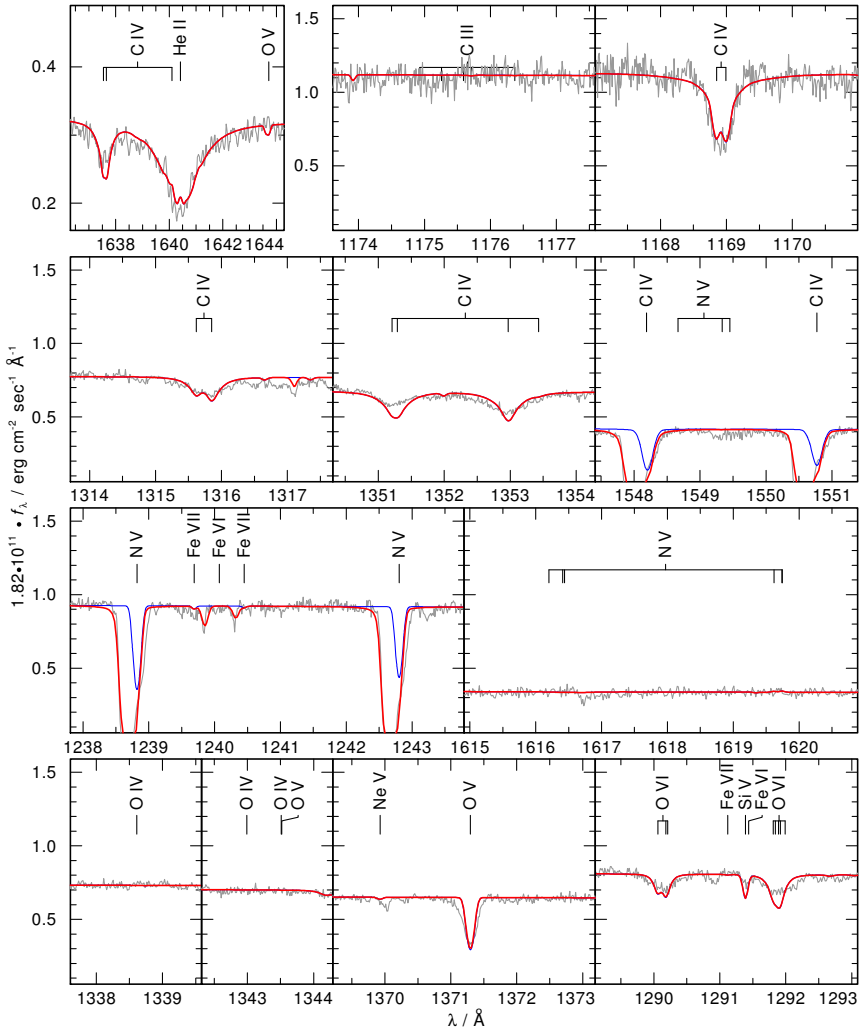
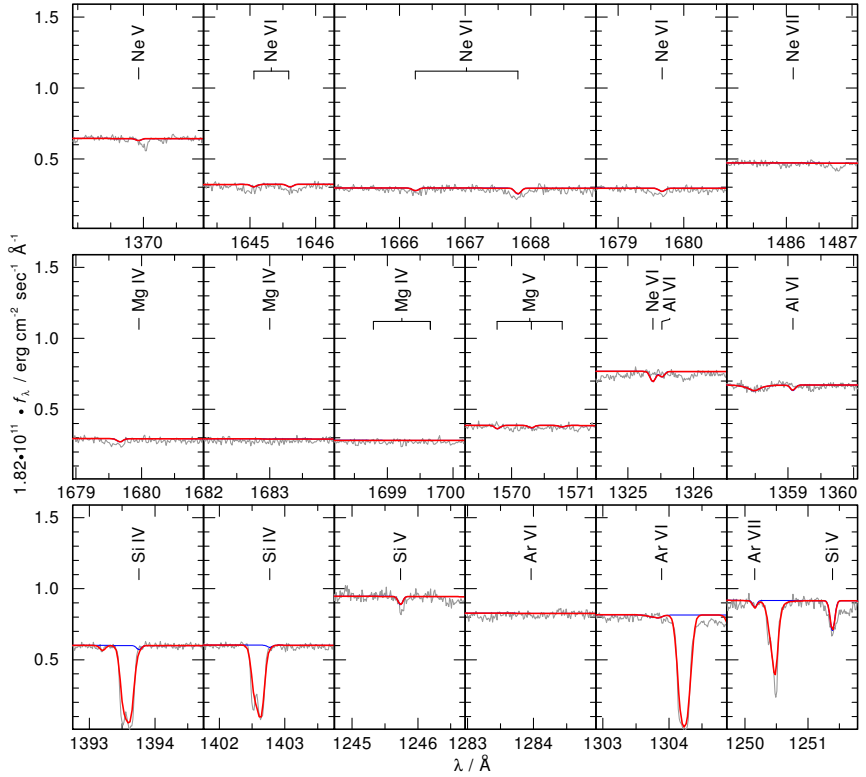


Figure E.65: He, C, N, and O lines in the STIS observation of NGC 4361.

Figure E.66: Ne, Mg, Al, Si, and Ar lines in the *STIS* observation of NGC 4361.

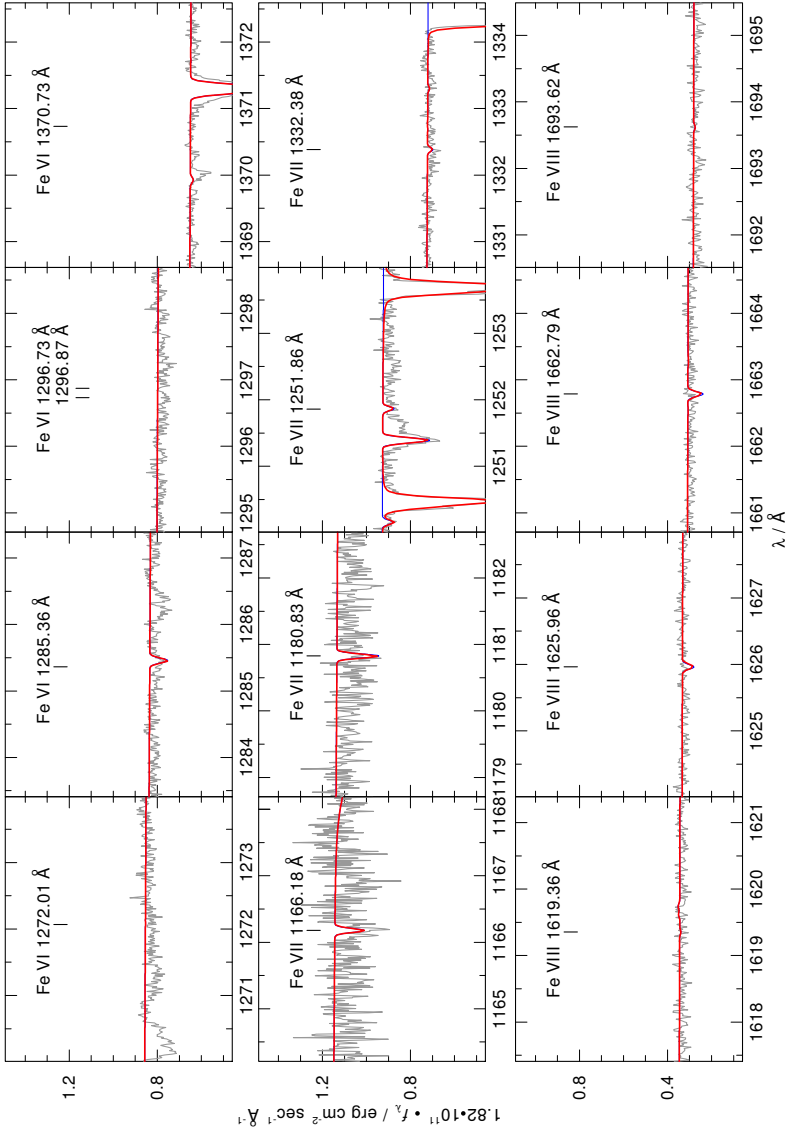


Figure E.67: Fe VI– VIII lines in the *STIS* observation of NGC 4361.

Table E.15: Abundances of NGC 4361

element (X)	mass fraction	number fraction	log eps	[X]	
H	6.6605E-01	9.0212E-01	11.970	-0.044	
He	2.6449E-01	9.0212E-02	10.970	0.026	*
C	6.3494E-02	7.2170E-03	9.873	1.429	*
N	5.5534E-05	5.4127E-06	6.748	-1.096	
O	3.9686E-03	3.3863E-04	8.545	-0.160	*
F	5.0489E-07	3.6280E-08	4.574	0.000	
Ne	9.2251E-04	6.2409E-05	7.810	-0.134	
Na	2.9247E-05	1.7367E-06	6.255	0.000	
Mg	1.7804E-04	1.0001E-05	7.015	-0.599	
Al	4.1792E-05	2.1146E-06	6.340	-0.124	
Si	1.5456E-04	7.5128E-06	6.891	-0.634	*
P	5.8290E-06	2.5692E-07	5.425	0.000	
S	3.0937E-04	1.3172E-05	7.134	0.000	
Ar	4.0091E-05	1.3701E-06	6.152	-0.263	
Ca	6.4186E-05	2.1863E-06	6.355	0.000	
Sc	4.6482E-08	1.4115E-09	3.164	0.000	
Ti	3.1206E-06	8.9001E-08	4.964	0.000	
V	3.1738E-07	8.5057E-09	3.945	0.000	
Cr	1.3459E-06	3.5338E-08	4.563	-1.091	
Mn	1.0826E-05	2.6901E-07	5.445	0.000	
Fe	9.8190E-05	2.4001E-06	6.395	-1.119	*
Co	4.2156E-06	9.7654E-08	5.005	0.000	
Ni	7.1300E-05	1.6579E-06	6.234	0.000	

APPENDIX F

List of Acronyms

- 2MASS** 2 Micron All Sky Survey
- AGB** Asymptotic Giant Branch
- CEMP** Carbon enriched metal poor
- CS** central star
- CSPN** central star of the planetary nebula
- EHB** extended horizontal branch
- EUV** extreme ultraviolet
- EUVE** Extreme Ultraviolet Explorer
- ESO** European Southern Observatory
- EXOSAT** European X-Ray Observatory Satellite
- FOV** Field of View
- FRUITY** FRANEC Repository of Updated Isotopic Tables & Yields
- FUSE** Far Ultraviolet Spectroscopic Explorer
- FUV** far-ultraviolet
- FWHM** full width at half maximum
- HB** Horizontal Branch
- HRD** Hertzsprung-Russell diagram
- HST** Hubble Space Telescope

ISM interstellar medium

IUE International Ultraviolet Explorer

LTE local thermodynamic equilibrium

LTP late thermal pulse

MAMA Multi-Anode Microchannel Array

MAST Multimission Archive at Space Telescope Science Institute

MS Main Sequence

NLTE non-local thermodynamical equilibrium

PDCZ pulse-driven convection zones

PN planetary nebula

PNIC Planetary Nebula Image Catalogue

POSS Palomar Observatory Sky Survey

RGB Red Giant Branch

SED spectral energy distribution

SDSS Sloan Digital Sky Survey

STIS Space Telescope Imaging Spectrograph

STScI Space Telescope Science Institute

TMAD Tübingen Model-Atom Database

TMAP Tübingen NLTE Model-Atmosphere Package

TP thermal pulses

UV ultraviolet

VLT Very Large Telescope

WD white dwarf

APPENDIX G

Acknowledgements

A work like this is impossible without the support of many people. I am sure the following list is incomplete and I apologize to all of those who might be forgotten here.

First and foremost I would like to thank my supervisor **Klaus Werner** for giving me the possibility to graduate in a scientific field that caught my interest already during my youth. Thank you for having patience with me, for always helping me out when help was in need, and for giving me the opportunity to visit various conferences already during my time as a student assistant. Thank you for all the experiences I could make during my time here at the institute.

I would like to thank **Thomas Rauch** for his nearly endless patience, for answering all my questions even if I asked them more than just once, and for the many useful ideas of how to improve this thesis.

I would like to thank **Thorsten Nagel** for proofreading this thesis several times. During my time at the institute the persons that shared the office with me changed a couple of times. I would like to thank **Agnes Hoffmann, Johannes Christoph Fleig, and Jens Adamczak** (in chronological order) for providing a good and comfortable working climate in the office.

I would like to thank the rest of the staff at the IAAT. I always felt very welcome during all the years and I couldn't name one to dislike.

I would like to thank my parents **Ute** and **Siegfried Ziegler** for raising me and supporting me in all I do. Without you I would not be the one I am today. You taught me to follow my dreams and I hope I will live up to that.

Thanks to my brother **Frank Ziegler** for being the best brother possible.

I would like to thank the families **Ziegler** and **Vogelgsang** for all the beautiful times we had throughout the years.

I would like to thank the lovely and unique **Phatcharin Saengchan** for opening my eyes for more than just my studies, for all her support during the years and the wonderful time we had and we will have in the future.

Thanks to my two best friends, **Janis Leifeld** and **Ludwig Sterz**, whom I know

since kindergarden and elementary school, respectively. I hope our friendship will stand the ups and downs of a lifetime. I am more than just lucky to have both of you as friends.

My time at the university would have been much less fun without my friends **Daniela Skoropad** and **Christoph Chen**. Thanks for all the times we had including the evenings and long nights of funny conversations and endless board games.

A special thank goes to my physics and astronomy teachers at school **Edwin Gakstatter** and **Jürgen Appel**, respectively, for increasing my fascination for the world of physics and astrophysics. You helped me to pursue my way in studying physics and finally writing this thesis.

Curriculum vitae

06.01.1981	Birth in Bad Mergentheim
08/1991 – 06/2000	Gymnasium with Abitur at the Deutsch-Orden Gymnasium, Bad Mergentheim
09/2001 – 02/2008	Studies of physics at the Eberhard Karls Universität Tübingen
02/2007 – 02/2008	Diploma thesis on “UV Spektralanalyse des Zentralsterns des Planetarischen Nebels NGC 7094” under the super- vision of Prof. K. Werner at the Institute for Astronomy and Astrophysics, Eberhard Karls Universität Tübingen
03/2008 – 5/2012	PhD thesis on “(F)UV Spectral Analysis of 15 Hot, Hydrogen-Rich Central Stars of PNe”, under the supervision of Prof. K. Werner at the Institute for Astronomy and Astrophysics, Eberhard Karls Universität Tübingen

My academic teachers were:

<i>Astronomy and Astrophysics:</i>	K. Werner, T. Nagel, W. Kley, J. Frauendiener, J. Peitz
<i>Experimental physics:</i>	G. J. Wagner, C. Zimmermann, D. Kölle, H. Clement, M. Weitz
<i>Theoretical physics:</i>	H. Reinhardt, M. Liu
<i>Mathematics:</i>	M. Wolff, U. Schlotterbeck
<i>Chemistry:</i>	J. Strähle

